UNIVERSITY OF CALIFORNIA SAN DIEGO

Exploring Structural Biological Materials and Their Structure-Property Relationships in Mineralized and Non-mineralized Systems

A dissertation submitted in partial satisfaction of the requirements for the degree

Doctor of Philosophy

in

Materials Science and Engineering

by

Audrey Velasco-Hogan

Committee in charge:

Professor Marc A. Meyers, Chair
Professor Javier Garay
Professor Olivia Graeve
Professor Vlado Lubarda
Professor Michael Tolley

2021

This Dissertation of Audrey Velasco-Hogan is approved, and it is acceptable in quality and form for publication on microfilm and electronically.

University of California San Diego

2021

DEDICATION

For my mother who helped me in all things great and small and my beloved Nova and Bryce who were by my side every step of the way.

TABLE OF CONTENTS

LIST OF FIGURES

LIST OF TABLES

ACKNOWLEDGEMENTS

Chapter 1, in part, is published as a review article in *Advanced Materials*, authored by A. Velasco-Hogan, J. Xu, and M. A. Meyers. The dissertation author is the primary investigator and author on this publication.

Chapter 2, in part, is published as a review article in *Journal of Materials Research and Technology*, authored by B. S. Lazarus, A. Velasco-Hogan, T. Gómez-del Río, M. A. Meyers, and I. Jasiuk. The dissertation author is the second author on this publication.

Chapter 2, in part, is under review in *iScience* authored by B.S. Lazarus, C. Charul, A. Velasco-Hogan, I. Jasiuk, and M. A. Meyers. The dissertation author is the third author on this publication.

Chapter 3, in full, is published in *Matter* authored by A. Velasco-Hogan, D. Deheyn, M. Koch, B. Nothdurft, E. Arzt, and M. A. Meyers. The dissertation author is the primary investigator and author on this publication.

Chapter 4, in part, is published in the *Journal of the Mechanical Behavior of Biomedical Materials,* authored by A. Velasco-Hogan and M. A. Meyers. The dissertation author is the primary investigator and author on this publication.

Chapter 5, in part, is under review in *Acta Biomaterialia* authored by A. Velasco-Hogan, W. Huang, C. Serrano, D. Kisailus, and M. A. Meyers. The dissertation author is the primary investigator and first author of this work.

Chapter 6, in part, is in preparation for submission authored by A. Velasco-Hogan, C. Chadha, I. Jasiuk, and M. A. Meyers. The dissertation author is the primary investigator and co-first author of this work. This work is funded by the National Science Foundation Mechanics of Materials and Structures Program with corresponding grant number 1926361.

Chapter 7, in part, is published in *Materials Science and Engineering C,* authored by T. N. Sullivan, T. Hung, A. Velasco-Hogan, and M. A. Meyers. The dissertation author is the third author on this work.

Chapter 8 is under preparation for submission authored by A. Velasco-Hogan, and M. A. Meyers. The dissertation author is the primary author on this work.

The authors thank the generosity of Prof. Michael Tolley and Ben Shih for assistance and allowing us to use their 3D printer which made much of this work viable. The authors thank Isaac Cabrera for his insightful discussions on the feather rachis. We thank the San Diego Zoo (April Gorow, Research Coordinator) for providing feather samples to us. This work is supported by the AFOSR MURI (AFSOR-FA9550-15-1-0009). This work was performed in part at the San Diego Nanotechnology Infrastructure (SDNI) of UCSD, a member of the National Nanotechnology Coordinated Infrastructure (NNCI), which is supported by the National Science Foundation (Grant ECCS-1542148).

The measurements on piranha were accomplished during the Roosevelt-Rondon Centennial Expedition, from 2014 to 2016. The participation of the New York Explorers Club by giving it an official Flag Expedition status, is warmly appreciated, as are the efforts of Colonels Hiram Reis de Silva and Ivan Carlos Angonese of the Brazilian Army. Drs. Julie and Tim Radke of the San Diego Explorers Club participated in the Paraguay River journey and their contribution was essential. The Brazilian Army provided logistic support which enabled the expedition.

We thank Prof. Joanna McKittrick for all of her contributions and inspiration to the field of structural biological materials.

VITA

2021 Ph.D. Materials Science and Engineering

University of California San Diego

Advisor: Marc André Meyers

2017 M.S. Materials Science and Engineering

University of California San Diego

2015 B.S. Chemistry

University of California Santa Barbara

PUBLICATIONS

Velasco-Hogan, Audrey and Meyers, Marc André. "Structure and Mechanical Properties of Primary Avian Flight Feathers Corresponding to Various Flight Styles", *In Preparation*

Velasco-Hogan, Audrey; Chada, Charul; Jasiuk, Iwona; and Meyers, Marc André. "Bioinspired Reinforced Tubule Structures", *In Preparation*

Velasco-Hogan, Audrey; Huang, Wei; Kisailus, David; and Meyers, Marc André. "A Comparative Study on Tooth Structure, Mechanical Properties, and Diet Specialization of Piranha and Pacu (Serrasalmidae)", *Acta Biomaterialia. Under Review*

Lazarus, Benjamin; Chada, Charul; **Velasco-Hogan Audrey;** Jasiuk, Iwona; Barbosa, Josiane; and Meyers, Marc André. "Engineering with Keratin: A Functional Material and a Source of Bioinspiration", *iScience* (2021).

Velasco-Hogan, Audrey and Meyers, Marc André. "Bite Force Mechanics and Allometry of the Piranha (Serrasalmidae)", *Journal of the Mechanical Behavior of Biomedical Materials* (2021). doi.org/10.1016/j.jmbbm.2020.104296

Lazarus, Benjamin; **Velasco-Hogan**, **Audrey;** Gómez-del Río, Teresa; Meyers, Marc André; and Jasiuk, Iwona. "A Review of Impact Resistant Biological Materials and Bioinspired Designs", *Journal of Materials Research and Technology* (2020). *doi.org/10.1016/j.jmrt.2020.10.062*

Sullivan, Tarah; Hung, Tzu-Tying, **Velasco-Hogan**, **Audrey;** and Meyers, Marc André. "Bioinspired Avian Feather Designs", *Mater. Sci. Eng. C* (2019). doi:10.1016/j.msec.2019.110066

Velasco-Hogan, **Audrey;** Deheyn, Dimitri D.; Koch, Marcus; Nothdurft, Birgit; Arzt, Eduard, Meyers, Marc André. "On the Nature of the Transparent Teeth of the Deep-Sea Dragonfish, Aristostomias scintillans", *Matter* (2019). doi:10.1016/j.matt.2019.05.010

Velasco-Hogan, Audrey; Xu, Jun; Meyers, Marc André. "Additive Manufacturing as a Method to Design and Optimize Bioinspired Structures", *Advanced Materials* (2018). doi:10.1002/adma.201800940

ABSTRACT OF THE DISSERTATION

Exploring Structural Biological Materials and Their Structure-Property Relationships in Mineralized and Non-mineralized Systems

by

Audrey Velasco-Hogan

Doctor of Philosophy in Materials Science and Engineering

University of California San Diego, 2021

Professor Marc André Meyers, Chair

This work is dedicated to characterizing unexplored structural biological materials in both mineralized and non-mineralized systems including the transparent teeth of the deep-sea dragonfish, a comparative study on the piranha and pacu teeth, and the feather rachis of primary flight feathers from birds with various flight styles. The insights gained are used to better understand how the structure across multiple length scales (micro, meso, and macro) relates to the optimization of tough, stiff, lightweight, energy absorbent, and impact resistant materials. We propose that these findings can be used to develop bioinspired structural designs for tailorable mechanical performance.

The transparent dragonfish teeth are found to be composed of nanostructured hydroxyapatite (~20 nm grain size) and collagen. They are devoid of microscale features such as microtubules which are typically found in the dentin layer. The nanoscale structure is responsible for the reduced Rayleigh light scattering and the increase in hardness and stiffness in the dentin layer. The optical transmittance of the teeth is found to be within the range of ~38% to ~78% and is found to depend on tooth location (tip, middle, base) and wavelength. The tip of the tooth is the most transparent to red light (700 nm) and least transparent to blue light (450 nm). We suggest that the nanostructured design of the transparent teeth enables predatory success as it makes its wide-open mouth armed with teeth effectively disappear against the darkness of the deep-sea.

The relationship between feeding mechanics and structure-property relationships are investigated with the comparison of two closely related species: the piranha (carnivorous) and the pacu (herbivorous). Typically, the morphology and form of the tooth are only used to indicate feeding performance, ignoring the hierarchical nature and relative tooth position within the jaw. Herein we investigate both types of teeth across multiple length scales and relate the findings to how the tooth performs during feeding. We suggest that tooth form, enamel thickness, structuring of the dentin-enamel junction, and microstructural characteristics of enamel influences the biomechanics required for each style of feeding.

Tubules are not only found in the dentin layer of teeth but also in horns, hooves, and many other natural energy absorbent materials. However, the effects of porosity, radius, or degree of reinforcing mineralization and the synergy with other design motifs (suture and gradient structures) on the mechanical properties have not been fully explored. We propose to 3D print tubule architectures to parametrically explore the above-mentioned effects in quasi-static

compression, fracture toughness, drop tower testing, Hopkinson bar, and dynamic mechanical analysis and compare them with numerical models.

The mechanics of the feather shaft are explored through 3D printed bioinspired designs to investigate structure-property relationships with respect to flight. The feather shaft is the predominantly load bearing component of the feather and is the focus of this work. Sandwich structures inspired by the feather shaft are printed with a foam core and without a foam core to investigate the flexural properties. The flexural strength of the sandwich structure increases with the addition of a foam core, due to the increase in the moment of inertia. However, the stiffness remains the same despite having or not having a foam core. Stiffness is only determined by the cortex since the foam provides negligible stiffness .

Chapter 1: Introduction and Objectives

1.1 Bioinspiration and Materials Science

The emerging field of bioinspiration—which relies on the translation of materials science and engineering principles to biological materials—is rapidly advancing [1–7]. This involves the use of a materials science and engineering approach to better understand the success of biological materials and how they have evolved to their environments with the ultimate goal of providing effective solutions for bioinspired design.

Biological materials are unique in their structures and functions. This sets them apart from engineered materials and provides the underling motivation for exploration. As summarized in Arzt's heptahedron[8,9], biological materials have at least seven distinct characteristics including:

- *Self-assembly*. Precursors, such as biological molecules, self-assemble to form a predetermined structure. Self-assembly and self-organization works across multiple length scales originating at the nanoscale to the macroscale. The most ubiquitous example is the folding of proteins. This synthetic method is also known as a bottom-up[10] approach which is in contrast to many traditional manufacturing processes. Typically, engineered materials are formed from bulk processing dictated at the macroscale. This lends itself difficult to control nanoscale features.
- *Self-healing.* The regenerative abilities of living biological materials is due to the cellular and vascularity of the organism. This is very difficult to accomplish in synthetic materials.
- *Evolution and environmental.* Biological materials have been in the process of evolution driven by natural selection for the past three billion years. Synthetic materials, on the other hand, have only been developed for the past thousand years at most.

- *Hydration.* Many biological materials thrive in a hydrated state with notable exceptions of few highly mineralized materials. The level of hydration influences their mechanical properties. Dramatic changes can occur when biological materials are dehydrated. Hydration effects are known to serve as reversible actuation mechanisms in response to environmental changes for effective seed dispersal [11].
- *Synthesized at ambient temperatures and pressures.* Unlike many traditional synthetic materials, biological materials are inherently synthesized at ambient temperatures (-50 to $+50^0$C) and pressures. Since natural materials do not have furnaces at their disposal, they must rely on alternative methods to achieve desirable properties. This often finds itself in their exceptional ability to organize internal components and structures.
- *Multi-functional.* Many tissues have more than one function, and this provides economy of space and mass. For example, the arthropod exoskeleton provides structural support for the body, protection from predators, serves as an attachment to the muscles, and controls the exchange with fluids with the surroundings, and is able to resist mechanical loads [12]. Since the exoskeleton can perform all of these functions, arthropods can conserve the need for additional specialized tissues.
- *Hierarchical*. The hierarchical structure of many biological materials is intrinsically tied to their mechanical properties. The overall architecture is defined by distinctive structures at the nano-, micro-, meso-, and ultra-levels. These levels are known to work together synergistically. One material that highlights the importance of hierarchy is the structure of bone, which has been described extensively in numerous reviews [13–15]. Collagen fibers and hydroxyapatite minerals are organized at the nanoscale to effectively build the microscale features consisting of lamellae sheets wrapped in concentric layers. The

microstructure ultimately forms the macrostructure defined as either cortical or cancellous bone.

Many of the desirable materials properties of biological materials, such as high stiffness and toughness, are due to the structural integration of an organic and a mineral phase. The organic component provides tensile strength, while the mineral component contributes compressive strength and stiffness. This is a key feature responsible for the superior mechanical response when compared engineered materials.

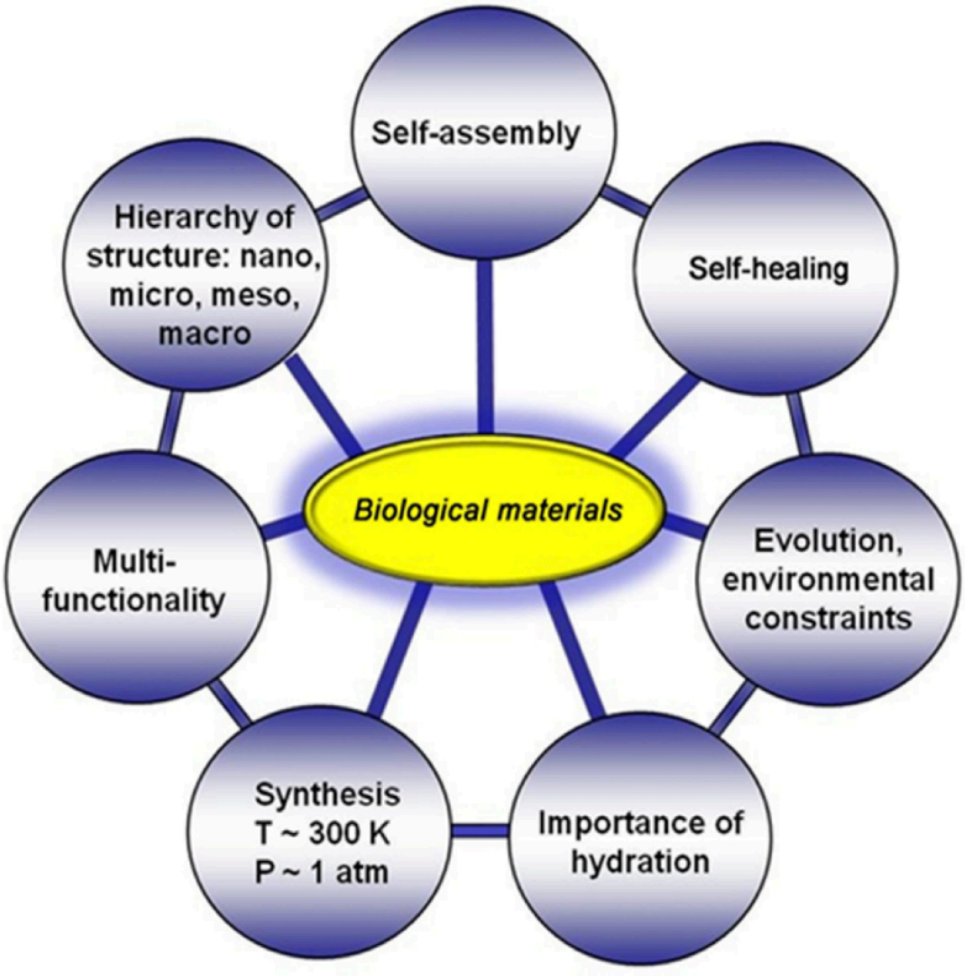

Figure 1.1 Seven unique characteristics of biological materials: the Arzt heptahedron. Adapted with permission [8]. Copyright 2006, Elsevier.

Biological materials are known to exhibit a desirable balance between stiffness and toughness. First introduced by Ashby et al.[16] and then modified by Fratzl et al.[15], Espinosa et al.[17] and Zavattieri et al.[18], Figure 2 describes the difference in trends associated with stiffness and toughness between engineered and biological materials. For engineered materials, as stiffness increases toughness drastically decreases; however, we see the inverse occur for biological materials. For example, ceramics have a comparable stiffness to bone yet bone is much tougher (Figure 1.2). This is primarily due to the aforementioned characteristics of biological materials: hierarchical structure and their composite nature (Figure 1.1). Bone relies on varying mechanical properties at different structural levels to mitigate crack propagation and enhance toughness while maintaining stiffness.

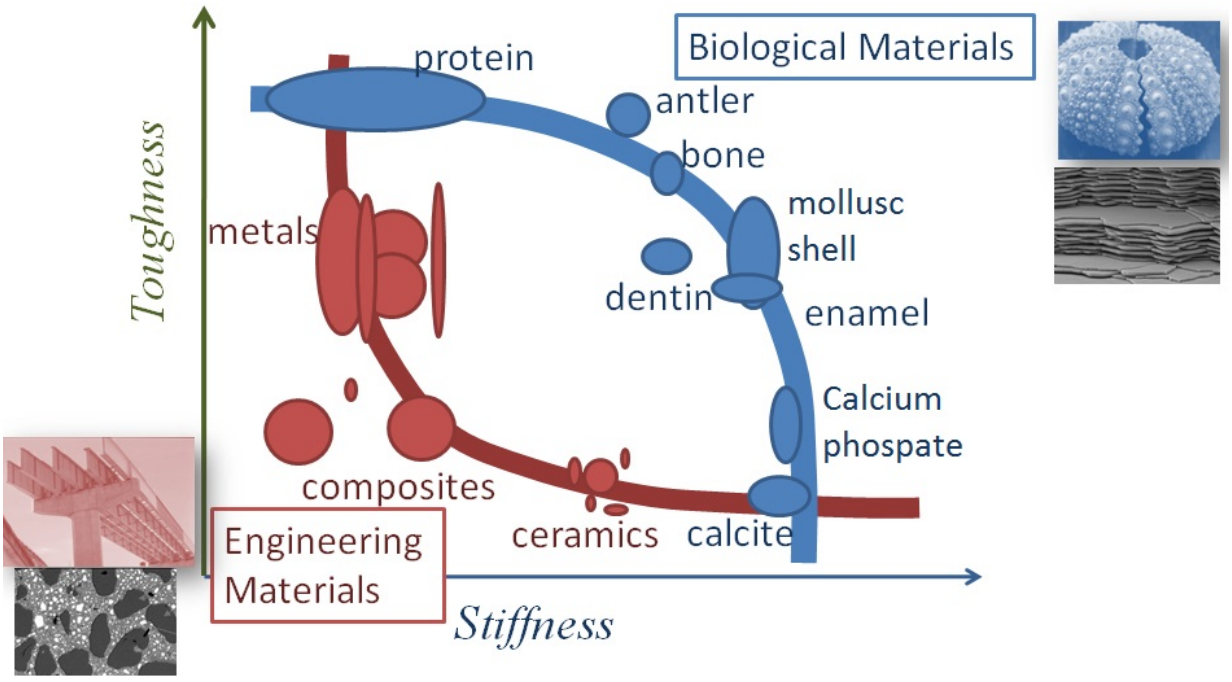

Figure 1.2 Relationship between toughness and stiffness for synthetic and biological materials. Notice that engineering materials have a drastic decrease in toughness with an increase in stiffness while biological materials can maintain toughness despite an increase in stiffness until a critical value. Reproduced with permission.[18] Copyright 2015, Elsevier

While there are many components of biological materials that make them suitable candidates for inspiration, this work focuses on the structure-mechanical property relationship. Throughout the biological realm there are a few design motifs that have proven to be structurally integral. These common structural designs were first identified by Naleway et al.[19] using an approach introduced by Meyers et al.[2]. These eight motifs are collectively known as *structural elements* and occur in different species but often serve the same function. These have developed through convergent evolution as shown in Figure 1.3 and are described below:

- *Fibrous structures.* They have high tensile strength when aligned in a single direction, and under compression readily undergo buckling resulting in low compressive strength.
- *Helical/Bouligand structures*. Common to fibrous or composite materials, they are characterized by the rotation of the fibers in sequential layers. Enhanced toughness results from the difficulty in propagating cracks; in-plane isotropy of strength and stiffness can be achieved with fibers.
- *Gradient structures.* Materials and interfaces that accommodate property mismatch (e.g., elastic modulus) through a gradual transition. This design aids in increasing toughness by avoiding the buildup of interfacial mismatch stress.
- *Composite/Layered structures.* Complex composites that increase the toughness of (most commonly) brittle materials through the introduction of interfaces. A classic example is the nacreous structure in shells, such as abalone.
- *Tubular structures*. Organized porosity that allows for energy absorption and crack deflection.
- *Cellular structures.* Lightweight porous or foam architectures that provide directed stress distribution and energy absorption.

- *Suture interfaces.* Compliant interlocking seams that connect stiffer components.
- *Articulated structures.* Overlapping plates that slide past each other to make a rigid yet flexible surface suitable for armor. Primary examples are fish and pangolin scales and the tail of the seahorse.

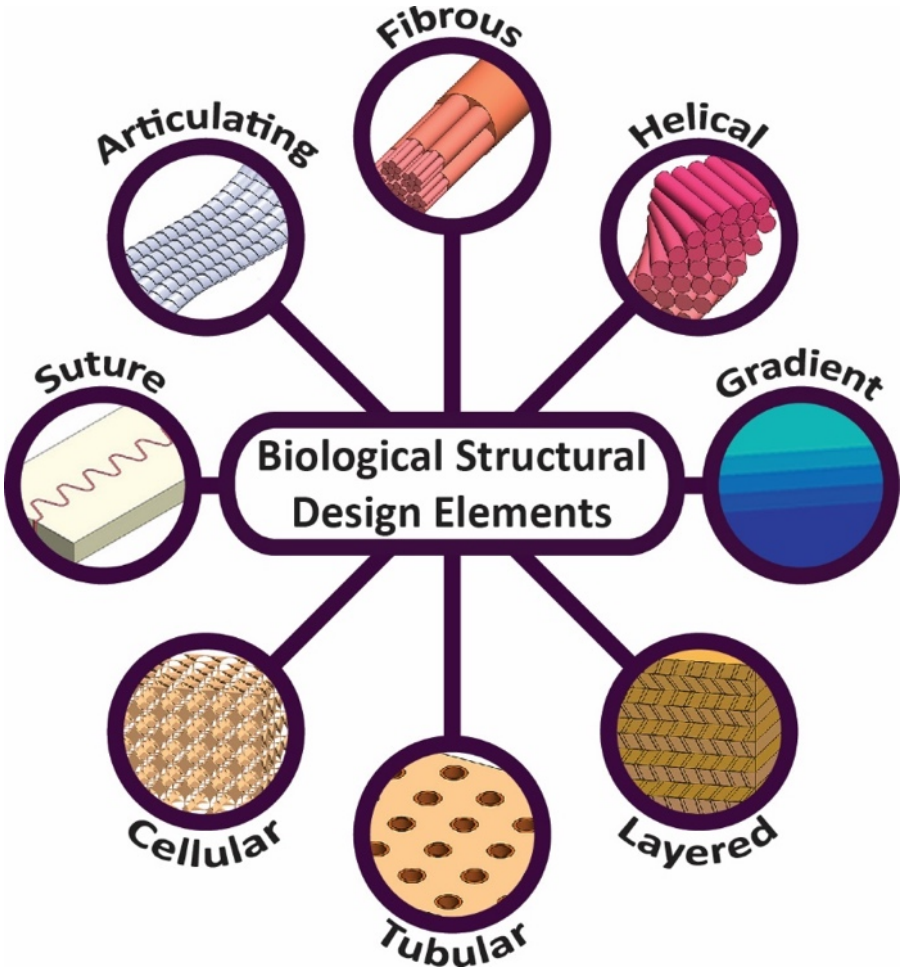

Figure 1.3 The eight principal structural design elements: motifs that appear in different species through the processes of convergent evolution and parallelism. Reproduced with permission.[19] Copyright 2015, Wiley.

This work will explore the advantages of tubular, cellular, layered, and suture structures to develop bioinspired structural designs. These reoccurring structures are predominantly found in teeth, horns, hooves (tubular, layered, and sutured), and feathers (cellular and sandwich structures).

While they have been extensively observed in nature, there is still much that can be gained from isolating and fabricating various designs for tailorable applications. This includes parametric studies in compression, bending, fracture toughness, impact testing, and dynamic mechanical analysis and comparison to analytical and numerical models (finite element analysis) to better understand strength, stiffness, and energy dissipation mechanisms to name a few.

1.2 3D Printing as a Technique to Design Bioinspired Materials

Traditional manufacturing methods have limited the creation of bioinspired designs due to their inability to synthesize and assemble materials with different hierarchical. With recent advancements in Additive Manufacturing (AM), which utilizes a bottom-up approach analogous to nature, this limitation has been resolved. Materials found in nature are synthesized via a bottom-up approach where their final structure is encoded in their precursors which self-assemble to the prescribed form. The assembly of building blocks across multiple length scales leads to the generation of hierarchical structures. On the contrary, traditional manufacturing processes use the top-down approach, where the desired material is formed from the reduction of the bulk material or by bulk solidification. This method, beginning with the bulk material, makes it difficult to generate hierarchies across many length scales. While many bottom-up manufacturing processes exist, such as physical vapor deposition (PVD), chemical vapor deposition (CVD), and sputtering they have severe size and thickness limitations and do not lend themselves well to the scale-up requirements of structural materials. AM has been the focus of significant research effort in recent years as it uses a bottom-up approach and can be scaled up. Although AM is not currently ideal for producing a large quantity of items at once, it opens a plethora of opportunities to prototype and research complex structures.

In the field of biological materials science, AM is being used in two principal modes: (1) to better understand the mechanical response of biological materials and to identify the governing mechanisms; and (2) in implementation of bioinspired designs. The use of AM to generate bioinspired materials and designs goes beyond the demonstration of principles. As Figure 1.4 indicates, the 3D printing of prototypes is followed by mechanical testing which provides guidelines for modifications and subsequent optimization. Since the synthetic materials used in AM have different properties than natural materials, the bioinspired design parameters must be modified accordingly. This sequential manufacturing and testing leads to a more complete understanding of the deformation, damage, and failure processes. Additionally, theoretical and computational models are used to complement AM experimental results by providing supportive evidence and even going beyond the limitations of AM to extend the scope of the study. Additive manufacturing can provide a greater depth of knowledge when used in combination with theoretical and computational analyses.

This work will rely primarily on the use of AM to provide a greater insight to the structures revealed in the biological systems studied (teeth – suture interface, hooves – tubules, and feathers – sandwich structures) and how their geometries influence mechanical properties and failure mechanisms. When appropriate, the results from AM and subsequent mechanical testing will be compared with analytical and numerical modeling with use of finite element analysis (FEA). This approach will provide a greater understanding of how specific structures contribute to the overall function of the biological material. Additionally, the structures in question which are often found on the micro- and meso-scale will need to be scaled up in size and simplified for both effective printing and mechanical testing.

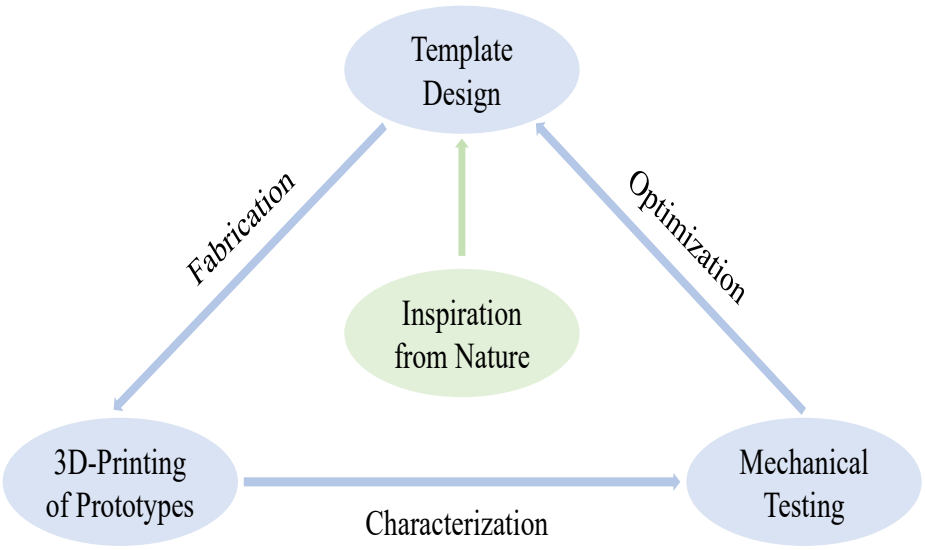

Figure 1.4 Process map detailing steps in the use of additive manufacturing for exploring biological materials and bioinspired design.[6]

While there are many 3D printing systems on the market, PolyJet multi-material technology (Stratasys Ltd.) is a favored printer among developing bioinspired designs due to its multi-material printing capabilities. PolyJet selectively jets liquid photopolymer droplets that are immediately cured by ultraviolet lamps in a layer-by-layer fashion. This feature ensures that upon completion of the layer-by-layer process, the build is completely cured without the need to immerse the object in a bath of uncured material. This decreases the amount of time required. Most importantly, its ability to simultaneously jet-deposit multiple materials with different mechanical properties distinguishes it from traditional 3D-printing methods. There are eight printheads capable of printing up to three different materials which can control local composition.[20] Both rigid and flexible materials can be printed simultaneously. This unique element is advantageous for the design of bioinspired materials that are often composites or have gradients in material properties. PolyJet technology is able to achieve a high resolution of 600 dots per inch (dpi) and the thickness of each layer is 16-30 microns.[20] This resolution is compared to other AM

techniques in Figure 1.5. Support material is needed to provide stability to jetted droplets and can be easily removed by hand or with a water jet. This technique is widely used to develop bioinspired structures.[6] A major reason for its popularity is its ability to print multiple materials simultaneously and it ability to produce high resolution samples.

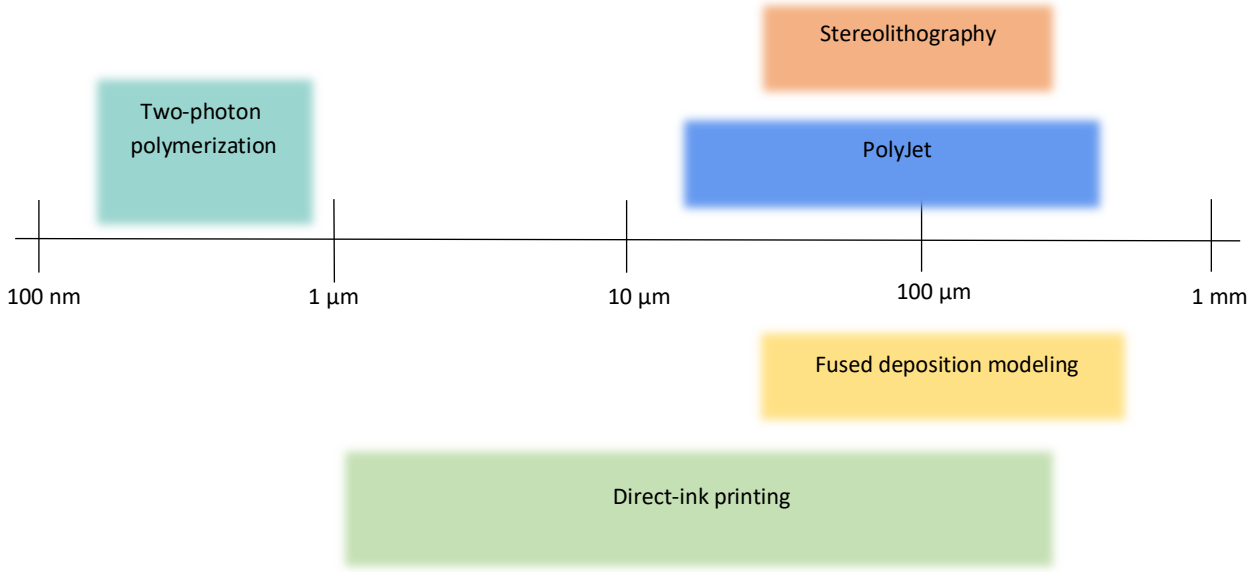

Figure 1.5 The minimum size ranges of features produced by principal AM printing methods. Adapted with permission.[21] Copyright Springer Nature, 2016.

Multi-material 3D printing allows for the generation of variable stiffness composites necessary to fully characterize and explore the mechanisms at hand that promote damage tolerance. The composite nature of biological materials is a leading feature that contributes to their exceptional resistance to damage. Therefore, it is desirable to both understand and replicate this structure synthetically. Bone and nacre are ubiquitous examples of biological composites and have inspired many studies.

1.2.1 3D Printed Layered Composites Inspired by Bone

Dimas et al.[22] investigated the fracture response in three different bioinspired layered composite materials: bone-like, biocalcite-like, and rotated-bone (helicoidal with sequential layers at different angles to the longitudinal axes), mimicking the osteon[23] structure. Comparing the three different architectures provides insight into the role that geometry plays in organizing stiff and soft phases. All composites were made using the PolyJet multi-material 3D-printing technique (Stratasys Ltd.) with 70% volume fraction of the rigid plastic and 20% volume faction of the softer phase. Deformation and fracture mechanics testing were performed on the three prototypes and compared to bulk samples of each constituent. As expected, the composites outperformed their constituents which is attributed to geometrical toughening. Toughening occurs due to the introduction of a significant stiffness mismatch which allows the crack to propagate through the more compliant material. The path that the crack travels is dictated by the topology

The bone-like topology, which can be described as a brick-and-mortar-like structure with stiff plates in a compliant matrix, generates significant delocalization of stress and strain (Figure 1.6 a,b). The compliant phase is continuous throughout the sample which allows it to distribute stress and strain more effectively. During the initial stages of crack propagation, non-localized failure occurs in the vertical compliant phase while the horizontal portion undergoes shear strain holding the system together. The AM samples did not fail at the interfaces which suggests that interfacial adhesion is sufficiently strong to keep the constituent materials together.

Rotated bone-like topology has an initial characteristic zigzag fracture path through the compliant phase which is able to continuously transfer the longitudinal strain (Figure 1.6 c). This is seen in both the experimental and computational systems. It is more energetically favorable for the crack to propagate in the compliant matrix which forces it to take a longer path and induces

toughening. The material is able to sustain increased deformation after significant loading due to delocalization of the soft matrix upon the onset of crack-tip blunting.

In the biocalcite-like topology, unlike the bone-like and rotated-bone-like, the stiff component is the continuous matrix, not the soft phase. This did not allow for the crack to propagate continuously through the soft phase resulting in a different fracture mechanism. The crack no longer meanders through the compliant matrix, but results in a rugged fractured surface as it attempts to minimize the distance it travels (Figure 1.6 d).

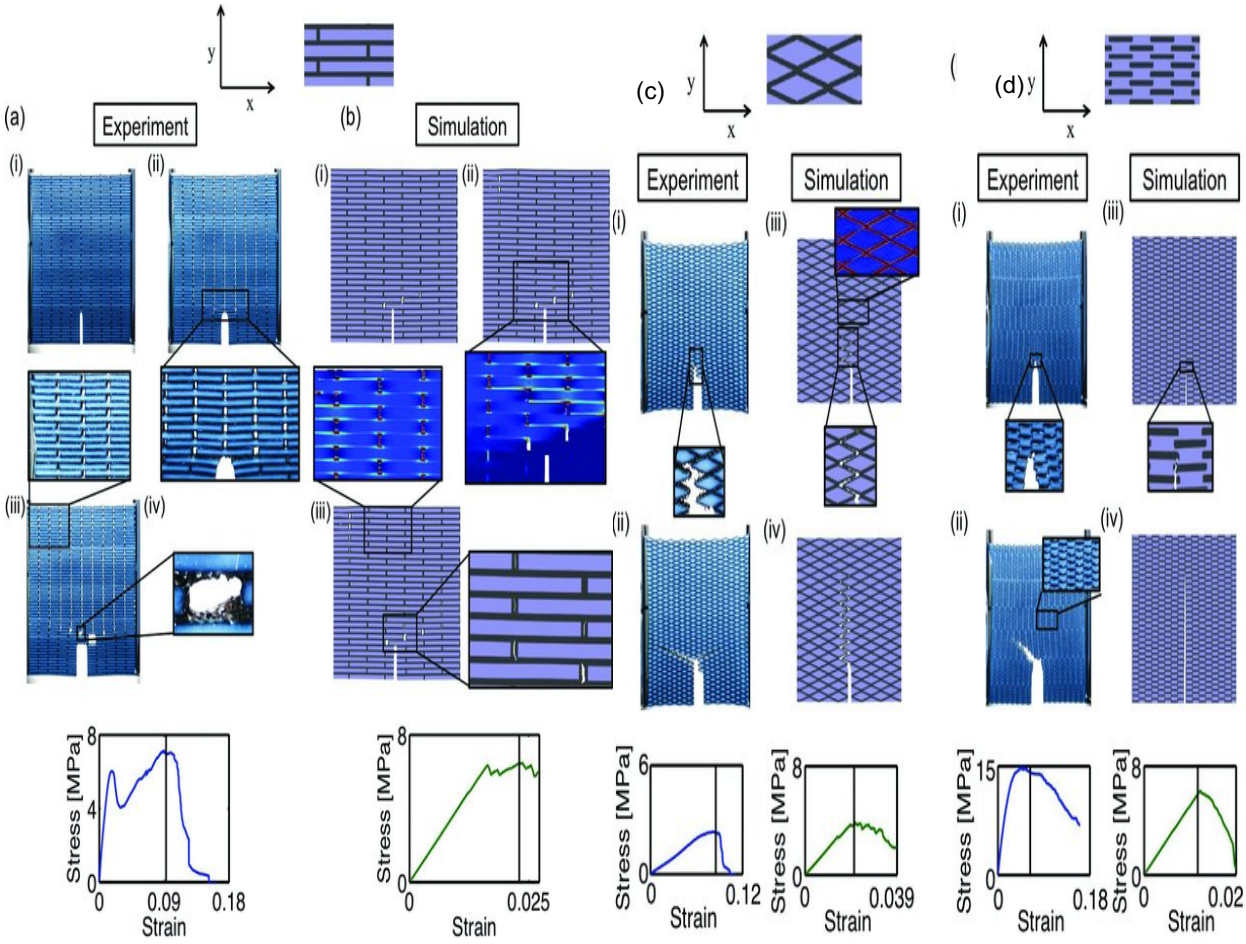

Figure 1.6 Comparison of deformation and fracture mechanisms in AM samples and simulation. a) The 3D-printed bone-like structure. b) Simulation of the bone-like topology. c) The rotated-bone-like structure. D) The bio-calcite-like structure. i-iii) Show evolution of fracture in both samples over time. Adapted with permission.[22] Copyright 2013, Wiley.

1.2.2 3D Printed Suture Interfaces Inspired by Interfaces in Nature

Sutures are a fundamental design motif found in nature consisting of compliant interlocking seams that connect stiffer components. They are found across a diverse range of biological materials (boxfish plates[24], skull bones[25], and turtle shells[26,27]) and contribute to the remarkable mechanical properties such as stiffness, strength, and toughness of such materials (Figure 1.7). Sutures can enhance the functionality of inherently brittle materials. It has been known that the geometry of the suture interface influences the mechanical properties. 3D printing has been recently utilized to identify the geometrical effects of sutures and validate analytical and computational models [28,29].

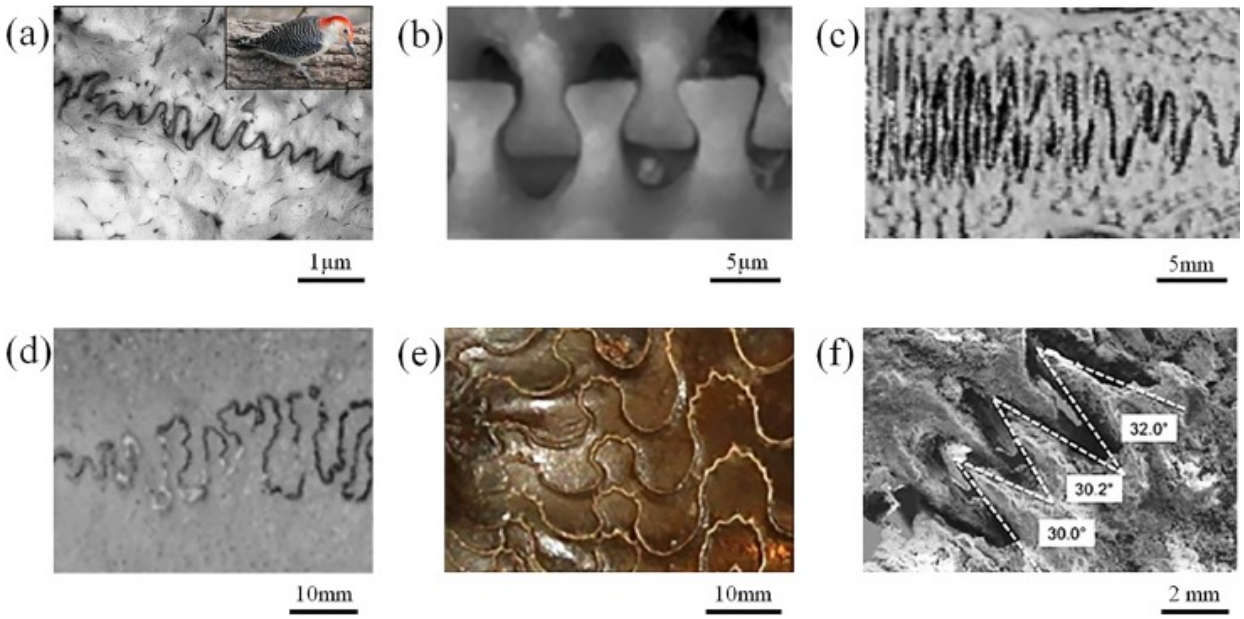

Figure 1.7 Examples of sutured interfaces found in nature and their various geometries: (a) red-bellied woodpecker, (b) diatom frustule, (c) stickleback fish scales, (d) cranial sutures, (e) ammonite shell, (f) leatherback sea turtle shell. Reproduced with permission.[28] Copyright 2017, Elsevier.

An important feature of sutures is the nonlinear traction behavior that occurs due to frictional pullout of the interlocking structures which accounts for strength and energy absorption. Malik et al.[28] characterized the pullout response of an interlocking jigsaw-like suture using AM and mechanical testing to verify and optimize analytical and finite element models. Jigsaw-like interlocked sutures were fabricated using digital light processing technology (Micro HiRes Machine, EnvisionTech) made with ABS (a relatively brittle polymer) with different interlocking angles: $\theta = 5°, 10°, 15°, 20°$ as shown in Figure 1.8.

Mechanical pull tests were performed and forces and displacements were measured to determine the full pullout response in terms of stiffness, strength, maximum elongation, and energy absorption and the effect of the interlocking angle [28]. It was shown that as the interlocking angle increases, the stiffness, strength, maximum elongation, and energy absorption all increased up to a critical angle (Figure 1.8). The greatest angle ($20°$) fractured prematurely and showed cracks initiating at the edges of the contact region. The increase in strength with an increase in interlocking angle can be attributed to geometrical interlocking, which resists pullout as the tabs stay in contact over a longer pullout distance.

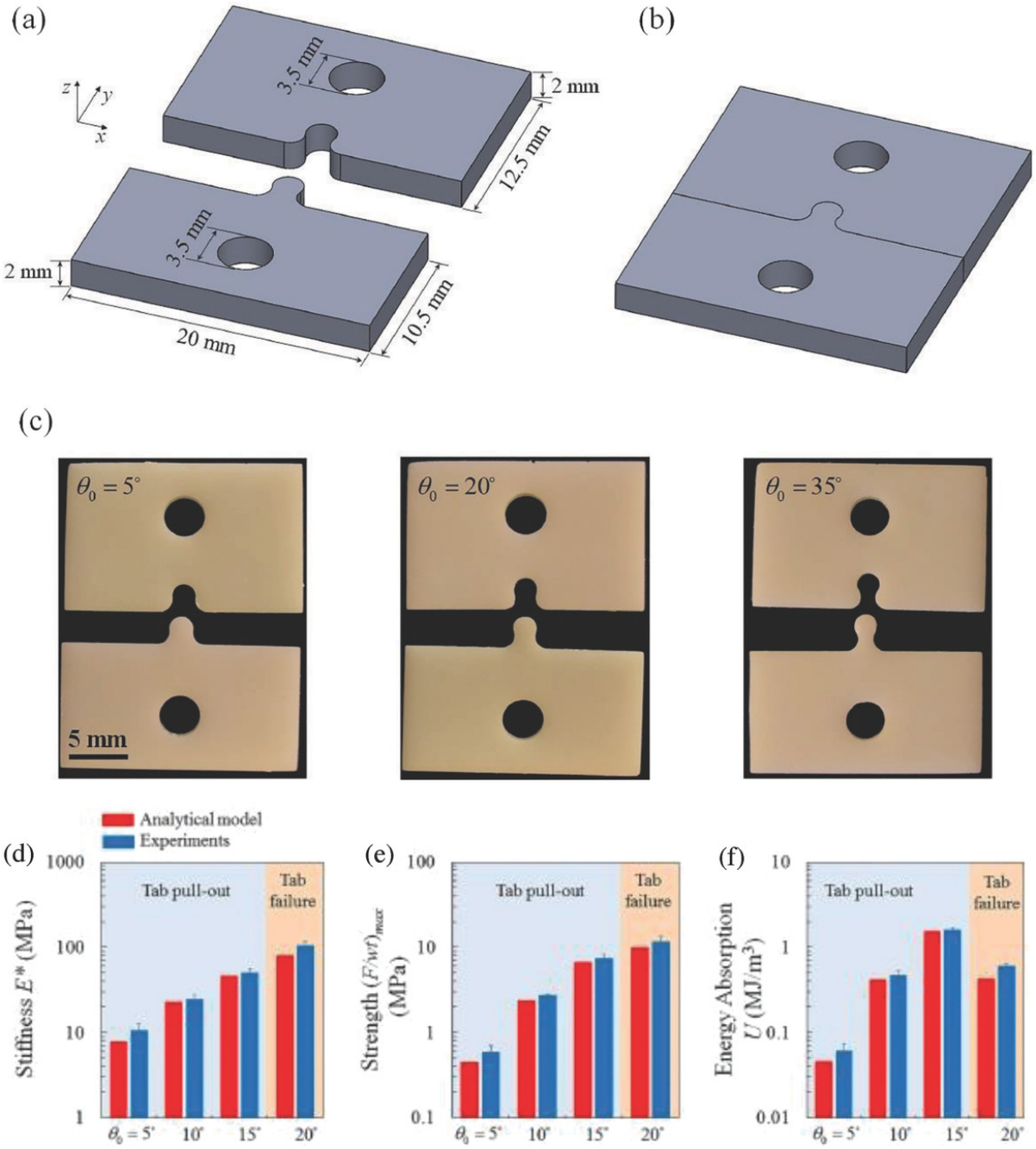

Figure 1.8 Examples of "jigsaw" sutured samples. a) CAD design of the "jigsaw" pieces of the sutures. b) Interlocking mechanism of the sutures. c) Images of 3D-printed prototypes with interlocking angles of 5°, 20°, and 35°. d) Stiffness as a function of interlocking angle. e) Strength as a function of interlocking angle. f) Energy absorption as a function of interlocking angle. Reproduced with permission.[28] Copyright 2017, Elsevier.

Finite element simulations were used to validate the mechanisms explored in the AM samples and to develop a platform that can be used to study more complex structures by including analysis of the coefficient of friction. This is a common trend, which involves using simulations to go beyond what is learned from the AM models. Their procedure tested 80 combinations of interlocking angle and coefficient of frictions. Increasing either the interlocking angle or the coefficient of friction improves the pullout response, but, as a consequence, introduces undesirable tensile stresses. Therefore, there exists an optimal angle and coefficient of friction that can maximize the pullout response. The optimization results for stiffness, strength, and extension showed that a maximum occurs when the coefficient of friction is zero and the interlocking angle is 13°. This occurs because the elimination of friction reduces tensile stresses. However, this optimization is not beneficial for energy absorption, as friction is a predominant mechanism to absorb energy, which results in poor toughness.

Overall, this study uses AM to generate tailored geometries to better understand the pullout response in relation to stiffness, strength, elongation, and energy absorption. AM provides a robust platform to validate and optimize models of complex geometries to provide greater insight into the fundamental mechanisms that account for the remarkable properties of suture-like features inspired by biological materials.

Additive manufacturing is becoming an integral component of exploring biological and bioinspired materials. It provides the capabilities to generate intricate designs needed to investigate geometrical effects on mechanical performance in bioinspired structures. AM is a rapidly evolving technique and while many methods exist for the design and fabrication of bioinspired materials, it is evident that Polyjet multi-material printing is an integral player in this field. Nature's reliance

on the integration of both soft and hard materials to achieve exceptional properties makes multi-material printing a necessity.

1.2.3 Current Challenges and Future Development of AM for Bioinspired Design

While AM has taken great strides in the past decade to prove itself useful in the development of bioinspired structures, there are still challenges that need to be overcome. A major concern is the inherent trade-off between resolution, build volume, speed, and cost. For amplified resolutions and increased build volume, the speed generally decreases, which in turn increases the cost of production. The following represent the most prevalent challenges:

- *Multi-scale.* The remarkable properties of biological materials are predominantly attributed to the organization of design from the nano- to macro-scale which allows for the combination of different toughening mechanisms along multiple length scales.[4,30] While commercial AM has the widest range of multi-scalability when compared to other traditional methods[31] (due to the diversity of printers and their resolutions), there does not exist a method to print continuously from nano- to macro-dimensions. Two-photon polymerization can reach resolutions in the nanoscale with an upper bound of ~1 μm.[32] On the other hand, many techniques (direct ink writing, photocurable inkjet, and stereolithography) can readily produce complex geometries with micrometer dimensions, but fail to achieve minimum features less than ~1 μm. True bioinspired constructs necessitate the control of material composition and structure from across great length scales which requires advancements in AM.
- *Multi-material interfaces*. Multi-material printing enables the comparable representation of biological composites; however, uncontrollable mixing occurs at the interface which

leads to unpredictable properties.[18] This topic is currently being explored and it is understood that the combinations of different materials, load directions, and mixing ratios all contribute to variations in interfacial properties with multiple consequences.[33] There exists a threshold above which the “composite effect” (when the size of the feature is two orders of magnitude larger than the inclusion size)[33] needs to be taken into account. The interfacial properties of multi-material printing need to be fully investigated to better control and tailor bioinspired prototypes.

- *Inherent defect control.* Additive manufacturing systems are known to produce prototypes with minor defects due to their inability to detect and correct errors during production.[34] These compounding errors often lead to voids and inconsistent prototypes. This is inherently detrimental to studying bioinspired designs, as structure and geometry play key roles in property determination. A proposed solution to quality assessment is the use of software imaging analysis.[34] This solution allows for the detection of defects where the filament has not been applied. While this technique only detects limited defects, it will be necessary to develop more robust solutions that can identify and correct a range of defects. It is important to note that defects are inherent in biological materials and can contribute to toughening and strengthening. These defects arise from the fact that most biological materials are multifunctional, which have channels or pores creating structural voids or empty spaces in the material. For example, the pores in bone tissue direct load from weak to strong areas. AM does not have to produce perfect architectures, but when performing a systematic study of various geometries on crack propagation the introduction of unwanted defects can introduce unintended and disruptive features as seen in the study by Dimas et al.[22].

For the future direction of the field of biological materials and AM, it will be important to increase functionality of fabricated components with the use of multi-process 3D printing. Multi-process 3D printing combines complementary processes to potentially include electronic, electromagnetic, optical, chemical, and thermal features [35]. Biological materials are known for their multifunctional capabilities[19], for example fish scales[36] can provide camouflage, mechanical protection, flexibility, and low water drag. A fundamental understanding of these systems can be applied to bioinspired material designs. To do so it will become necessary to use multi-process 3D printing. Additionally, the patterns and structures reported here are far removed from the complexity found in nature. While the goal of this work is not to exactly reproduce what nature has accomplished, the next stage is to match a more similar degree of complexity that will lead to fine-tuned features and properties necessary to develop novel synthetic materials. This will require advances in resolution and multiscalability. Additive manufacturing's growth projection is dynamic and rapidly improving which gives unlimited potential for future work in bioinspired design and integration.

While there are considerable advancements that need to occur in AM technology to enhance the field of bioinspired materials, it is also important to improve our understanding of the fundamental behavior of biological materials. As we develop superior characterization and analytical techniques, such as in situ cryo-electron microscopy, we can reveal with more accuracy the molecular assemblies of chemically unmodified specimens. Biological materials are a part of living systems and therefore it is important to study them in an unaltered state. Another important consideration, is understanding how the overall mechanical behavior of the material influences the governing mechanisms which we may not be able to capture when only looking at a particular length scale. To drive the field of bioinspired materials forward, we need to obtain a more holistic

understanding of biological materials, which comes with better hypothesis and advancements in the technological tools to unearth what is unknown.

Additive manufacturing is becoming an integral part of research on biological and bioinspired materials as clearly demonstrated here. It provides the capabilities to generate intricate designs needed to investigate geometrical effects on mechanical performance in bioinspired structures. AM is a rapidly evolving technique, and while many methods exist for the design and fabrication of bioinspired materials, it is evident that PolyJet multi-material printing (Stratasys Ltd.) and two-photon polymerization (Nanoscribe) are integral players in this field. Nature's reliance on the integration of both soft and hard materials to achieve exceptional properties makes multi-material printing a necessity. With the advancement of powerful lasers, two-photon polymerization has emerged with the capability of nanoscale dimensions to generate structures on a fundamental scale that is critical to the success of biological materials. AM provides a tailorable tool to explore cardinal structural interactions and optimize properties. This phenomenal tool can be used in two primary modes:

1. To assist in our understanding of the mechanisms and response to external loads (deformation, damage, and failure). Specific structural designs are identified in biological materials and are then translated into additive-manufactured designs. These are then manufactured and tested under distinct conditions to identify the mechanisms, test the hypotheses, and improve our understanding. This can be extended to the development of parametric studies that rely on AM to produce iterations of distinctly different structural units.
2. Lessons from nature are translated into designs that use the principles at hand and are tailored to suit a particular application, which may be quite different from the natural

system. One example that stands out is the potential industrial application of gecko-inspired dry adhesives. Once we understand the mechanisms at hand we can control the structural design for tailorable applications.

1.4 Research Focus and Motivation

Biological materials science thrives at the intersection of biology, materials science, and engineering. This work focuses on applying the above-mentioned principles of materials science and engineering to investigate unexplored biological materials and the development of bioinspired structural designs. This is accomplished on two fronts: (1) biological materials characterization via traditional materials science characterization techniques and (2) 3D printing of bioinspired designs followed by subsequent mechanical testing and numerical modeling to better understand their structure-property relationships. The goal of this work is to contribute to the overarching question that lays the foundation of biological materials science: **how do biological materials structure and organize their relatively weak constituents to achieve the properties that allow them to perform the specific functions they need to thrive in their respective environments?** Additionally, how is this accomplished in both mineralized (teeth) and non-mineralized (keratin) systems?

To answer the above question I have broken down these goals into the following aims:

Aim 1: Characterize the hierarchical structure of teeth among diverse feeding strategies of fish.

1.1 What is the relationship between hierarchical structure and mechanical properties of the transparent teeth of the deep-sea dragonfish and what ecological function does transparency serve?

1.2 Can micro- and meso-structural differences in teeth account for the distinct diets of the piranha and pacu?

Aim 2: Characterize the structure and mechanical properties of primary flight feathers of birds with various flying strategies which include high- and low-frequency flapping styles.

1.1 Investigate the scaling of the feather shaft at different orders of hierarchy which include foam, rachis width, and ratio of cortex to medulla.

1.2 Investigate the bending properties of various feather shafts under quasi-static and dynamic loading conditions to understand how the structuring of the sandwich structure can tailor flight performance.

Aim 3: Produce bioinspired structures for the development of 3D printed designs for mechanical testing and computational modeling.

1.1 Investigate the influence of porosity, geometry, and a reinforcing layer on the tubule architecture found in horns and hooves.

1.2 Investigate the geometry of the dentin-enameloid junction (DEJ) found in the piranha and pacu and how the suture structure influences stress distribution under compression.

1.3 Investigate the geometry of the feather rachis under three-point bending.

In order to accomplish these aims, it is imperative to first characterize the unique features of biological materials to not only better understand the success of biological systems but to also extract potential sources of inspiration. From Aim 1, this work includes the structure, optical, and mechanical property characterization of fish teeth (deep-sea dragonfish, piranha, and pacu) through scanning electron microscopy, transmission electron microscopy, hyperspectral imaging, μ-CT scanning, nanoindentation, and computational modeling. From Aim 2, The feather shaft of flying birds is explored through scanning electron microscopy, three-point bending, and dynamic

mechanical analysis to investigate their structure-property relationship with respect to flight. More specifically, the rachis which is responsible for supporting the primary load of the feather during flight will be analyzed.

From Aim 3, prior work from the literature is used to develop and explore energy absorbent and tough bioinspired structures inspired by the reinforced tubular architecture found in teeth, horns, and hooves. These designs are mechanically tested in quasi-static compression, fracture toughness, and dynamic mechanical analysis to determine structural influences on mechanics. Bioinspired interfaces from the DEJ of the piranha and pacu are printed and mechanically tested to better understand how the geometry of the interface influences the stress distribution. Bioinspired feather shafts are built and tested in three-point bending and dynamic mechanical analysis to discern relationships between cortex-to-medulla-thickness ratios and the presence of a foam-filled center on bending and energy absorption and dissipation.

1.5 Acknowledgements

Chapter 1, in part, is published as a review article in *Advanced Materials*, authored by A. Velasco-Hogan, J. Xu, and M. A. Meyers. The dissertation author is the primary investigator and author on this publication.

Chapter 2: Background

2.1 Tooth Structure and Composition

Teeth are considered one of the oldest forms of mammalian tissues. They are a complex, graded structure composed of three distinct regions: enamel, dentin, and cementum. Enamel is the highly mineralized, hard, but brittle, external layer that is exposed to the environment. The dentin layer is found below the enamel and between the pulp chamber and is less mineralized and more tough. Dentin is considered the largest component in consideration of both weight and volume [37]. Cementum serves as the connection to the jaw attached by periodontal ligaments and alveolar bone [5]. This work will focus only on the enamel and dentin layers. Unlike a majority of biological tissues, enamel and dentin are unable to regrow and repair from damage. Therefore, they must work together to be able to withstand millions of cycles of mastication forces. Despite the enamel being extremely hard, brittle, and having low toughness (comparable to glass), teeth are still able to withstand mastication forces though the synergistic effect of the underlying dentin layer. The interface between the dentin and enamel is known as the dentin-enamel junction (DEJ). It provides a crack-arresting barrier for flaws formed in the brittle enamel [38].

Enamel and dentin are composed of three constituents: a mineral phase (hydroxyapatite (HAP)), an organic phase (collagen), and water. Enamel is the hardest tissue in the human body due to its high mineral content ~96 wt%. The enamel functions as a wear-resistant surface to protect the softer underlying dentin [39]. Enamel is primarily made up of large hexagonal hydroxyapatite crystals that are often calcium deficient and substituted with carbonate. Similarly orientated crystals bundle to form prisms that are rod-like in structure as shown in Figure 2.1. These prisms are separated by a thin organic matrix known as interprismatic enamel.

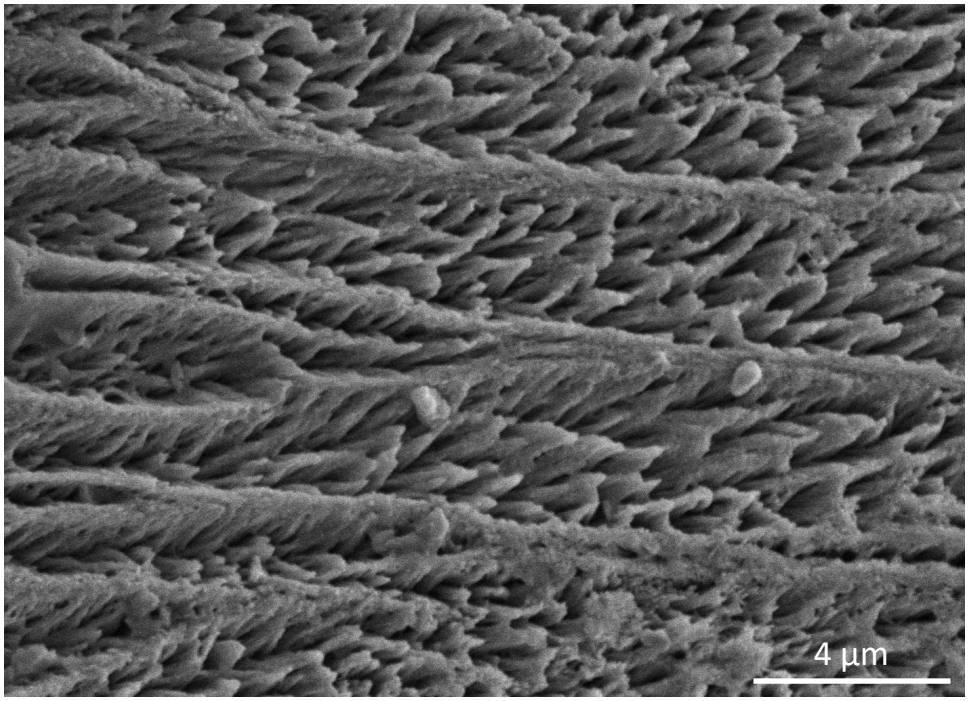

Figure 2.1 Scanning electron micrograph of enamel. This surface has been acid etched to reveal the enamel rods.

Dentin is composed of a matrix of mineralized collagen fibers (~70 wt% mineral, 20 wt% organic, and 10 wt% water).[40] The structure of dentin is responsible for its toughness. At the microscale, it is composed of an array of ~1 µm diameter dentinal tubules that originate from the pulp and radiate out in an "S" shape terminating in the DEJ (Figure 2.2). Dentinal tubules are reinforced by a thin layer of mineral, known as peritubular dentin. The reinforced mineral layer readily initiates microscopic cracks under loading which is an example of an extrinsic toughening mechanism [41]. When a crack propagates in dentin, it will follow the path of least resistance moving through the more compliant phase (tubules). Tubules are organized in a gradient distribution with their highest concentrations being closer to the pulp and decreasing towards the DEJ (Figure 2.2).

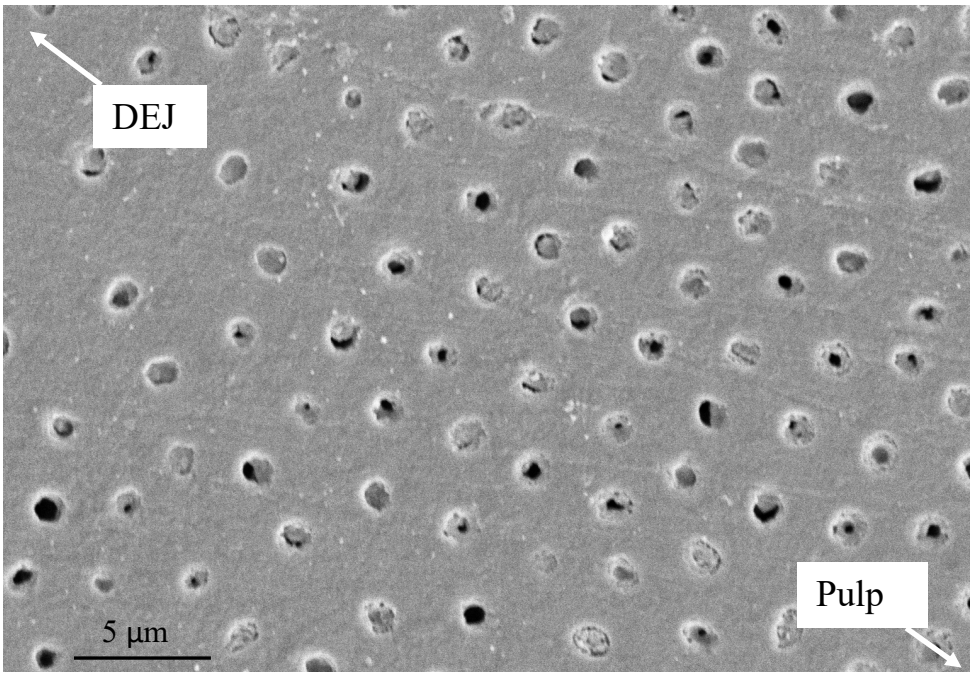

Figure 2.2 Scanning electron micrograph of dentin microtubules. The lighter regions surrounding the microtubules indicate regions of higher mineralization (peritubular dentin). There is a noticeable gradient in tubule porosity decreasing towards the DEJ.

2.2 Tooth Mechanics

The mechanical properties of enamel, dentin and the DEJ have a strong dependence on microstructure geometry and orientation. Specifically, variations in prism orientation are known to affect hardness, stiffness, and fracture toughness in the enamel layer. The dentin layer has a strong dependence on tubule orientation, tubule density, and tubule radius. The microstructure of the dentin and enamel layers and their corresponding interface (DEJ) dictate distinct mechanical properties which synergistically work together to create an efficient hierarchically layered composite.

The enamel layer is highly anisotropic and has a dependence on the orientation of its crystallite rods on the micro scale. This has been determined both macroscopically and microscopically. Macroscopic methods include acoustic impedance, flexural, and tensile testing to

determine the elasticity, strength, and toughness [42–47]. One study on bovine enamel shows that the elastic modulus is dependent on testing orientation were the occlusal and longitudinal directions measure 125 and 115 GPa respectively [48]. Fracture toughness of enamel is also dependent on enamel rod orientation as crack propagation occurs preferentially along the inter-rod spaces parallel to the rod axes [44]. Additionally, the micromechanical properties of teeth are direction dependent. Typically microhardness and nanoindentation are used to probe the micromechanical behavior of enamel [49,50]. Microhardness testing performed by Xu et al.[51] determined that hardness and Young's modulus were higher in the occlusal section when compared to the longitudinal section. Modified atomic force microscopy for nanoindentation has been used to study the anisotropic behavior of single enamel rods with orientations parallel and perpendicular to the rods and at different locations within the tooth (occlusal vs longitudinal). It was shown that the hardness and Young's modulus parallel to the rods was 3.93 GPa and 87.5 GPa respectively which was greater than perpendicular to the rods (3.3 GPa and 72.2 GPa respectively) (Figure 2.3) [42].

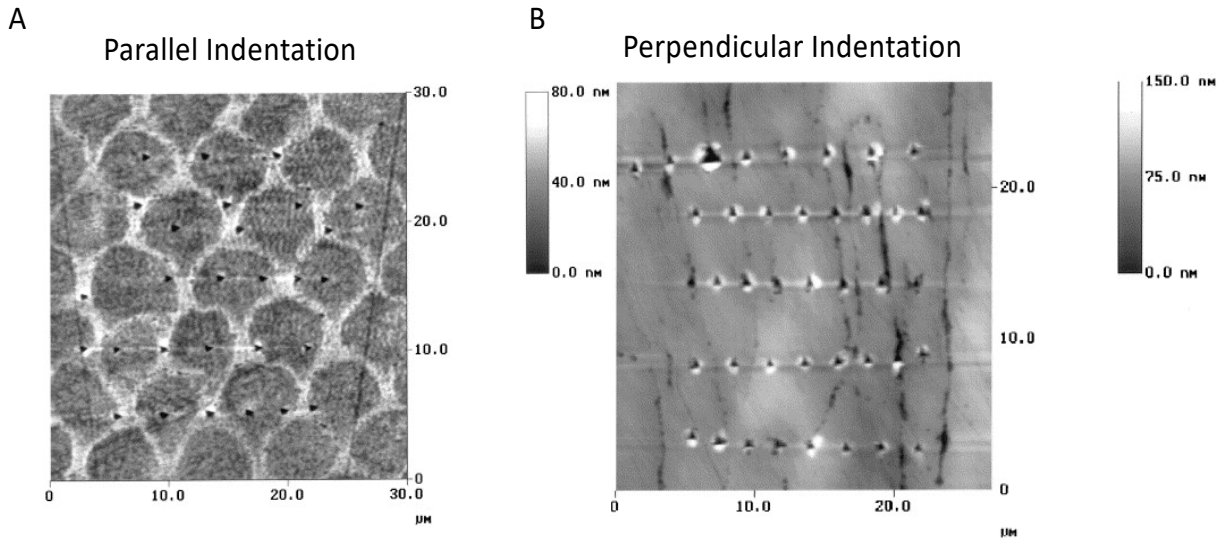

Figure 2.3 Atomic force microscopy detailing nanoindentation surface of enamel in different orientations. A) Nanoindentation performed parallel to the enamel rods. B) Nanoindentation performed perpendicular to the enamel rods. Reproduced with permission.[42] Copyright 2001, Elsevier.

When the loading direction is orientated parallel to the tubules the flexural strength is greater when compared to loading perpendicular (Figure 2.4) [52]. Additionally, the collagen fibrils contribute to the anisotropy of dentin and play a significant role in amplifying strength. As tubule density increases the ultimate tensile strength, hardness, and elasticity have been shown to decrease [53,54]. This creates a gradient in strength from the pulp to the DEJ and is responsible for its crack arresting and toughening capabilities. The degree to how large the tubule radius is also contributes to the mechanical properties of dentin. With age, the dentin tubules fill and the effective radius becomes smaller. Flexural strength and toughness both decrease as dentin tubules deteriorate and fill with carbonated apatite [55]. Crack bridges are formed by the filled tubules and fewer microcracks and microbranching of the tubules occur [55].

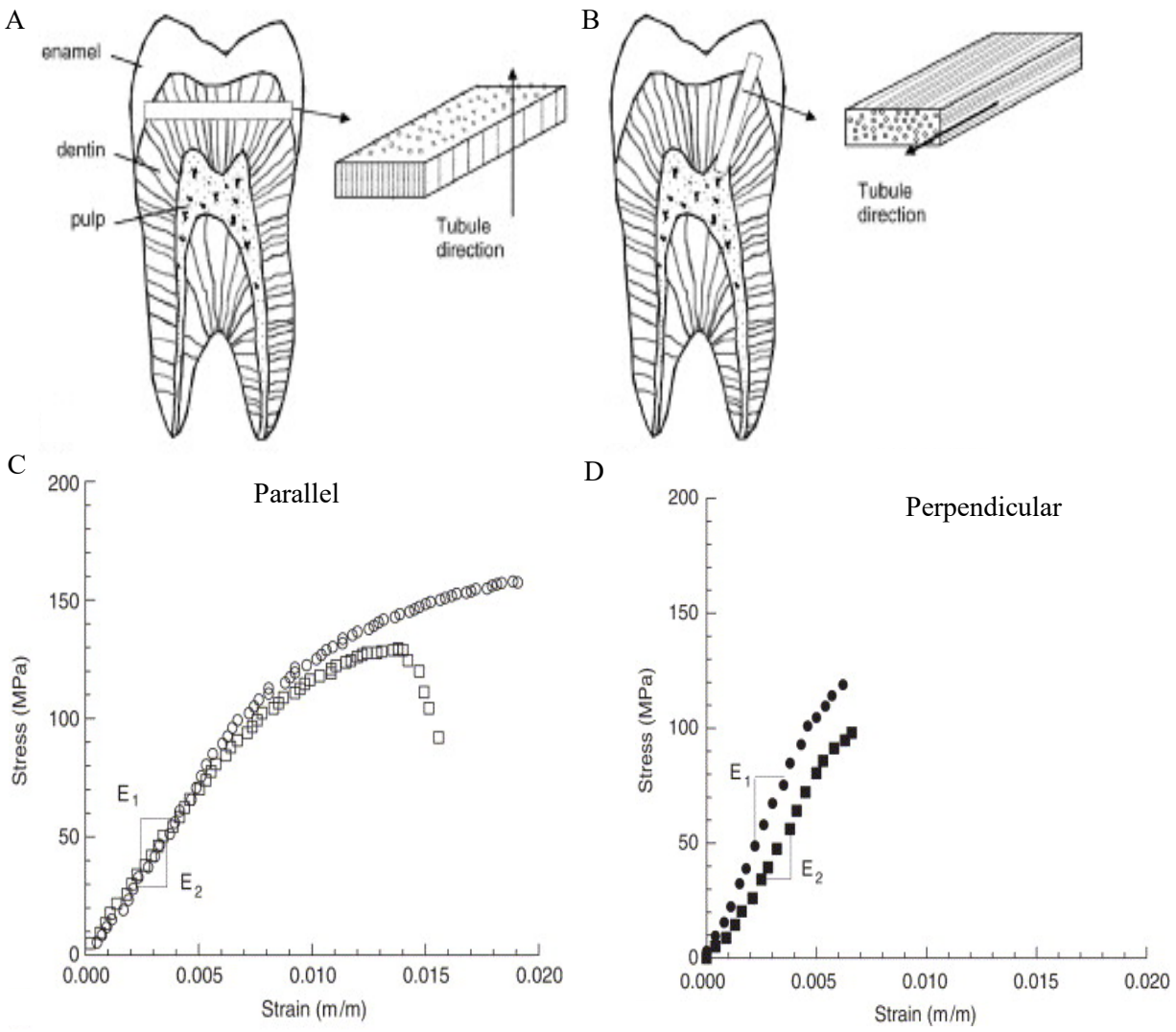

Figure 2.4 Structure of teeth and dependence on orientation. A. General tooth structure highlighting the relative positions of enamel and dentin. Tubules are orientation perpendicular to the surface. B. Tooth showing tubules orientation and a sample orientation parallel. C. Flexural response of a sample orientated with the load parallel to the tubule direction. D. Flexural response of a sample orientated with the load perpendicular to the tubule direction. Adapted with permission [52]. Copyright 2006, Elsevier.

2.3 Keratin

Keratin is an ubiquitous biological polymer comprising the bulk of mammalian, avian, and reptilian epidermal appendages which includes nails, hair, outer layer of skin, feathers, beaks, horns, hooves, whale baleen, claws, scales, and gecko feet and has been the subject of many review articles [23,56–60]. Keratin and its basic structural and material properties will be reviewed here as it is an important constituent in feathers and hooves which will be a primary focus of this work. Despite their omnipotent presence across a diverse range of biological materials these keratin based architectures are not limited in function. Instead, keratin-based biological materials are able to perform a broad range of functions from the impact resistance of hooves and horns, to light-weight yet stiff feathers that resist buckling under aerodynamic loads, and even the reversable dry adhesive mechanism in gecko feet that allows them to climb walls [2,61,62]. The ability of keratin-based materials to perform diverse functions is derived from the ingenious structuring and tailorability of keratin across many length scales.

2.3.1 Structure of keratin

Keratin filament-forming proteins form a complex hierarchical arrangement which relies on the synergisms between amorphous and crystalline phases to achieve the diverse range of functions across keratinized biological materials. At the nano-scale keratin is distinguished as polypeptide chains of either α- or β-keratin. Typically mammalian keratin is found in the α-keratin form, while avian and reptilian keratin are β-keratin; however, one mammal the pangolin is known to have both α- and β-keratin domains found in its scales [63]. Alpha-keratin is characterized as forming a right-handed α-helix secondary protein structure, where the primary protein structure is defined by its amino acid sequence [64,65]. Two of these polypeptide chains then twist together to form a dimer known as a coiled-coil [66]. The coiled-coil dimers then aggregate together bonded

length-wise by disulfide bonds to form protofilaments. Two protofilaments align to form a protofibril, in which four protofibrils bonded together form an intermediate filament (IF) [67]. The intermediate fibril ~7 nm in diameter is then embedded in an amorphous matrix of keratin which can have variations in IF alignment, orientation, and matrix properties which account for the large variation of keratin structures. The IF-matrix composite is characteristically found on the nano-scale. The hierarchical structure of α-keratin from the molecular to the nano-scale is shown in Figure 2.5 A.

Similarly to α-keratin, β-keratin is a filament forming protein that forms intermediate fibrils ~3-4 nm in diameter embedded in an amorphous matrix. The biggest difference is that β-keratin has a different secondary protein structure which is classified by the formation of β-pleated sheets.[68] The β-keratin pleated-sheets consist of laterally packed polypeptides which are held together by hydrogen bonds. The planarity of the peptide bond and the lateral hydrogen bonding are what accounts for the formation of the pleated sheet [69]. Four β-strands (a dimer) twists to form a distorted β-sheet where two β-sheets make up a β-keratin intermediate filament. These intermediate filaments are then embedded in an amorphous matrix of keratin. The hierarchical structure of β-keratin is shown in Figure 2.5 B. For both α- and β-keratin the IFs bundle to form fibrils (submicron scale), which then subsequently group to form macro fibrils (~400-500 nm in diameter), and finally forming fibers (~6 μm).

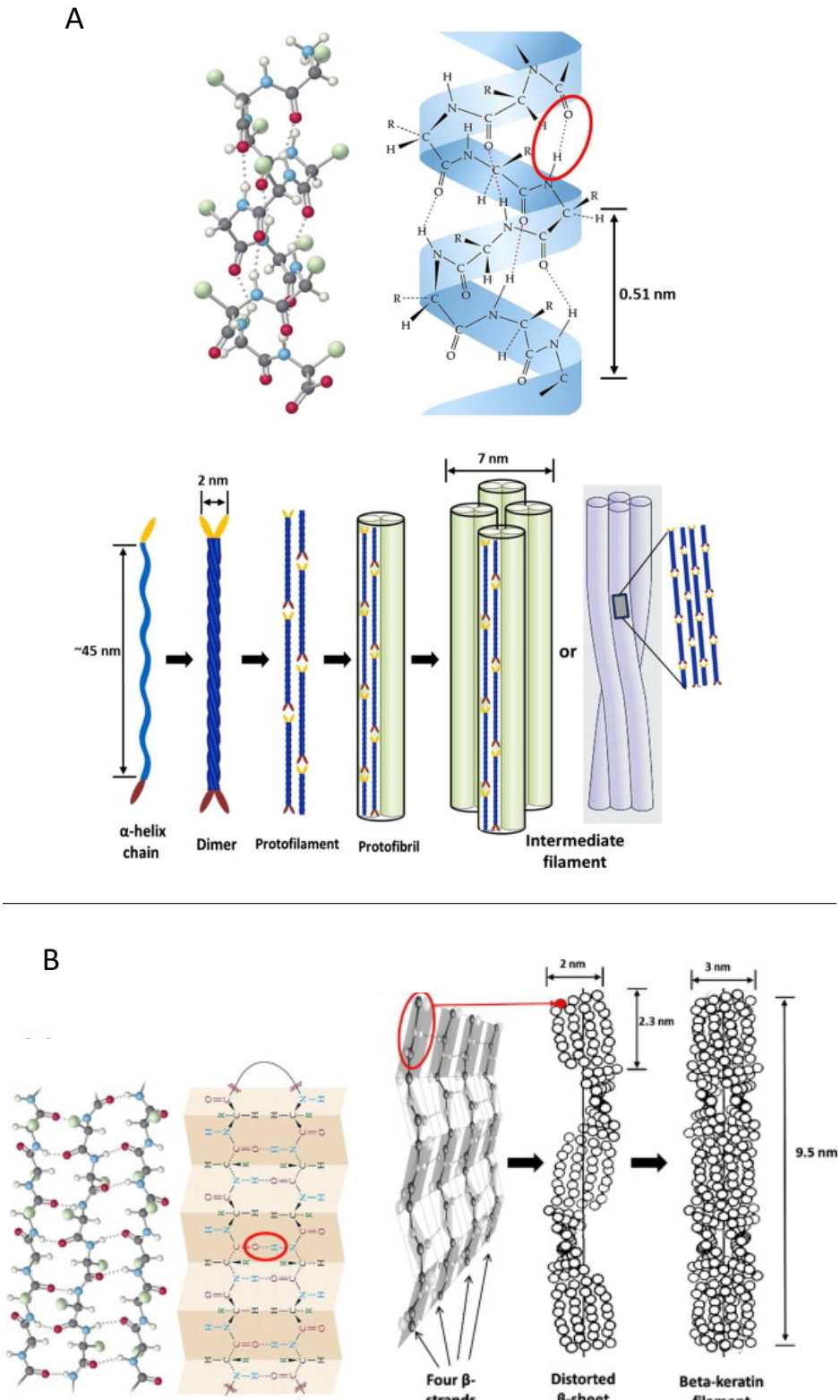

Figure 2.5 Schematic of A) alpha and B) beta-keratin and their structures from the secondary protein structure to the filament forming protein.

2.3.2 Mechanical properties of keratin

The polymeric nature of keratin lends itself to a wide range of mechanical properties that are inherent to its amino acid composition, structure, and hydration content.[58,70–73] The amino acid sequence and their corresponding residues dictates the availability of di-sulfide bridges. The amino acid cysteine has a thiol group which allows for a covalently bonded di-sulfide bond to be formed with another cysteine further along the chain which creates a fold in the protein. This cross-link increases the energy required to pull apart keratin. The amount of sulfur cross-links is strongly related to the hardness of keratins. A low amount of sulfur is indicative of soft keratins (outer layer of skin i.e. stratum corneum), while a high amount of sulfur corresponds to hard keratins (hair, nails, feathers, hooves etc.) [74–76]. Intra- and inter-species hydration variation greatly influences the stiffness and strength of keratin. Increasing humidity and water content decreases the stiffness and strength[70,77,78] This is attributed to the interaction of water molecules with the amorphous matrix which breaks stabilizing hydrogen bonds and increases the mobility of the fibers within the matrix [79].

In general, keratin is shown to have a high tensile strain which is primarily due to the stretching and sliding of the polymer chains. The hagfish slime threads have the highest tensile breaking strain of 2.2 when tested in sea water [80]. There are large variations in tensile strength across species. The tensile strength ranges from 2 MPa in the stratum corneum to 530 MPa in the dry slime threads of the hagfish. Under tensile loading at strains greater than 0.3, alpha-keratin can undergo a transformation to beta-keratin which also accounts for its high tensile strain. This is described as the α-helical coiled coil unravelling to form the β-pleated sheet structure [81–83]. This transformation increases keratin's ability for energy-absorption capacity under tensile loading.

Additionally keratin is known to be highly strain-rate sensitive which is related to its viscoelasticity i.e. it's time-dependent response.[84,85] The general trend for keratinous materials is that increasing strain rate increases stiffness and strength while decreasing breaking strain as shown in Figure 2.6. [78,86–88] Thus, most keratin materials undergo an elastic to ductile-plastic to brittle transition with increasing strain rate. This characteristic is not unique to just keratin materials, in fact, most biological materials including bone and wood show a similar ductile to brittle transition with increasing strain rate (Figure 2.6). Again, this is predominantly attributed to the inherent viscoelastic nature of biological materials. This rate-dependent behavior has important implications for impact resistant biological materials suggesting that under dynamic conditions these materials can withstand greater stresses and have different failure mechanisms when compared to quasi-static conditions.

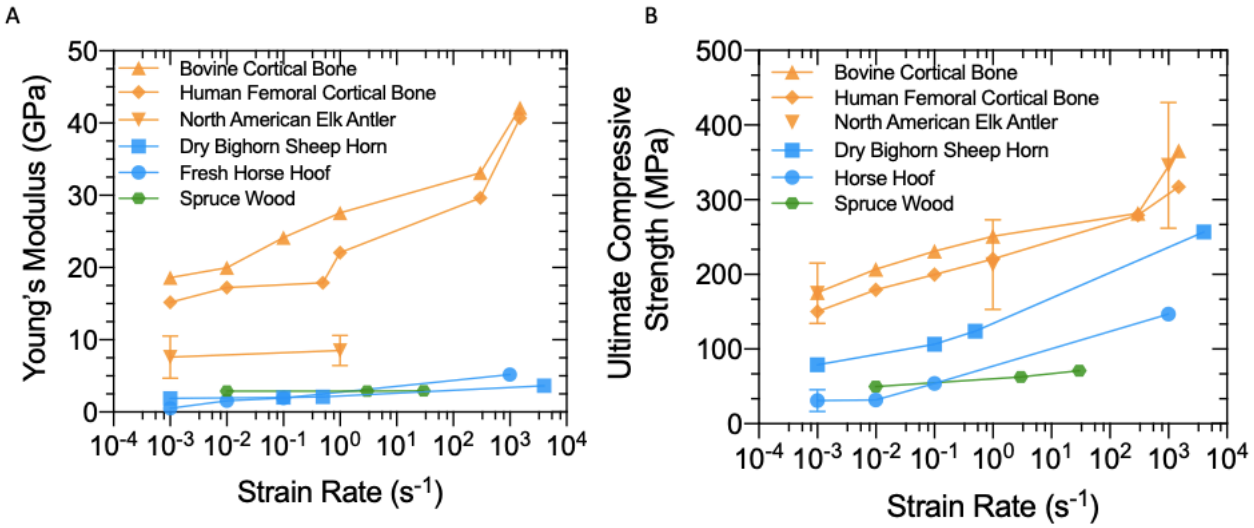

Figure 2.6 Strain-rate sensitivity of various biological materials including keratin (bighorn sheep horn and horse hoof). As strain-rate increases, stiffness and strength decrease.

Keratin is one of the toughest biological materials despite being only composed of a biopolymer and lacking a mineralized phase. It also achieves a simultaneous high degree of toughness and stiffness as shown in the Ashby diagram in Figure 2.7. This high degree of toughness is related to keratin's hierarchical structure and the synergistic toughening mechanisms across each length scale. The matrix is primarily responsible for distributing the applied load and the fibers serve to arrest cracks. Many keratin materials have micro-scale structures, such as tubules, which also enhance toughness by deflecting and arresting cracks. Due to fiber orientation and alignment and the presence of tubules along a specific direction, toughness is typically found to be anisotropic [89].

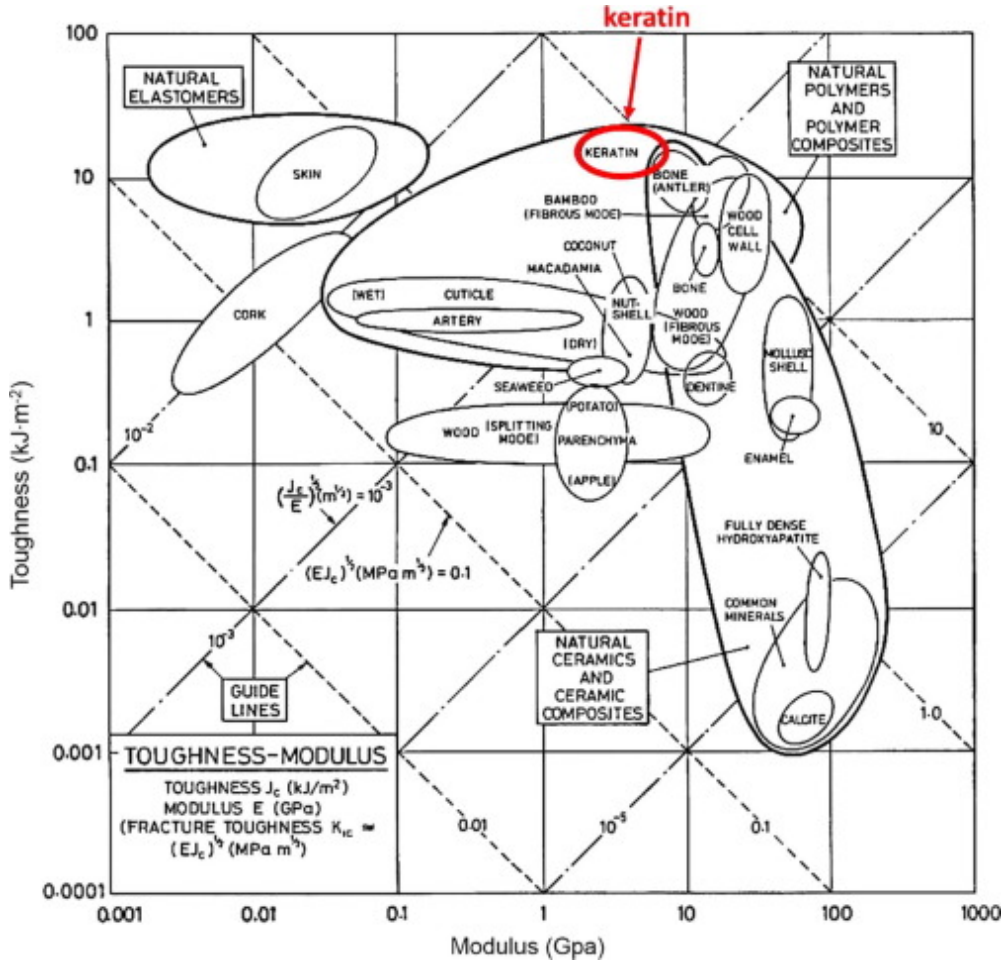

Figure 2.7 Ashby diagram of toughness and Young's modulus. This highlights how keratin has both a high toughness and modulus which makes it a desirable material for a wide variety of functions.

2.3.3 Hydration-induced shape recovery

Keratin systems often function as a protective layer which undergoes significant deformation. Many of these systems are permanent and cannot remodel or self-heal through biological processes after experiencing considerable deformation such as the bighorn sheep horn which presents complications for longevity [90]. A solution to this is the ability of keratin to undergo hydration-assisted recovery. This process is described as water infiltrating the amorphous matrix of keratin causing swelling which forces the deformed crystalline regions of the IFs to regain their initial shape by way of breaking and reforming hydrogen bonds.[90] Hydration-

induced shape recovery has been found to occur in hair[91,92], horn [90], feathers [93,94], and pangolin scales[95]. Bighorn sheep horn was shown to recover shape by soaking in water after severe compression of 50% strain which was further assisted by the presence of tubules.[90] Additionally, the feather shaft has also shown to have hydration-assisted shape and strength recovery [93,94]. The feather shaft was subject to bending and then allowed to soak in water for 24 hours and after one cycle it was found to recover its strength by ~80%.[94] A similar mechanism of recovery as the bighorn sheep horn was proposed. Water molecules penetrate the amorphous matrix and cause swelling which forces the crystalline IFs to realign as shown in Figure 2.8.

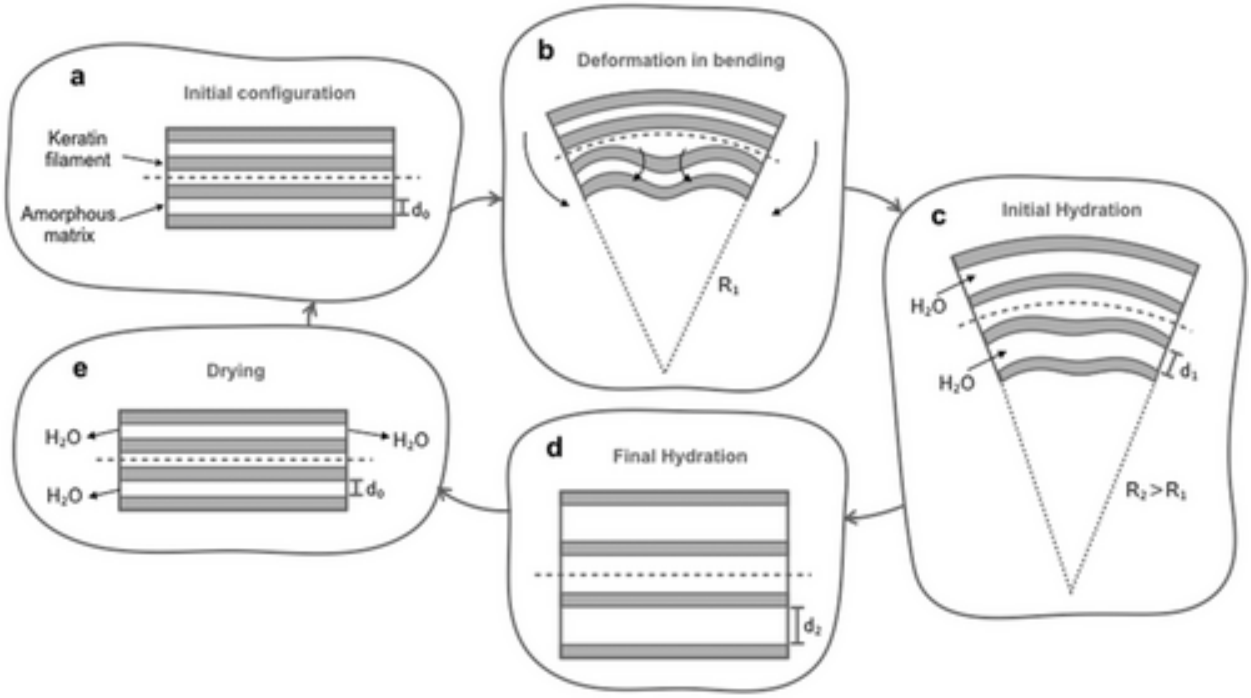

Figure 2.8 Hydration-induced recovery mechanism of the feather shaft. This shows how the water infiltrates and expands the amorphous layer which causes the keratin filaments to straighten to their original shape

2.4 Natural Energy Absorbing Materials

Many remarkable energy absorbent materials are found in nature including bones, teeth, horns, and hooves. These materials harness energy absorbing strategies, despite being composed of relatively weak constituents, through structural organization. Additionally, they are able to serve a wide variety of functions regardless of similarities in composition and microstructure. Again, this is achieved by optimizing their structural organization across various length scales. They are commonly composed of an organic phase consisting of biopolymers (collagen, keratin, elastin, cellulose, or chiton) and a mineral phase (calcium carbonate, hydroxyapatite, or silica). These natural materials are able to support a variety of purposes:

- *Protection.* Exoskeletons and bones are intended to protect the soft internal tissues and organs. These materials need to be strong and tough to withstand external forces yet light-weight to reduce energy expended on mobility.
- *Aggression.* Claws, horns, antlers, tusks, and teeth are examples of materials that nature relies on for evolutionary success and dominance. These materials typically need to be impact resistant and have high resistance to bending and shear deformation.
- *Support.* Bones, mollusk shell, an hooves are used to support the general weight and activities of organisms. The largest concerns for these materials are behavior under compression, impact, and fatigue loading.
- *Mastication*. Teeth are needed to break down food for more efficient digestion. In this process, teeth are required to withstand biting forces and large compressive loads.

These remarkable features are accomplished by the synergistic efforts of the compliant (organic phase) and stiff (mineral phase) components that often exceed expectations based on the rules of mixtures. The capabilities for nature to extend their bulk properties beyond the relative mixing of

their constituents is demonstrated in Figure 2.9. For example, bone is composed of collagen and hydroxyapatite. The fracture toughness of bone is able to exceed the expectation of its components through advanced hierarchical organization which hinders crack propagation at multiple length scales and offers extrinsic toughening mechanisms.

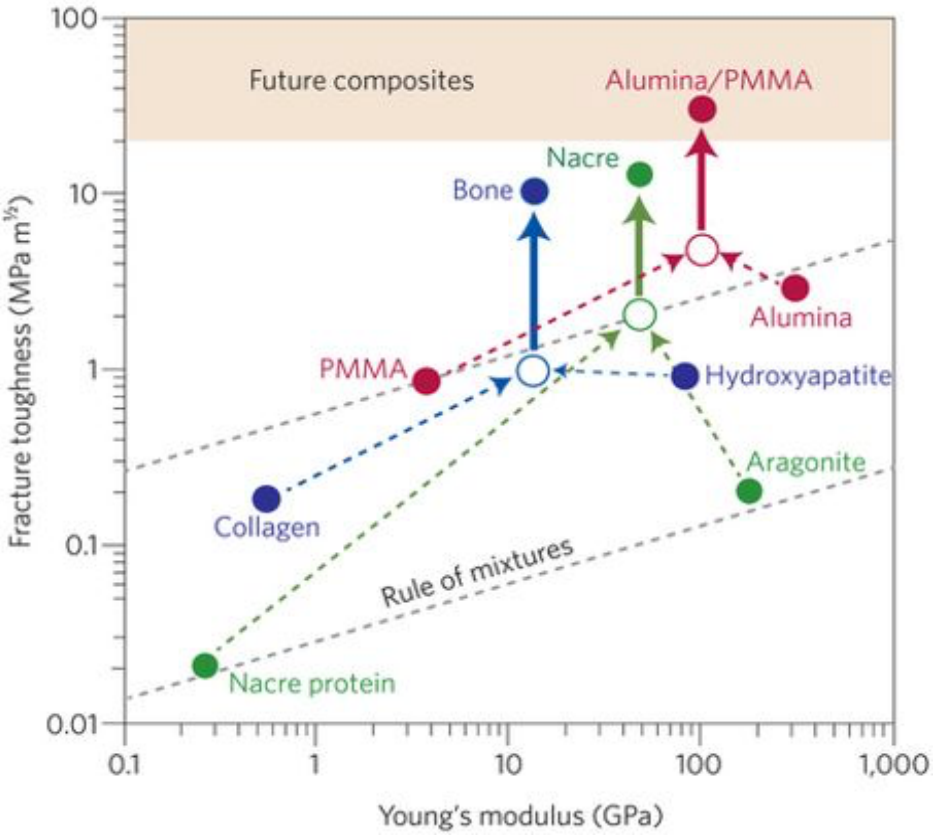

Figure 2.9 Natural composite materials have toughness values that exceed what is expected from mixing their relative constituents. When biological materials structural solutions are applied to synthetic materials we see the same result. This suggests that efficient structural organization can lend itself to enhanced materials properties. Reproduced with permission.[5] Copyright 2015, Nature.

A striking similarity among many energy absorbent natural materials is the reoccurring design of the tubule structure. It is found in horns, hooves, exoskeletons, bones, teeth, antlers. And even wood (Figure 2.10). This structure is present typically on the micron scale and ranges in

diameter from ~1—100 μm. Additionally, it is not limited by material i.e. it is found in both mineralized (hydroxy apatite and calcium carbonate) and polymeric (keratin and cellulose) biological systems. Its presence across a diverse range of biological materials strikes particular interest into how the tubule structure influence the mechanical properties and function within these systems.

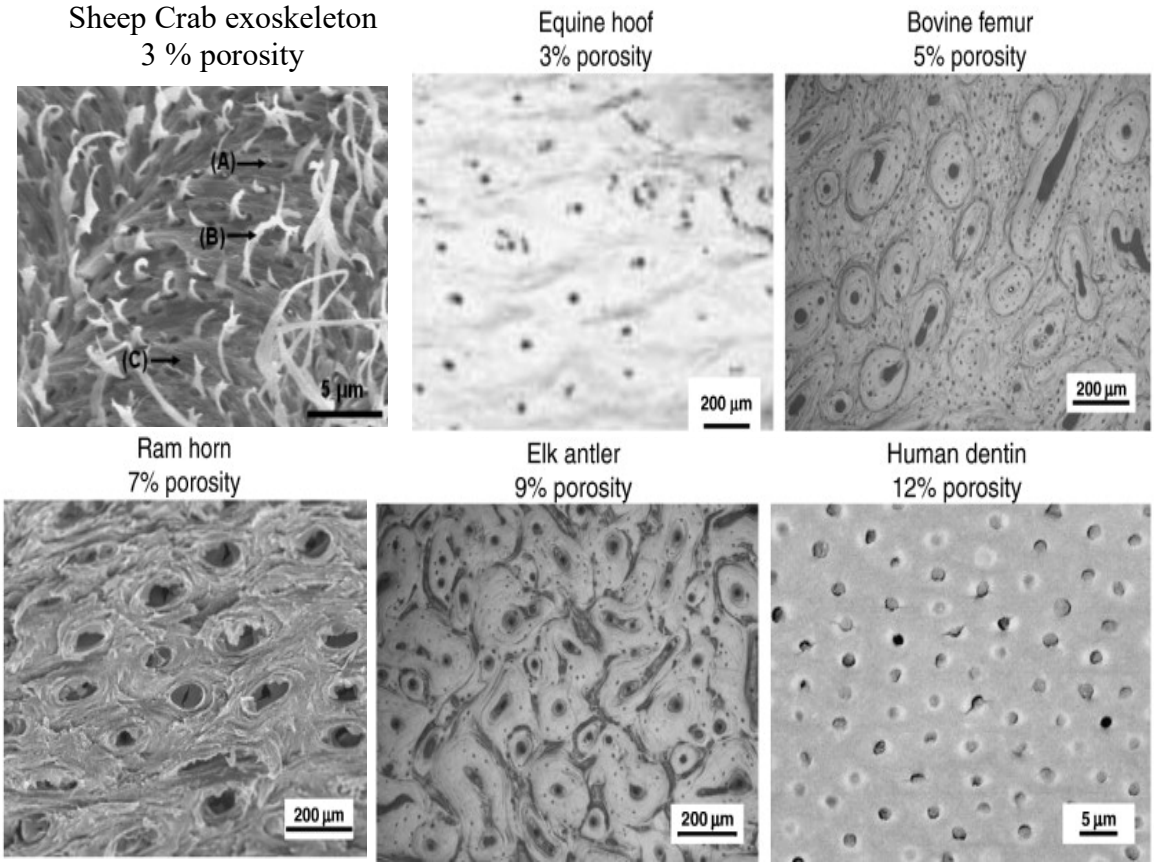

Figure 2.10 Similarities between microstructures of exoskeleton, hoof, bone, horn, antler, and dentin. Adapted with permission [96,97].

2.4.1 Hooves

Hooves are a hierarchical structure composed of α-keratin fibers that are formed into circular lamellae that surround micrometer sized hollow empty channels (Figure 2.11). In relation to the structural design elements (Figure 1.3), this is defined as the "tubular" structure. On the nanoscale, the equine hoof is considered a polymer composite composed of crystalline keratin intermediate filaments (IFs) ~7-10 nm embedded in an amorphous keratin matrix [67,98,99]. In equine hooves (which will be the focus of this study), tubules are known to only serve a mechanical purpose and while it has been suspected they are not intended for transporting water for hydrating the hoof [100,101]. The matrix surrounding the tubules is referred to as the intertubular region. The stiffness and hardness of the tubular region is greater than the intertubular region [102]. Similar to teeth there exists a gradient in porosity. The highest density of tubules is found at the outer surface and gradually decreases in density as it reaches the inner region. Interestingly, this is the opposite for teeth—dentin tubule concentration is greatest near the center and decreases outwardly.

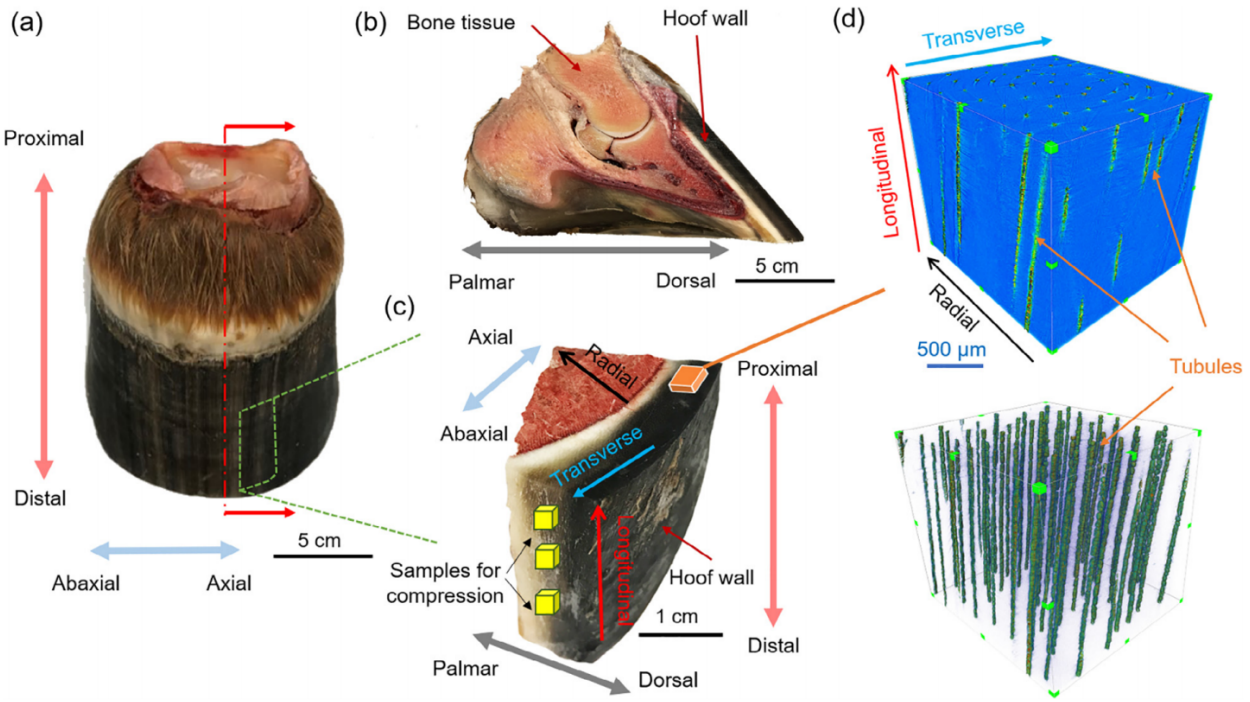

Figure 2.11 Hierarchical structure of the hoof wall showing the three defined orientation: radial, transverse, and longitudinal. Reproduced with permission.[102] Copyright 2019, Elsevier.

The hoof wall on the macro scale behaves as an isotropic material. Its response to compression is dependent on the loading orientation. The compressive stiffness and strength are greater in the transverse and longitudinal directions when compared to radial direction for various strain rates [102]. This effect is due to the tubule orientation which main axes runs longitudinally within the hoof wall. The tubule areas are stiffer and harder and serve to reinforce the intertubular area by protecting it from shear-banding and cracking. The higher stiffness and hardness are due to the thick lamellar keratin cells that surround the hollow cavity of the tubule [102]. These thicker cells concentrate stresses and localize deformation.

The dominating loading conditions of the hoof are a combination of compression and shear which occur at medium strain rates during galloping. Since the hoof wall is angled slightly off of the hoof and the hoof itself strikes the ground obliquely, there exists complex loading resulting in

a combination of compression and shear; unlike ram horns, which typically collide normal to the surface. The compressive load is predominantly applied longitudinally along the major axis of the tubules, but depending on the gate of the horse and the angel at which is strikes the ground this can induce shear. Much of the pre-existing literature on horse hooves focuses on The predominant deformation mechanisms when tested in transverse, longitudinal, and radial are elastic buckling and cracking of the tubules [102]. Even after 60% compressive strain there is no shear-banding or severe cracking in the intertubular region which indicates the energy absorption properties of the tubular region [102]. The tubules serve to reinforce and support the hoof wall from catastrophic failure. The failure mechanisms were determined using *in-situ* synchrotron x-ray computed tomography (Figure 2.12).

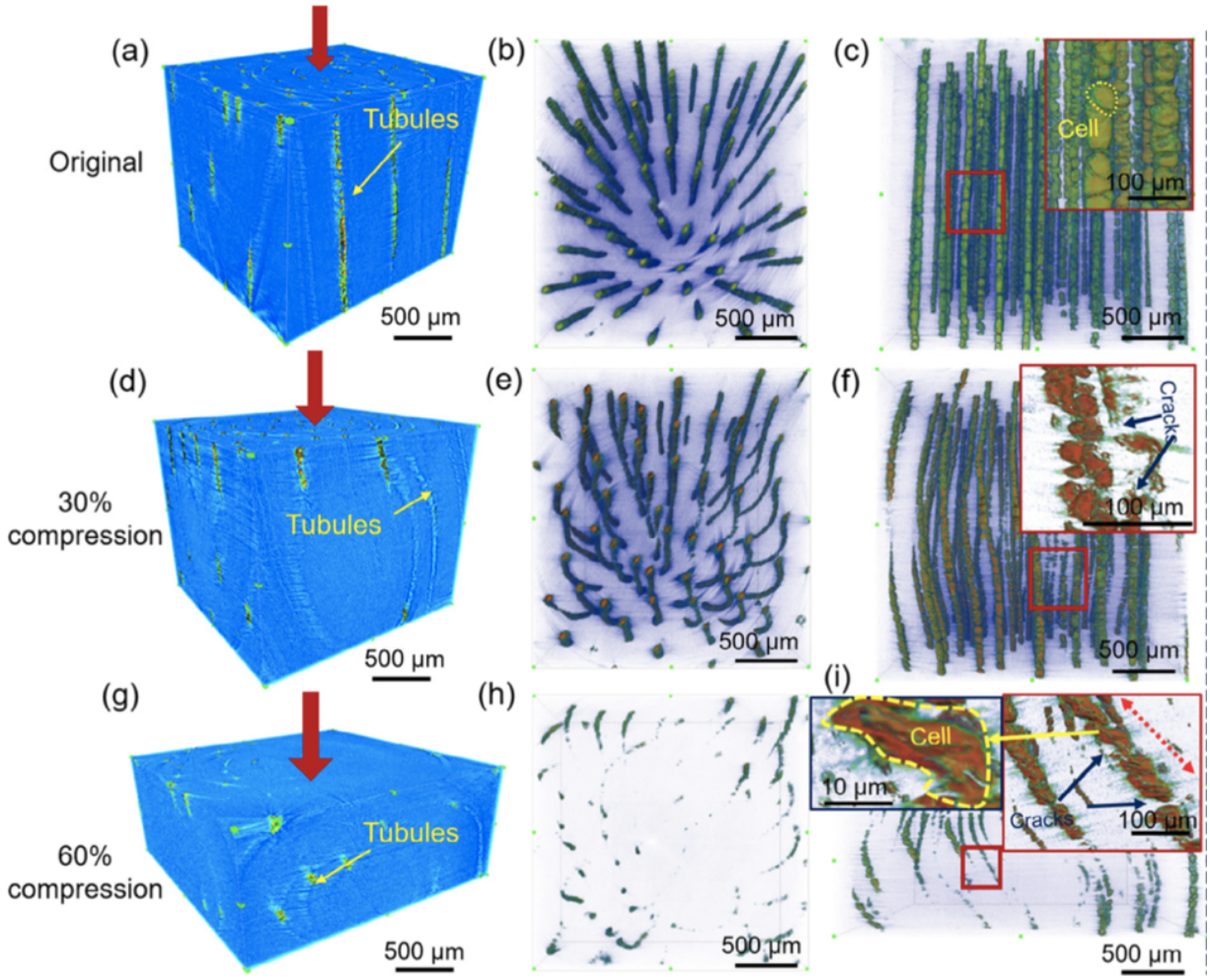

Figure 2.12 In-situ synchrotron x-ray computed tomography (XCT) compression of a fresh sample. (a) 3D reconstructed XCT image of the undeformed sample. (b) Proximal view of the undeformed sample showing the tubules. (c) Abaxial view of the undeformed tubules. Higher magnification image of tubules shows keratin cells surrounding the chambers of medullary cavities. (d) 3D reconstructed XCT image of the sample after 30% compression in the longitudinal direction. (e) Proximal view after 30% deformation, where buckling of tubules are shown. (f) Abaxial view of buckled tubules at 30% deformation. Cracks in the tubules are also observed in the higher magnification image. (g) 3D reconstructed XCT image after 60% compression in the longitudinal direction. No obvious cracks are observed. (h) Proximal view after 60% deformation. Tubules start disappearing due to the severe deformation. (i) Abaxial view of severely buckled tubules. Tubules have collapsed and compressed after 60% compression. Red dashed arrow indicates longitudinal tubule is severely buckled in the diagonal direction. Reproduced with permission.[102] Copyright 2019, Elsevier.

2.4.2 Horns

Horns are similar to hooves in that they are primarily composed of α-keratin fibers that hierarchically form distinct structures at multiple length scales to providing toughening and energy absorbing mechanisms during impact. The horn of the bighorn sheep (*Ovis canadensis*) is known to withstand impact forces as large as ~3400 N when it uses its horns to battle and assert its dominance over other rams [103]. During combat the sheep horns need to reliably absorb the impact energy to minimize transmission and damage to the skeletal system and soft organs. It is estimated that the collisions of the bighorn sheep, which occurs very rapidly ~2 ms, are experienced at a strain rate of 10^2~10^3 s^{-1}[104]. The physiological requirements of the horn demand it to be stiff yet strong, tough enough to avoid fracture, and lightweight enough to allow for mobility [90].

The hierarchical structure of horns is very similar to hooves (Figure 2.13). They are composed of α-helical crystalline intermediate filaments (IFs, 7~10 nm in diameter), embedded in an amorphous non- helical keratin matrix [64,66,105]. The anisotropy of the organized keratin cells plays an important role in the orientation-dependent mechanical properties. It is important to note that the tubules in horns are not reinforced by thick lamellar cells as in the horse hoof. This has significant consequences in the failure and deformation mechanisms of the horn which differ from the horse hoof.

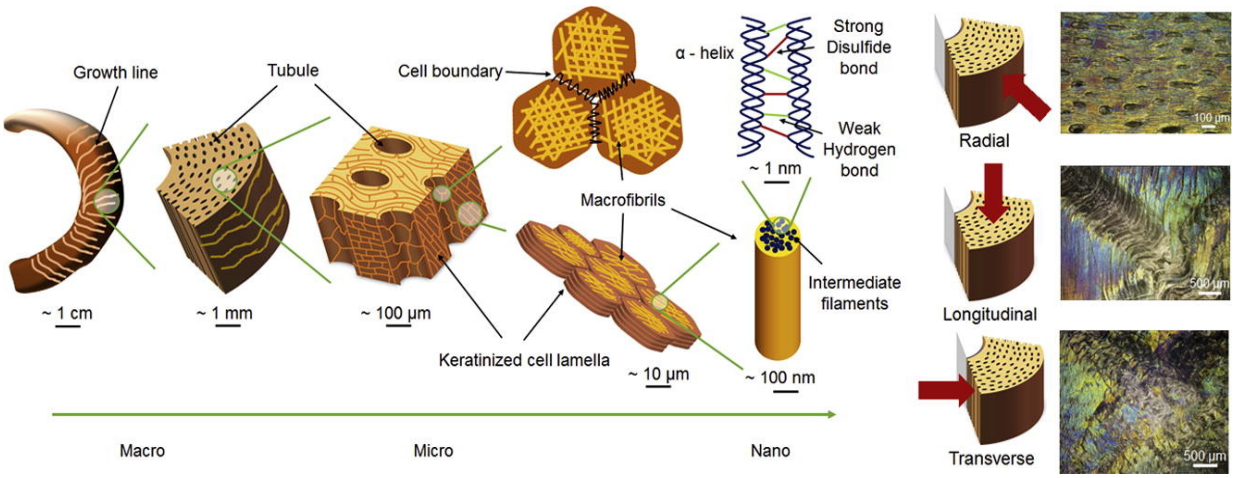

Figure 2.13 Hierarchical structure and deformation mechanisms relative to orientation of the bigsheep horn. During compression in the radial orientation the failure response is closure of the tubules. During compression in the longitudinal orientation there is formation of shear bands from the buckled and kinked lamella. The transverse orientation creates an X-shaped shear band. Reproduced with permission.[90] Copyright 2017, Elsevier.

While the horse hoof is an isotropic material, the horn is anisotropic. This leads to a difference in energy absorbing mechanisms between the hoof and the horn. The most impact resistant and energy absorbent direction in the horn is the radial direction (perpendicular to the horn surface) [90]. This is not surprising as this is the direction that the horn experiences during combat and defense. The hoof on the other hand is isotropic with respect to impact resistance and energy absorbance. The radial direction in the horn absorbs energy due to closure of the hollow tubule cavity (Figure 2.7) [90]. The longitudinal and transverse orientation failure mechanisms are shear-banding and buckling of the tubule walls (Figure 2.7) [90]. These failure mechanisms are lower in energy when compared to closing of the tubule walls. These main differences can be attributed to differences in microstructure. More specifically, the horn lacks reinforcement of tubules to help stiffen and provide structural integrity. The reinforced tubules in the horse hoof allow for elastic buckling and cracking which is a greater energy absorption mechanism when

compared to the horn [102]. Overall, the equine hoof wall is a superior energy absorbent material than the horn.

2.4.3 Suture structures and impact resistance

Biological systems can be decomposed into specific structural features across discrete length scales. Of these specific structural features, the suture structure has been found across a diverse range of biological materials including those that are known to withstand large impact forces: human skull [25,106], woodpecker beak [107], turtle shells [26,27], boxfish plates [24], pangolin scales [63], and horse hooves to name a few. Suture interfaces are defined as a compliant interlocking junction that connects adjacent components allowing for regional control over strength, stiffness, and energy absorption. The suture structure is incorporated in both mineralized (bone) and non-mineralized materials (keratin). Typically, there also exists a viscoelastic material within the gap of the suture interface, often collagen, that holds the plates together. Thus, there exists a dependence on performance with material properties such as elastic modulus. Additionally, there is a wide range of geometrical features that span across biological materials including degree of interdigitation, shape (triangular, trapezoidal, sinusoidal, etc.), and hierarchical ordering. Therefore, both the material properties and geometry of the suture structure are important in determining its ability to dissipate energy during impact.

The response of suture structures to impact is widely studied with respect to human skulls due to the implications of traumatic brain injuries. This is primarily accomplished through parametric studies on material property and geometry with the use of finite element analysis and/or mechanical testing of 3D-printed prototypes. The suture structure is often simplified and reduced in complexity to isolate the design features of interest (interlocking angle, waviness, hierarchical order, etc.).

For example, Zhang and Yang[108] used a sinusoidal model with two orders of hierarchy in a two-dimensional finite element model to describe how suture morphology influences stress attenuation and energy absorption under dynamic loading conditions. The first order of hierarchy is a simple sinusoidal function (model B) and the second order of hierarchy contains the pure sinusoidal function with an additional sinusoidal wave on a smaller length scale (model C) (Figure 10 A). Analysis was also performed on a flat interface as a control labeled as model A (Figure 10 A). Each interface joined two neighboring bone pieces labeled L-bone and R-bone (left and right respectively). An impulsive load q (50 kPa) was applied on the outer surface of L-bone for 0.04 μs which represents physiological dynamic loading conditions.

The sectional stress was measured at R-R' (labeled in Figure 2.14 A) and plotted in Figure 10 B to highlight the influence of suture morphology and hierarchical order. The flat interface has the largest average von Mises stress while the second order hierarchical suture has a significant reduction in stress (Figure 2.14 B). This suggests that the higher ordered suture structure acts as a transmission barrier to better attenuate the impact stress. This agrees with stress wave theory as increasing the hierarchy effectively increases the contact area with the transmitted stress wave. The suture morphology is also important in efficiently distributing the stress uniformly across the entirety of the bone (Figure 2.14 C). This is caused by scattering at the interface. The higher order hierarchy also correlated to an increase in the strain energy ratio implying its ability to store energy during impact. Additionally, this study evaluated the effect of elastic modulus on strain energy and demonstrated that as elastic modulus of the suture increases the strain energy decreases. This indicates that stiffness can be tailored to optimize strain energy storage. This study purposefully omitted the viscoelastic response that is typically associated with the suture interface to isolate the dependence on morphology.

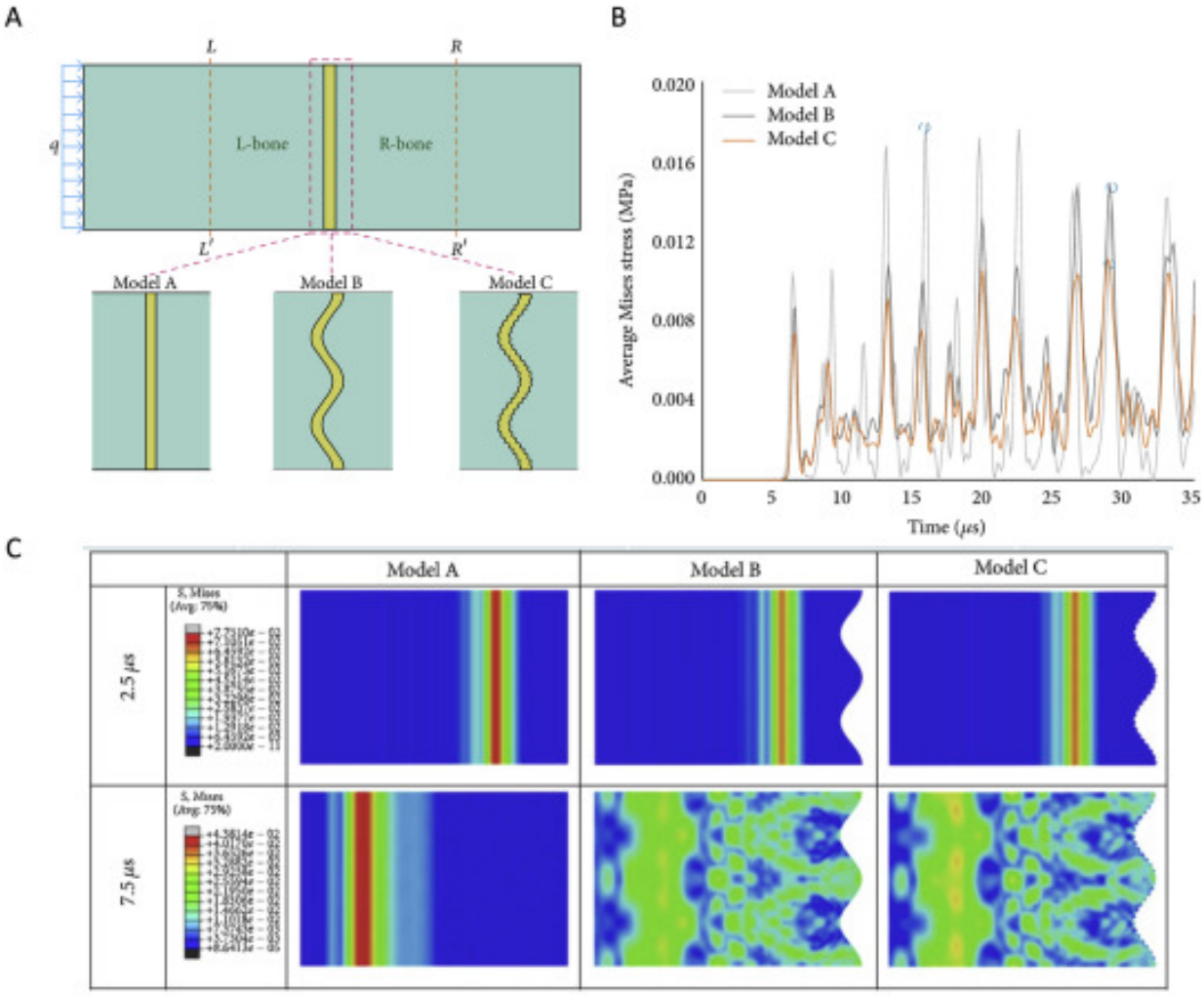

Figure 2.14 Bioinspired suture designs with increasing hierarchy. A) Three tested suture hierarchies and loading conditions. Model A is the flat interface. Model B is the simple sinusoidal suture. Model C is the second-order, hierarchical sinusoidal suture. B) Average von Mises stress at position R–R′ for the three different morphologies. C) Illustrates the time-dependence and stress distribution among the different morphologies. Copyright 2015, Z. Q. Zhang and J. L. Yang. Adapted with permission[108] Copyright 2014, IOP Publishing.

While Zhang and Yang[108] formally described the ability of sutured interfaces to attenuate stress, there was a lack of understanding of the exact mechanisms at hand. Lee et. al[109] used a similar two-dimensional finite element analysis under dynamic loading conditions to compare how stress waves were mitigated between a sinusoidal suture interface and a flat interface.

Different to Zhang and Yang[108], Lee et. al[109] applied a loading direction perpendicular to the interface (Figure 2.15 D). They examined the damping capabilities and showed that the flat interface was able to reduce the initial pressure wave by 53% while the sutured interface had a reduction of 90%. The dominating mechanism at hand is the conversion of compressive waves (S11) to shear waves (S12) and orthogonal flexure waves (S22) due to scattering at the interface as shown in Figure 2.15 E. Another attenuation mechanism was described by the viscoelastic response within the gap of the suture that allowed for strain energy storage (Figure 2.15 G).

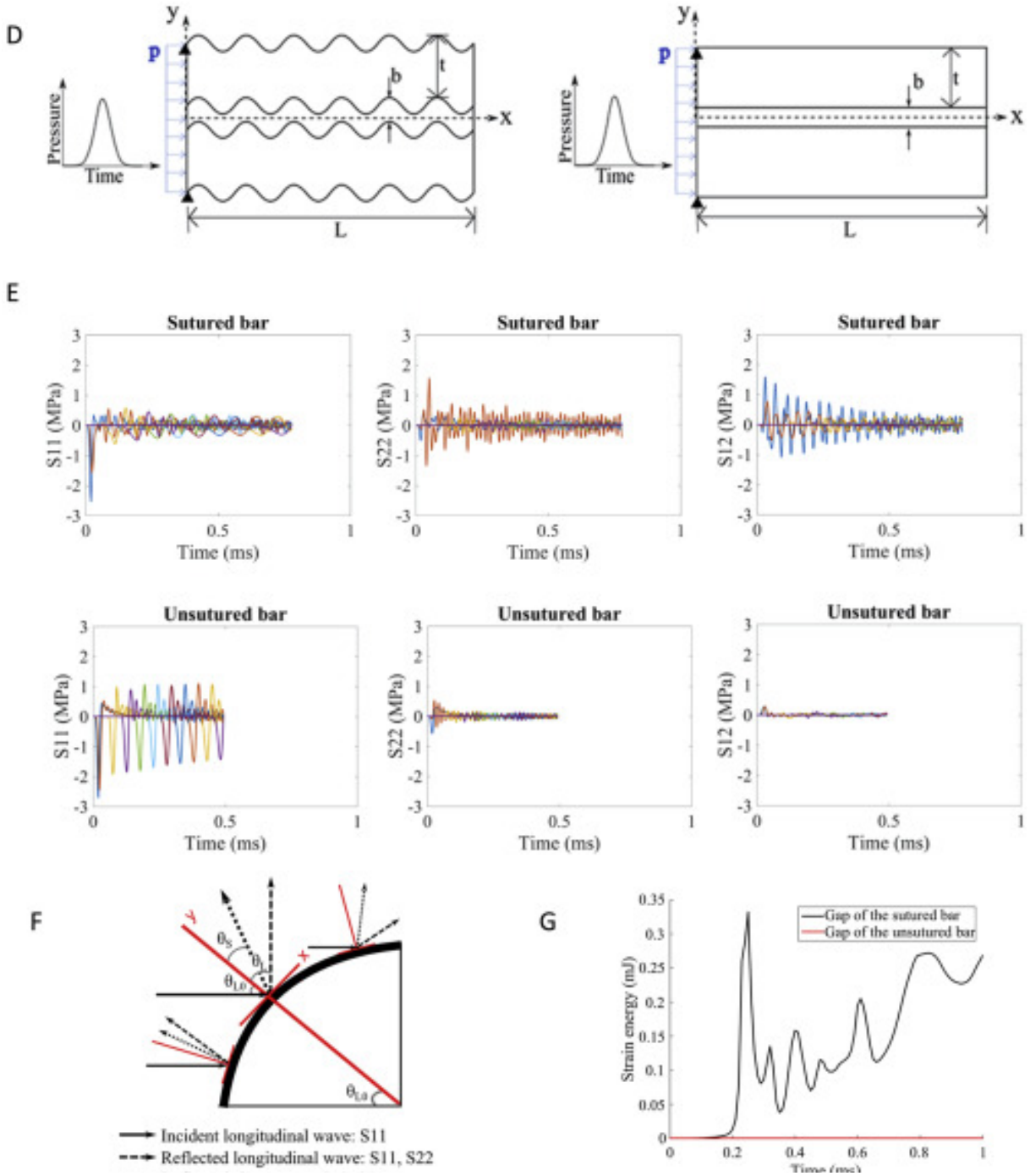

Figure 2.15 Bioinspired suture designs with increasing hierarchy. A) Three tested suture hierarchies and loading conditions. Model A is the flat interface. Model B is the simple sinusoidal suture. Model C is the second-order, hierarchical sinusoidal suture. B) Average von Mises stress at position R–R′ for the three different morphologies. C) Illustrates the time-dependence and stress distribution among the different morphologies. Copyright 2015, Z. Q. Zhang and J. L. Yang. Adapted with permission[108] Copyright 2014, IOP Publishing.

Lee et al.[109] performed a parametric study across a range of geometrical constraints including waviness, ratio of the suture height to the thickness of the bar, gap thickness, and type of boundary. The one geometric design that was shown to have the most effect on damping was the ratio of the suture height to the bar thickness. The pressure loss was the greatest in the sample that had the largest height of the suture when bar thickness was conserved. Interestingly, they did not see a huge influence with respect to waviness (wave height divided by wave period). They analyzed damping based off of waviness from 0.25 to 1.5 while a higher range is seen in nature, 1 (woodpecker) and 2.4 (bison)[109].

While the two aforementioned studies prove that suture interfaces are more superior than flat interfaces in damping and attenuating stress despite loading direction (parallel vs perpendicular), it is necessary to compare how loading direction influences impact response. The contribution of Maloul et al.[110] demonstrates the distinction between loading direction (parallel vs perpendicular) and strain energy. Loading parallel to the suture interface resulted in the highest strain energy output. This suggests that the parallel direction is more efficient in absorbing energy. For both loading directions, the highest stresses are observed at the peaks of the sutures. While the loading conditions in nature are much more complex and difficult to predict, this study provides the basis for tailorable design for specific applications under dynamic conditions.

Overall, there are limited studies that have investigated the geometrical and material property relationship found in sutures under dynamic loading conditions and the studies that do exists rely heavily on FEA. These few studies have shown the important role that sutures play in distributing stress and dissipating energy under high strain rates. There is clear evidence that suture geometry, elastic modulus, viscoelastic properties, and loading direction work synergistically to enhance performance under dynamic conditions.

2.5 Feather Structure and Composition

Bird feathers are composed exclusively of *β*-keratinous material arranged in a hierarchical order from the molecular to the macro-level (Figure 2.16). They exhibit a characteristic filament-matrix structure found in all keratins [70]. At the molecular level keratin polypeptide chains form into *β*-sheets held together by hydrogen bonds which make up *β*-keratin filaments (~3 nm in diameter) [57,111]. The filament forming proteins are embedded in an amorphous keratin matrix [112]. These filaments bundle together to form fibrils (~100 nm in diameter) which group to form macro fibrils (~400-500 nm in diameter), and finally forming fibers (~6 µm). The micro-, meso-, and macro-scale features of the feather will further be described here.

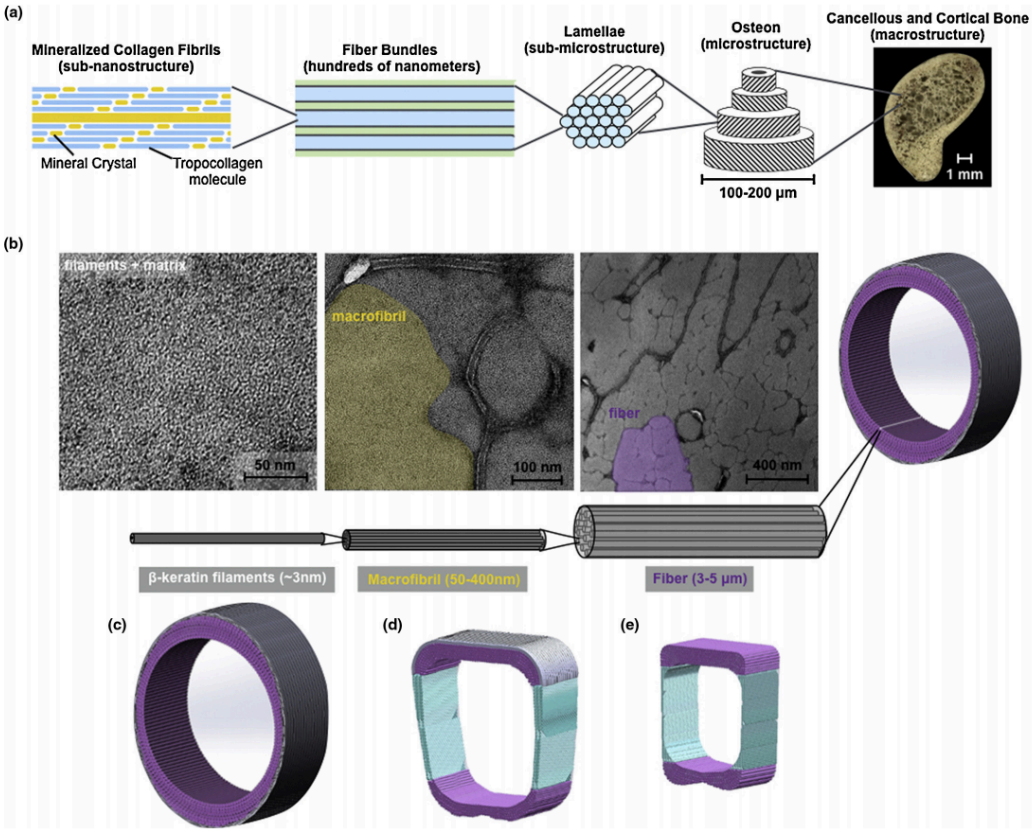

Figure 2.16 Hierarchical structure of the bird feather and bird bones. A) Hierarchical structure of bird bones. B-E) Hierarchical structure of the bird feather. Reproduced with permission.[113] Copyright 2017, Elsevier.

The feather consists of two sections: the shaft and the vane (Figure 2.17). The feather shaft runs down the middle of the feather and is further divided into the rachis and the calamus. The calamus develops from the follicle and is embedded within the skin keeping the feather attached to the body. The calamus is not exposed and is inserted within the wing. The rachis is the external part of the shaft which provides support for the feather vane.

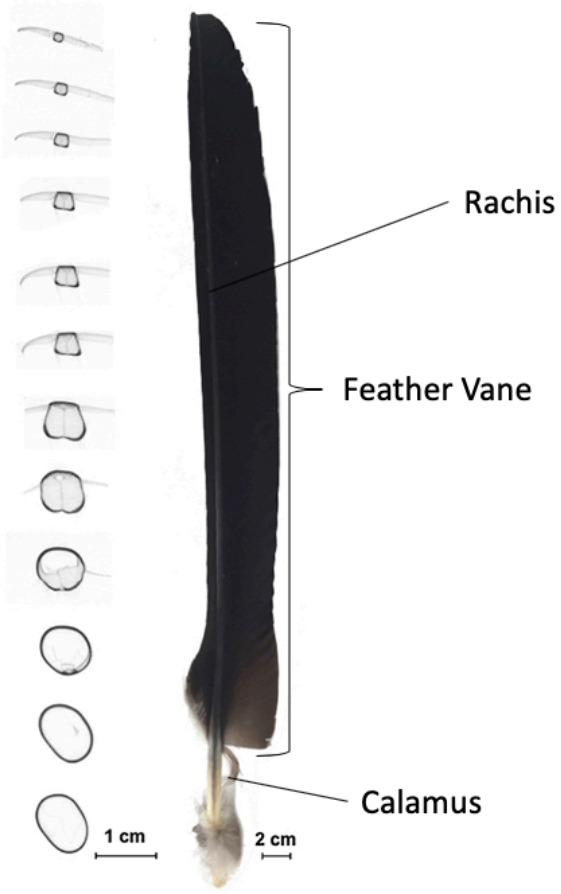

Figure 2.17 Structural components of the feather. The main shaft runs through the middle of the feather and contains the rachis and calamus. Within the vane, barbs branch from the rachis and barbules stem from barbs. Barbules are hooked on one side and grooved on the other providing an interlocking material that effectively captures air. Adapted with permission.

The feather vane is directionally permeable which effectively captures air for lift [114,115]. This mechanism is controlled by the geometry and stiffness of the branching barbs and

interconnecting barbule network that creates the feather vane as shown in Figure 2.18 [114,115]. Barbs branch from the rachis which are further branched into barbules. The barbules have hooklets (hamuli) on the end which fit into the groove of the neighboring barb creating a highly ordered lattice of interconnected adjacent barbs. More specifically, the distal barbule hooklet attaches the groove of the adjacent proximal barb. Each barbule has ~4-5 hooklets on the end. Having multiple hooklets increases both the adhesion and the probability that two neighboring barbs will stay connected. These adhesive design allows for localized deformation which helps to mitigate catastrophic failure of the whole vane. The interconnected network of the feather vane, provided by this adhesive mechanism between the barbs and barbules, is credited as the most essential element that allows for flight in birds [115]. The barb is asymmetric which leads to rotation when undergoing bending. A study by Sullivan et al.[115] has shown that when the barbs are zipped i.e. they are connected to a neighboring barb through the hook and groove adhesion, they are less likely to rotate when subjected to bending. This torsional resistance is due to the stabilization of the connected neighboring barb. Therefore, the reversible adhesive mechanisms is primarily responsible for the structural integrity of the feather vane. The barbule has a similar structure to the rachis which is a sandwich structure of compact keratin encompassing a center of medullary keratin, and in turn has similar bending properties (Figure 2.18).

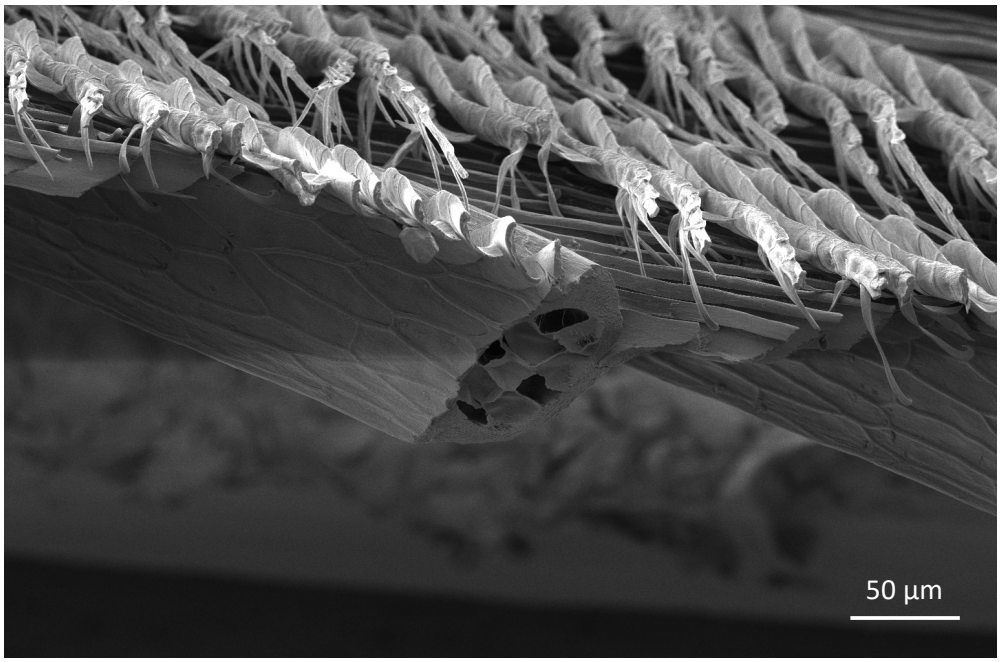

Figure 2.18 The feather vane showing the cross section of a barb. The barb is a sandwich structure with compact keratin enclosing a cellular structure. The barbs have branching barbules which terminate into hooklets. Here the hooklets can be seen fitting into the grooves of the neighboring barb.

The rachis can be considered a sandwich composite with a stiff outer cortex composed of compact keratin (cortex) and a foamy medullar center (medulla) (Figure 2.19). Although both the cortex and the medulla are composed of β-keratin, they differ in density and structure and therefore modulus. The density of the cortex ranges from 0.66-0.81 g/cm^3 and the density of the medulla ranges from 0.037-0.08 g/cm^3 [116,117]. Thus, we can predict that the cortex is much stiffer than the medulla. Indeed, it is found that the cortex is over 100 times stiffer than the medulla. The elastic modulus of the cortex is 2.5-6.5 GPa, while the modulus of the medulla is 0.01-0.03 GPa [116–120]. This great difference between moduli suggests that the load experienced by the rachis is primarily distributed and carried by the cortex [116,118,121]. Therefore, the cortex dominates the flexural stiffness of the feather shaft.

The cross section of the rachis is known to change shape along the length from calamus to tip which controls bending stiffness [118]. This is attributed to the changes in moment of inertia

with cross-sectional area. The shape changes from circular near the calamus to square within the rachis section as shown in Figure 2.17. In the rachis, the dorsal and ventral sides are thicker when compared to lateral sides. This provides support in dorsal-ventral bending which is the primary load of the feather during flight. The square cross section increases the rigidity of the rachis and resistance to dorsal-ventral flexure.[122] Additionally, the rachis diameter decreases from proximal to distal forming a tapered end. As the diameter decreases, the area of the cortex and medulla does not remain constant. Towards the tip of the rachis the cortex becomes to the more dominating material.

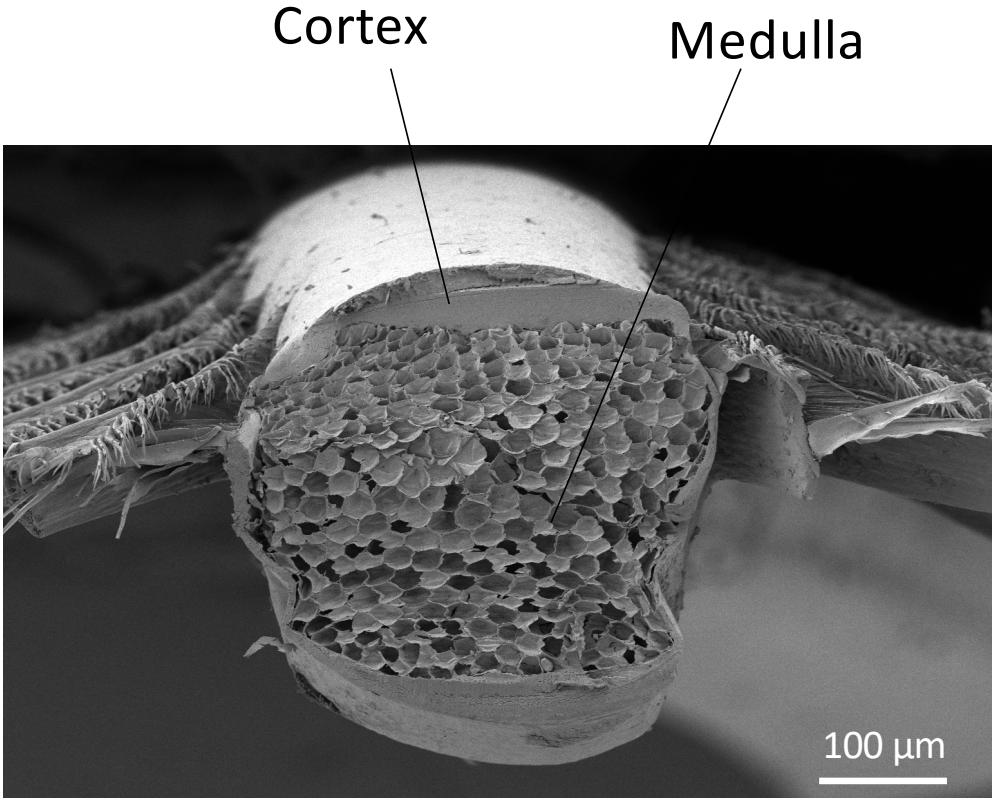

Figure 2.19 Scanning electron micrograph of a cross section of the feather rachis from a superb starling showing its sandwich structure. The outer cortex is composed of compact keratin and the foamy center is the medulla.

During flight, the wing is predominantly supported by the flight feathers. Prior experiments indicate that the outermost primary feathers are important for flight by generating lift and thrust during flapping in flight [123]. Flight feathers must be lightweight yet satisfy the constrains and aerodynamic loads without excessive damage due to flexure or torsion. A solution to these constraints is the adaptation of a sandwich structure. This consists of a solid stiff shell that surrounds a lightweight cellular core. The cellular core increases the moment of inertia and therefore increasing the resistance to buckling. The feather shaft is the primary energy absorbing material and withstands a majority of the load during flight.

2.5.1 Foams and sandwich structures

Since the feather shaft's success against buckling relies heavily on its sandwich structure which consists of a stiff outer cortex and low-density foamy center, the mechanical properties of foams, also referred to as cellular solids, and sandwich structures will be reviewed here.

The properties of cellular solids, or foams, are directly related to the shape and structure of the cellular unit comprising the foam. This unit can be described as open- or closed-cell foams. In open-cell foams, the cell is unenclosed and gas is not constrained within the cell, while in closed-cell foams the cell is enclosed by a membrane and gas is effectively trapped within the cell (Figure 2.20). Under compression, foams present three distinct regions of deformation. Initially, the foam experiences (I) linear elastic bending of the cell edges which eventually leads to (II) stress plateau where the cell collapses by buckling, yielding, or crushing and then finally (III) densification at large strains (Figure 2.21) [124]. While the modulus of open-cell foams only relies on edge bending, closed-cell foams have an additional resistance to deformation due to face stretching and gas compression [124]. The cell membrane will stretch perpendicular to the applied compressive

load and the gas pressure within the cell, if significant, will need to be overcome which typically lends to an increase in modulus. The medulla of the feather shaft can be considered as a closed-cell foam as it has partially covered faces as shown in Figure 2.19; however, the membrane is permeable so the gas pressure within the cell can be assumed to be atmospheric pressure and effectively negligent to its mechanical properties [125].

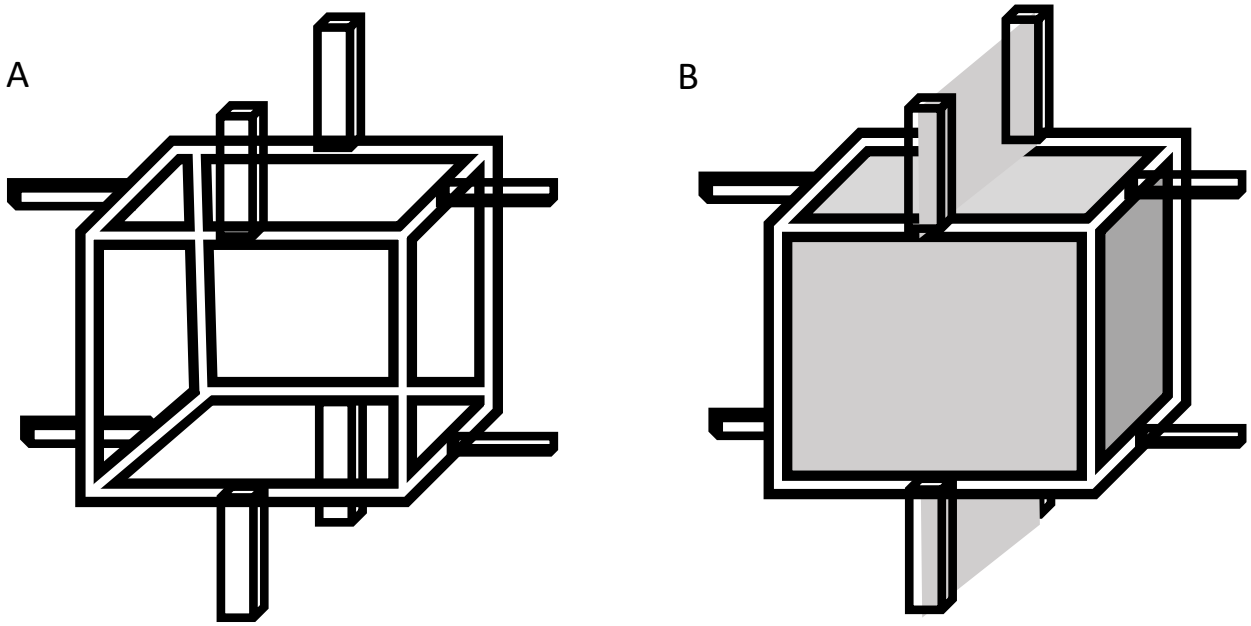

Figure 2.20 Unit cell of open- and closed-cell foams. A) Schematic of an open-cell foam. B) Schematic of a closed-cell foam.

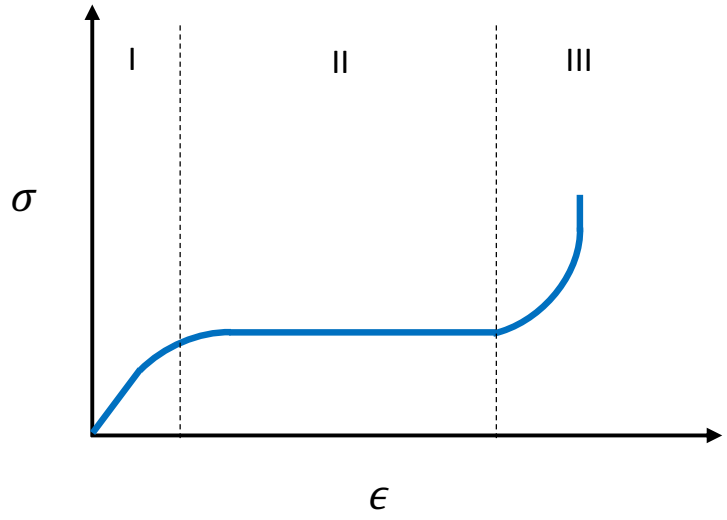

Figure 2.21 Typical stress-strain curve of foams with three distinct regions. In region I, the foam experiences linear elastic bending of the cell edges. In region II, the foam reaches a stress plateau where the cell collapses due to buckling, yielding, and/or crushing. Finally in region III, the foam reaches densification at large strains.

One of the most defining characteristics of foams is its relative density, $\frac{\rho^*}{\rho_s}$ where $\rho^*$is the density of the foam and ρ_s is the density of the solid from which the foam is derived. Generally, the relative density of cellular solids can range from 0.3 to 0.003 [124]. The relative density for open- and closed-cells can be calculated from their geometry as follows [124]:

Open-cell: $\frac{\rho^*}{\rho_s} = c_1 \left(\frac{t}{l}\right)^2$

Closed-cell: : $\frac{\rho^*}{\rho_s} = \frac{2}{\sqrt{3}} \frac{t_f}{l} \left\{1 + \frac{\sqrt{3}}{2A_r}\right\}$ (2.2)

where $t_f$is the thickness of the foam cell wall, l is the foam cell edge length, and A_r is the aspect ratio of the foam cell (h/l).

The relative density can be directly related to the modulus of the foam through the following [124]:

Open-cell: $\frac{E^*}{E_s} \approx \left(\frac{\rho^*}{\rho_s}\right)^2$ (2.3)

Closed-cell: $\frac{E^*}{E_s} \approx \phi^2 \left(\frac{\rho^*}{\rho_s}\right)^2 + (1-\phi)\frac{\rho^*}{\rho_s} + \frac{p_0(1-2v^*)}{E_s(1-\frac{\rho^*}{\rho_s})}$ (2.4)

where $E^*$is the modulus of the foam, E_s is the modulus of the solid material the foam is made from, p_0 is the initial pressure, $v^*$is the Poisson's ratio of the foam, and ϕ is the volume fraction of the cell located in the cell edges [124]:

$$\phi = \frac{t_e^2}{t_e^2 + \frac{Z_f}{\bar{n}} t_f l} \quad (2.5)$$

where t_e is the thickness of the foam cell edge at the corner, $Z_f$is the number of faces that meet at an edge on a single cell, and $\bar{n}$ is the average number of cells per single cell.

In engineering applications, sandwich structures are used for their ultra-lightweight, energy absorption capabilities, and comparable mechanical strength to bulk materials. Sandwich structures can be tailored by controlling the properties of the face (outer cortex) and core (foamy center) and the geometry. Typically, sandwich structures will be constructed with a high modulus face and a low modulus core to achieve a light-weight yet stiff material which often have rectangular cross sections. Some examples of materials used for the core are aluminum and other low-density metals and fiber-reinforced composites. Typical core materials are based on cellular structures and with recent advancements in processing can be formed from a multitude of materials ranging from two-dimensional honeycombs (e.g. aluminum honeycombs) to three-dimensional cellular solids from polymers, metals, ceramics, and glasses. The sandwich structure is often used in applications that require light-weight materials such as airplanes (flooring panels), vehicles (chassis), boats (hull), satellites, and impact-resistant packaging. Sandwich structures are not limited to engineered materials and are found across a diverse range of biological materials including skulls [126], antlers [127], beaks [128], turtle carapace [129], and fruit peels[130].

Unlike engineered materials, the faces and core of biological materials are both made of the same material which occur in distinct phases: the face being more densified, while the core is a foam.

Typically, sandwich structures undergo bending as their predominant loading mode. This causes compression in the top face and tension in the bottom face, while the core undergoes shear. If the adhesion between the core and the faces is too weak, delamination will occur. The low-velocity energy absorption mechanisms occur in the faces and the core synergistically as follows: (1) cracking, wrinkling, fracture, and delamination in the top face (2) core buckling, (3) debonding from the faces and the core, (4) core densification and compaction, (5) shearing and cracking of the core, (6) fiber pullout in the faces, and (7) damage initiation in the bottom face [131–135].

Since bending is the primary loading that the feather shaft experiences during flight, it is important to understand the basic mechanics equations that relate the applied force to the internal stress of the face in the sandwich structure. Here the core is ignored due to the modulus of the face being much greater than the modulus of the core. The maximum bending stress is expressed as [124]:

$$\sigma_{max} = \frac{Mc}{\mathrm{I}} \tag{2.6}$$

Where $M = Fd$, in which F is the maximum force applied and d is the moment arm. The distance from the neutral axis to the outer face is denoted as c and I is the area moment of inertia. A basic understanding of this equation shows that the bending stress increases when c becomes larger. Feathers take advantage of this by having a foam-filled core to effectively increase c. Material positioned further from the neutral axis is more effective in resisting bending. Therefore, the characteristic of the rachis having a thin, dense exterior with a foam core is desirable for bending conditions.

Additionally, the rachis is subjected to torsion. The maximums shear stress is expressed as [124]:

$$\tau = \frac{Tc}{\mathrm{J}} \tag{2.7}$$

Where T is torque, *c* is the radius of the section, and J is the polar moment of inertia.

With respect to feathers, this work will focus on the structure-property relationships of the rachis due to its integral role in supporting the weight of the bird and the respective aerodynamic loads during flight with considerable constraints of being lightweight. We will investigate the sandwich-like structure of the rachis with its foam-filled-keratin medulla surrounded by a stiff cortex and how this structure is tailored for flight.

2.6 Acknowledgements

Chapter 2, in part, is published as a review article in *Journal of Materials Research and Technology*, authored by B. S. Lazarus, A. Velasco-Hogan, T. Gómez-del Río, M. A. Meyers, and I. Jasiuk. The dissertation author is the second author on this publication.

Chapter 2, in part, is under review in *iScience* authored by B.S. Lazarus, C. Charul, A. Velasco-Hogan, I. Jasiuk, and M. A. Meyers. The dissertation author is the third author on this publication.

This work is funded by the National Science Foundation Mechanics of Materials and Structures Program with corresponding grant number 1926361.

Chapter 3: Transparent Teeth of the Deep-Sea Dragonfish

3.1 Introduction and Significance

In spite of the recent abundance of research on biological materials[2,3,9,23], including those of marine origin [136–139], organisms that live in great ocean depths have been virtually unexplored, both in terms of their structure-property relationships and potential for bioinspiration. This is in no small part due to the difficulty in accessing these pelagic depths (down to 4,000 m on average) and extracting specimens to study. The physics driving the biology of deep-sea animals (and therefore the biological materials they make) is indeed complex, and still poorly understood with regards to its regulatory effects on biological processes. In order to predict some of the "deep-sea effects" on biological materials, a number of unique features characteristic of deep-sea environments need to be noted: lack of ambient light[140], low temperatures, and high pressures[141,142]. As a result of these extreme conditions, fascinating adaptations have evolved.

A unique observation is that the teeth of several deep-sea fishes are rather transparent. These teeth have heretofore not been studied, and until now their structure, mechanical properties, and ecological function were unreported. One particular species of interest is the deep-sea dragonfish. Deep-sea dragonfish, belonging to the family Stomiidae, are apex predators which typically feed on smaller myctophiform and gonostomatid fishes[143,144]. Thus, they have proportionately enormous jaws capable of a special mechanism of opening and closure referred to as "loosejaw." This mechanism allows the dragonfish to open its jaw bigger than a conventional jaw of similar size, and enables it to ingest preys up to 50% of its own size[145]. This design allows for effective predation as the dragonfish can ingest large prey for sustained energy, which are often scarce in the deep-sea. It has also been reported that the jaw muscles of the dragonfish are weak[145] and therefore the large fangs must be sharp, as confirmed by their slim and pointed

outline, to pierce prey effectively. These teeth, although “large” relative to the jaw, and in fact sticking out of it in many cases, are difficult to see because they range from translucent to transparent to light depending on whether in air or water, respectively.

Herein, we show that the teeth of the deep-sea dragonfish are composed of two homogeneous concentric layers, namely enamel-like and dentin, which constitute the wall of the teeth, and that they are nanostructured, resulting in reduced Rayleigh scattering of light. We suggest that the nanostructured design of the transparent dragonfish teeth enables predatory success as it makes its wide-open mouth armed with saber-like teeth effectively disappear, showing no contrast to the surrounding blackness of the fish, nor the background darkness of the deep-sea.

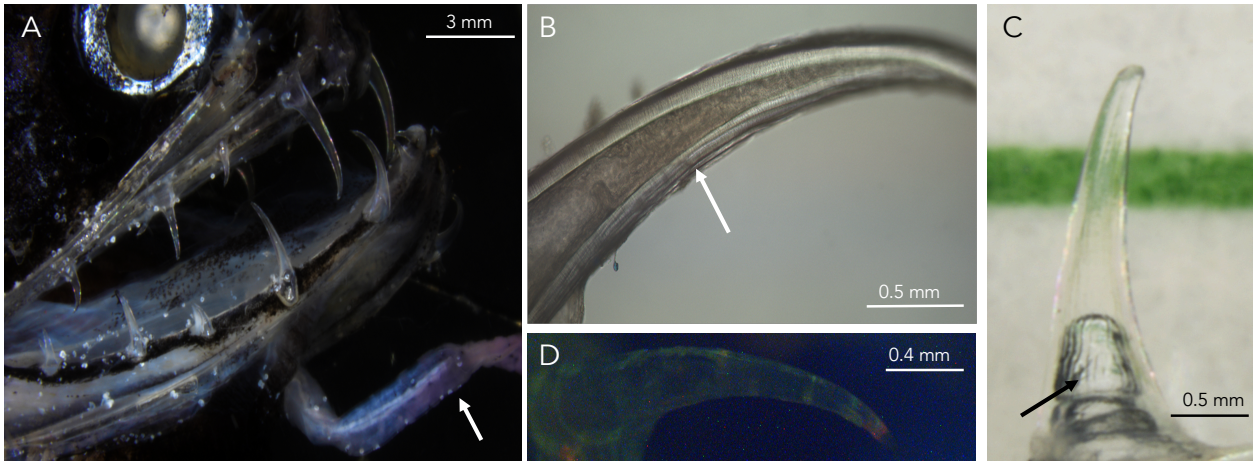

Figure 3.1 Light microscopy of dragonfish teeth. **(**A) Head of a freshly collected specimen showing the row of teeth erecting outward from the jaw. Arrow points to the barbel. Image taken of the head in filtered seawater and captured using a polarizing filter. (B) Close-up, showing optical evidence of concentric layers and hollowness of the tooth. Image taken in filtered seawater with an immersive lens. Arrow points to the striations seen on the concave side. (C) Tooth imaged in seawater with color line behind to demonstrate transparency. The arrow indicates an air bubble within the hollow cavity of the tooth due to dissection from the jaw. Image captured with a polarizing filter. (D) Tooth under fluorescence excited at a broad band excitation 440-490 nm and collected with a long pass filter (>515 nm). This image shows little florescence. Image taken of a dry specimen in air.

3.2 Optical Performance in Transmittance and Reflectance

In terms of spectral translucency, the teeth analyzed in filtered seawater showed light transmittance that changed gradually with the color spectrum, increasing from~38% in the blue range which gradually increased to ~73% of light in the red range (Figure 2B). This is a significant increase of transmittance when compared to analysis done in air which showed transmittance around ~32% of light in the blue range to ~35% of transmittance in the green-red (Figure S1). Although a limited amount of this difference could come from technical challenges of capturing light transmittance in water rather than air, the difference is likely to originate mainly from differences of refractive indices between the inside of the tooth material and the outside medium (water vs air). In water, the interfaces with the tooth material shows a smaller difference of refractive index than for air, causing light to be less diffracted sideways when penetrating and existing the tooth, resulting in making it more transparent than in air. To analyze the effect of tooth material (tooth thickness and relative mineralized density) on the transparency, hyperspectral analysis was performed at three different locations along the tooth (tip, middle, base) considering that the μ-CT data (Figure 3.2A) clearly showed a gradient structure along the length of the tooth. The base is thicker and less mineralized (indicated by the cooler colors) while the tip is thinner and more mineralized (indicated by the hotter colors). The tip transmits less light in the blue range and more light in the red range when compared to the base and middle sections. As expected, all sections of the tooth transmit less light in the blue range, which is due to an increase in Rayleigh scattering that is inversely proportional to the fourth power of wavelength.

The transparency of the teeth of the deep-sea dragonfish *Aristostomias scintillans*, both in terms of level of transparency and spectral difference, is comparable to that of the shell of the shallow-water oyster *Placuna placenta*. In this shell, transmittance ranges from ~20% in the blue

range up to ~80% in the red range, which is homogenous spatially for various thicknesses (71—660 μm).[146] The *Placuna placenta* is a shallow-water oyster. Transparency in shallow waters where sunlight is abundant is critical for camouflage but also for sunlight to reach photosymbionts that could live under shell structures.[147] At such great depths where the dragonfish is found, there is only light from bioluminescence which causes the effectiveness for transparency to increase dramatically.[148] For example, the contrast threshold for a cod's eye increases from 0.02 at light intensities found in 200 m to 0.5 at 650 m where it would be unable to detect tissues with a transparency greater than 50%.[148] This suggests that the transparent teeth, while comparable to a shallow-water oyster, are much more effective in the greater depths of the ocean.

While transmittance is an indicator of transparency by measurement of how much light can pass through a material without being lost (e.g. via scattering, absorbance), it is also valuable to analyze reflectance. Reflectance is important from an ecological standpoint as it signifies the amount of light that would shine back from the tooth surface and can therefore illuminate the fish's presence. Reflectance was analyzed with hyperspectral imaging at three similar positions as for transmittance (tip, middle, base) to differentiate between structural effects along the tooth. The teeth were analyzed with a white background, and since they are translucent, the background influences the reflectance. Reflectance near 100% indicates how closely matched to the background the material is (the more transparent it is). Anything less than 100% reflectance suggests that the light was lost due to various mechanisms such as scattering, absorbance, etc. The teeth analyzed showed reflectance in filtered sea water from 39% of light in the blue range to 86% of light in the red range (Figure 2C). The base of the tooth had the greatest reflectance 70% in the blue range and 86% in the red range. Again, reflectance in the blue range was decreased due to an increase in Rayleigh scattering for blue light. The reflectance analysis shows that the teeth match

fairly well to the white background and therefore are not likely to reveal the presence of the dragonfish to either prey or predator.

We believe that the elaborate structural arrangement of the teeth, which provides mechanical strength combined with transparency, enhances predatory performance of the fish. The dragonfish is indeed a top predator of the deep-sea, with a dark sleek body that is equipped with rows of photophores[149] along the ventral region and a light-producing barbel attached to its chin[150]. The ventral photophores' light emission matches that of downwelling environmental light camouflaging its silhouette[149]. While the barbel is used to attract the attention of its prey, the dragonfish body and mouth in particular must remain hidden for effective hunting[150,151]. We suggest that the transparent teeth provide an additional successful camouflage strategy by reducing the scattering of light (from any possible bioluminescence from the dragonfish itself and/or its possible prey) and being therefore concealed against the darkness of the mouth and/or deep ocean.

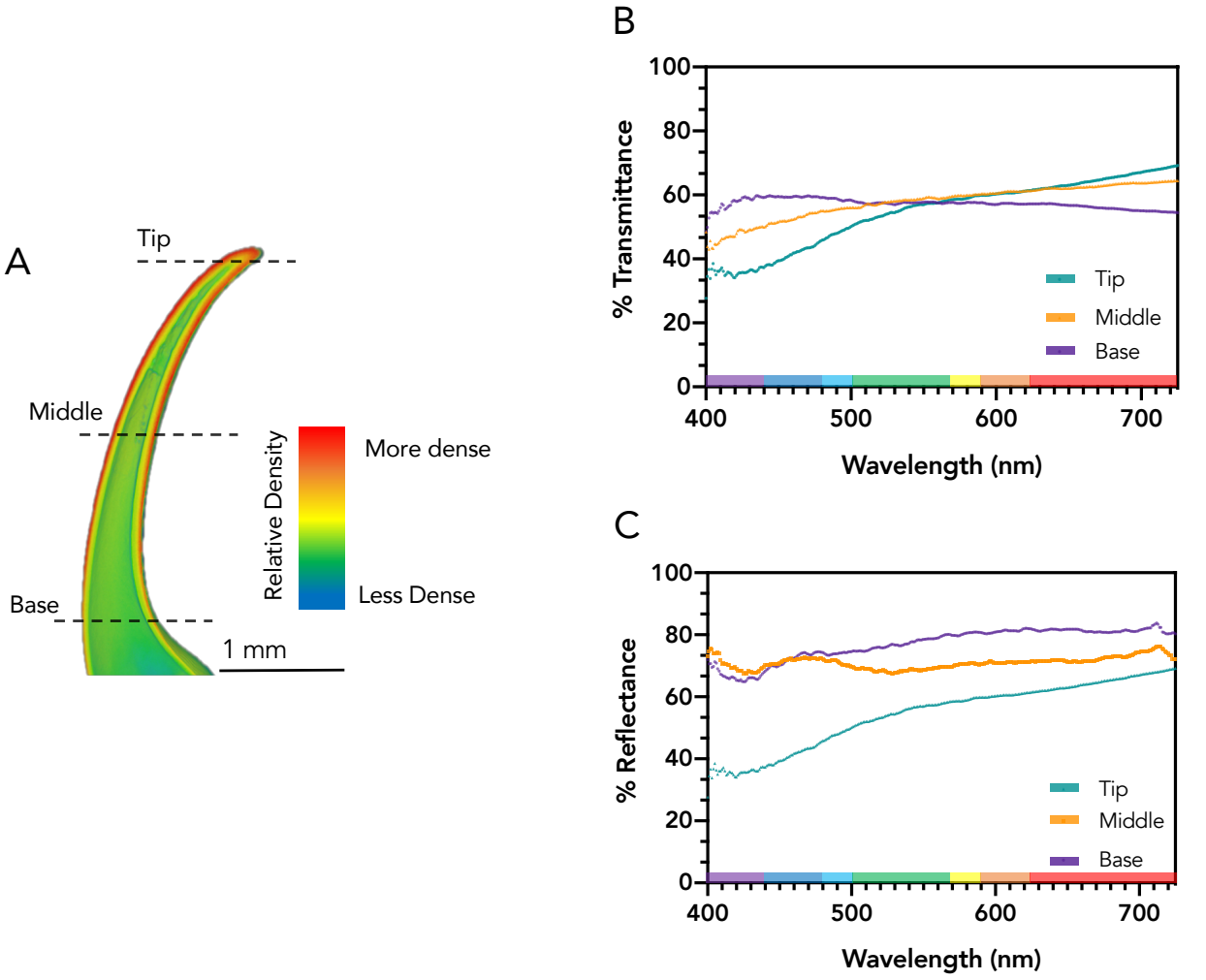

Figure 3.2 Optical properties in transmittance and reflectance. (A**)** Micro-CT scan of a longitudinal cross-section of a representative tooth. The color mapping indicates relative density signifying degree of mineralization. Hotter colors (red) are more dense while cooler colors (blue) are less dense. Dashed lines represent relative locations where analysis was performed**.** (B) Transmittance for three sections of one tooth (tip, middle, base) with respect to wavelength**.** (C) Reflectance for three sections (tip, middle, base) with respect to wavelength.

3.3 Structural Characterization of Enamel-Like and Dentin Layers

Under white light illumination, it was detected that the teeth have two types of surfaces: smooth and striated (Figure 3.1B, and 3.2). The rough surface is located mainly on the concave section of the tooth and consists of longitudinal striations and ridges. The smooth surface is located elsewhere on the tooth, which is thus characterized by an absence of significant surface features. All observed teeth have longitudinally aligned ridges on the concave surface, which are shown for eight representative teeth in Figure 3.2. The ridges are spaced ~20 μm, are sharp (radius at the tip~1-2 μm); and can effectively cut tissue. Some of the teeth show perforations at the base, which can act to increase their flexibility as the prey might be wiggling when caught (Figure 3.2)[152].

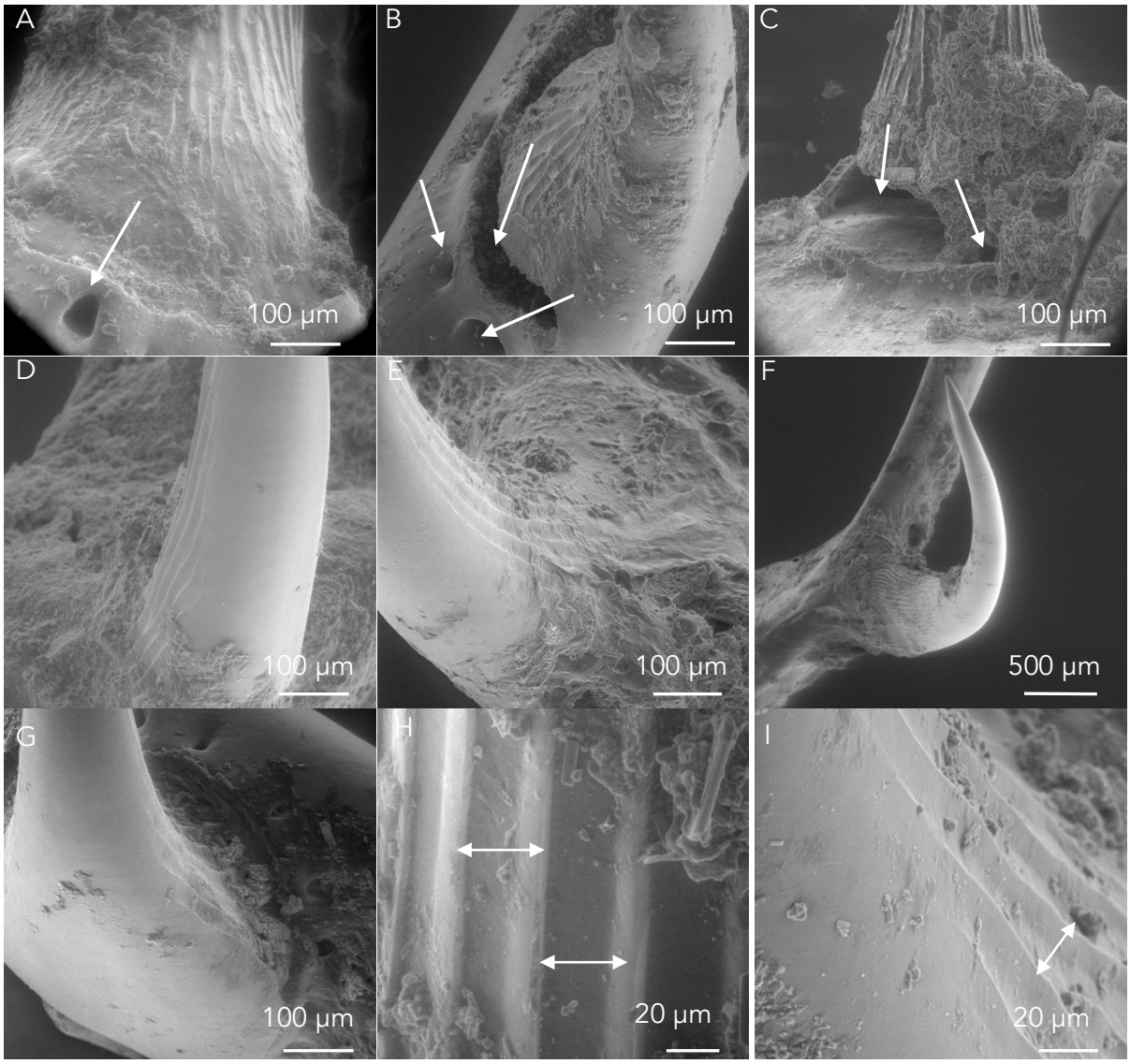

Figure 3.3 Details of the concave surface of representative teeth showing longitudinal striations. (A-C) Not perforation in bottom of teeth marked with arrows; (D-G) different teeth; (H,I) detailed view of ridges that are ~20 µm apart and have a radius of curvature, at the apex, of approximately 1-2 µm.

The teeth were observed under electron microscopy to obtain their principal morphometry, nanoscale structure, and composition. Overall, all teeth were found to have radii of curvature at the tip ranging from 2.5 to 5 μm. This is extremely sharp when compared to piranha teeth[153] that have a radius of ~14 μm and the sharpest knives that have a radius of ~1 μm[154]. A notable number of teeth have significant wear and tip fractures, revealing the pulp cavity as shown in Figure 3.3. The fracture surface in Figure 3C, D highlights two sub-surface layers: a smooth, apparently more brittle layer ~ 3 μm thick (marked 1) and a rougher layer (marked 2).

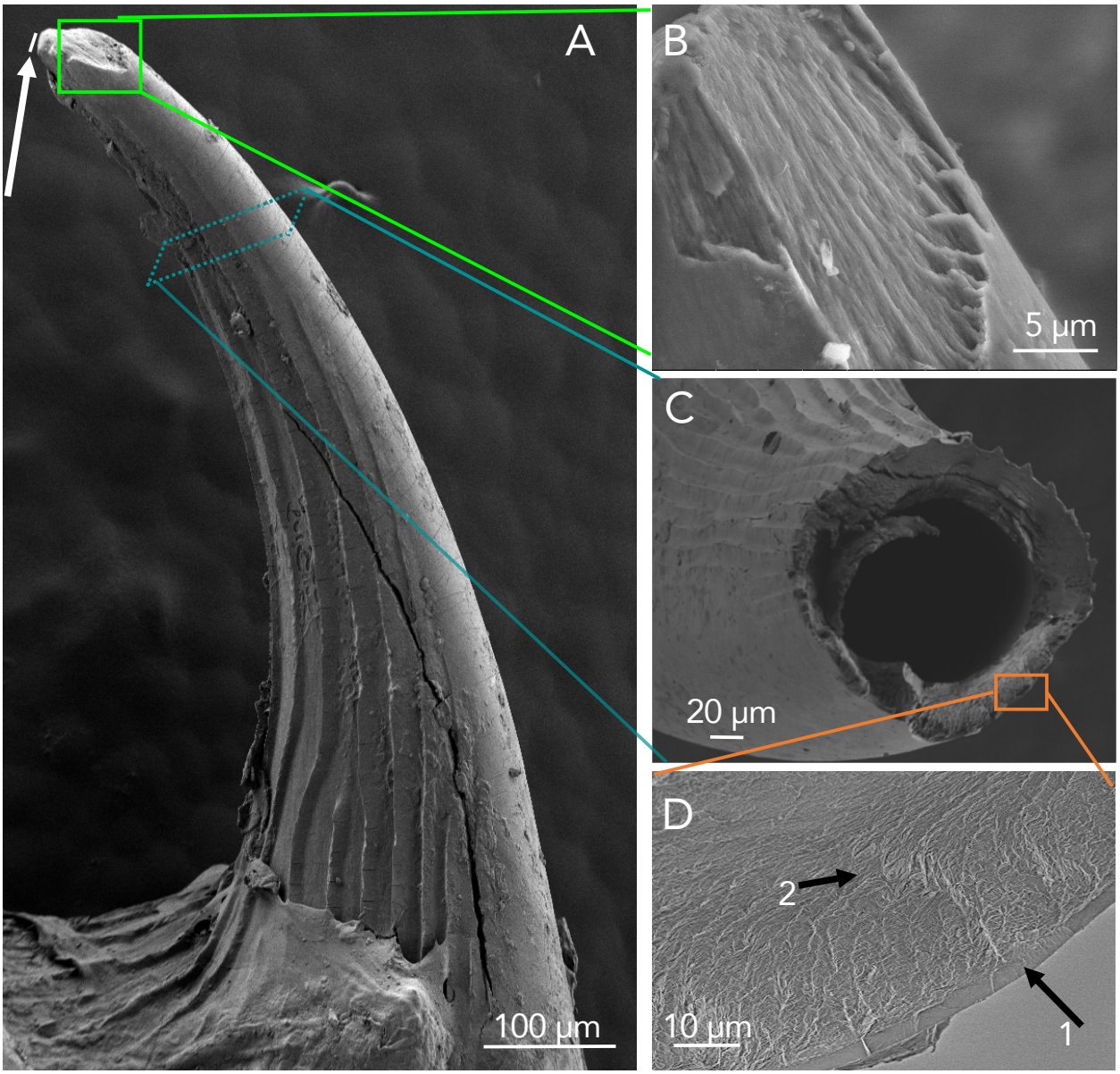

Figure 3.4 Characteristic teeth exhibiting longitudinal striations on concave side. (A) Shorter tooth from lower jaw with broken/worn tip. Arrow indicates radius of curvature. (B) Surface wear near the tip of the tooth revealing the thin enamel-like surface and dentin layer which has preferred orientation in the longitudinal direction**.** (C) Transverse section showing detail of hollow pulp cavity. (D) Enhanced transverse-cross section showing enamel-like outer layer (~ 3 µm, marked 1) with smooth fracture surface and dentin (marked 2) with an irregular surface.

The features in the fracture surface align with the longitudinal tooth direction (Figure 3A, B). The surface of the tooth also exhibits a pattern of circumferential cracks that do not extend through the entire thickness but are restricted to the outside layer. This pattern of cracks is evidently produced by flexure of the tooth which eventually led to its intentional fracture for observation (Figure S4A). The dentin layer, as will be seen later, has a structure that can provide greater toughness. A specimen for transmission electron microscopy was extracted by focused ion beam (FIB) and it is shown that cracks initiating at the surface arrest before reaching the dentin-enamel junction (Figure S4B).

Atomic resolution TEM on specimens that were further thinned to ~40 nm shows the characteristics of both the enamel-like and dentin layers (Figure 4A). The enamel-like layer consists of individual crystallites (Figure 4B) which, upon stacking, form Moiré patterns. The edges of the crystals are rounded, supporting the hypothesis that they are embedded in an amorphous matrix. The diffraction pattern (Figure 4C) exhibits a clear circular pattern (with individual spots embedded in the circle) and circular segments. One can distinguish a preferential orientation from the segments, and the diffraction pattern is similar to the one observed by Mahamid et al. (Figures 3Bb and Bc)[155], which they describe as poorly crystalline and clearly crystalline, respectively. The diameters of the rings coincide with those of Mahamid et al.[155] (002) and (004) (Table 1). A simple manner to interpret the structure is to consider it as a mixture of amorphous and nanocrystalline phases. The crystals have approximate dimensions of 5x20 nm. They are difficult to resolve because their size is significantly smaller than the thickness of the foil (~80 nm). However, additional characterization on a specimen subjected to a different preparation procedure, confirmed the nanoscale features and Moiré pattern formation.

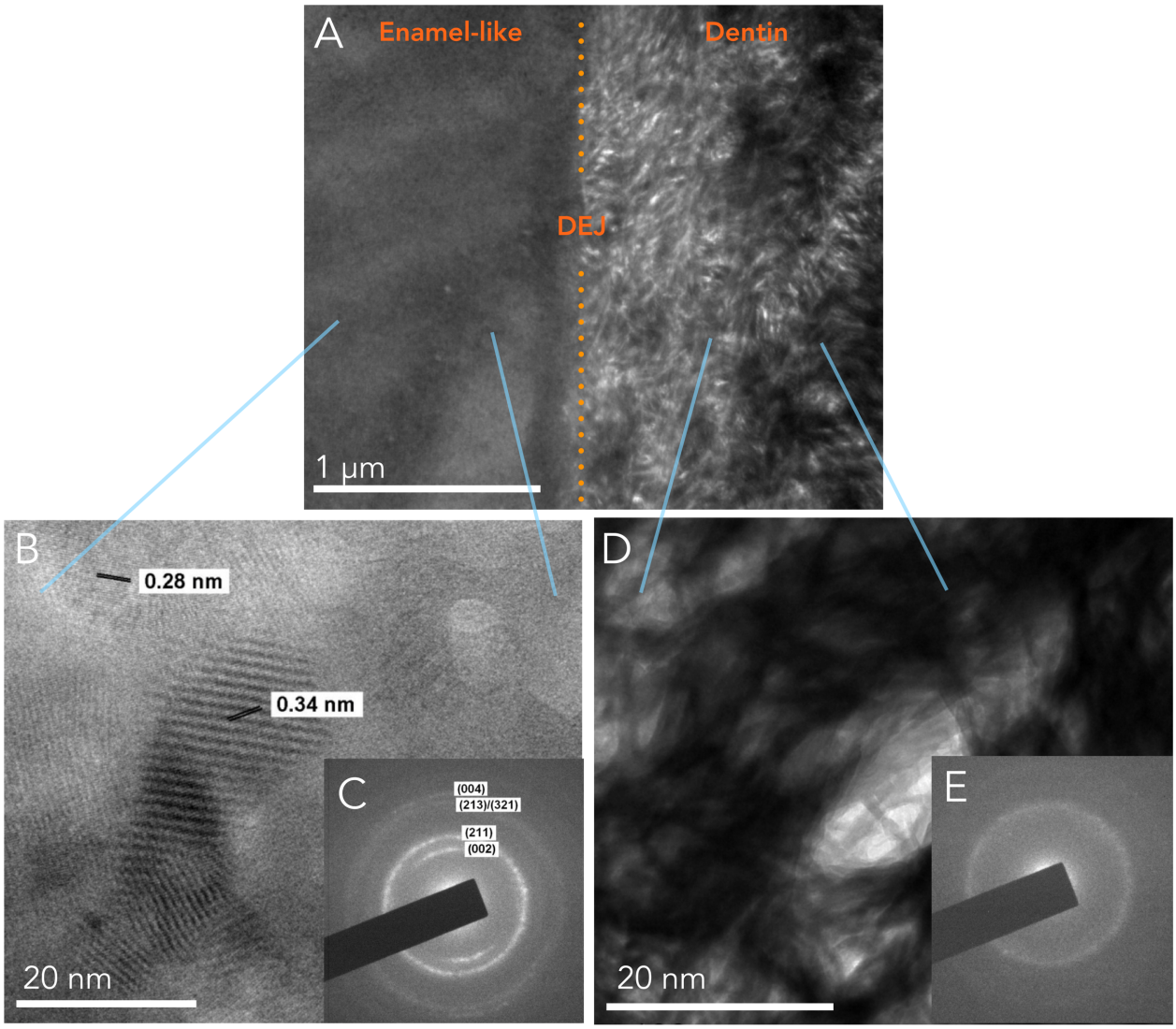

Figure 3.5 TEM of the nanostructured enamel-like and dentin layers. (A) TEM showing the dentin-enamel-like junction (DEJ). (B) TEM showing organized structuring of the enamel-like layer. (C) Diffraction pattern of the enamel-like layer showing discrete spot characteristics of nanocrystalline structure and an amorphous structure (indicative of the diffuse background). (D) TEM showing dentin consisting of a woven pattern of nanometer rods (~5 nm diameter). (E) Diffraction pattern of dentin which shows greater amorphous characteristics than the enamel-like layer.

The dentin structure (Figure 3.4A, D) consists of nanometer-size rods (~5 nm diameter) forming an interwoven pattern by virtue of their 'curvy' nature. There is also a degree of nanoscale

porosity in the structure suggested by the spatial variation in electron transmission (darker and brighter regions adjoining each other). The diffraction pattern (Figure 3.4E) is more representative of an amorphous structure when compared to the enamel-like layer which has clear diffraction spots embedded in the rings. The diffraction pattern shows a spacing of ~0.8 nm, which suggests that these are the (001) planes of hydroxyapatite (Table 3.1).

Table 3.1. Identification of Lattice Spacings from Diffraction Rings and Comparison with de Wolff[156].

Diffraction Files $Ca_5(PO_4)_3(OH)$	Intensity/spacing (nm)	Enamel-like (nm)	Dentin (nm)
(100)	12/0.817		
(002)	40/0.344	0.34	
(211)	100/0.281	0.27	0.28
(112)	60/0.278		
(300)	60/0.272		
(400)	12/0.1721	0.171	
(213)	40/0.184		0.18

3.4 Composition

To determine the mineral nature, the teeth were first observed under blue light illumination for fluorescence detection. Teeth of mammalian organisms fluoresce in the green when excited in UV light (350—400 nm). Such fluorescence has been extensively reported[157] and attributed not only to the organic matrix (collagen) of the teeth[158,159] but also to the mineral itself (dentin, enamel, and/or aragonite[160–162]). In the case of the dragonfish teeth, only limited fluorescence was observed when excited at 355 and 390 nm (Figure 3.1D-E). This indicates that the teeth are

not made of a brightly fluorescent mineral such as aragonite, and that any organic material is poor in aromatic amino acid known to have fluorescence, such as tryptophan, tyrosine, and histidine.

The diffraction patterns of the teeth allow for the identification of hydroxyapatite (HAP) $Ca_5(PO_4)_3(OH)$, as predicted. Table 3.1 provides the spacings and intensities, in the enamel-like and dentin layers, of the diffraction patterns[156]. Bright-field and dark-field TEM were used to determine the respective location of organic and inorganic material. As shown in Figure 3.5B, the dark-field micrograph highlights the individual nanorods which are primarily composed of inorganic material. This suggests that the crystalline inorganic material is HAP which is embedded within an organic matrix which is further characterized as collagen. The formation of HAP nanorods suggests preferential nucleation on collagen fibrils with diameters in the 5-10 nm range.

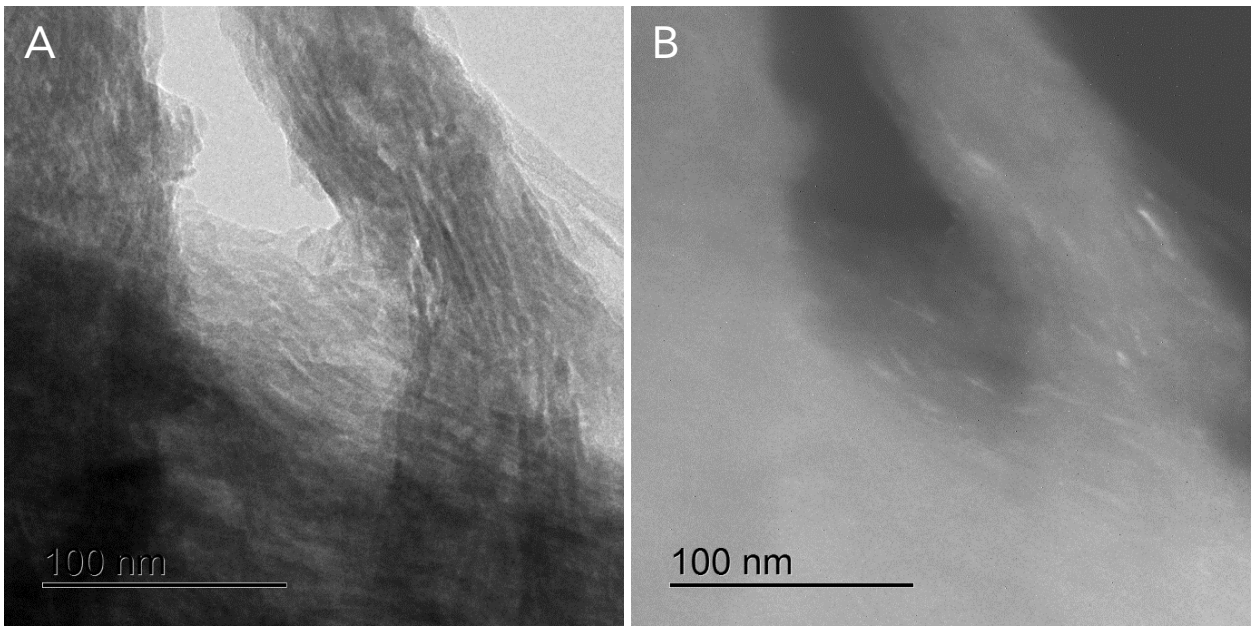

Figure 3.6 Comparative TEM to distinguish between location of inorganic and organic constituents (A) bright-field TEM showing arrangement of nanorods and (B) dark-field TEM highlighting individual nanorods which are composed of inorganic material (HAP) surrounded by an organic matrix.

The presence of carbon in several of the quantitative scans (Figure 3.6) indicates collagen. This is confirmed using Fourier-transform infrared spectroscopy (FTIR), which illustrates the intensity of functional groups detected by changes in dipole moment during molecular vibration. The functional groups that reveal the presence of collagen are the Amide I, II, and III bands which occur at 1632, 1536, and 1240 cm^{-1}, respectively (Figure 3.7 and Table 3.2)[163,164]. Additionally, FTIR validates the presence of HAP with intensity bands corresponding $v_4PO_4^{3-}$, $v_2CO_3^{2-}$, $v_3PO_4^{3-}$, $v_3CO_3^{2-}$ at 554 and 600, 870, 1024, 1410 cm^{-1}, respectively (Figure 3.7 and Table 3.2)[165].

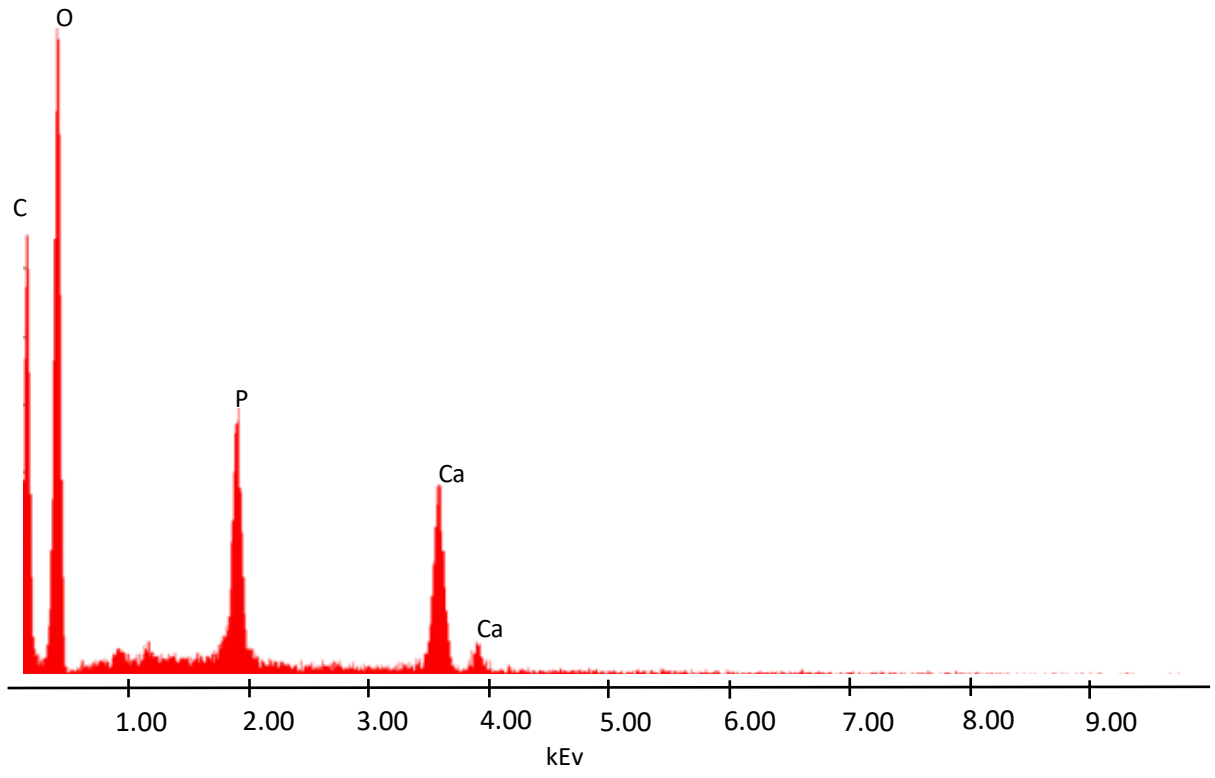

Figure 3.7 EDX composition scans of a single tooth**.** This shows presence of carbon, oxygen, phosphorous, and calcium which are all constituents of HAP and collagen.

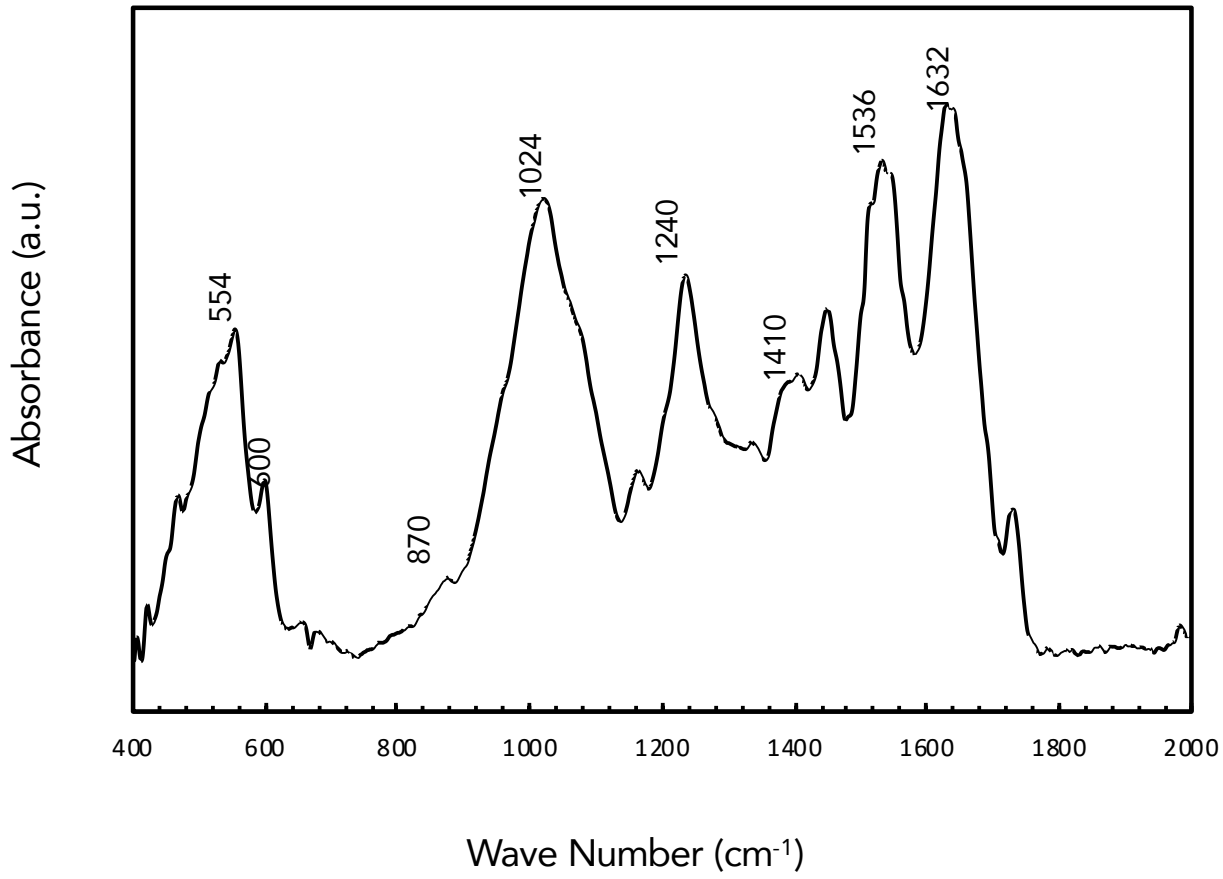

Figure 3.7 Fourier-transform infrared spectroscopy of a single tooth. Characteristic bands of hydroxyapatite and collagen. Amide I, II, and III bands characteristic of collagen, occur at 1632, 1536, and 1240 cm^{-1} respectively. Hydroxyapatite bands are: $v_4PO_4^{3-}$, $v_2CO_3^{2-}$, $v_3PO_4^{3-}$, $v_3CO_3^{2-}$ at 554 and 600, 870, 1024, 1410 cm^{-1}, respectively. See also Table S1.

Table 3.2 Fourier-transform infrared spectroscopy absorption bands for a tooth sample and their functional groups.

Wave number (cm^{-1})	Assignment	Reference
554, 600	$v_4PO_4^{3-}$	[165]
870	$v_2CO_3^{2-}$,	[165]
1024	$v_3PO_4^{3-}$,	[165]
1240	Amide III	[163]
1410	$v_3CO_3^{2-}$	[165]
1536	Amide II	[163]
1632	Amide I	[163,164]

3.5 Reduced Rayleigh Scattering

Rayleigh scattering is a well-known phenomenon with a characteristic particle-size dependence. Rayleigh scattering applies to particles that are much smaller than the interacting wavelength of light satisfying the condition $x \ll 1$ where $x = 2\pi r/\lambda$, r is the radius of the particle, and λ is the wavelength of light. Rayleigh scattering numerical solutions work best for idealized systems of homogenous spherical particles. This makes it difficult to apply to the system of the transparent teeth where the main constituent is randomly orientated nanorods. Scattering is highly dependent on particle size and orientation, therefore, spherical approximations are not sufficient for analyzing nanorods.[166]

For this reason, the Rayleigh-Gans-Debye approximation (RGD) is used for randomly orientated nanorods. Along with the conditions for Rayleigh scattering, RGD particles must be optically soft which is described by having a refractive index, when compared to the surrounding medium, that is close to unity, $|m-1| \ll 1$ where $m = n/n_0$. Additionally, $x|m-1| \ll 1$

where $x = 2\pi r/\lambda$ must be met. In accordance with RGD, the light scattering efficiency coefficient, Q_S^R, for randomly orientated nanorods has been derived by Shapovalov[167]. For a randomly orientated cylinder with a height *H* and a radius *a,* the light scattering efficiency coefficient is:

$$Q_S^R = \frac{k^4 a^3 H\left(n^2-1\right)^2}{32\pi^2} \cdot QC(H,a) \tag{3.1}$$

where,

$$QC(H,a) = \frac{4\pi^2}{3}\left\{8 - \frac{22}{45}(kH)^2 - \frac{38}{15}(ka)^2 + \frac{13}{105}(ka)^2(kH)^2\right\}, \tag{3.2}$$

and where $k = 2\pi/\lambda$. The light scattering efficiency coefficient is determined by dividing the light scattering cross section by the cross section area of projection of a particle on a plane and describes how efficiently light can be scattered.[167] In Figure 7, Q_S^R is plotted against radius for three different wavelengths (450, 550, and 650 nm), H= 20 nm, n=1.66 (the refractive index for HAP). This demonstrates how scattering efficiency decreases as the radius decreases. From TEM micrographs (Figure 4), we conclude that the radius of the nanorods ranges from 0.5 to 1.5 nm and that the height ranges from 5 to 25 nm, which is predicted to produce negligible scattering. Although the RGD is an approximation, it is sufficient to show the scattering dependence on particle size and provides insight to why the teeth are transparent.

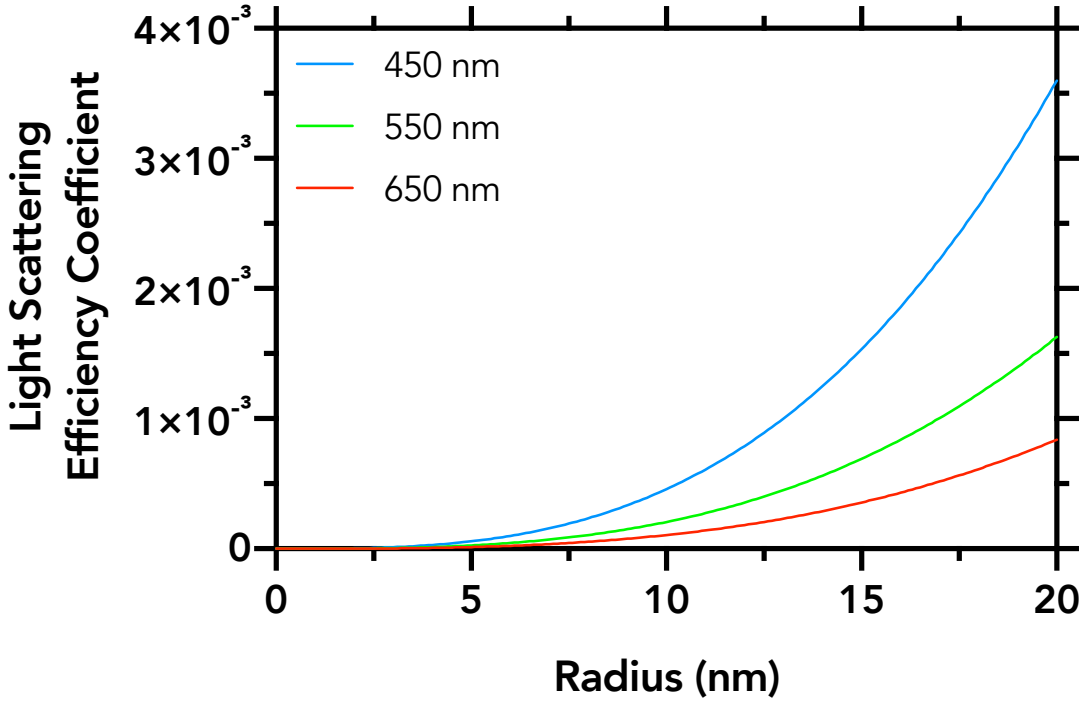

Figure 3.9 Light scattering efficiency coefficient for randomly orientated nanorods against radius. This is plotted for three different wavelengths of light (450, 550, and 650 nm). The height of the cylinder was kept constant at 20 nm as the radius varied from 1—20 nm and n=1.66.

3.6 Nanoindentation and Mechanical Properties

The hardness and reduced Young's modulus (mean ± SD) of the enamel-like and dentin layers were measured using a nanoindenter (Figure 3.9). The enamel-like layer is the hardest and stiffest with an average hardness of 4.2 ± 1.1 GPa and a reduced modulus of 43.3 ± 15.8 GPa. The hardness is comparable to the teeth of the great white shark and piranha which are reported as 4.1 ± 1.1 GPa and 4.1 ± 0.9 GPa, respectively[168]. Despite the significant differences in size, morphology, and habitat, the mechanical properties of the enamel-like layer of these predatory species are strikingly similar (Figure 3.10). The dentin has an average hardness of 2.1 ± 1.2 GPa and a reduced modulus of 16.4 ± 7.3 GPa. When compared to the dentin of the great white shark

and piranha, with reported hardnesses of 0.7 ± 0.2 GPa and 0.8 ± 0.3 GPa, respectively, the dragonfish dentin (2.1 ± 1.2 GPa) is much harder, suggesting that it has a higher degree of mineralization and nanoscale structural arrangement, both of which should contribute to transparency.

The teeth are found to have a gradient in mineralization (Figure 3.9A) which accounts for the variability in hardness with location of indentation. While we report the hardness and reduced modulus as an average value, it is important to note the range. The enamel-like layer was only indented at the tip of the tooth where the surface is large enough to reduce effects from the dentin-enamel junction (DEJ) and the surrounding epoxy. The enamel-like layer has a hardness that ranges from 2.6 GPa to 5.4 GPa while the reduced modulus ranges from 26.8 to 67.9 GPa (Figure 3.9). The dentin hardness ranges from 0.4 GPa to 3.9 GPa and the reduced modulus ranges from 3.5 GPa to 38.4 GPa (Figure 3.9).

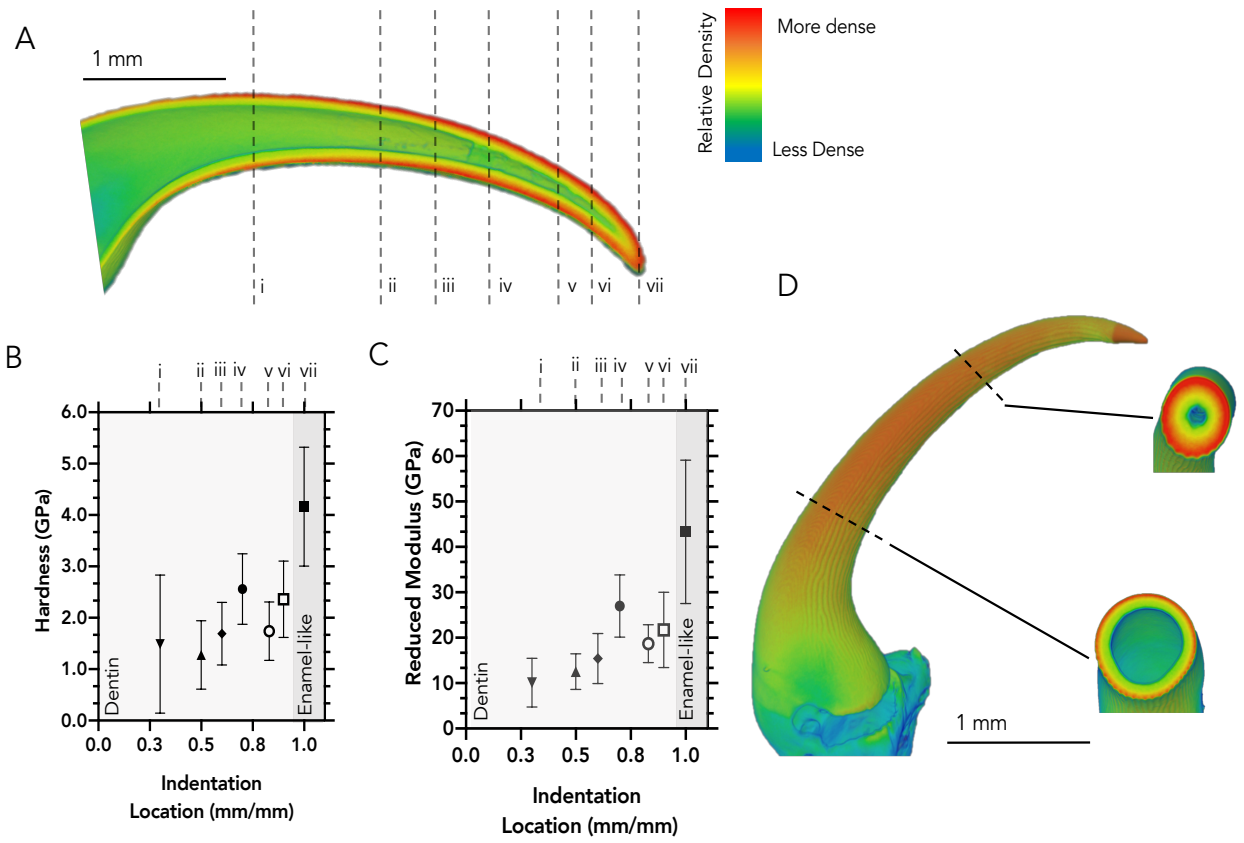

Figure 3.10 Influence of mineralization gradient on nanoindentation location. (A) μ-CT scan of the longitudinal cross-section of a representative tooth. The color mapping indicates relative density signifying degree of mineralization. Hotter colors (red) are more dense while cooler colors (blue) are less dense. There exists a gradient in mineralization that increases from the base towards the tip of the tooth. Roman numerals i—vii mark the relative cross-sections where nanoindentation was performed and align with the designated indentation locations in (B) and (C). (B) The hardness values (mean ± SD) from nanoindentation are dependent on location within the tooth due to the gradient in mineralization as indicated by the μ-CT scan. (C) The reduced modulus values (mean ± SD) from nanoindentation are affected by the degree of mineralization. (D) μ-CT scans of transverse cross-sections that indicate the surface in which nanoindentation was performed. The two representative slices demonstrate that the degree of mineralization increases towards the tip of the tooth and outwards radially. The same color mapping was used in parts (A) and (D).

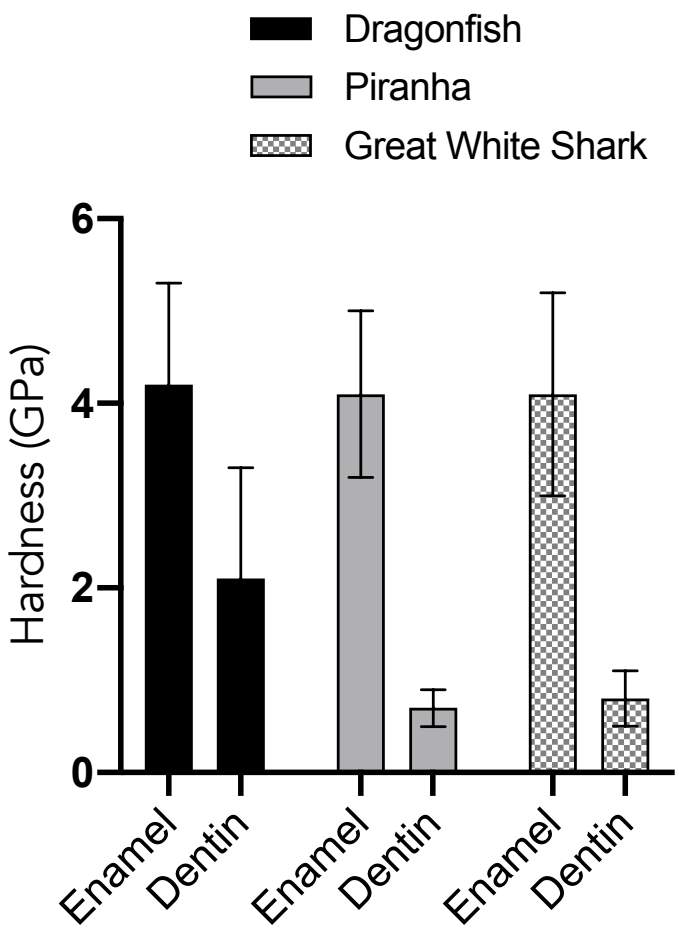

Figure 3.11 Comparison of hardness amongst the dragonfish, piranha[168], and great white shark[168], with respect to their enamel in dentin.

The degree of mineralization was quantified using thermogravimetric analysis. The resulting value of ~80% mineralization (Figure 3.11) is indeed greater than the average dentin reported for the teeth of humans ~75% mineralization, who have similar hardness as the teeth of piranha and great white shark.[169,170] The minimal amount of dispersed collagen fibrils likely reduces scattering. Additionally, the dragonfish teeth lack microscale features such as dentin tubules. Dentin tubules are known to provide energy absorption properties[96] and inherently reduce the stiffness. The absence of tubules not only accounts for the high stiffness of the dentin layer but also the transparency. The typical coloration of the dentin layer, as seen in human teeth, is associated with scattering that occurs due to the presence of tubules[171].

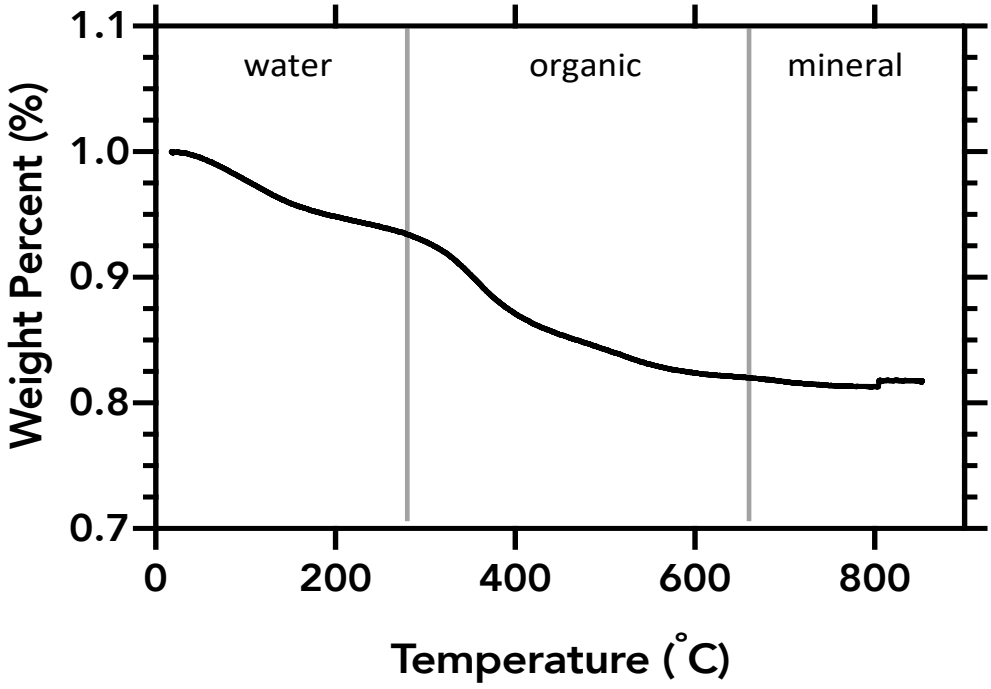

Figure 3.12 Thermogravimetric analysis of dentin. This shows the relative composition of dentin (water, organic, and mineral). The relative weight percent of water, organic, and mineral is roughly 7%, 12%, and 81% respectively.

3.7 Conclusions

We show that the teeth of dragonfish owe their transparency to a nanoscale structure of hydroxyapatite and collagen, which is devoid of microscale features such as dentin tubules; they are also sufficiently thin (~60 μm) to reduce Rayleigh scattering. The enamel-like layer is highly mineralized, consisting of amorphous/nanocrystalline hydroxyapatite (~ 20 nm grain size), while the dentin consists of an array of interpenetrating nanorods (~ 5 nm diameter) of hydroxyapatite embedded within a collagen matrix. This transparency is a unique property that is the result of the nanoscale structure of the teeth, in contrast with the teeth of other animals and humans. Thus, it is

an adaptation to thriving in the aphotic zone, where biological light (bioluminescence) drives the predator-prey interactions.

The mechanical properties of the enamel-like layer are similar to those of the piranha and the great white shark, despite vast differences in size, morphology, and habitat. However, the dentin, comparatively, is much harder and stiffer with a higher degree of mineralization and a lack of tubules that is a mechanical trade-off to ensure transparency by reducing scattering. The nanoscale structure also contributes to this higher hardness.

This report is the first to study one species of deep-sea fish *Aristostomias* scintillans and their transparent teeth. We demonstrated using a variety of characterization techniques that the teeth are extremely hard and sharp, being comparable to those from great white sharks or piranhas. This surprising finding correlates well with the fact that the dragonfish is an efficient predator where food is scarce. In the deep-sea, many organisms are able to produce light and use this to navigate around and spot/escape potential preys/predators. Within this context of biological light, the teeth of the dragonfish remain invisible, being built to show no contrast with the surrounding water. Thus, in combination with the blackness of its skin, the array of hard sharp teeth from the dragonfish represents a deadly invisible weapon for an efficient predator.

Our investigation highlights the importance of using the materials science approach to better understand specialized dentition in response to feeding habits which can be used to explore the ecology of deep-sea organisms and their unknown properties.

3.8 Experimental Methods

The specimens of *Aristostomias* scintillans were collected during the April 29, 2017 SIO research cruise on the ship R/V Robert Gordon Sproul, off San Diego in the San Diego Trough.

The trough is a deep canyon with an average depth of 1,000 m. Pelagic organisms were collected using mid-water trawling with a net, from a depth of ~500 meters. Upon retrieval on the boat deck, organisms were placed directly in cold seawater and sorted for use. Surprisingly, many fishes were still alive and able to survive in a tank for several hours. If (or when) showing no signs of life, the organisms were placed in a -20˚C freezer, or in liquid nitrogen (both available on the ship). Back in the laboratory, the samples were stored in -20˚C or -80˚C freezers until use.

Optical characterization

For optical observation, we defrosted the specimen at laboratory temperature, and photographed the fish and teeth under a Nikon SMZ 1500 stereoscope equipped with a QImaging Retiga 2000R color digital camera. The system also has an annular ring illumination system to provide omni-directional lighting, polarizers, and several fluorescence cubes to allow excitation at 355, 390, 470 nm using an EXFO X-Cite 120 W mercury lamp (long-pass filters were used to visualize the emission). Samples were imaged in air and filtered sea water.

After imaging under the stereoscope, the head was sectioned off the main body using a clean razor blade. The entire head was then either micro-dissected for “extracting” teeth with minimum flesh attached and analyzed for transparency or it was dehydrated using step-wise increments of increasing ethanol concentration from 40-100%. This step was necessary for observation by scanning electron microscopy. Additionally, critical point drying was used to remove excess water and specimens were coated with molybdenum. Fresh specimens were also studied and compared to those that were critically dried to discern between the artifacts from drying. There are no apparent differences between the teeth that were freshly examined and those that were critically dried.

To look at teeth transparency, we used a PARISS® hyperspectral imaging system (www.lightforminc.com), using teeth separated from the head (see below). The analyses were performed on a Nikon 80i microscope outfitted with a monochrome Retiga 2000DC, CCD camera (QImaging, BC, Canada). Wavelength calibration was performed with a MIDL Hg+/Ar+ emission lamp (LightForm, Inc, NC, USA) and accuracy was recorded and verified to be better than 2 nm. The tip, middle, and base of teeth were mapped for spatial distribution of spectra. The analyses were made in both air and filtered sea water. Air makes them turn less transparent because of changes of refractive index in the air medium (versus water [172]). However, this helped us visualize the spectral distribution in the teeth (translucent rather than transparent). In all cases, 100% of the pixels of the mapped areas showed different ratios of five representative spectra, called "reference spectra." Distribution of these reference spectra across the pixels of an image was used as a proxy of homogeneity in the sample with regards to letting certain wavelengths pass through the sample. Here, we adopted a Minimum Correlation Coefficient of 98.5% for the analyses, indicating that pixels (or areas of the image) showed the same reference spectrum when having more than 98.5% similarity with the specific reference spectrum. The transmittance and reflectance percentage were calculated by dividing the scan of the tooth by the background. Although five different teeth were analyzed, the data were similar across them and thus only a representative tooth is presented here for the hyperspectral analysis.

Microstructural characterization

Over 40 teeth from 10 different specimen were imaged using scanning electron microscopy and fresh samples were imaged using environmental scanning electron microscopy (ESEM) FEI Quanta 400 FEG in low vacuum mode (P = 100 Pa, accelerating voltage 10 kV)

equipped with an EDAX Genesis V6.04 X-ray spectrometer. Specimens for TEM (JEOL JEM-2100 LaB_6 operating at 200 kV accelerating voltage) were either extracted by a FEI Versa3D focused ion beam and post-thinned using a Fischione nanomill or prepared by scratching a single tooth on sand paper and investigating the enamel-like layer. A beam current of 30 pA/cm^2 and a voltage of 30 kV was used.

For x-ray microscopy, an individual tooth was imaged (Xradia 510 Versa, ZEISS, Jena, Germany) with a voxel size of 4.542 μm and an acceleration voltage of 40 kV, resulting in 996 projection images. The images were processed using Amira® software (FEI, Oregon, USA).

Compositional analysis

For FTIR, whole teeth were individually used to collect the spectra. The spectra were collected in the absorbance mode in air with ~25 N of force applied to the specimen measurement surface using an ATR Spectrum Two (PerkinElmer, Waltham, MA, USA). A background spectrum was first taken for background subtraction using Spectrum 10™ software (PerkinElmer, Waltham, MA, USA). The resultant collected wavelengths were from 400 cm^{-1} to 4000 cm^{-1} wherein the main mineral and collagen signals were captured. The baseline of each spectrum was corrected using Spectrum 10™ software (PerkinElmer, Waltham, MA, USA).

Thermogravimetric analysis (SDT Q600 Simultaneous TGA/DSC, TA instruments, New Castle, DE, USA) was used to determine the mineral composition of the dentin. The enamel layer was scraped away using polishing paper to isolate the dentin. On average fifteen teeth from more than eight different specimens were used per each sample to produce a significant mass (~ 2 mg) that could be detected by the TGA. Samples were then heated from room temperature to 800ºC at a rate of 10ºC/min under nitrogen. The temperature values to determine each phase composition

were used from Vargas-Becerril et al.[169] After 600ºC the water and organic phase is considered to be removed. The mass percentage was calculated by dividing the mass recorded by the initial mass.

Mechanical characterization

The hardness and reduced modulus of the enamel-like and dentin layers were measured using a nanoindentation testing machine (Nano Hardness Tester, Nanovea, Irvine, CA, USA) equipped with a Berkovich diamond indenter tip. Five dried teeth from four different specimens were embedded in epoxy and polished perpendicular to the tip to expose the transverse region. These samples were then mounted with super glue onto a steel block with the transverse region exposed. The maximum penetration depth of the indenter tip into the tooth was 2.67 μm. All indentations were performed by penetrating through each layer with a load of 15 mN, loading and unloading rates of 30 mN/min, and 20 seconds of hold time. A total of 5-10 indents were made on each layer and averaged.

3.9 Acknowledgements

Chapter 3, in full, is published in *Matter* authored by A. Velasco-Hogan, D. Deheyn, M. Koch, B. Nothdurft, E. Arzt, and M. A. Meyers. The dissertation author is the primary investigator and author on this publication.

This work was performed in part at the San Diego Nanotechnology Infrastructure (SDNI) of UCSD, a member of the National Nanotechnology Coordinated Infrastructure (NNCI), which is supported by the National Science Foundation (Grant ECCS-1542148). We graciously thank the Humboldt Foundation for granting a research award and the Air Force Office of Research for

support under the MURI Program (AFOSR grant no. FA9550-15-0009). Funding from ‘‘The Biomimicry for Emerging Science and Technology Initiative’’ (The BEST Initiative; to D.D.D.) and from the Air Force Office of Scientific Research (AFOSR) grant #FA9550-10-1-0555 (MURI BIOPAINTS) for the hyperspectral imager is acknowledged by D.D.D. INM support and hospitality to M.A.M. are gratefully acknowledged. We also thank Prof. Jennifer Taylor, SIO/UCSD, for organizing the specimen collection cruise for the SIO125 class (funding provided by UC Ship Funds). Eric Bushong was extremely helpful with X-ray microscopy. Michael Allen is acknowledged for his tremendous help with performing hyperspectral imaging.

Chapter 4: Bite Force Mechanics and Allometry of Piranha (Serrasalmidae)

4.1 Introduction and Significance

The bite force of the piranha (Serrasalmidae) has drawn considerable attention due to its ability to effectively capture and masticate prey. Herein, we analyze theoretical anterior bite forces using a lever approach and compare them to *in-vivo* maximum bite forces. We provide a mechanics analysis that explains the scaling allometry of the bite force (F_{output}) with the length of the fish (l), $F_{output} \, \alpha \, l^2$.

The Serrasalmidae are a family of specialized biters known to be composed of three major subclades: (1) the piranha-clade (carnivorous), (2) the pacu-clade (herbivorous), and (3) the *Myleus*-clade (omnivorous).[173] This family has been traditionally distinguished by their distinct feeding habits and notable dentition [174]. Piranha usually have triangular-shaped, tricuspid, and serrated teeth found within a single row. The teeth interlock with their adjacent neighbors' lateral cusps creating a unified unit that regenerates as a row simultaneously [175]. Piranha teeth are also heterodont, meaning tooth morphology is dependent on location within the jaw. *Serrasalmus rhombeus*, commonly known as the Black piranha, have been shown to have the most powerful bite force relative to its size with a maximum recorded bite of 320 N for a 1.1 kg specimen [176]. This is primarily attributed to its large adductor mandibulae complex which makes up over 2% of its total body mass [176]. While there are studies that successfully compare theoretical bite forces to *in-vivo* anterior bite forces, there has yet to be a mechanics-based analysis which explains the scaling allometry [176,177].

4.2 Allometric Scaling

Allometry is the study of biological scaling and the relationship of co-varying biological measurements such as anatomical lengths (arm, beak etc.), mass, volume, and surface area. The term allometry was first coined in 1936 by Huxley and Tessier when studying the growth of the fiddler crab's extraordinarily large claw. The crab was measured at various stages of growth and it was found that the large claw was dissimilar to the growth of its body i.e. the claw was growing faster than the length of its carapace [178]. Figure 4.1 shows the work by Huxley and Tessier where the relationship of the body of the crab is plotted against the size of the claw. This is a length to length comparison of a single species, but there has been an increasing development in exploring allometric relationships across diverse species and of more complicated biological measurements such as body size and metabolism [179], skin thickness and elasticity and viscoelasticity[180], and as we show here fish length and bite force of the piranha.

When the work of Huxley and Tessier is transformed to a log-log scale the data follows a linear relationship (Figure 4.1). This linear regression when transformed to a log-log scale is a key indicator of allometry. When transformed to a log-log scale, the slope of the plot represents the allometric scaling constant. A scaling constant of one is referred to as isometric scaling, where the length of the body part grows similarly to the rest of the body as a whole. The mathematical expression of allometric scaling is further described below.

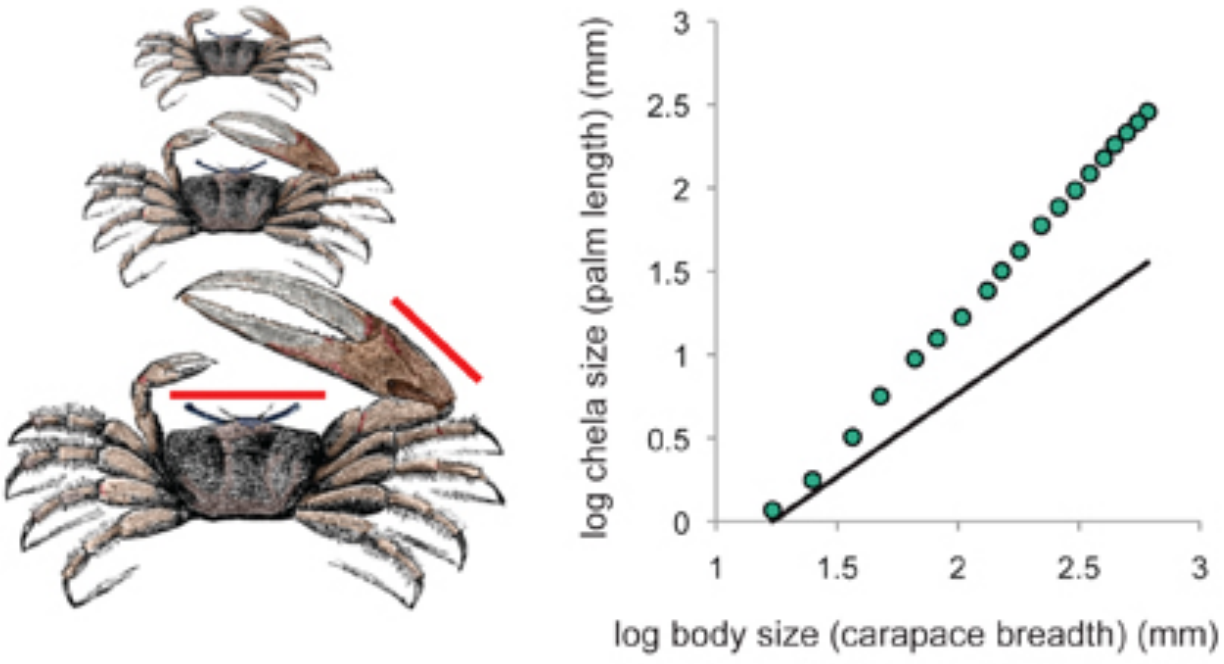

Figure 4.1. Huxley and Tessier's work on the allometric scaling of the claw of the fiddler crab. The body size and length are transformed to $\log_{10}$ and represented by the blue dots. The solid line represents a slope equal to one which indicative of isometric scaling. The deviation of the experimental points from the slope of one indicates non-isometric scaling or allometry. Since the experimental points show a slope greater than one, this is referred to as positive allometry.

Allometry is used to refer to the deviation from self-similar scaling and can be described mathematically as follows:

$$y = bx^{\alpha} \tag{4.1}$$

Where, α is referred to as the scaling constant when x and y are the respective anatomical parts that are being related. When (4.1) is transformed to $\log_{10}$ we can rearrange as follows:

$$\log y = \alpha \log x + \log b \tag{4.2}$$

And when plotted, (4.2) can be related to the linear equation $y = mx + b$ where the slope of the line is equal to the allometric scaling constant α. Thus, the log transformation of the two anatomical parts that are being related can be plotted with a linear regression to obtain the allometric scaling if such allometric relationship exists. When $\alpha > 1$, the allometric scaling is defined as positive and when $\alpha < 1$ the scaling is defined as negative. Isometric scaling is defined when $\alpha = 1$. Isometric scaling is the direct, self-similar scaling of an anatomical part (e.g. claw) with another anatomical part, typically a whole body feature (e.g. mass, surface area, volume).

4.3 Derivation of Allometric Scaling

The theoretical bite force of the piranha can be estimated from the geometry of the maxilla and the size of the adductor mandibulae muscles using an approach developed by Westneat[181] and adapted by Meyers et al.[182] In this adaptation, the closing of the lower jaw can be modeled as a third-order lever (Figure 4.1A). Three major subdivisions of the adductor mandibular muscle are responsible for closing, referred to as A1, A2, and A3 (Figure 4.1 B and C). The major force generators in the jaw are the A2 and A3 subdivisions. Measured values of the angles ($\alpha_1, \alpha_2,$ and α_3) with respect to the vertical direction, segment lengths (d_1, d_2, d_3, and d_o), and maximum cross sections of the three-muscle groups are measured from piranha specimens.

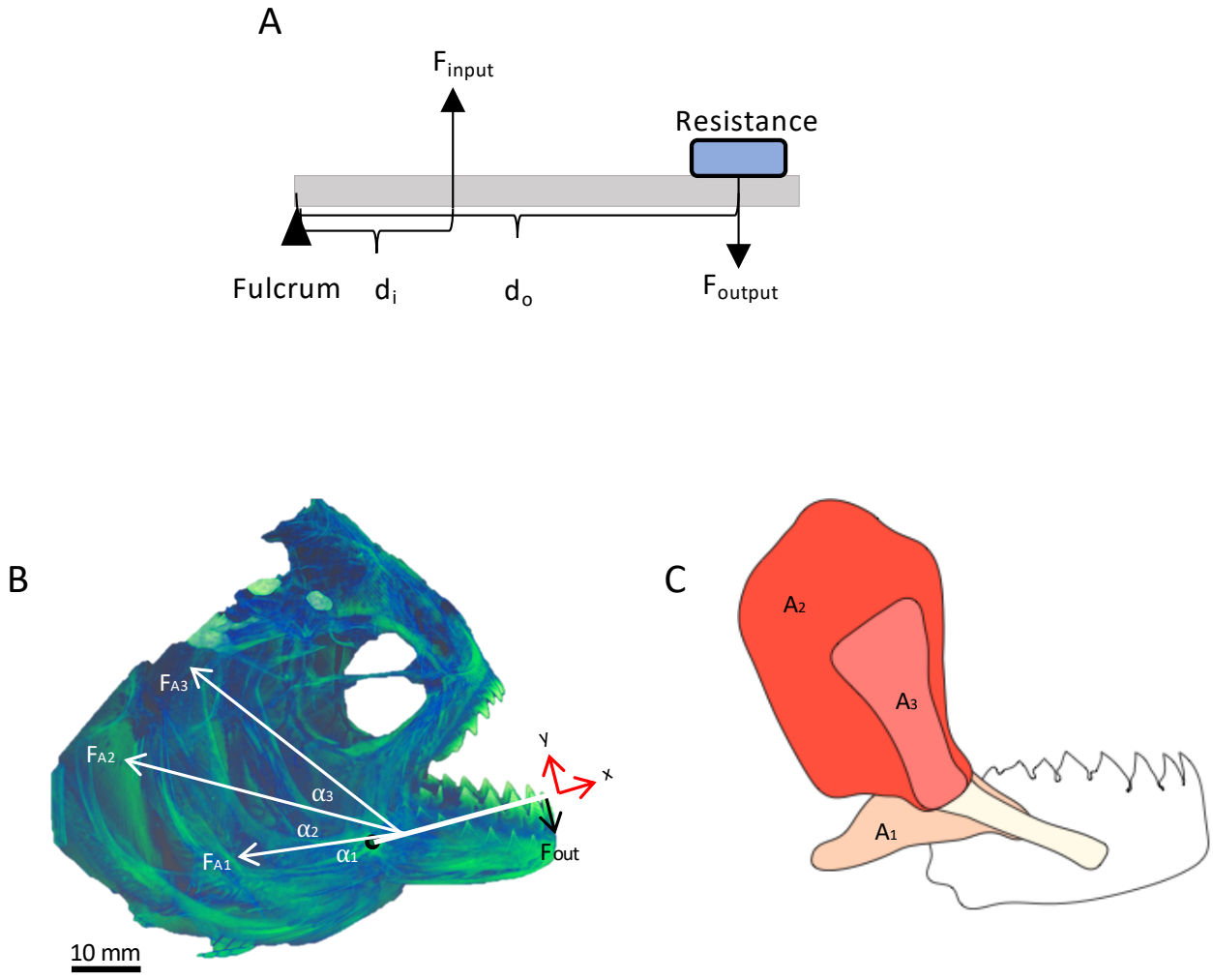

Figure 4.1 Third-order lever applied to piranha jaw muscle system. A) Simplified third-order lever. B) Relative muscle positions with the skull of a piranha. C) Schematic of the subunits of the mandibular muscle (A_1, A_2, and A_3) with respective size and orientation.

The equation of equilibrium for the moments is:

$$\sum ME = F_{A1}\sin(\alpha_1)d_1 + F_{A2}\sin(\alpha_2)d_2 + F_{A3}\sin(\alpha_3)d_3 - F_{output}d_o = 0 \quad (4.3)$$

The force of the muscles (F_{A1}, F_{A2}, and F_{A3}) can be approximated knowing the cross-sectional area of the muscle group and the maximum stress produced by muscle (σ_{max}); a value of 0.2 MPa is

used, which is the highest range for red muscles as indicated by Westneat[181]. The maximum isometric stress in muscle has been shown to vary from 0.1 to 0.2 MPa depending on muscle location and fiber type.[183,184] The segments (d_1, d_2, d_3) are the lengths between the fulcrum and the attachment point for each muscle and d_o is the length from the fulcrum to the most anterior tooth tip. Assuming that the jaw length and mandibular muscles scale isometrically with the size of the fish (which has been supported by Richard and Wainright[185]) a direct self-similar scaling constant (k) can be found when Equation (1) is divided by d_o:

$$F_{output} = \frac{d_1}{d_o} F_{A1} \sin(\alpha_1) + \frac{d_2}{d_o} F_{A2} \sin(\alpha_2) + \frac{d_3}{d_o} F_{A3} \sin(\alpha_3) \tag{4.4}$$

Therefore d_1/d_o, d_2/d_o, and d_3/d_o are fixed and independent of the size. Thus,

$$k_1 = d_1/d_o, \quad k_2 = d_2/d_o, \text{ and } k_3 = d_3/d_o \tag{4.5}$$

The geometric and angular parameters are assumed, to a first approximation, to be constant. The maximum force that the muscles can impart is proportional to the cross-sectional area (A) of the muscle. Assuming a constant maximum muscle stress of σ_{max},

$$F_{A1} = \sigma_{max} A_1 \, , F_{A2} = \sigma_{max} A_2, \text{ and } F_{A3} = \sigma_{max} A_3 \tag{4.6}$$

Additionally, assuming that the area of the muscle can be represented as proportionality constant (k') multiplied by the length of the fish squared (l^2),

$$A = k' l^2 \tag{4.7}$$

When substituting Equation (4.5), (4.6), and (4.7) into (4.4) we obtain,

$$F_{output} = l^2 * [k_1 k_1' \sin(\alpha_1) + k_2 k_2' \sin(\alpha_2) + k_3 k_3' \sin(\alpha_3)] * \sigma_{max} \quad (4.8)$$

This provides a direct proportionality between F_{output} and l^2. This allometry is indeed closely obtained from the measurements, shown in Figure 1C. This is a classical expression of non-isometric allometry: the bite force scales as the square of the standard length (SL), where the standard length of the fish is measured from the tip of the nose to its last vertebrae. The maximum stress that the teeth can impart can be assumed to be limited by the compressive strength of the dentine-enameloid complex. The mechanical properties of enamel and dentine are a function of structure and composition and are, to a first approximation, independent of size. Therefore the maximum stress that the teeth can undergo is dependent on the strength of the enamel-dentine composite. This is equal to, to a first approximation, to F_{output}/t^2, where t is a characteristic tooth dimension, which scales isometrically with l. This is the same allometry.

4.4 Allometric Scaling of *In-vivo* and Calculated Bite Forces

Here, we record a scaling constant of 1.842 for the calculated bite force which includes the average data from Huby et al.[177] on their calculated bite forces for *Pygocentrus nattereri* (Figure 4.2). This scaling constant is equivalent to the allometry parameter. We also conducted *in-vivo* measurements on three piranha whose values, along with the average of Huby et al.[177] for *in-vivo Pygocentrus nattereri,* are presented in Figure 4.2. The scaling constant for the *in-vivo* bite force is 1.985 which is very close to the expected allometry from Equation 6.

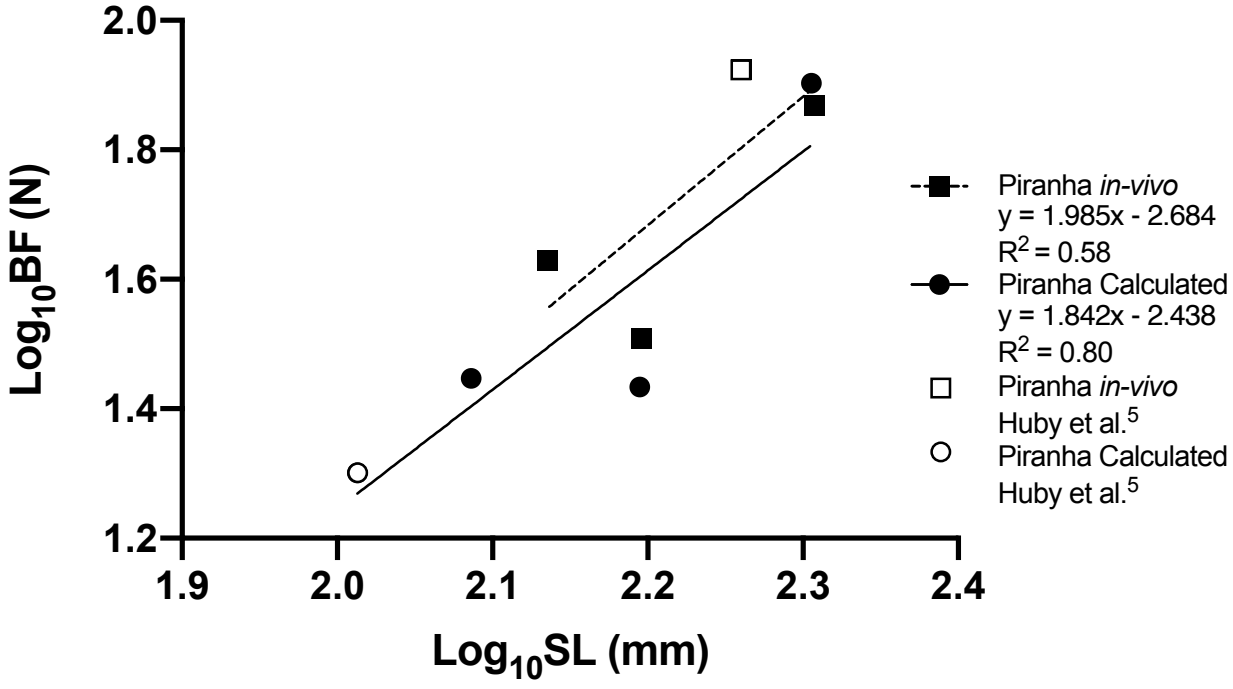

Figure 4.2 Calculated and *in-vivo* piranha bite forces including findings from Huby et al.[177] transformed to $\log_{10}$ and fitted to a simple linear regression against standard length of the fish (SL).

Additionally, we transformed the average *in-vivo* bite forces with respect to standard length obtained by Huby et al.[177] for nine different piranha species to $\log_{10}$ and when fit to a linear regression we produce an allometric scaling constant of 2.014 (Figure 4.3). While our reported values, along with Huby et al.[177], are in agreement with the proposed allometric scaling, they are slightly lower than Grubich et al.[176] who record a scaling constant of 2.30 for *in-vivo* bite forces of *Serrasalmus rhombeus*.

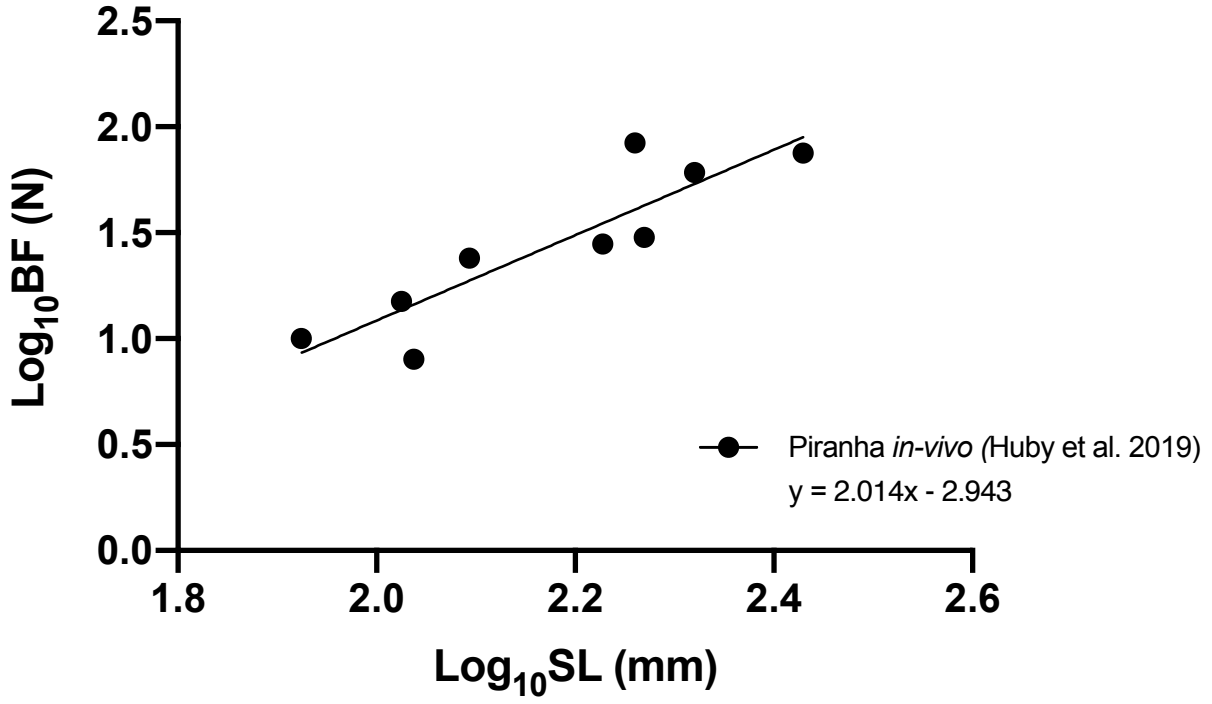

Figure 4.3. Positive allometry of piranha bite forces from nine different species. Average *In-vivo* bite force measurements from Huby et al.[177] and their respective standard lengths are $\log_{10}$ transformed and plotted with a linear regression. This plot shows an allometric scaling constant of 2.014 which is in agreement with our recorded and calculated values for a single species (*Pygocentrus nattereri*).

Possible sources of error can be attributed to the dissimilarity in bite force performance of the piranha under natural conditions and the use of the bite force tester. Additionally, the most anterior tip of the tooth is used to calculate bite force which can be difficult to place in reality i.e. our calculated values may not agree with *in-vivo* as the placement of the bite force tester can provide a reading from several teeth. Additionally, the tip of the tooth may not necessarily provide the largest output force. The piranhas may underperform when tested with the apparatus. During bite-force testing the piranha exhibits multiple rapid bites at various force levels (Table 4.1).

Table 4.1. *In-vivo* piranha bite force (BF) measurements taken along the Paraguay river. Standard length (SL).

Specimen	Mass (kg)	SL (mm)	Maximum BF (N)	Average BF (N)	Standard Deviation BF
1	0.75	203	73.85	33.40	20.7
2	0.64	157	32.31	26.31	5.7
3	0.50	136	42.37	25.12	12.8

4.5 Conclusions

The impressive biting capabilities of the piranha have sparked considerable investigation into *in-vivo* and calculated anterior bite forces which have extensively shown a positive allometric relationship. Here, we contribute to the growing literature by providing a mechanics based understanding of this allometric relationship. We propose that $F_{output}\ \alpha\ l^2$ which is in agreement with our *in-vivo* and calculated lever approach which includes data from Huby et al.[177] on *Pygocentrus nattereri.* This has considerable

4.6 Experimental methods

Specimens

Three adult piranha (*Pygocentrus nattereri*) specimens were purchased from local fish markets in Brazil already deceased. Specimens were transported overnight packed in ice. Upon retrieval specimens standard lengths were recorded and their in-tact skulls preserved and placed in a -20˚C freezer until use. Specimens were hydrated in Hank's balanced salt solution (Thermo Fisher Scientific) before jaw muscle dissection. Muscle area, jaw length, lever length of muscle attachment, and angle of attachment were recorded for bite force calculations.

Bite force analysis

The measurement on live piranhas was made on specimens caught along the Paraguay river and their bite forces were measured using a force gauge assembled with a Flexiforce™ A401 sensor (Tekscan) as shown in Figure 4.4. Two force gauges were constructed (Gauge 1 and Gauge 2). The sensor was placed between two wood strips and the assembly was inserted into the piranha's mouth as indicated in Figure S2. The change in resistance was recorded and converted into a force through the following equations dependent on which gauge was used. Each piranha recorded 5-10 bites (Table S1). These values are consistent with the measurements from Huby et al.[177] The maximum bite force for each fish was plotted in Figure 1C. Their mass and length were recorded and they were released back into the river. The measurements on piranha were accomplished during the Roosevelt-Rondon Centennial Expedition, from 2014 to 2016.

Gauge 1: $y = 16.158x^{-0.66}$

Gauge 2: $y = 12.41x^{-0.69}$

Figure 4.4 Demonstration of how the bite force of the piranha was recorded using the force gauge described in the experimental methods. The piranha shown here is a black piranha and its corresponding bite forces were not used in this study on the red-bellied piranha. This image is simply for demonstration of principles in recording bite forces.

4.7 Acknowledgements

Chapter 4, in part, is published in the *Journal of the Mechanical Behavior of Biomedical Materials,* authored by A. Velasco-Hogan and M. A. Meyers. The dissertation author is the primary investigator and author on this publication. The measurements on piranha were accomplished during the Roosevelt-Rondon Centennial Expedition, from 2014 to 2016. The participation of the New York Explorers Club, by giving it an official Flag Expedition status, is warmly appreciated, as are the efforts of Colonels Hiram Reis de Silva and Ivan Carlos Angonese of the Brazilian Army. Drs. Julie and Tim Radke of the San Diego Explorers Club participated in

the Paraguay River journey and their contribution was essential. The Brazilian Army provided logistic support which enabled the expedition. This work was performed in part at the San Diego Nanotechnology Infrastructure (SDNI) of UCSD, a member of the National Nanotechnology Coordinated Infrastructure (NNCI), which is supported by the National Science Foundation (Grant ECCS-1542148). We thank Prof. Joanna McKittrick for all of her contributions and inspiration to the field of structural biological materials.

Chapter 5: A Comparative Study on Tooth Structure, Mechanical Properties, and Diet Specialization of Piranha and Pacu (Serrasalmidae)

5.1 Introduction and Significance

The relationship between diet, bite performance, and tooth structure is a topic of great interest unifying ecologists, biologists, materials scientists, and engineers. The highly specialized group of biters found in the Serrasalmidae family offers a unique opportunity to explore their functional diversity. Surprisingly, the piranha, whose teeth have a primarily cutting function and whose main diet is soft flesh, is capable of exerting a larger bite force than the pacu, who feeds on a hard durophagous diet. Herein, we expand our understanding of diet specialization in the Serrasalmidae family by investigating the influence of elemental composition and hierarchical structure on the local mechanical properties, stress distribution, and deformation mechanics of teeth from piranha (*Pygocentrus nattereri*) and pacu (*Colossoma macropomum*). Microscopic and spectroscopic analyses combined with nanoindentation and finite element simulations are used to probe the hierarchical features to uncover the structure-property relationships in piranha and pacu teeth. We show that the pacu teeth support a durophagous diet through its broad cusped-shaped teeth, thicker-irregular enamel, interlocking interface of the dentin-enamel junction, and increased hardness of the cuticle layer due to the large concentrations of iron present. Comparatively, the piranha teeth are well suited for piercing due to its conical-shaped tooth which we report as having the greatest stiffness at the tip and evenly distributed enamel.

The dynamics of prey consumption and processing are strongly linked with tooth morphology and function. Teeth have long played a key role in assessing dietary adaptation in

mammals as highlighted by 18th century naturalist Georges Cuvier: “show me your teeth and I will tell you who you are” [186–189]. However, there remains little investigation into the hierarchical structure, property, and function relationships of teleost fishes especially of those belonging to families of highly specialized biters. Teeth, being composites of hydroxyapatite and collagen, form complex structures at various orders of hierarchy ranging from the nano- to macro-scale as a result of their bottom-up growth and self-assembly from the molecular level. This hierarchical organization and the respective local material properties ultimately determines the overall mechanical properties and performance of the tooth. This information is important in establishing relationships between structural variation, mechanical performance, and diet specialization among understudied teeth such as those of teleost fishes.

Teeth are a crucial evolutionary adaptation to vertebrates allowing for diet specialization [190–194]. Despite the vast range of morphological differences at the macro-scale including size, shape (conical, pointed, flat, cusps, etc.) and numbering, teeth have a highly-conserved structure at the meso-scale which consists of three layers: (1) enamel/enameloid, (2) dentin, and (3) pulp in order from outer-to-inner respectively [195,196]. The enamel and enameloid are highly mineralized tissues which covers the functional surface of the tooth providing wear-resistance and hardness [197]. Enamel is typically found in mammalian-vertebrates and enameloid in non-mammalian vertebrates. They are primarily distinguished by their development. Enamel is secreted by the inner-dental epithelium cells (ameloblasts) which first produce an organic matrix of collagen, proteins, proteoglycans, and lipids from where the hydroxyapatite nucleates and grows [197,198]. Enamel initiates mineralization at the dentin-enamel junction, after development of dentin, and then grows outwards towards the surface [197]. In contrast, enameloid is secreted between the inner-dental epithelium and the ectomesenchymal cells of the dentin papilla which

differentiate into odontoblasts and grows in conjunction with the dentin layer [197–200]. Enamel and enameloid have similar composition, having a high mineral content (~95 vol% of hydroxyapatite ($Ca_5(PO_4)_3OH$)) which forms highly crystalline hexagonal rods. In both enamel and enameloid, hydroxyapatite is known to contain impurities including carbonate, magnesium, and sodium. The enameloid of actinopterygians (bony fishes) occurs in two regions: (1) cap enameloid at the tip of the tooth, and (2) collar enameloid on the shaft of the tooth [197,201]. The dentin layer is much less mineralized (~45 vol%) than the enamel/enameloid and is formed by odontoblasts [201,202]. The dentin layer is characterized by a tubule structure which results from the formative tracks of odontoblastic cells. Finally, the pulp is the central part of the tooth which is non-mineralized and contains blood vessels, connective tissue, and nerves [202].

The teleost class is known to employ three primary feeding modes involved in prey-resource capture: (1) ram-feeding, where the fish propels its body and engulfs its prey with its large agape mouth [203,204], (2) suction-feeding, where prey is drawn into the mouth driven by a negative pressure in the buccal cavity [205,206], and (3) manipulation-feeding or biters which crush or tear prey with a robust oral jaw system [207,208]. Of the three feeding modes, manipulation-feeding or biters require high mechanical advantage for jaw-closing, a large adductor mandibulae for powerful force-generating capacity, and functional teeth which act as cutting/crushing tools [208]. Unlike many families in the teleost class, Serrasalmidae, a monophyletic family of South American freshwater fishes, are exclusively manipulative feeders, also referred to as biters, and thus represent a unique opportunity in which to investigate the relationships between diet, tooth hierarchical structure, composition, and mechanical properties.

The Serrasalmidae family contains highly specialized biting fishes categorized by three subclades: piranha-clade, pacu-clade, and *Myleus*-clade. These subclades are distinguished by their

distinct feeding habits and remarkable dentition (Figure 5.1)[209]. The work here will focus on the piranha- and pacu-clade. Piranha typically have triangular-shaped, tricuspid, and serrated teeth found within a single row. The teeth interlock with their adjacent neighbors' lateral cusps creating a unified unit that regenerates as a row simultaneously [175]. This interlocking mechanism is described as a "peg and socket" where the adjacent lateral cusp inserts within its neighbors' cusp acting as a cap. It is hypothesized that the interdigitation helps to distribute the stress that acts on a few teeth across the entire row during mastication [175]. Piranha also possess heterodont dentition where their tooth morphology is distinct depending on location within the jaw [175]. *Serrasalmus rhombeus*, commonly known as the Black piranha, has been shown to have the most powerful bite force relative to its size with a maximum recorded bite of 320 N for a 1.1 kg specimen [176]. This is primarily attributed to its large adductor mandibulae complex which makes up over 2% of its total body mass [176]. The piranha is famously known for being piscavory and carnivorous [210,211] as it relies on its sharp pointed teeth to slice and tear through fleshy meat [212,213]. In contrast, the pacu is herbivorous feeding on hard-shelled fruits, seeds, and leaves [214,215]. The pacu are known to have one and/or two rows of broad incisiform-to-molariform teeth depending on location within the jaw [174,213,216]. Thus, pacu teeth are highly heterodont. Their teeth have large occlusal surface areas with conical projections. Similar to piranhas, the teeth of the pacu support their adjacent neighbors and regenerate as a row simultaneously [175]. However, the interlocking mechanism in the pacu teeth is much more subtle and does not fully interdigitate and can be described as a "buttress" where the adjacent lateral sides slightly overlap providing support [175]. The pacu uses its incisiform and molariform teeth for masticating hard substances [215].

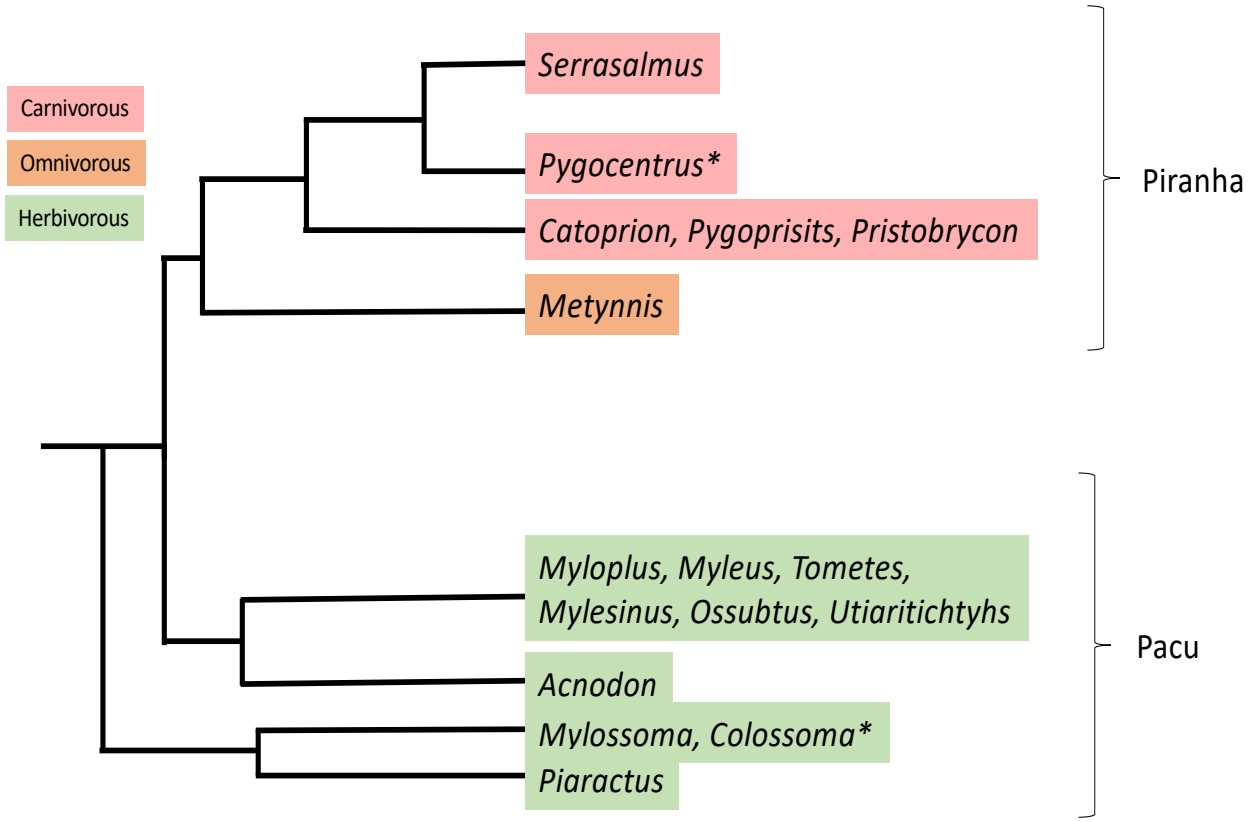

Figure 5.1 Phylogenetic tree of the Serrasalmidae family. This shows the distribution of their distinct feeding habits: carnivorous, omnivorous, and herbivorous. All pacus are herbivorous while piranhas are mostly carnivorous with the exception of *Metynnis* which is an omnivore. Astricts on *Pygocentrus* and *Colossoma* denote species that are the focus of this study.

These known differences in diet between the piranha and pacu have led to the proposal that pacus have larger jaw muscles and bite forces needed for crushing hard substances when compared to their carnivorous counterparts. This prediction has been demonstrated by studies in which species with a more durophagous diet typically are capable of exerting larger bite forces [217–222]. Recently, this hypothesis in relation to the bite force capacities between piranhas and pacus has been disproven by Huby et al.[177] in a comprehensive study dedicated to characterizing the oral jaw system in Serrasalmidae fishes. The resulting study showed that *in vivo* and theoretical bite forces are significantly greater in piranhas which is due to their proportionally larger adductor

mandibulae muscle [177]. It was found that the mass of the adductor mandibulae muscle is four times greater in the piranha-clade than the pacu-clade [177]. However, this proportionality is not distributed equally among the three main muscle subdivision. The pars rictalis is four times larger in the pacu-clade, the pars malaris is twice as large in the piranha-clade, while the pars stegalis is equivalent in both [177]. These differences in the subdivision of the adductor mandibulae have important implications in the mechanical advantage of their respective jaw systems. This suggests that the pacu-clade transmits relatively more force to the most anterior teeth in the lower jaw, while the piranha-clade transmits relatively more force to the most posterior teeth in the lower jaw [177]. While general trends point towards a relationship between durophagy and greater bite forces, this study is not the only one to suggest that durophagy can be achieved despite a respectively low bite force[223]. We suggest that the mechanical properties of the molariform teeth of the pacu, as dictated by their hierarchical structuring, allow for the pacu to effectively facilitate consumption of a specialized durophagous diet.

A recent study by Delaunois et al.[224] describes the microstructure and composition of the enameloid in piranha, *Pygocentrus nattereri*, and pacu, *Piaractus brachypomus*. It was found that the enameloid, in both species, has three distinctive regions: (1) cuticle, the outermost layer, (2) outer enameloid described by a parallel-structured layer, and (3) inner enameloid, described by a woven layer, which highlights the preservation of histological traits in the tooth structure of Serrasalmidae. However, there were differences in cuticle thickness between the two species which can be related to their distinct diets, herbivorous versus carnivorous. It was found that the pacu has a thicker cuticle (1.90 μm) compared to the piranha cuticle (0.79 μm) [224]. Additionally, the pacu cuticle has a higher concentration of iron which is known to increase hardness and stiffness [224,225]. Therefore, it is suggested that the thicker pacu cuticle can help reduce

detrimental wear resistance as an adaption to its durophagous diet. Despite the greater presence of iron in the pacu teeth, the piranha teeth were shown to be more mineralized [224].

This study highlights the important microstructural and compositional variations between two closely related species with distinct feeding habits and serves great inspiration into their local mechanical properties via nanoindentation. While nanoindentation has been performed on piranha teeth by Chen et al.[168] this study only examined the transverse cross section, despite the fact that teeth have consistently shown to have highly anisotropic properties and nanoindentation of pacu teeth is absent in the literature [51,226–228]. Our work on characterization of the mechanical properties of the piranha and pacu teeth will fill this void.

Through a materials science and engineering approach, we investigate the relationship between composition, meso- and micro-structural differences, and the local mechanical properties and stress distribution within the anterior teeth of the piranha and pacu to better understand the implications of diet specialization. This hierarchical approach focuses on structural characterization from the macro-scale which capture the morphology of the teeth, the meso-scale which focuses on enamel thickness and degree of irregularity, the microstructure of the enameloid, and dentin layers and the dentin-enamel junction, and the nanostructure of the rod-like architectures. Additionally, local mechanical properties are probed using nanoindentation and the stress distribution within the whole tooth is analyzed using finite element analysis.

5.2 Theoretical Anterior Bite Force and Allometry

In order to better understand how the piranha and pacu teeth distribute stress during biting, the anterior bite forces are calculated. The theoretical bite force of both the piranha and pacu can be estimated from the geometry of the maxilla and the size of the adductor mandibulae muscles using an approach developed by Westneat[181] and adapted by Meyers et al.[182] In this

adaptation, the closing of the lower jaw can be modeled as a third-order lever. There are three major subdivisions of the adductor mandibulae muscle that are responsible for closing, referred to as A1, A2, and A3. The major force generators in the jaw are the A2 and A3 subdivisions. Measured values of the angles ($\alpha_1, \alpha_2,$ and α_3), segments (d_1, d_2, d_3, and d_o), and maximum cross sections of the three-muscle groups are used to calculate the forces. The equations of equilibrium are:

$$\sum ME = F_{A1}\sin(\alpha_1)d_1 + F_{A2}\sin(\alpha_2)d_2 + F_{A3}\sin(\alpha_3)d_3 - F_{output}d_o = 0 \quad (1)$$

The force of the muscles (F_{A1}, F_{A2}, and F_{A3}) can be approximated knowing the cross-sectional area and the muscle stress of 200 kN•m^{-2} which is the highest range for red muscles as indicated by Westneat.[181] The segments (d_1, d_2, d_3) are the lengths between the fulcrum and the attachment point for each muscle and d_o is the length from the fulcrum to the most anterior tooth tip.

The theoretical maximum anterior bite force for the piranha is larger than the pacu with respect to standard length (Figure 5.2A). This agrees with prior studies who measured *in vivo* and theoretical bite forces.[177] Our bite forces for the piranha ranged from ~20 to 80 N and for the pacu ~6 to 72 N with dependence on specimen standard length. This is consistent with Huby et al.[177] who calculated values of ~1 to 42 N for the piranha and ~1 to 17 N for the pacu [177]. Additionally, we report both theoretical bite forces scale allometrically with the standard length of the fish with allometric constants of 1.842 and 1.77 for the piranha and pacu respectively (Figure 5.2B). Indeed, these allometric constants are close to the expected value of 2.0. Even for similarly sized fish the piranha significantly outperforms the pacu (Figure 5.2). This difference is attributed to the piranha's larger adductor muscle. The piranha's adductor mandibulae is proportionally larger than the pacu's which accounts for the greater anterior bite force.

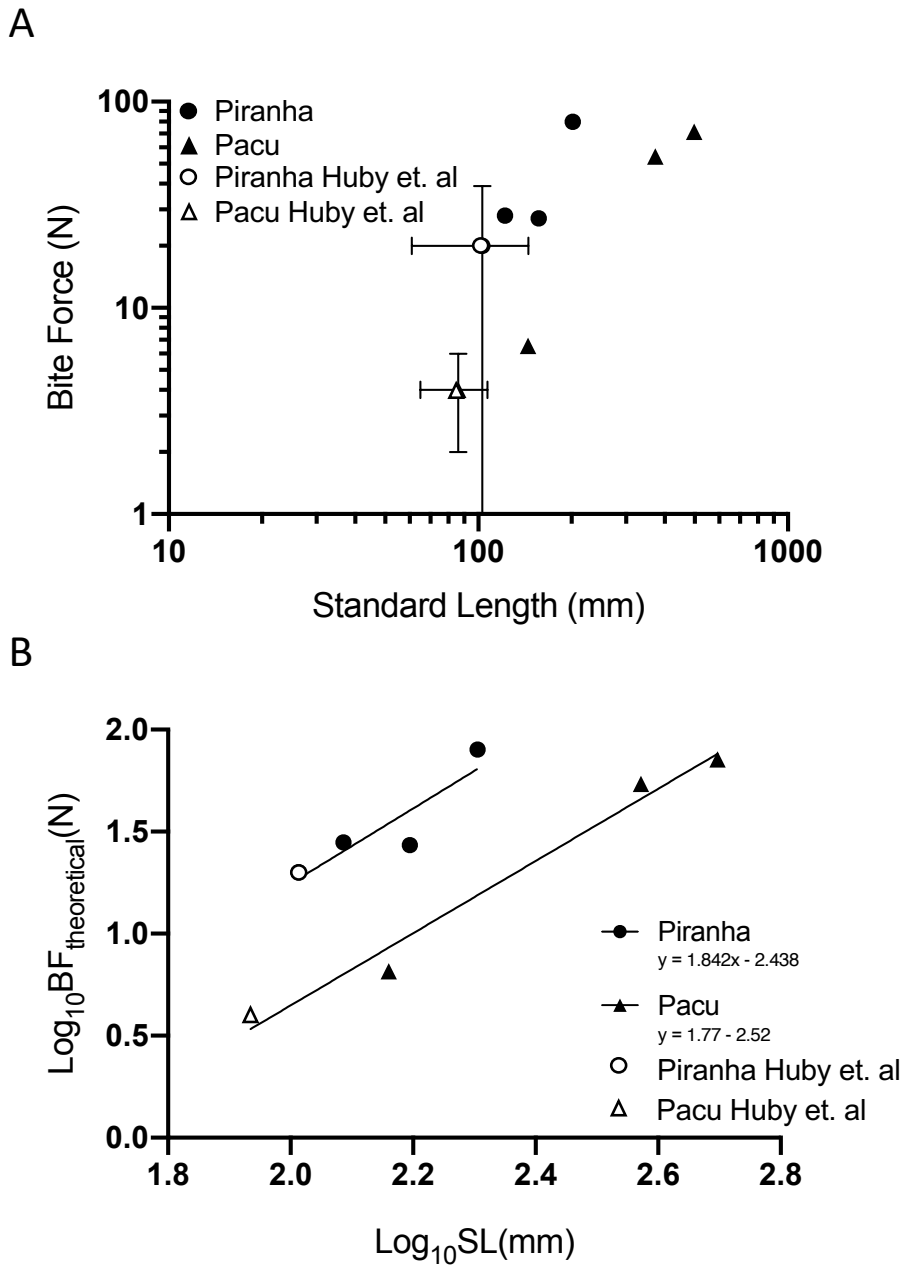

Figure 5.2 Theoretical bite forces of piranha and pacu specimens with addition of the average values obtained by Huby et. al which shows how bite force scales with the standard length of the fish. A) Theoretical bite force with respect to the standard length of piranha and pacu which includes the average data collected from Huby et. al. This show a bite force for the piranha which ranges from ~1-80 N and ~4-72 N for the pacu. Despite the larger size of the pacu, the piranha still manages a larger bite force. B) Log transformed theoretical bite force and standard length which demonstrates a positive allometric relationship.

We explored the forces necessary for consumption based on typical food sources for the piranha and pacu. The palm seed fruit is a common food source for the pacu and is used here to indicate the forces required to crack open hard-shelled fruits. When analyzed under compression it was found to require ~8 N to initiate a crack and ~25—35 N to propagate the crack (Figure 5.3A). In comparison to the theoretical anterior bite forces, the pacu can reach ~8 N and induce a crack in this example of a hard-shelled fruit if it is sufficiently large (Figure 5.3A). While crack propagation, from this experiment, requires much larger species (SL > 130 mm), this value can be considered as an over-estimation as it was an example of a singular bite. During mastication and with repeated bites the pacu can easily damage the nut by fatigue which would require smaller forces over many cycles.

To better understand the forces required for a carnivorous diet, piranha and pacu teeth were attached to a testing machine and advanced into the meat of a whole fish. Figure 5.3B shows the load-penetration curves for both piranha and pacu teeth. The piranha teeth easily penetrate the scales and into the flesh at ~2—5 N as indicated by the rapid drop in force (highlighted in orange). The pacu teeth are unable to pierce the meat and instead cause a flattening effect. This provides evidence as to how the conical shaped teeth are designed for piercing while the cusped-teeth of the pacu are more suitable for crushing. The estimation of the bite forces required for feeding is necessary to better understand the stress distribution and the load carried by individual teeth. The values obtained here will serve as a guide to what forces will be used for the finite element analysis.

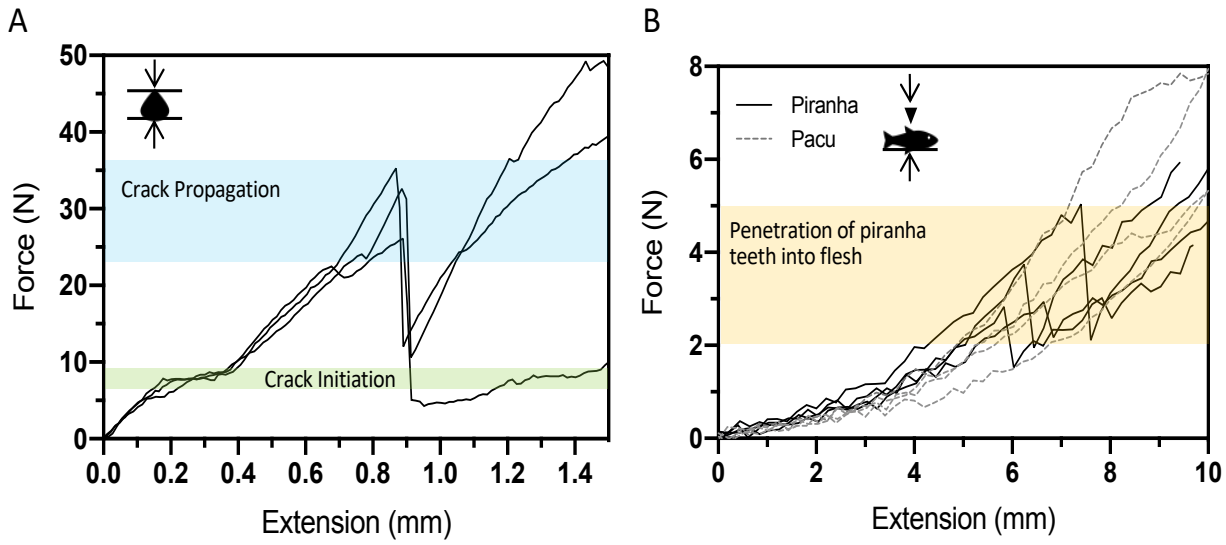

Figure 5.3 Replicative forces required for respective diets. A) Compression testing of brazil nuts. Brazil nuts are a known food source of the pacu. It requires ~7 N to initiate a crack (green) and ~30 N to propagate the crack (blue). F) Force-penetration curves into fish meat by individual piranha and pacu teeth. It requires ~2—5 N for the piranha tooth to penetrate the scale surface into the flesh. The pacu teeth are not able to penetrate and instead compress and flatten the meat.

5.3 Tooth morphology, enamel thickness, and distribution

The anterior mandibular teeth of the piranha and the pacu are strikingly different in shape and morphology. The piranha tooth is prominently tricuspid, has a conical shaped tip, and a wide base making it effective at piercing and slicing (Figure 5.4A). The pacu tooth on the other hand has a broadly shaped occlusal surface with a projecting cutting ridge which is advantageous for crushing and grinding (Figure 5.4D). In addition to their general morphological differences, both teeth have differences in enameloid thickness and distribution. It is widely accepted that enamel shape and thickness are highly related to diet. The consumption of hard-objects such as seeds and nuts is correlated with an increase in enamel thickness for mammals [229]. From the micro-computed tomography images, it can be seen that the molariform teeth of the pacu have thicker enameloid when compared to the piranha. The pacu enameloid is thickest on the cusps (1.46 ± 0.70 mm), while the piranha enameloid is more evenly distributed across the tooth (0.49 ± 0.30

mm) (Figure 5.4). For both teeth, there is a gradient in enameloid distribution which increases from the base towards the tip. This gradient is most likely a consequence of the growth and development of the enameloid layer but has desirable implications for their respective mechanical performances. Enameloid being a hard, stiff, and a wear resistant material provides rigidity to the tips of both teeth which enables effective puncturing and crushing. While the enameloid is relatively evenly distributed in the piranha (Figures 5.4B and C), for the pacu, the enameloid is strongly concentrated on the vestibular surface and protrudes to a maximum thickness of ~2 mm while being marginally thin on the lingual surface (Figures 5.4E and F). This large concentration of thick enameloid provides a robust ledge for crushing and grinding. These differences in enameloid distribution are related to how the teeth are attached to the jaw.

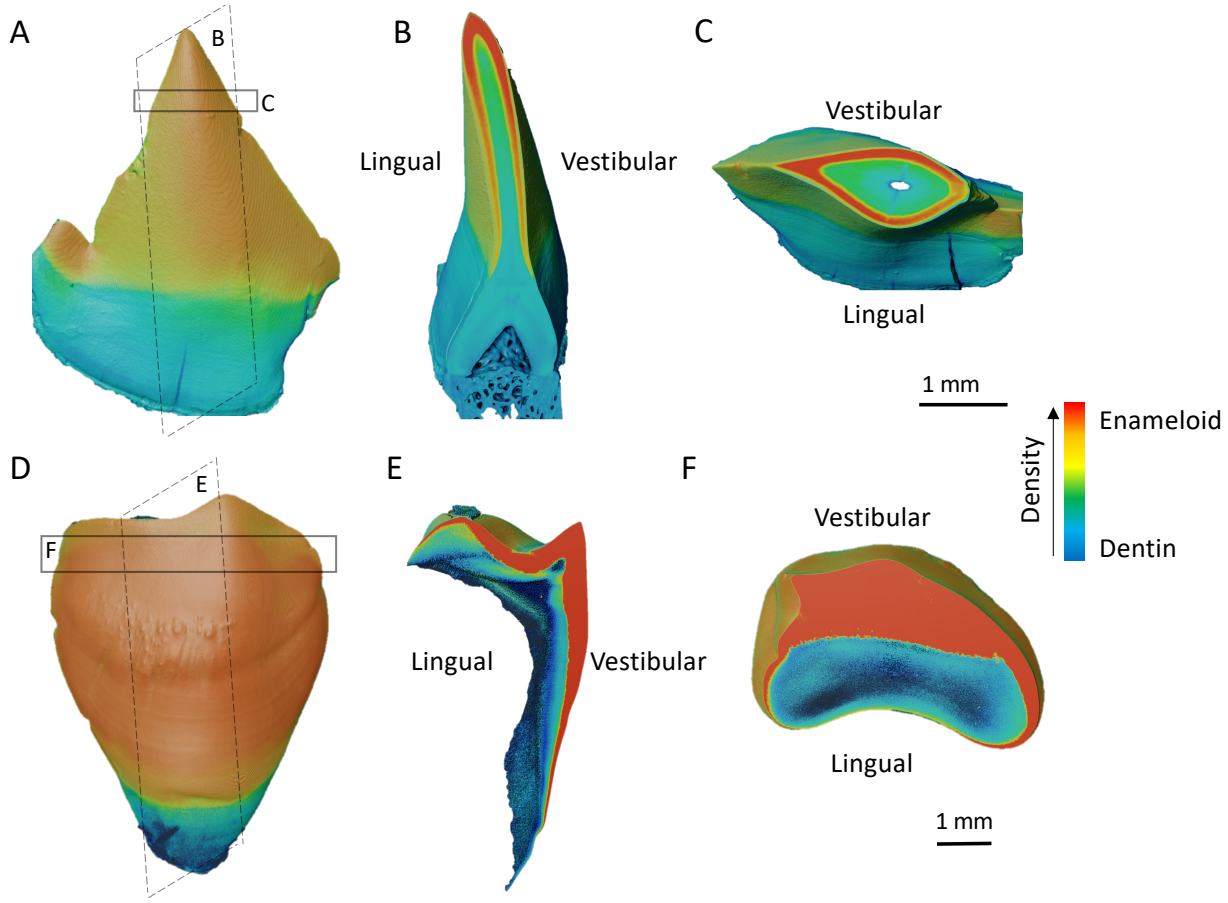

Figure 5.4 Micro-computed tomography images of anterior piranha and pacu teeth which are pseudo-colored. The coloration is a relative density map where the hotter colors correspond to a more dense and mineralized phase (enameloid) and the cooler colors correspond to a less dense and less mineralized phase (dentin) and in the case of the piranha the bone is shown in blue as well. A) Vestibular surface of the piranha tooth. B) Longitudinal cross section of the piranha tooth. C) Transverse cross section of the piranha tooth. D) Vestibular surface of the pacu tooth. E) Longitudinal cross section of the pacu tooth. F) Transverse cross section of the pacu tooth.

In addition to their differences in general morphology and enameloid thickness, both teeth are attached to the mandible at different surfaces which has implications for how the load is distributed during mastication. The piranha tooth is embedded into the bone at its base allowing for both the lingual and vestibular surfaces to be exposed to the environment (Figure 5.4B). This

allows for greater penetration and piercing action of the tooth. However, the pacu tooth does not have a defined base and is instead embedded into the mandible predominantly along the lingual surface leaving only the vestibular and occlusal surfaces exposed (Figures 5.4E and 5.5). Unlike the piranha, the pacu tooth is more grounded within the jaw, allowing for greater stabilization during compression and translation of mastication forces into the mandible. Thus, the thickness of the occlusal surface that is exposed above the mandible is minimal, which supports its primarily crushing mode.

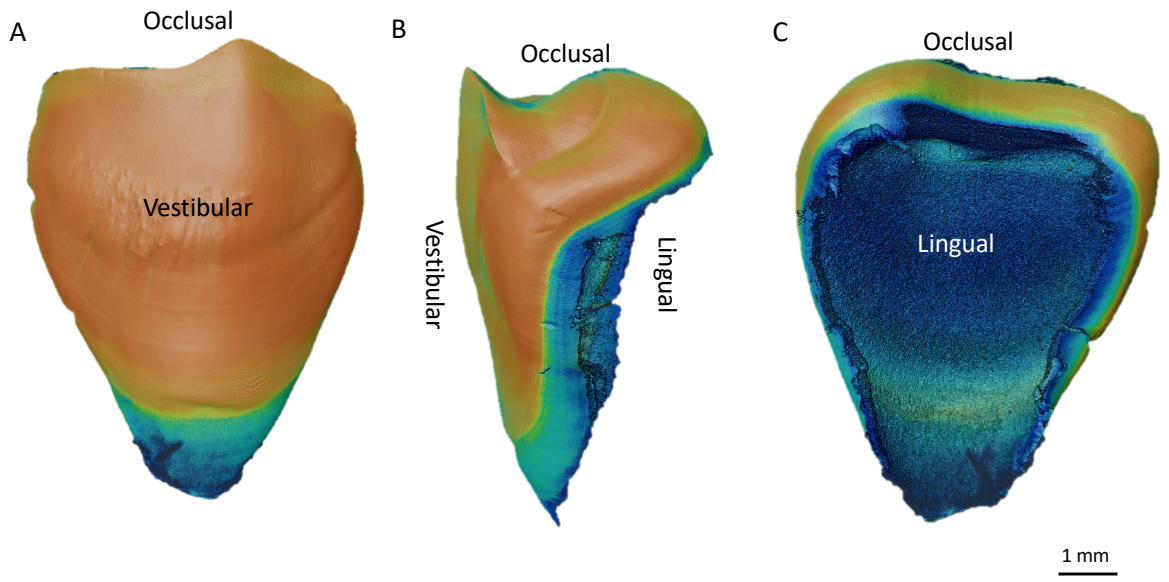

Figure 5.5 Micro-computed tomography images of an anterior mandibular pacu tooth in pseudo color showing that the lingual surface is predominantly attached to the bone. A) Vestibular surface of the tooth. B) Side-view showing both vestibular, lingual, and occlusal surfaces. Noting that the lingual surface is where it attaches to the mandible. C) Lingual surface of the tooth showing the pulp cavity and where it was formerly attached to the mandible (rough edges in dark blue).

5.4 Microstructure characterization of enameloid and dentin layers

5.4.1 Enameloid

The enameloid is highly mineralized and can be decomposed into two layers in both the piranha and pacu: (1) inner-enameloid (IE), where there is a high degree of interwoven HAP mineralized collagen fibers, and (2) outer-enameloid (OE), which is defined by aligned regions perpendicular to the surface (vertical lines in Figure 5.6). Demineralization with HCl was used to reveal the microstructure which can be concealed by amorphous regions. The inner-enameloid in both piranha and pacu shows no significant differences in the organization, size, and dispersion of the mineral-coated collagen fibers (Figures 5.6B and E). The thickness of the fibers in the piranha and pacu measures 2.50 ± 0.79 μm and 2.48 ± 0.77 μm (mean ± standard deviation) respectively and the angle between fibers which cross over each other are 54.5° ± 16.5° and 56.0° ± 11.2° respectively. These similarities are attributed to equivalences in tissue development. The imbrication found in the IE has the potential capability of arresting and deterring cracks from propagating through the enameloid and may act as a toughening mechanism for the inherently brittle material [230]. The OE responded differently to the demineralization process in both teeth. The OE of the piranha teeth show a higher degree of demineralization when compared to the OE of the pacu teeth (Figure 5.6C and F). This is possibly explained by the differences in iron concentration. As shown by Delaunois et al.[224] and corroborated in Section 5.5, the pacu teeth have a larger concentration of iron which has been shown to improve resistance against acid attack in mammalian teeth [225].

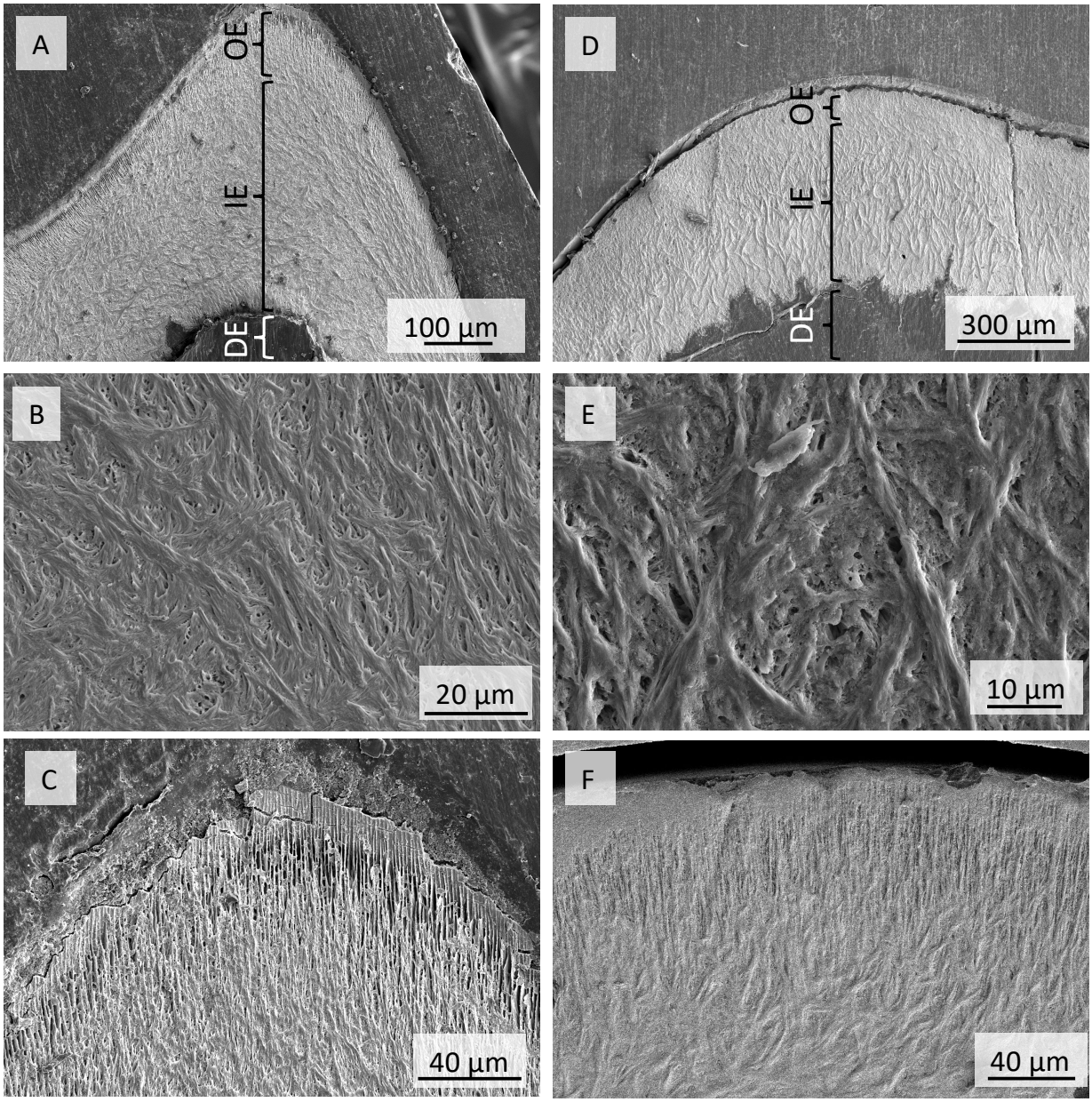

Figure 5.6 SEM images of acid-etched enameloid of piranha and pacu which shows the following layers: outer enameloid (OE), inner enameloid (IE), and dentin (DE). A) Longitudinal cross section of a piranha tooth showing the three layers: OE, IE, and DE. B) Magnification of the IE from the piranha tooth showing the woven fibrous network. C) Magnification of the OE of the piranha tooth showing the parallel oriented rods that are perpendicular to the surface. D) Longitudinal cross section of a pacu tooth showing the three layers: OE, IE, and DE. E) Magnification of the IE from the pacu tooth showing the woven fibrous network. F) Magnification of the OE showing the parallel orientated rods.

5.4.2 Dentin

The dentin layers are similar in both species and are characterized by the presence of tubules (Figure 5.7). The tubules are generally circular in shape, but depending on the cross section can appear elliptical if viewed obliquely. The average radius of the tubules in the piranha dentin were found to be 0.69 μm which is comparable to the pacu dentin (0.71 μm). Both dentin layers exhibit a highly mineralized reinforcing layer which surrounds the tubule as denoted by the brighter regions in the SEM in Figure 5.7.

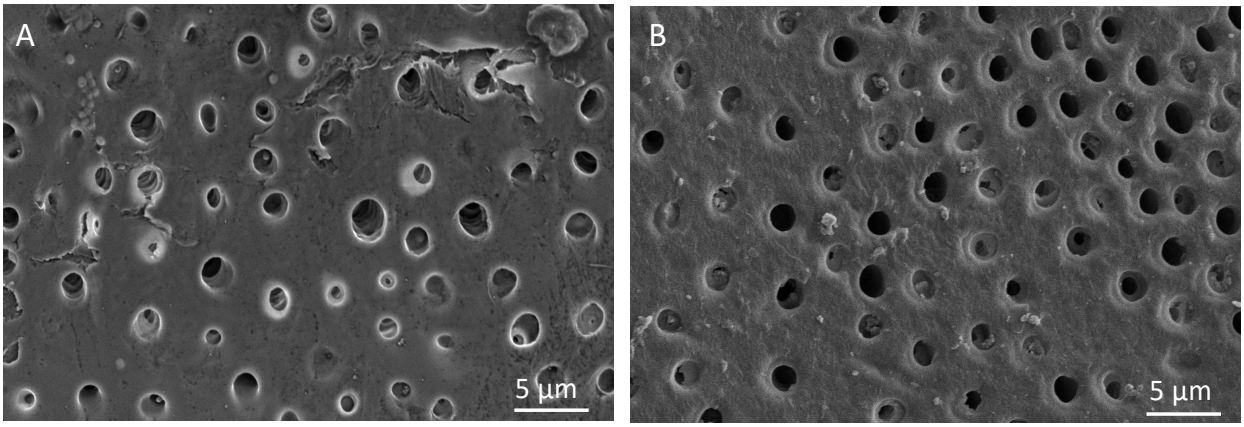

Figure 5.7 SEM images of transverse cross sections showing the tubule structure in the dentin layer. A) Piranha tubular dentin. B) Pacu tubular dentin.

5.4.3 Dentin-enamel junction

The dentin-enameloid junction (DEJ) of the pacu teeth has a distinct interlocking interface while on a similar length-scale the piranha is relatively smooth and uninterrupted (Figure 5.8). This interdigitating suture interface is found across a variety of biological materials (carapace of the red-eared slider[231], mammalian skulls[106], boxfish scute junctions[24], and diatom frustules[232]) and is known to provide intrinsic strength and flexibility to material interfaces [19]. The DEJ plays a critical role in maintaining the biomechanical integrity of the teeth by joining the

hard, brittle enameloid and subjacent softer, tougher dentin. Thus, it provides a crack arresting barrier. Its resistance to mechanical failure and delamination is predominantly attributed to the presence of collagen fibrils which bridge the DEJ acting as a fiber-reinforced composite. The DEJ of mammalian teeth has been characterized as having a similar scalloped interface although it is much less angular than the DEJ of the pacu [233–235]. This scalloped interface has been shown to effectively support the mechanical performance during mastication by reducing stress concentrations at the interface and preventing sliding of the underlying dentin layer [236]. A study on the scallop interface in permanent human teeth by Brauer et al.[237] found a relationship between tooth position and scallop size where the most posterior teeth (higher masticatory loads) were shown to have larger and more pronounced scallops. This suggests that a scalloped interface benefits teeth that undergo significant stresses due to crushing and grinding.

The suture structure seen in the pacu teeth ranges from triangular to trapezoidal and is much less rounded and more irregular than the scalloped interface seen in mammals. Despite differences in geometry, we suggest that the DEJ found in the pacu serves a similar function as that reported by the scalloped interface in mammals. Suture geometry is important in determining stiffness, strength, failure modes, and stress field distribution and can be tailored to optimize mechanical performance [238]. We suggest that the interlocking nature of the DEJ in the pacu teeth helps to enhance mechanical bonding between the dentin and enameloid and effectively distributes the stress field during compression making it advantageous for a durophagous diet.

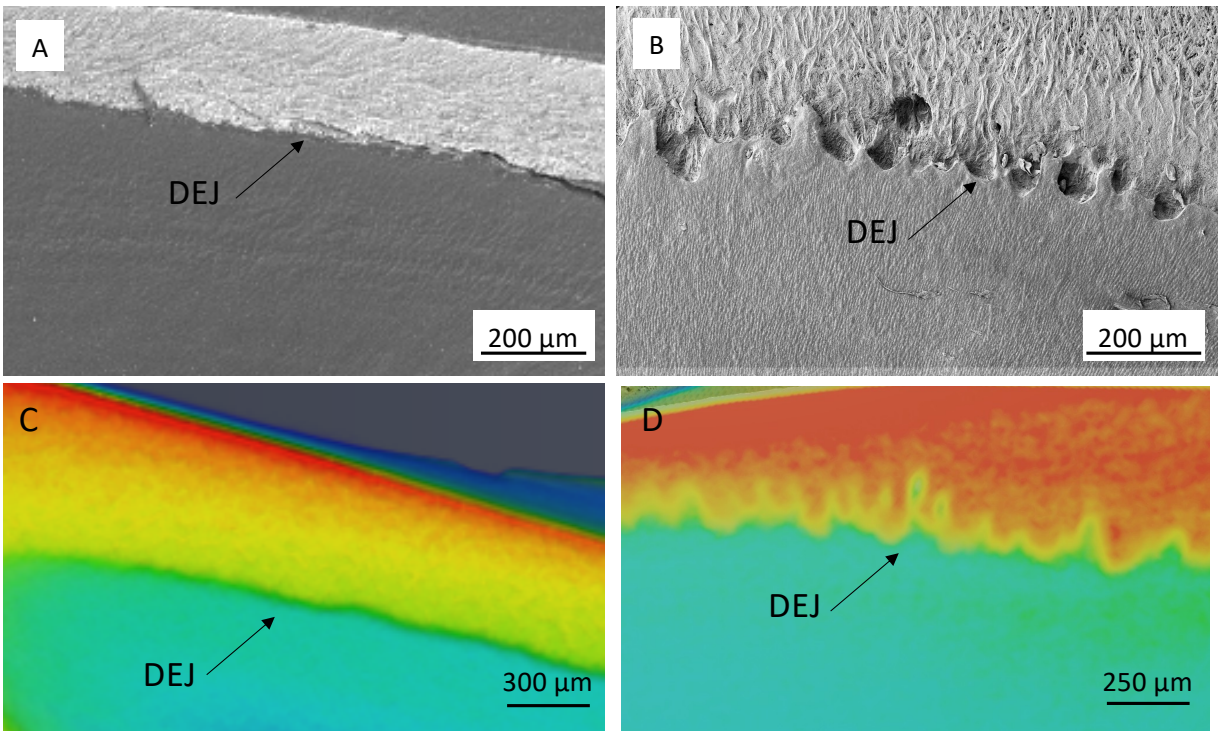

Figure 5.8 SEM and micro-CT images of the dentin-enamel junction (DEJ) in the teeth of the piranha and pacu. A) SEM micrograph of a longitudinal cross section of the piranha tooth showing the relatively smooth DEJ. B) SEM micrograph of a longitudinal cross section of the pacu tooth showing the sutured DEJ that contains a combination of triangular and trapezoidal shaped interfaces. C) Micro-CT image of the piranha tooth in pseudo-color showing again the relatively flat interface of the DEJ. D) Micro-CT image of the pacu tooth in pseudo-color showing the interlocking interface of the DEJ.

5.5 Compositional analysis by energy dispersive spectroscopy

Quantitative elemental analysis of the piranha and pacu teeth was performed using energy dispersive spectroscopy (EDS). False-colored maps of calcium (blue), phosphorus (pink), and iron (teal) in longitudinal and transversally polished sections of the pacu and piranha teeth is shown in Figure 5.9. Both pacu and piranha are observed to have large concentrations of calcium and phosphorous which is indicative of hydroxyapatite $Ca_{10}(PO_4)_6(OH)_2$. Calcium and phosphorous occur in greater quantities in the enameloid as indicated by the brighter regions in both the piranha and pacu. This is in agreement with the enameloid layer being more mineralized than the

underlying dentin layer.

Additionally, iron is present in both teeth but in different quantities. Iron occurs in significantly larger amounts in the pacu teeth than the piranha teeth. Iron in the pacu teeth occurs in such large quantities that it is referred to as pigmented enameloid forming an observable rust-colored layer (Figures 5.10 and 5.11A). In the piranha, the presence of iron is considerably less and cannot be visualized in the EDS maps but can be detected by point analysis. In both teeth, iron is greatest in the cuticle for the pacu (1.685 ± 0.075 at%) and piranha (0.398 ± 0.034 at%) and gradually diminishes towards the center of the tooth towards the dentin (Table 5.1). For the pacu, there are trace amounts of iron that reach the outer-dentin layer, while in the piranha detectable iron only reaches as far as the outer-enameloid layer. The iron is not uniformly distributed in the pacu cuticle layer as larger concentrations are found on the concave and lingual surfaces with minimal iron at the occlusal surface (tip). This may be due to an increase in wear at the tip during the lifetime of the tooth as a result of its durophagous diet.

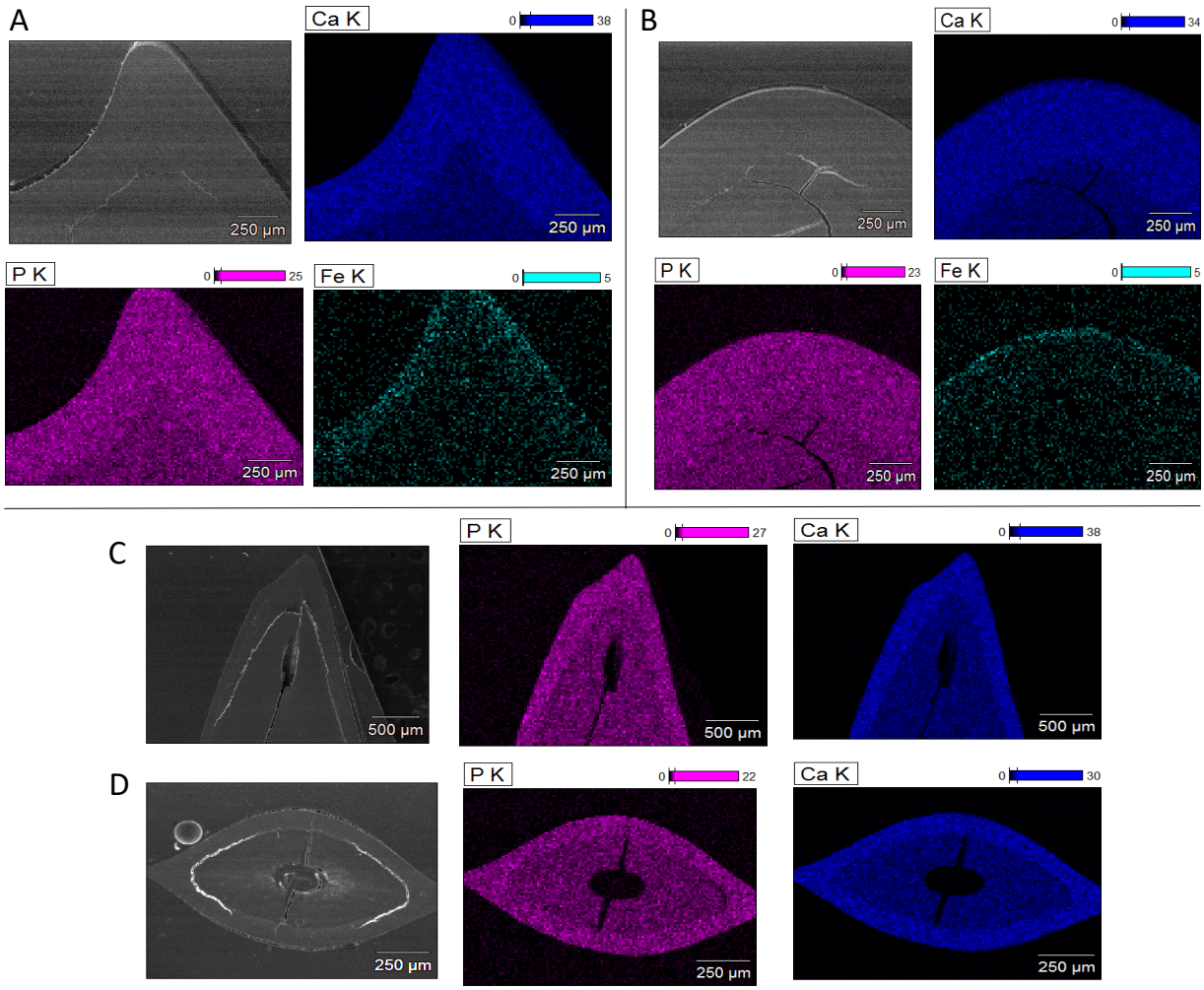

Figure 5.9 Energy dispersive X-ray spectroscopy maps of the pacu and piranha teeth showing the relative dispersion of Ca, P, and Fe in false-color. A) Longitudinal cross-section of the pacu tooth showing false-colored maps of calcium (blue), phosphorus (pink), and iron (teal). Iron is localized in the cuticle and decreases in a gradient fashion towards the center. There are concentrations of iron on the concave and buccal surfaces. B) Transverse cross section of the pacu tooth showing the relative dispersion of Ca, P, and Fe. While iron is still present in the cuticle and shows to be distributed across a gradient, the transverse section is inherently further away from the tip which may be why the concentration is respectively lower than the transverse surface. C) Longitudinal cross section of the piranha tooth. D) Transverse cross section of the piranha tooth.

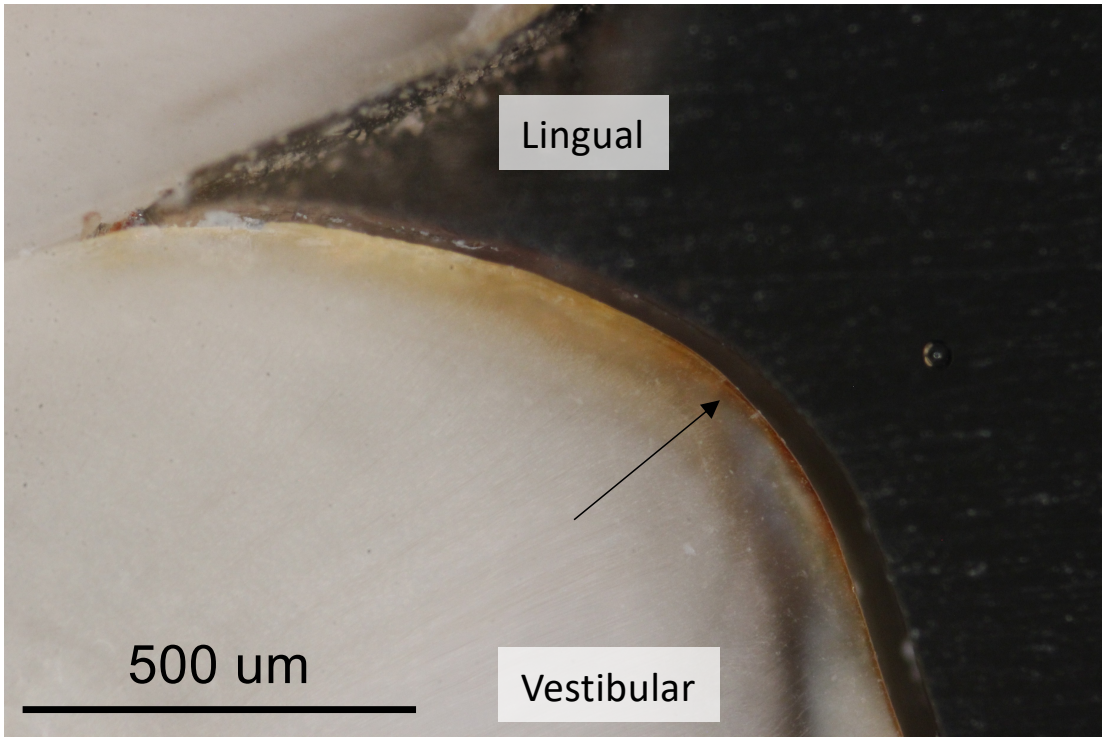

Figure 5.10 Longitudinal cross section of a pacu tooth showing the pigmented enamel. The rust color is due to the presence of iron.

Table 5.1 Concentration of iron in various layers of the piranha and pacu teeth. There is a gradient which is highest in the outermost layer (cuticle) and decreases inwards towards the dentin. This data is taken from point-scans of EDS.

	Iron Concentration (at.%)				
Species	Inner Dentin	Outer Dentin	Inner Enameloid	Outer Enameloid	Cuticle
Colossoma Macropomum	0	0.174 ± 0.020	0.191 ± 0.034	0.800 ± 0.041	1.685 ± 0.075
Pygocentrus nattereri	0	0	0	0.034 ± 0.015	0.398 ± 0.034

5.6 Nanoindentation

High-resolution nanoindentation was performed to ascertain the local hardness and modulus of the piranha and pacu teeth with respect to compositional gradients in mineralization and iron across the cuticle, enamel, and dentin layers. Indents were performed on both longitudinal and transverse polished sections such that the middle plane of the tooth was exposed. Due to these constraints, the cuticle layer was either too thin or absent in the transverse cross sections and could therefore not be accurately indented.

Modulus and hardness maps of the longitudinal and transverse cross sections of the teeth reveal that the stiffest and hardest portion occurs in the cuticle layer and is at a minimum in the dentin layer. This is in agreement with the compositional gradients in mineralization and iron which are greatest in the cuticle layer and decrease towards the dentin. The cuticle of the pacu teeth (5.80 ± 0.23 GPa) is found to be harder than the piranha teeth (4.92 ± 0.57 GPa) (Figure 5.11). This is not surprising as the pacu cuticle has a significantly larger concentration of iron which increases the hardness. The hardness of the cuticle of the pacu teeth is comparable to the pigmented enamel found in beaver teeth (5.85± 0.27 GPa) where the high hardness is also due to iron [225].

Despite the high hardness in the pacu cuticle, the piranha cuticle is significantly stiffer with a modulus of 104.3 ± 10.8 GPa compared to the modulus of the pacu cuticle of 78.7 ± 2.35 GPa. This can be explained by the piranha teeth typically having a higher degree of mineralization [224]. Additionally, the comparatively lower modulus measured in the pacu teeth can be a result of the high hardness combined with the indentation technique. In nanoindentation, the modulus is measured using the slope of the force-displacement curve upon unloading. During the applied load, it is possible that cracks are generated as a result of its high hardness which could influence the

unloading response and effectively soften the material. The local mechanical response of the cuticle layer in the pacu and the piranha is consistent with their specialized diets. Having a stiff cuticle is beneficial for the piranha to maintain its rigidity as it effectively pierces through prey, while a high degree of hardness provides the necessary strength and wear resistance for the crushing and grinding mechanisms necessary for the pacu's durophagous diet.

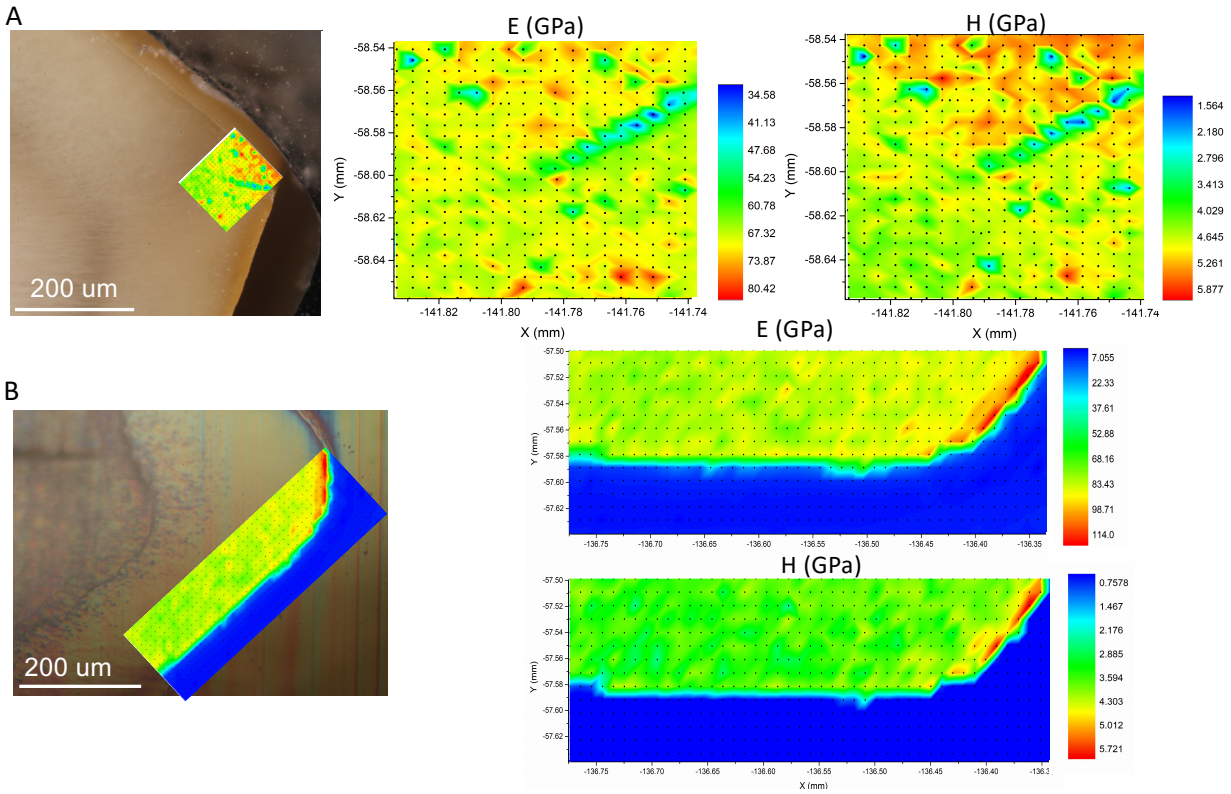

Figure 5.11 Nanoindentation characterization of longitudinal sections of cuticle and enameloid layers in the piranha and pacu teeth of modulus (E) and hardness (H). A) Pacu tooth, noting the pigmented cuticle in the optical micrograph. B) Piranha tooth.

Despite large differences in the mechanical properties in the cuticle layers, the enameloid and dentin are relatively similar in the pacu and piranha (Figure 5.12). The modulus of the enameloid in the teeth in the longitudinal and transverse orientations are 83.2 ± 4.5 GPa and 76.65 ± 5.75 GPa for the piranha and 72.9 ± 7.0 GPa and 75.6 ± 4.8 GPa for the pacu. Thus, the enameloid of the piranha is only slightly stiffer than that of the pacu which again can be related to its high

degree of mineralization and functional constraints of rigidity. The inner enameloid can be described, by virtue of its three-dimensional interwoven structure, as isotropic while the directionality of the parallel orientated structuring in the outer enameloid lends itself to being more anisotropic. It is likely that differences in these layers within the enameloid were captured in the piranha teeth. Similar to the trend seen in the cuticle layer, the hardness of the enameloid is slightly larger in the pacu teeth than the piranha teeth in both orientations. The hardness of the enameloid in the longitudinal and transverse orientation for the pacu teeth are 3.7 ± 0.6 GPa and 3.8 ± 0.4 GPa while the piranha teeth are 3.67 ± 0.36 GPa and 2.86 ± 0.41GPa respectively. Again, this hardness can be attributed to the higher degree of iron in the enameloid layer of the pacu teeth than the piranha teeth. The hardness of the piranha teeth is significantly different in the longitudinal and transverse orientations for the piranha teeth while in the pacu teeth there is no significant difference. Both the hardness and modulus of the enameloid occur in a gradient with higher values towards the exterior of the tooth as can be seen best in Figure 5.12.

The modulus of the dentin layers is the most consistent with respect to orientation and in the piranha is found to be 23.3 ± 8.3 GPa and 23.4 ± 3.6 GPa for the longitudinal and transverse cross sections. For the pacu, the modulus of the dentin layer is 22.04 ± 2.95 GPa and 21.8 ± 3.8 GPa for the longitudinal and transverse cross sections. Similar to the cuticle and enameloid layers, the modulus of the dentin is larger in the piranha teeth than the pacu teeth. The hardness of the dentin layer for the piranha in the longitudinal and transverse cross sections are 1.06 ± 0.46 GPa and 0.72 ± 0.19 respectively. A similar range of hardness is found in the dentin layer of the pacu at 0.85 ± 0.18 GPa for the longitudinal cross section and 1.01 ± 0.28 GPa for the transverse cross section. The modulus and hardness with respect to the longitudinal and transverse orientations across the cuticle, enameloid, and dentin are summarized in Table 5.2.

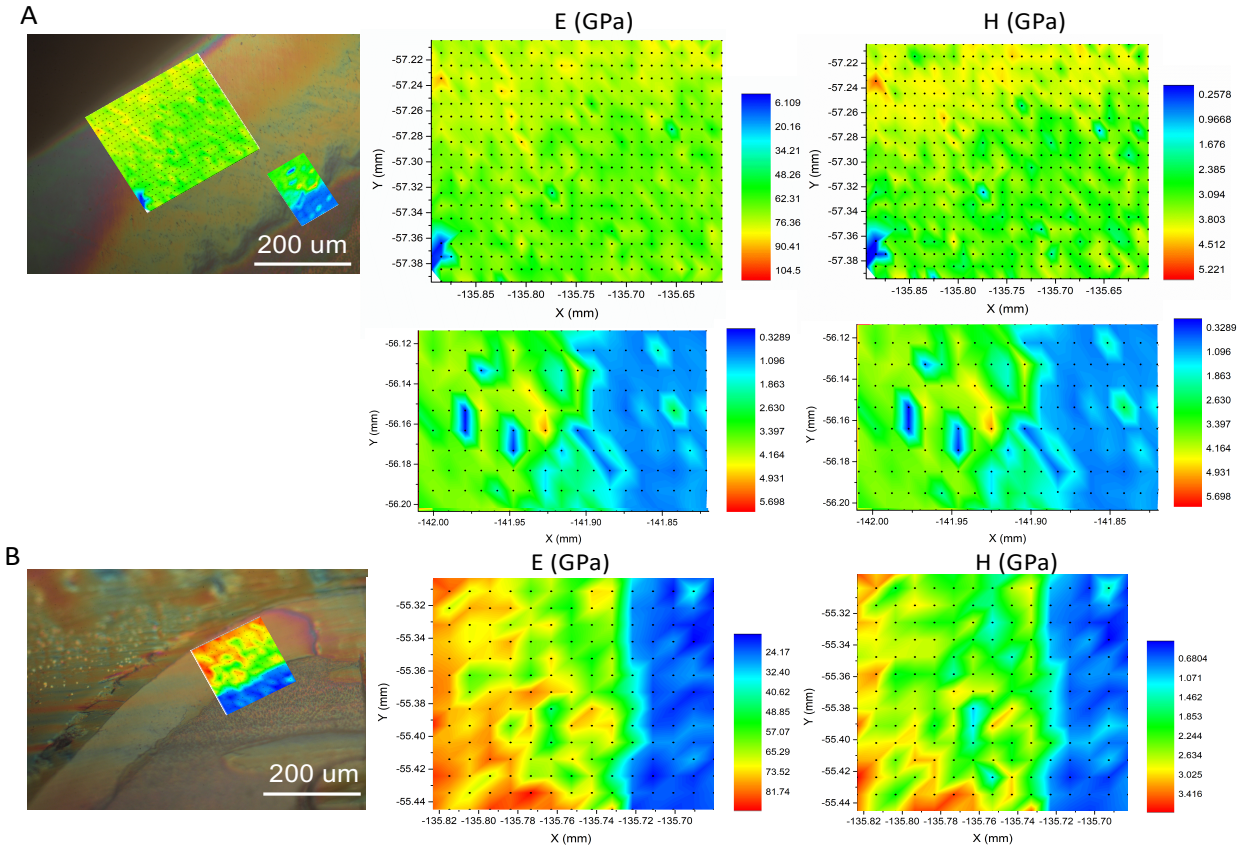

Figure 5.12 Nanoindentation characterization of transverse cross sections of enameloid and dentin layers in the piranha and pacu teeth representing modulus (E) and hardness (H). A) Pacu tooth, notice the gradient in modulus and hardness from the OE to the IE (yellow to green) B) Piranha tooth with a similar gradient.

Table 5.2 Modulus and hardness from nanoindentation of *Pygocentrus nattereri* and *Colossoma Macropomum* across the cuticle, enamel, and dentin with respect to the longitudinal and transverse direction (mean ± standard deviation).

	Pygocentrus nattereri		*Colossoma Macropomum*	
	Longitudinal	Transverse	Longitudinal	Transverse
Cuticle modulus (GPa)	104.3 ± 10.8	--	78.7 ± 2.35	--
Cuticle hardness (GPa)	4.92 ± 0.57	--	5.80 ± 0.23	--
Enameloid modulus (GPa)	83.2 ± 4.5	76.65 ± 5.75	72.9 ± 7.0	75.6 ± 4.8
Enameloid hardness (GPa)	3.67 ± 0.36	2.86 ± 0.41	3.7 ± 0.6	3.8 ± 0.4
Dentin modulus (GPa)	23.3 ± 8.3	23.4 ± 3.6	22.04 ± 2.95	21.8 ± 3.8
Dentin hardness (GPa)	1.06 ± 0.46	0.72 ± 0.19	0.85 ± 0.18	1.01 ± 0.28

5.7 Finite element analysis

To better understand how tooth shape and enameloid thickness influences stress distribution within the tooth during compression we performed computational simulations on the most anterior teeth of the piranha and pacu using finite element software Abaqus (v.6.14). A three-dimensional representation of each tooth was obtained using X-ray micro-computed tomography and subsequently digitized into an appropriate mesh to obtain the CAD geometry. It is important to use a non-homogenous model to account for both the dentin and enameloid material properties as it has been shown that a major portion of the load is primarily supported by the enamel layer in mammalian teeth.[239] Each model was divided into two mechanically distinct regions which were modeled with a linear elastic model with Young's modulus obtained directly from the nanoindentation experiments: piranha enameloid (E = 80 GPa), piranha dentin (E = 23 GPa), pacu enameloid (75 GPa), and pacu dentin (22 GPa). A force of 15 N was translated to a pressure dependent on the area of the tip of each tooth. This force was used as it was attainable by both species when compared to the theoretical anterior bite forces and was sufficient enough for both replicative diets (enough force to initiate a crack in a hard-shelled fruit and to penetrate flesh). The piranha tooth was fixed at the base of the tooth, while the pacu tooth was fixed on the exposed edges of its lingual surfaces. This is representative of the attachment of the teeth to the jaw. The boundary conditions are shown in Figure 5.13.

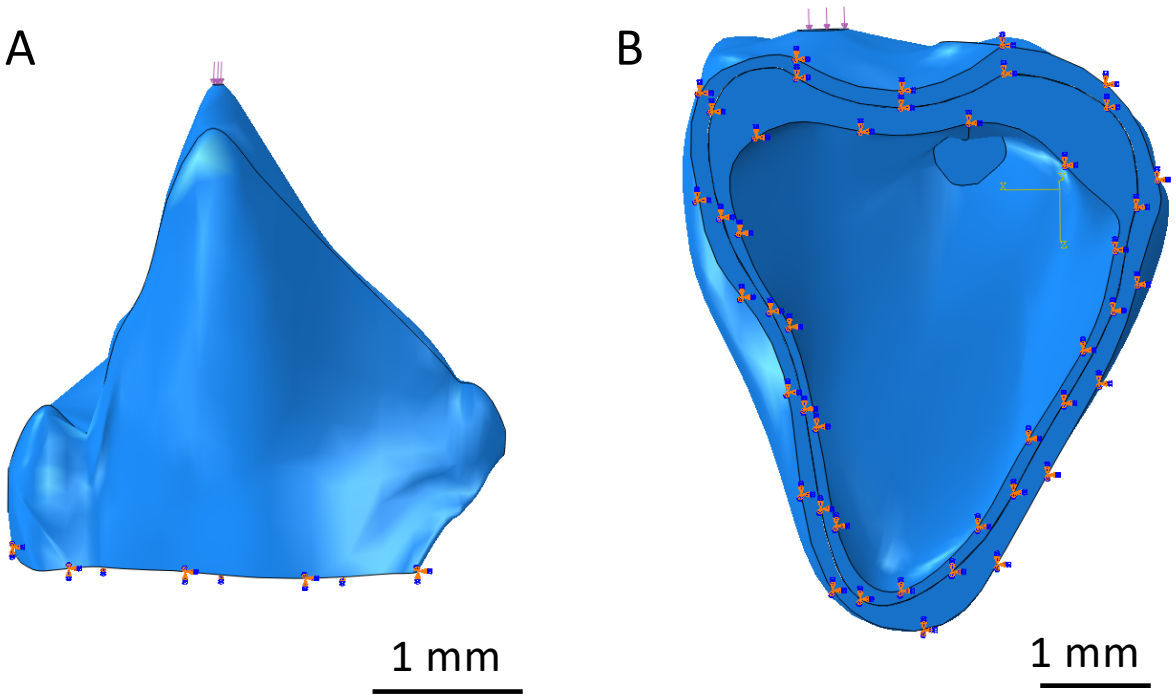

Figure 5.13 Boundary conditions for the finite element models. A) For the piranha tooth the load is applied at the tip and fixed at the base. B) for the pacu tooth the load is applied on the top surface and fixed on the lingual surface.

The stress distribution in each tooth under compression is revealed by the finite element model. In Figure 5.14, von Mises stresses are mainly distributed within the enameloid and reduced in the dentin layer. The piranha localizes stresses at the tip, while the broad cusps of the pacu teeth help to more evenly distribute the stress. The curvature of the piranha tooth leads to an uneven stress distribution within the enameloid with higher stresses occurring on the concave side. The portion of the piranha tooth that would interlock with its neighboring tooth shows a localized concentration of stress in the enameloid. While only one tooth was simulated, the interlocking nature of the piranha teeth may help to distribute this stress. The thicker enameloid in the pacu

leads to a reduction in the stress within the dentin layer. Additionally the thickest parts of the enameloid in the pacu show a reduction in stress. The more evenly distributed and minimization of the von Mises stress may also be attributed to the differing boundary conditions and how each tooth is attached to the jaw. The stress distribution pattern in the pacu teeth suggests greater efficiency and lower deformation during compression when compared to the piranha teeth.

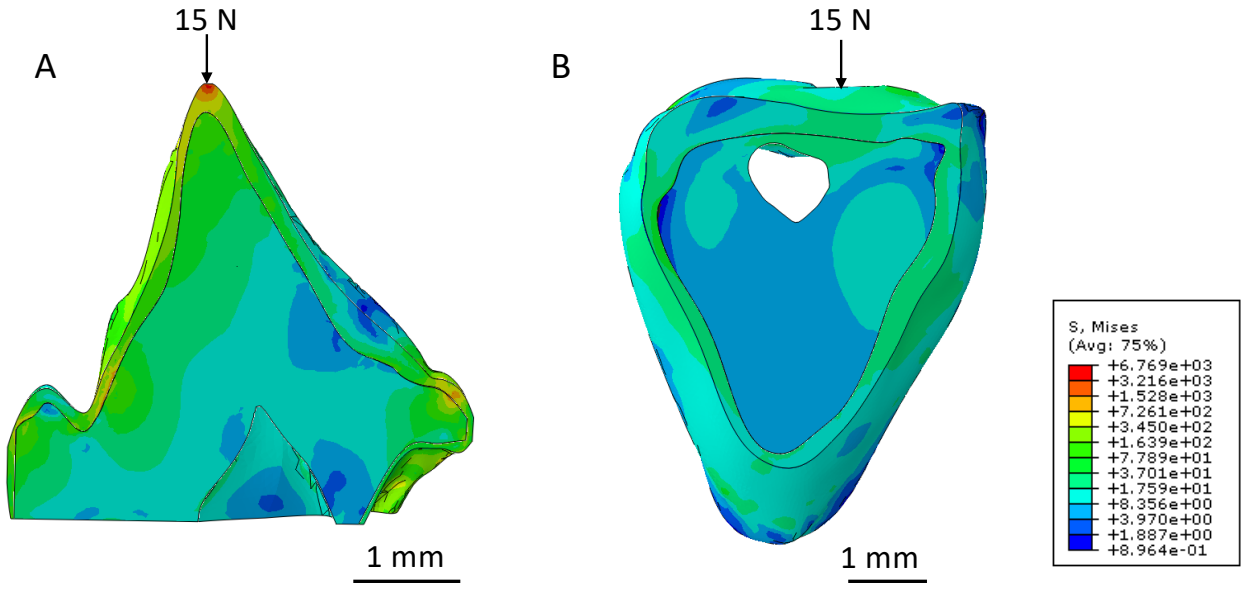

Figure 5.14 Finite element analysis of longitudinal cross sections of anterior piranha and pacu dentition under compression with a load of 15 N. Distribution of stresses is dependent on the size of the tooth, morphology, and enamel thickness. A) Piranha teeth exhibits high stress concentration at the tip. B) The pacu tooth more evenly distributes the applied stress which is minimized at the thicker cusps of the enameloid.

5.8 Bioinspired interfaces

From this study, it is evident that the pacu teeth are hierarchically structured to better respond to compressive forces than the piranha teeth. One important microstructural feature that contributes to this is the sutured interface of the DEJ. Here we use a simplified prototype inspired by the suturing in the DEJ of both the piranha and the pacu to better understand the mechanisms at hand. Two prototypes (flat interface vs sutured) are analyzed using numerical modeling and 3D printed and mechanically tested using quasi-static compression paired with digital image correlation to visualize the strains. Both prototypes are composites with a stiff layer (Veroclear) meant to represent the enameloid stacked upon a softer layer (Flex9985) meant to represent dentin. The sutured interface is triangular with a 45^{o} tip angle.

Using FEA we compare two layered structures with different interfaces: (1) flat inspired by the piranha and (2) triangular sutures inspired by the pacu. In Figure 5.15, the stress is more evenly distributed under compression when there is an interlocking interface. Most importantly, the maximum stresses are concentrated on the tips of the triangles that terminate into the inner enameloid and are thus disconnected. This localizes and constrains the maximum stress in the enameloid. The microstructure of the inner enameloid, being interwoven, likely inhibits crack growth that may initiate at these sites. With a flat interface the stress concentrates on both sides of the interface—there are large stresses both in the enameloid and dentin regions. This simple design provides insight into how the structuring of the DEJ works cooperatively with the microstructure of the inner enameloid and enables the pacu to fulfill a durophagous diet.

Using digital image correlation we compared the two layered structures (Figure 5.15C and D) to determine how the triangular interlocking interface influences the strain distribution. With a

flat interface the shear strain concentrates on the corners of the interface and at the base of the structure. With a sutured interface the shear strain decreases and is more uniformly distributed.

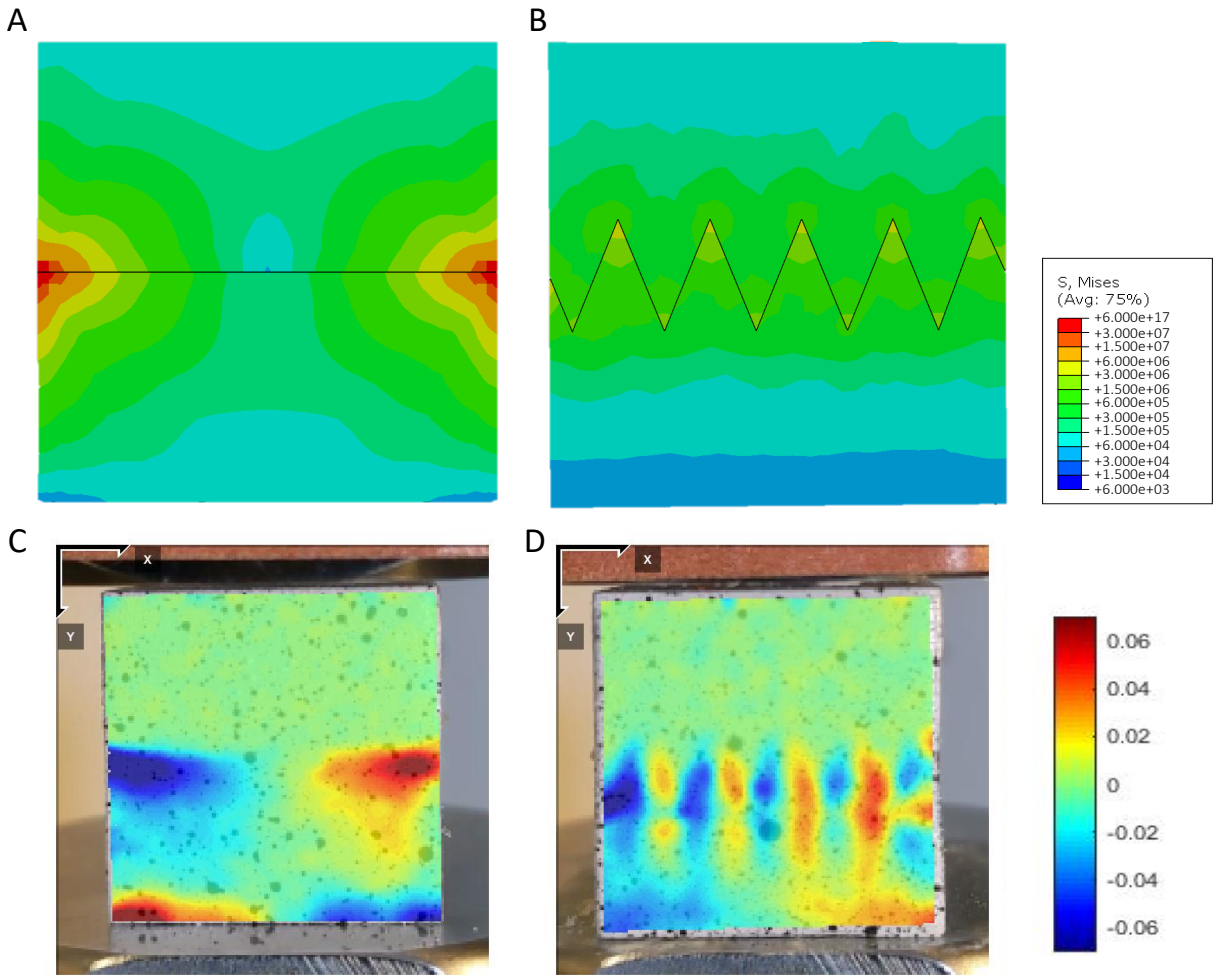

Figure 5.15 Interfaces inspired by the piranha and pacu. A) FEA results of the flat interface inspired by the DEJ of the piranha showing stress concentrations at the edges. B) FEA results of the interlocking triangular interface inspired by the DEJ of the pacu showing how the stress is more evenly distributed. C) DIC analysis of the shear strain of the flat 3D printed interface. D) DIC analysis of the shear strain of the 3D printed sutured interface.

5.9 Conclusions

The teeth of the piranha and the pacu are complex hierarchical composites optimized for their respective diets. There are notable differences in tooth morphology, enameloid thickness and

distribution, suturing in the dentin-enameloid-junction, increased hardness of the cuticle layer due to the larger concentrations of iron present, and ability to more evenly distribute the applied load. These suggest that the pacu teeth are more suited for withstanding large compressive loads when compared to their carnivorous counterpart whose dentition is optimized for slicing. These factors provide insights into the design and fabrication of wear-resistant materials for applications that require compressive loading conditions.

5.10 Experimental methods

Specimens

Three adult piranha (*Pygocentrus nattereri*) and three adult pacu (*Colossoma macropomum*) specimens were purchased from local fish markets in Brazil already deceased. Specimens were transported overnight packed in ice. Upon retrieval specimens standard lengths were recorded and their in-tact skulls preserved and placed in a -20˚C freezer until use. Specimens were hydrated in Hank's balanced salt solution (Thermo Fisher Scientific) before jaw muscle dissection. The lower jaws were removed and only the most anterior teeth were examined further. The anterior teeth were sonicated to remove debris and critically dried using a critical point dryer (Autosamdri-815, Tousimis, Rockville, MD, USA). The anterior teeth were stored at room temperature and then embedded in epoxy for further sectioning and polishing.

Bite force analysis

The measurement on live piranhas, was made on specimens caught along the Paraguay and Roosevelt Rivers and their bite forces were measured using a force gauge assembled with a Flexiforce™ A401 sensor (Tekscan). Two force gauges were constructed (Gauge 1 and Gauge 2). The sensor was placed between two wood strips and the assembly was inserted into the piranha's

mouth as indicated in Figure 4.S1. The change in resistance was recorded and converted into a force through the following equations dependent on which gauge was used. Each piranha recorded ~10 bites. Table 1 shows the recorded force values from the live piranhas. These values are consistent with the measurements from Huby et al.[177] Their mass and length were recorded and they were released back into the river.

Gauge 1: $y = 16.158x^{-0.66}$

Gauge 2: $y = 12.41x^{-0.69}$

Quasi-static compression

Four palm seeds were tested in quasi-static compression using a mechanical testing machine, Instron 3367 load frame (Instron, High Wycombe, United Kingdom) to determine the forces required to initiate and propagate a crack under compression. A strain rate of 10^{-2} s^{-1} was used. The force-displacement curves and failure mechanisms were highly repeatable for all nut samples tested.

Four piranha teeth and four pacu teeth were superglued to screws at the base of the tooth that could then be attached to a mechanical testing machine that was used to penetrate into the flesh of a fresh fish purchased at the local market. Samples were compressed at a rate of 2 mm/s. The fish was unmodified with its scales and skeleton still attached. The force-displacement curves and failure mechanisms were highly repeatable for both the piranha and pacu teeth.

Embedding, grinding, and polishing

Anterior mandibular teeth were extracted and embedded in Epo-Tek 301 epoxy and allowed to polymerize overnight at 25 °C. Samples were then ground and polished in either the

transverse or longitudinal orientation. The surface was ground using subsequently finer grits of Buehler SiC grinding paper (320, 600, 800, & 1200 grit). Ground samples were polished using 3 μm and 1.0 μm polycrystalline aqueous diamond polishing suspensions on a Buehler Trident polishing cloth. Samples were rinsed with water and dried under flowing argon gas.

Acid etching

Freshly polished, epoxy-embedded samples were etched for 1 minute at 25 °C in 30% HCl. Acid etching was used to reveal microstructural patterns in the enameloid and dentin. Upon grinding and polishing mineral can fill the voids in the dentine tubules and obscure microstructural details.

Scanning electron microscopy

For SEM imaging, samples were sputter coated with iridium at 85 μA for 8 seconds at a deposition pressure of 10^{-2} Pa of Ar gas to reduce charging using a sputter coater (Emitech K575X, Quorum Technologies Ltd, East Sussex, UK). Micrographs were collected using FEI Quanta 250 operating at 5 kV with a spot size of 3 in high vacuum mode.

Energy dispersive spectroscopy and X-ray mapping (EDS)

Polished and sputter coated samples (not acid-etched) were used to collect standardless quantitative elemental analysis using the FEI Quanta 250 with the Pathfinder X-ray microanalysis software (Thermo Fisher Scientific) and a Thermo Scientific™ UltraDry EDS Detector Model: INTX-10P-A . An operating voltage of 30 kV with a spot size of 5 was used. X-ray maps were collected at 512 x 512 pixel with an acquisition time of 50 seconds.

Micro-computed X-ray tomography

Four anterior mandibular teeth (two pacu and two piranha) and six additional teeth (three piranha and three pacu in anatomical order embedded in the jaw bone from the most anterior) were

imaged (Xradia 510 Versa, ZEISS, Jena, Germany) with a voxel size of ranging from 4.129—9.579 μm (depending on tooth size) and an accelerating voltage of 80 kV. The images were processed using Amira® software (FEI, Oregon, USA).

Nanoindentation

High-resolution nanoindentation was performed to ascertain the regional hardness and modulus of both anterior teeth. Nanoindentation experiments were conducted using a TI-950 TriboIndentor (Hysitron, USA) with a low-load transducer. Samples were tested using a diamond cube corner probe. All maps featured an array of indents with a spacing of 10 μm in the horizontal and vertical directions. Indents were controlled in displacement between 200 nm and 500 nm. Partial unload tests were first conducted in each sample to determine the appropriate minimum depth to overcome surface roughness. A trapezoidal load function consisting of a 5 s load, 2 s hold, and 5 s unload was used for all mapping experiments. Indents were performed on both longitudinal and transverse cross sections of polished sections. The analysis plane was chosen such that the midplane of the tooth was exposed and the enameloid, DEJ, and dentin could be mapped. As a consequence of indenting on the midplane, only the longitudinal section allowed for indention of the cuticle layer as the cuticle layer decreases in thickness away from the tip of the tooth.

Modeling

Individual teeth from both pacu and piranha were isolated and subjected to micro-computed x-ray tomography to obtain 3D meshes. The image slices obtained from x-ray microscopy were rendered and segmented using the threshold tool in Amira® software (FEI, Oregon, USA) and outputted as STL files. These files were then used in Meshmixer (Autodesk) to simplify and reduce cracks and holes in the mesh. The mesh was then finalized in Autodesk fusion 360 and converted into a .SAT file that could be readily inputted into Abaqus.

Computational simulations on the most anterior teeth of the piranha and pacu were performed using finite element software Abaqus (v.6.14). The models were separated into two mechanically distinct parts (dentine and enameloid). Dentin and enamel phases were modeled as linear elastic materials with different values of modulus obtained directly from the nanoindentation experiments: i) the enameloid with two elastic moduli (80 GPa for the piranha and 75 GPa for the pacu), and ii) the dentin with two elastic moduli (23 GPa for the piranha and 22 GPa for the pacu). The Poisson's ratio for both layers was assumed to be 0.3. All nodes in the bottom surface of the piranha tooth were fixed in all directions, while all nodes on the exposed lingual surface of the pacu tooth were fixed in all directions. A uniaxial pressure was applied to the surface of the tip of each tooth that corresponds to a 15 N load. The model was fully meshed using C3D10 elements (10-node quadratic tetrahedron elements) and a mesh convergence study was carried out. Nonlinear effects were excluded. The interface between the enamel and dentin was assumed to be perfectly bonded.

The bioinspired structures were subjected to a similar protocol. The prototypes were drawn using Autodesk Fusion 360 allowing for them to be directly imported into Abaqus. The models were separated into two mechanically distinct parts (Veroclear and Flex). The phases were modeled as linear elastic materials. All nodes in the bottom surface of each prototype were fixed in all directions. A uniaxial pressure was applied on the top surface to compress the prototypes. The interface between the two layers was assumed to be perfectly bonded. The model was fully meshed using hexahedral elements and a mesh convergence study was carried out. Nonlinear effects were excluded.

Mechanical testing of bioinspired prototypes

The bioinspired prototypes with differing interfaces (flat vs interdigitating) were designed in Autodesk Fusion 360 and printed using the Objet360 Connex3 (Stratasys, Poway, CA USA) with UV-cured material Veroclear (representing the enameloid) and Flex (representing the dentin). After printing, the support material was physically removed. The prototypes were designed as cubes with a side length of 20 mm. Both prototypes have equal masses as material composition was preserved.

Quasi-static compression tests were performed using a mechanical testing machine, Instron 3367 load frame (Instron, High Wycombe, United Kingdom). Three samples of each prototype were tested (flat interface vs triangular suture interface). A load was applied with a constant speed of 0.20 mm/s. The force-displacement curves and failure mechanisms were highly repeatable and consistent for all samples.

5.11 Acknowledgements

Chapter 5, in part, is in preparation for publication authored by A. Velasco-Hogan, W. Huang, C. Serrano, D. Kisailus, and M. A. Meyers. The dissertation author is the primary investigator and first author of this work.

This work was performed in part at the San Diego Nanotechnology Infrastructure (SDNI) of UCSD, a member of the National Nanotechnology Coordinated Infrastructure (NNCI), which is supported by the National Science Foundation (Grant ECCS-1542148). M.A.M. thanks Air Force Office of Research for support under the MURI Program (AFOSR Grant No. FA9550-15-0009). A.V.H. and C.S. thank UCSD for support under the Chancellor's Interdisciplinary Collaboratories funding. We thank Eric Bushong for his expertise with x-ray microscopy.

The measurements on piranha were accomplished during the Roosevelt-Rondon Centennial Expedition, from 2014 to 2016. The participation of the New York Explorers Club by giving it an official Flag Expedition status, is warmly appreciated, as are the efforts of Colonels Hiram Reis de Silva and Ivan Carlos Angonese of the Brazilian Army. Drs. Julie and Tim Radke of the San Diego Explorers Club participated in the Paraguay River journey and their contribution was essential. The Brazilian Army provided logistic support which enabled the expedition.

The authors thank the generosity of Prof. Michael Tolley and Ben Shih for assistance and allowing us to use their 3D printer which made much of this work viable. We thank Isaac Cabrera for his helpful discussions and insight on numerical modeling. We thank Dr. Steve Naleway for his initial interest in the investigation of the jaws of the piranha and pacu and for his guidance in discussions. We thank Prof. Joanna McKittrick for all of her contributions and inspiration to the field of structural biological materials.

Chapter 6: Reinforced Tubule Architectures and Bioinspired Design

6.1 Introduction and significance

A striking similarity among many energy absorbent natural materials is the reoccurring design of the tubule structure.[96] Typically found on the microscale, the tubule structure can be described as a semi-periodic porous array where the longitudinal axis of neighboring hollow cylinders are aligned along a similar direction. It is a predominant structure found in both mineralized and non-mineralized biological materials that are known to withstand impact loading such as horns, hooves, exoskeletons, bones, and teeth. While the tubule structure is similarly found on the microscale, it greatly differs within these biological materials by way of the following: orientation with respect to the loading direction, cross-sectional geometry (circular to ellipsoidal), size, volume fraction, and presence of a reinforcing layer surrounding the tubule. Additionally, the tubule structure can be distributed as a gradient with respect to size, shape, and porosity.

Equine hooves and bighorn sheep horns are preferential candidates for exploring the differences in tubule structure and respective mechanical properties, which play a considerable role in energy absorption and impact resistance, due to their similar material composition and hierarchical structures. In both systems, tubule medullary cavities are found within an intertubular matrix which is composed of lamellar stacked keratin cells.[240,241] However, the hoof has a more complicated arrangement of keratin cells. Orientation of the lamella, due to change in shape of the keratin cells, changes from the inner tubule to the matrix. [61] Additionally, there is a higher concentration density of keratinocytes surrounding the medullary cavity which acts as a stiff reinforcing layer in the hoof which is absent in the bighorn sheep horn.[102]

For both systems, tubules are aligned longitudinally in the direction of tissue growth (proximal to distal) as shown in Figure 6.1. Due to their differences in position on the body,

function, and shape, the tubules experience contrasting loading conditions. The tubules in the hoof wall experience loading at an offset angle from parallel with respect to its longitudinal axis while the tubules in the bighorn sheep horn experience loading perpendicular to its longitudinal axis (Figure 6.1).[242] The hoof wall when in static contact with the ground creates a ~ 47° contact angle (Figure 6.1 B). Upon striking the ground, the surface of the hoof makes contact with the ground at various angles depending on the gait. This results in complex loading conditions where tubules are compressed at a range of angles offset to the longitudinal axis. The bighorn sheep horn is more simple. Due to its head-on combat and curvature of its horns the tubules generally experience loading perpendicular to its major axis.

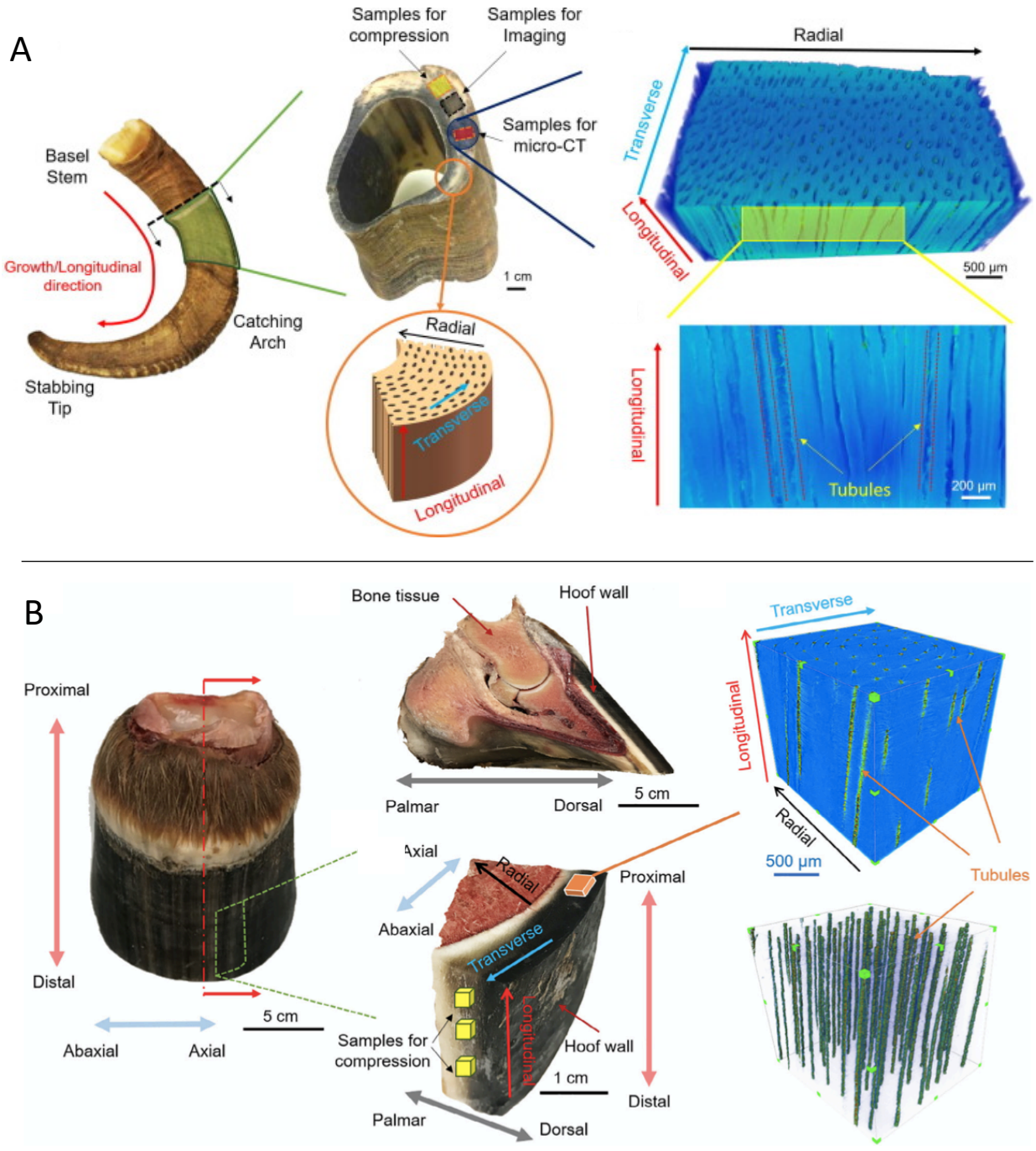

Figure 6.1 Structure and orientation of tubules in the bighorn sheep horn and the equine hoof wall. A) Hierarchical structure of the bighorn sheep displaying orientation of tubules. B) Orientation of tubules in the equine hoof wall.

In bighorn sheep horn, the tubules are elliptical in shape where the major axis is ~100-80 um and the minor axis is ~ 40 um which has been shown to influence macroscopic anisotropic behavior in all three directions (longitudinal, radial, and transverse) [243,244]. In the hoof wall, the cross section changes from circular (~37—44 um from internal to external) to elliptical towards the surface (major axis ~62 um and minor axis ~31 um).[241] The equine hoof wall shows macroscopic isotropic behavior [102]. While they are on the same order of magnitude, the bighorn sheep horn tubules are larger which corresponds with it having a greater porosity. For both systems the degree of hydration influences stiffness and hardness [90,102]. As hydration increases stiffness and hardness decrease. Nanoindentation testing on the hoof wall showed the intertubular matrix to have an elastic modulus of 7 GPa for dry, 5.4 GPa for fresh, and 0.12 for hydrated while the reinforced tubular area has an elastic modulus of 8 GPa for dry, 6.3 GPa for fresh, and 0.9 for hydrated [102]. There is currently no recorded nanoindentation data for bighorn sheep horn. It is important to note that not all sheep horns have tubules. No tubules were found in mountain goat horns and this is believed to relate to its fighting style which relies more on piercing. This suggests that tubules provide tailored mechanical properties for specific biological functions. The structure and properties of the tubules found in the equine hoof wall and the bighorn sheep horn are summarized in Table 6.1.

Table 6.1 Comparison between tubule structure and properties in the equine hoof wall and the bighorn sheep horn.

Tubule Structural Design	Equine Hoof	Bighorn Sheep Horn
Percent area of a single medullary cavity	3% [241]	7% [240]
Gradient in porosity	Decreases from external to internal (~6% to 0.6%)[241]	Decreases from external to internal (~12-8% to 0%)[240]
Geometry	Gradient from circular to elliptical from internal to external	Elliptical
Size	Circular ~50 um	major axis (100-80 um) minor axis (40 um)
Degree of reinforcement	~30% reinforced tubular ~70% medullary cavity	0% reinforced tubular 100% medullary cavity
Loading direction	Angle offset from parallel to longitudinal axis	Perpendicular to longitudinal axis
Local stiffness from nanoindentation (GPa	Dry: ~8.0 tubular, ~7.0 matrix Fresh: ~6.3 tubular, ~5.4 matrix Hydrated: ~0.34 tubular, ~0.38 matrix	--

Despite the comprehensible work done to characterize the structural characteristics and mechanical influence of the tubule structure in horns and hooves there lacks a systemic investigation into how tubule porosity, geometry, presence of reinforcing layer, and loading orientation influence deformation mechanics and stress distribution. Herein, we use finite element analysis to perform a systemic study on the geometrical effects of the tubule structure.

6.2 Effects of Porosity

When examining the diverse range of biological materials that utilize the tubule structure it is noticed that there is large range of porosity. The sheep crab exoskeleton is ~3% porous while human dentin is ~12% porous [96,97]. Here the effects of porosity are investigated on stiffness, strength, fracture toughness, and viscoelastic properties related to energy dissipation and dampening.

In quasi-static compression stiffness and ultimate compressive strength both decrease as porosity increases (Figure 6.2). In this study the radius of the tubule remains constant and the number of tubules is increased to increase porosity. When tested in different orientations (loading parallel to the main axis of tubules vs perpendicular), it was discovered that parallel is both stiffer and strong. This is due to changes in moment of inertia due to the anisotropy of the tubules. Loading parallel there is a greater moment of inertia that needs to be overcome to cause buckling in the tubules. The experimental stiffness of the two directions are compared to theoretical models for mixing using the Voigt and Reuss models. The theoretical stiffness is significantly higher than the experimental stiffness, which can be attributed to defects due to printing and effects of the microstructure the comes with layered deposition of material.

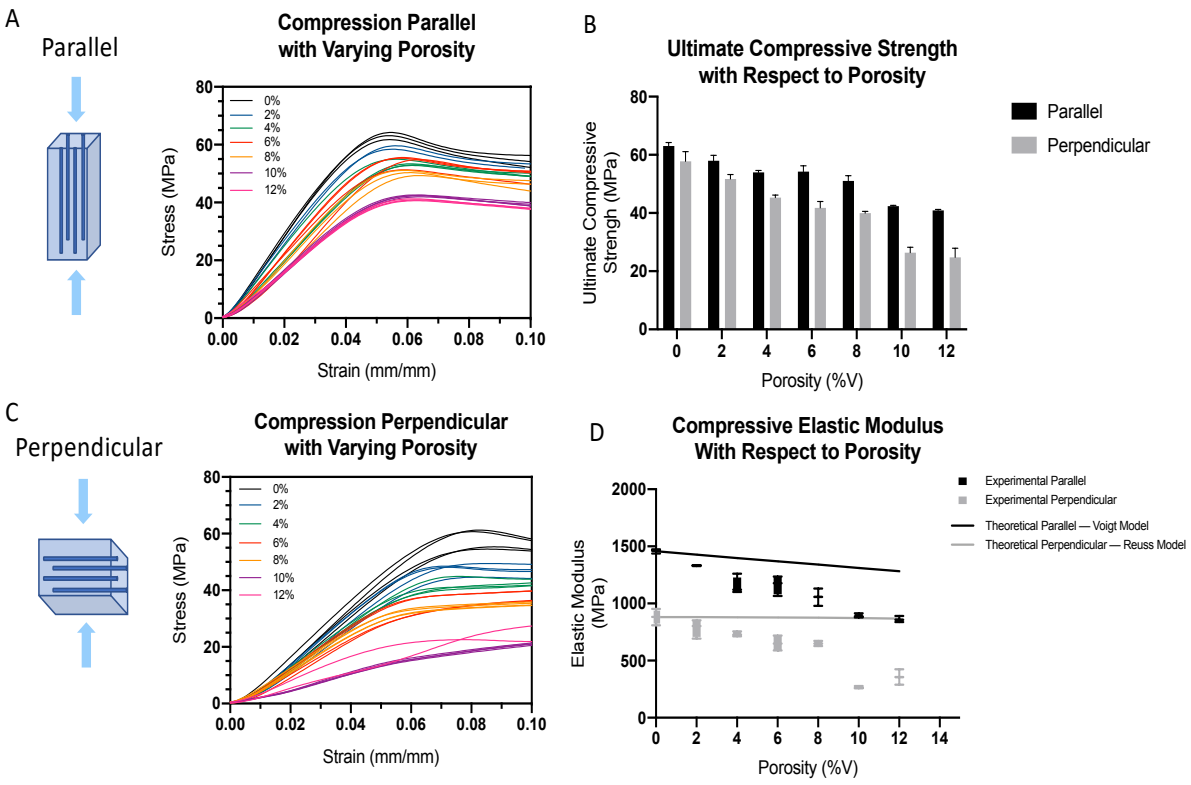

Figure 6.2 Effects of porosity in quasi-static compression. A) Quasi-static compression stress-strain curves parallel to the main axis of the tubules. B) Ultimate compressive strength with respect to porosity in both the parallel and perpendicular loading directions. C) Quasi-static compression stress-strain curves perpendicular to the main axis of the tubules. D) Compressive elastic modulus with respect to porosity in both the parallel and perpendicular loading directions.

Fracture toughness testing using single-edge notched bending specimens bending was used to determine K_{IC} with respect to porosity (Figure 6.3). The brittle behavior of fracture allows for valid determination of K_{IC}. It was found that fracture toughness (K_{IC}) decreases as porosity increases. While this is counterintuitive as the empty spaces of the tubules is perceived to impeded crack growth, this trend may be due to manufacturing and size effects. It is possible with the increase in interfaces between the tubules and the matrix as the number of tubules increases with porosity there may be more defects. These defects may be at the appropriate length scale which may increase the ease of crack propagation. Additionally, as the designs are scaled up for 3D

printing this may cause issues with the tubules being an inappropriate size to interact with the crack favorably.

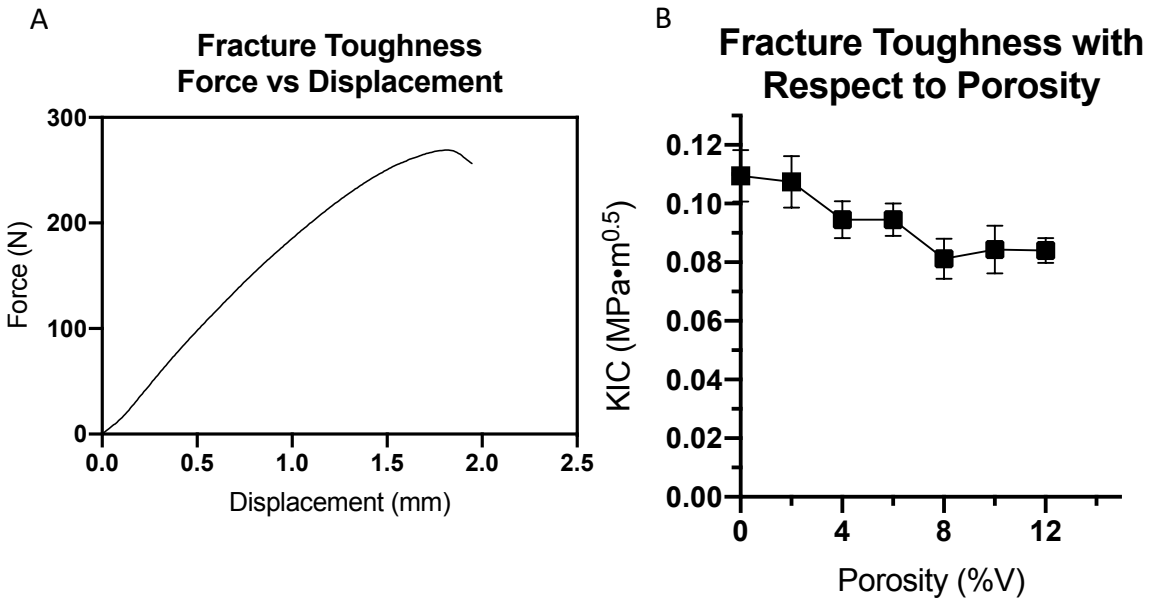

Figure 6.3 Fracture toughness testing of tubule architectures. A) Typical force displacement curve demonstrating brittle behavior. B) Fracture toughness with respect to porosity. As porosity increases, fracture toughness decreases.

Digital image correlation used to map the strains and displacements of the bending specimens. As porosity increases the displacements and strains increase, which suggests that the structure become more deformable (Figure 6.4). Deformation under bending can be a useful way to absorb energy which might be a useful purpose of the tubules.

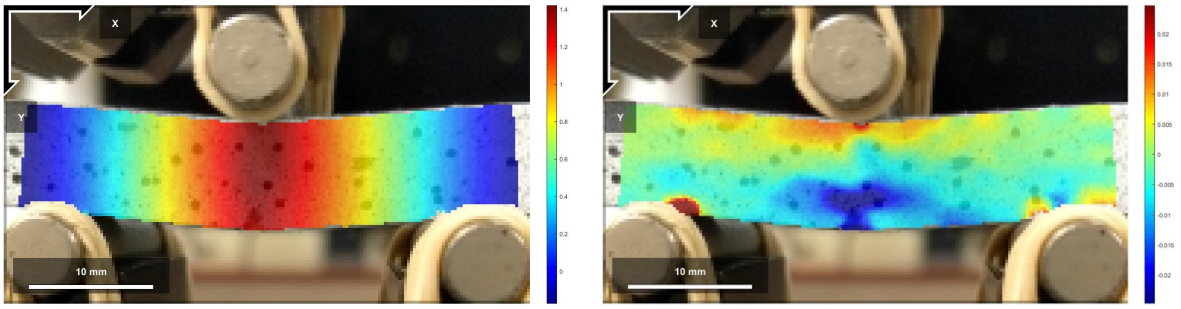

Figure 6.4 Results from digital image correlation mapping displacement (left) and the Eulerian strain (E_{yy}) (right) of a sample with porosity of 2%.

Energy dissipation and dampening properties and the influence of porosity were investigated using dynamic mechanical analysis (DMA) (Figure 6.5). As porosity increases tan delta increases which suggests that dampening ability can be controlled by porosity. As porosity increases the loss modulus increases which suggests that the ability to dissipate energy is dependent on the volume fraction of tubules. The addition of tubules may be used by nature to tailor the dampening ability and energy dissipation.

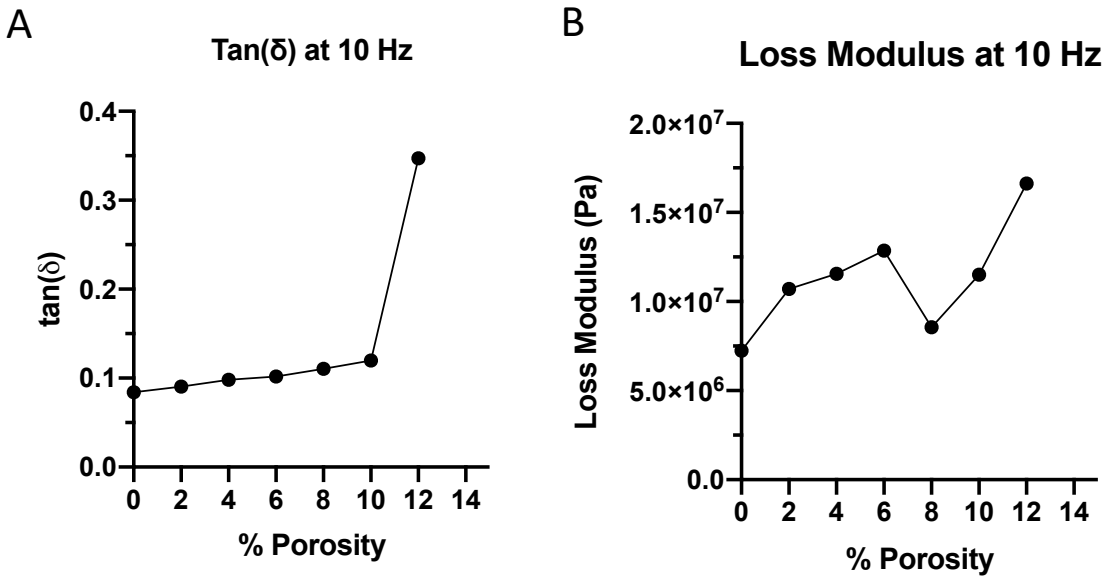

Figure 6.5 Dynamic mechanical analysis of tubule architectures with various degrees of porosity. A) Tan delta as a function of porosity. As porosity increase the dampening ability increases. B) Loss modulus as a function of porosity. As porosity increases the ability to dissipate energy increases.

6.3 Experimental Methods

The bioinspired tubule architectures were designed in Autodesk Fusion 360 and printed using the Objet360 Connex3 (Stratasys, Poway, CA USA) with UV-cured material Veroclear (representing the stiffer phase) and RGD8730 (representing the softer phase). After printing, the support material was physically removed.

Quasi-static compression tests were performed using a mechanical testing machine, Instron 3367 load frame (Instron, High Wycombe, United Kingdom), with a 30 kN load cell. Three samples of each prototype were tested (flat interface vs triangular suture interface). A load was applied with a constant speed to achieve a strain rate of 10^{-2} s^{-1}. The force-displacement curves and failure mechanisms were highly repeatable and consistent for all samples.

6.4 Acknowledgements

Chapter 6, in part, is in preparation for submission authored by A. Velasco-Hogan, C. Chadha, I. Jasiuk, and M. A. Meyers. The dissertation author is the primary investigator and co-first author of this work.

The authors thank the generosity of Prof. Michael Tolley and Ben Shih for assistance and allowing us to use their 3D printer which made much of this work viable. This work is funded by the National Science Foundation Mechanics of Materials and Structures Program with corresponding grant number 1926361.

Chapter 7: Exploration of the Foam Core in the Feather Rachis

7.1 Introduction and Significance

Avian flight feathers have developed, through evolution, an intricate architecture with multi-functional structures that are essential for flight. These lightweight and resilient appendages motivate the invention of bioinspired designs. Here we fabricate various structures inspired by significant concepts identified in the feather. Additive manufacturing is used to develop bioinspired sandwich prototypes based on the feather-shaft. The exquisite architecture of the rachis, consisting of an outer cortex of compact keratin filled with foamy keratin center, is simulated in a bioinspired design that demonstrates the synergy of the two components in enhancing the flexural strength. The prototypes are 3D printed and experimental tested under three-point bending and compared to a numerical model. These structures provide an enhanced understanding of the mechanisms operating in feathers and suggest highly efficient solutions which can contribute to creating innovative materials inspired by the feather.

7.2 Effects of Foam Core

The architecture of the rachis is another source of inspiration. Disregarding the internal structure of organized filaments, bioinspired prototypes were fabricated with the intention of isolating the integral design motif which includes a reinforcing foam-filled center (Figure 6.1). Two rachis-inspired designs were explored: (1) thin-walled-square-cross-section shells without foam-filled core and (2) with a foam-filled core (Figure 6.1b). These architectures were mechanically tested using three-point bending to demonstrate that the presence of foam has an advantaged by increasing the maximum force (F_{max}) and the maximum bending stress (σ_f) despite an increase in weight.

The stiffness (k) was calculated from the force-displacement curve in the elastic regime (Figure 10a).

$$k = \frac{\delta F}{\delta x} \tag{7.1}$$

The stiffness of the foam-filled structures was not significantly different than the hollow shell with $p > 0.05$ (unpaired t-test, $p = 0.265$) (Figure 6.1c**)**. The foam does not contribute to the stiffness, since the stiffness of the shell is much greater than the stiffness of the foam.

While the foam does not influence the stiffness, it does affect the maximum force and the maximum bending stress. The foam-filled core acts as an elastic foundation that resists the buckling of the shell. The maximum bending stress of the hollow shell (σ_f^{hollow}) was calculated using the following:

$$\sigma_f^{hollow} = \frac{My}{I} \tag{7.2}$$

where M is the bending moment ($F_{max}L/4$), y is the vertical distance from the neutral axis, and I is the moment of inertia around the neutral axis. The maximum bending stress of the foam-filled structure was calculated using the following equations derived from Gibson and Ashby [124] for sandwich structure composites:

$$\sigma_f^{foam-filled} = \frac{MyE_f}{(EI)_{eq}} \tag{7.3}$$

where,

$$EI_{eq} = \frac{E_f bt^3}{6} + \frac{E_c bc^3}{12} + \frac{E_f btd^2}{2}, \tag{7.4}$$

and E_f and E_c are the Young's moduli of the face and the core, respectively, b is the width, c is the thickness of the foam, d is the thickness of the sandwich composite, and t is the thickness of the shell (Figure 6.1b).

The maximum force and maximum bending stress are significantly greater for the foam-

filled shell than the hollow shell (Figure 6.1d and e). Even when normalized for the additional weight of the foam, the maximum bending stress for the foam-filled composite is far superior to the hollow shell (Figure 6.1f). This demonstrates that the addition of a foam core increases both the force and the maximum bending stress while maintaining a lightweight structure.

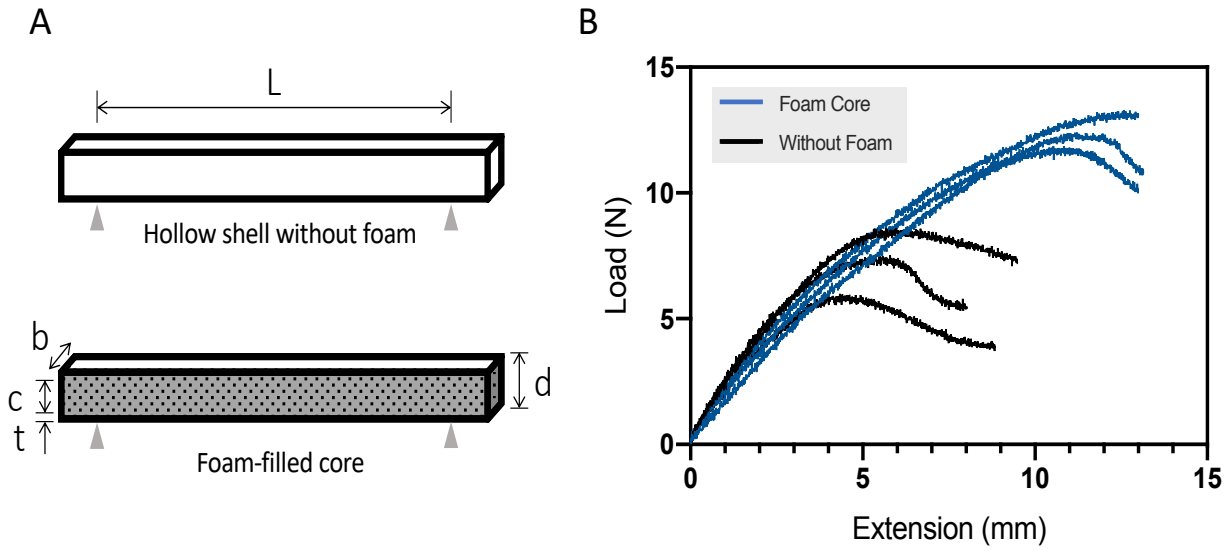

Figure 7.1 Three-point bending of 3D-printed bioinspired rachis design. (A) Schematic of samples tested and respective dimension as described in Table 6.1 Both samples are the same dimension the hollow shell excludes a foam-filled core (above) while the foam-filled core is included which mimics the rachis (below). (B) Force-displacement curve from three-point bending of designs with foam (blue) and without foam (black) for three samples each.

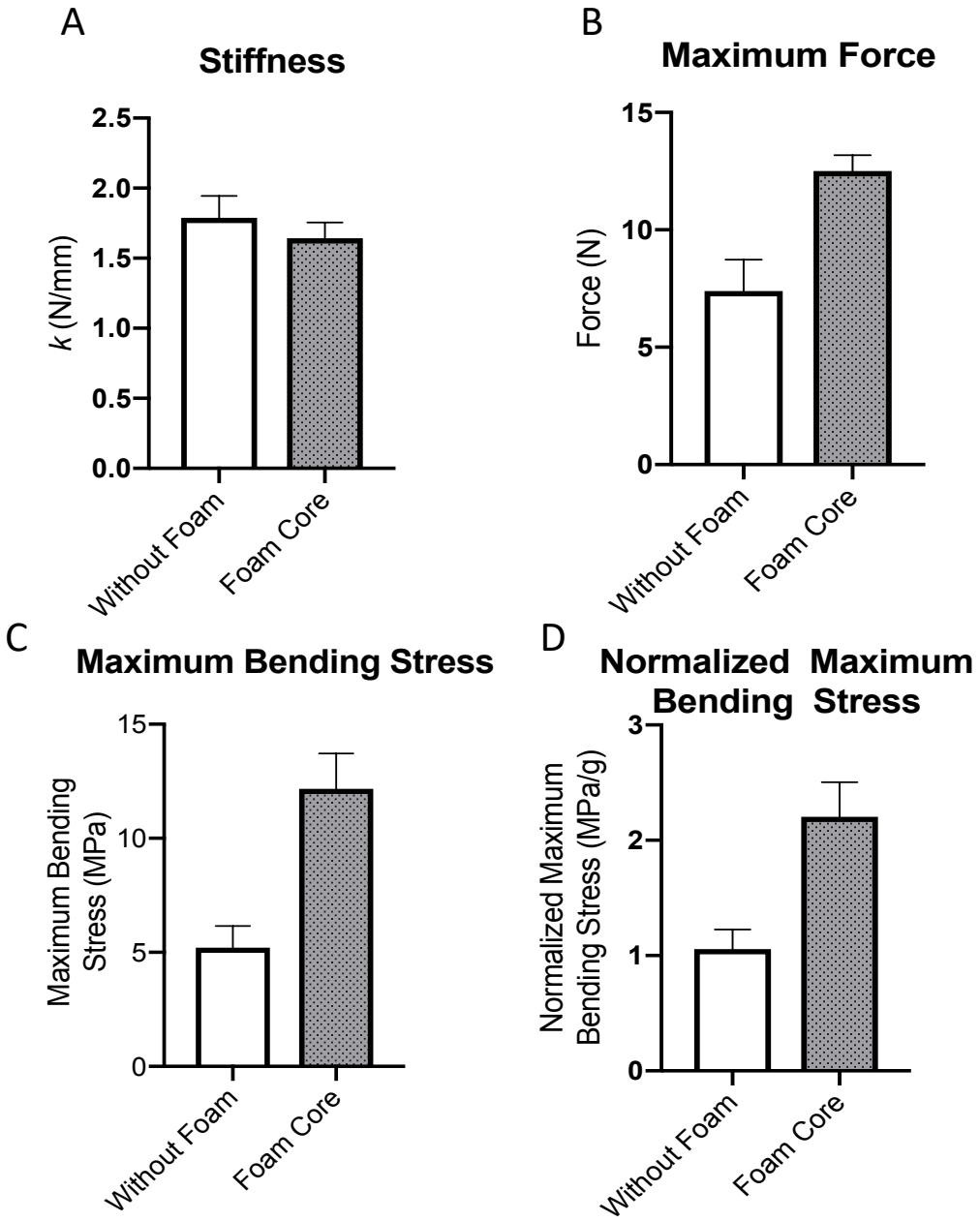

Figure 7.2 Analysis of three-point bending of rachis bioinspired designs with and without a foam-filled core. (A) Stiffness values (mean ± SD) for with foam and without foam. (B) Maximum force (mean ± SD) for with foam and without foam . (C) Maximum bending stress (mean ± SD) with foam and without foam. (D) Normalized Maximum bending stress (mean ± SD) with foam and without foam.

7.3 Finite element analysis

Finite element analysis is used to better understand how the stress is distributed along both sandwich structures (with and without a foam-filled core) under three point-bending loading conditions to compliment the experimental results. For this analysis there were three mechanically distinct regions: (1) The outer shell, (2) the foam-filled core, and (3) aluminum rods to replicate the three-point bending loading conditions as performed experimentally. Each region is modeled as a linear elastic model with different values of Young's modulus obtained from compression tests from prior studies on the the 3D printed and foam material. The outer cortex is represented by RDG8730 (E = 1.5 GPa), the foam-filled center is a high-density polyurethane foam (E = 35 MPa), and the aluminum rods (E = 68.9 GPa). A 3 mm displacement was applied on the middle aluminum pin while the bottom two pins were fixed. The three parts are shown in Figures 3 and 4.

The stress distribution of the sandwich structures under three-point bending are revealed by the finite element model (Figures 6.3 and 6.4). In particular, Figure 6.3 shows a longitudinal cross section of the y-z plane. The maximum stresses are mainly distributed by the outer-shell, while the foam-filled core provides buckling resistance. For the sandwich structure with the foam-filled core, the stresses are concentrated in the outer cortex which leads to a higher stress in this region. The hollow cortex has a lower maximum stress which is primarily due to the increase in deformation and buckling at the center. Figure 6.4 shows a transverse cross-section of the x-y plane which further highlights how the outer cortex carries the stress and the absence of a foam-core allows for increased buckling.

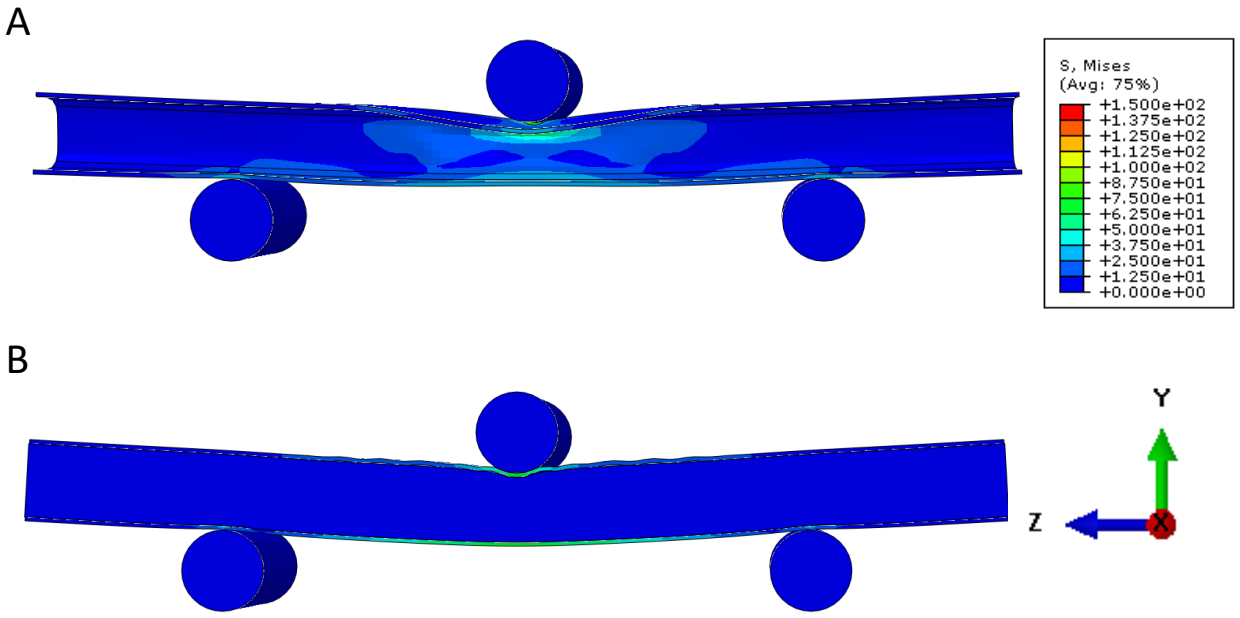

Figure 6.3 Longitudinal cross-section of the three-point bending models. A) Hollow cortex which has greater deformation in the center and higher buckling, but overall a reduction in the maximum Von Mises stress. B) Foam-filled core reduces buckling while the stresses are concentrated in the outer cortex leading to a higher maximum Von Mises stress.

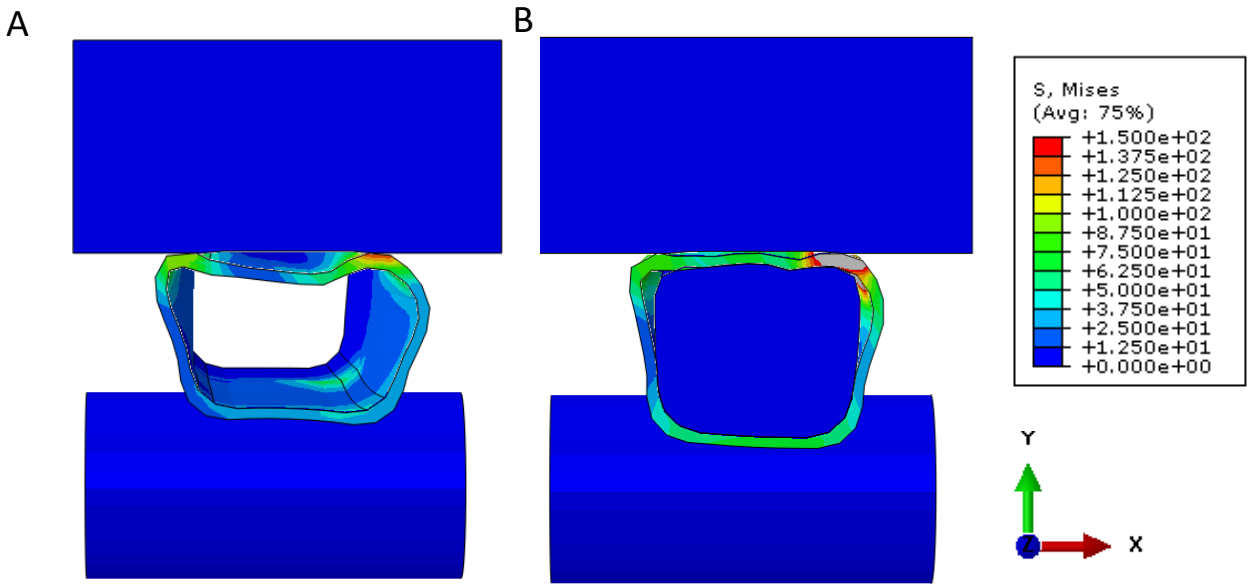

Figure 6.4 Transverse cross-section of the three-point bending models. A) Hollow cortex showing greater buckling and deformation due to the absence of the foam-filled center. B) Foam-filled center provides resistance to buckling while the stress is maintained in the outer cortex.

7.4 Experimental methods

Sample preparation

The hollow shell was prepared in Autodesk Fusion 360. The samples were printed with an Objet360 Connex3 (Stratasys, Poway, CA USA) using UV-cured material RGD8730 (a proprietary blend between Veroclear and TangoBlackPlus). After printing, support material was physically removed. Half of the printed samples were infiltrated with high density polyurethane based foam. The prototypes have dimensions listed in Table 6.1 which correspond to the schematic in Figure 6.1 b.

Table 7.1 Dimensions of the sandwich structure.

Dimension	Dimension variable	Length (mm)
Total length	--	200
Length of span	L	160
Total width of sandwich	b	10
Thickness of foam core	c	9
Thickness of outer shell wall	t	0.5
Total thickness of sandwich	d	10

Mechanical testing

Three-point bending tests were performed using a mechanical testing machine, Instron 3367 load frame (Instron, High Wycombe, United Kingdom), with a 30 kN load cell. Three samples of each prototype were tested (with foam and without foam) with a support span (L) of 160 mm. A load was applied with a constant speed of 4.26 mm/min. The force-displacement curves and failure mechanisms were highly repeatable and consistent for all samples.

Finite element analysis

Three dimensional finite element models were created to observe the stress distribution as experienced by the bioinspired shafts under three-point bending. The models developed in Autodesk Fusion 360 were imported into Abaqus as .SAT files and separated into three mechanically distinct parts (outer shell and foamy center of the sandwich structure and aluminum rods of the three-point bending apparatus). The materials were assumed to be isotropic and behave as linear elastic solids. The Poisson's ratio for the outer shell and foamy center was assumed to be 0.3 and 0.33 respectively. The elastic modulus for RGD8730 and the foam are 1.5 GPa and 35 MPa respectively. For the aluminum rods a Poisson's ratio of 0.32 and an elastic modulus of 68.9 GPa was used. The model was fully meshed with 3D 8-node linear hexahedrals using C3D8R elements. For the non-foam model a global size of 2 mm was used which resulted in the generation of 2000 elements for the hollow shell. The size was chosen as it is significantly small enough as determined by the mesh convergence analysis. Non-linear effects were excluded. The interface between the foam and the shell was assumed to have a frictional penalty of 0.2. A displacement controlled boundary condition (3 mm in the z-direction) was applied to the middle aluminum pin while the lower two rods were fixed as traction-free which induces three-point bending.

7.6 Acknowledgements

Chapter 7, in part, is published in *Materials Science and Engineering C,* authored by T. N. Sullivan, T. Hung, A. Velasco-Hogan, and M. A. Meyers. The dissertation author is the third author on this work.

The authors thank the generosity of Prof. Michael Tolley and Ben Shih for assistance and allowing us to use their 3D printer which made much of this work viable. The authors thank Isaac

Cabrera for his insightful discussions on the feather rachis. We thank the San Diego Zoo (April Gorow, Research Coordinator) and the San Diego Natural History Museum (Phil Unitt, Curator of Birds and Mammals) for providing feather samples to us. This work is supported by the AFOSR MURI (AFSOR-FA9550-15-1-0009). This work was performed in part at the San Diego Nanotechnology Infrastructure (SDNI) of UCSD, a member of the National Nanotechnology Coordinated Infrastructure (NNCI), which is supported by the National Science Foundation (Grant ECCS-1542148).

Chapter 8: Morphological Characterization and Mechanical Properties of Primary Flight Feathers from Various Flying Styles

8.1 Introduction and Significance

Feathers are of great interest due to their lightweight, strong, yet stiff capabilities for flight. The rachis is the major load-bearing component of the feather and as such we are interested in further exploring its structure-property relationship. Specifically, we are interested in the structural and mechanical differences among birds with varying flights styles (non-flying, flapping and bounding, flapping and gliding, flapping and slope soaring, and dynamic soaring). The structural differences include ratio between area of cortex and medulla, geometry of the rachis and its corresponding second area moment of inertia, foam cell size, and density of foam and relate this to mechanical properties (stiffness and strength), DMA, and three-point bending.

The rachis is the primarily load-bearing component of the feather which provides support for the feather vane and branching barbs and barbules which is necessary for flight. It is composed of a thin outer-layer of compact keratin (cortex) and a foamy keratinous inner-layer (medulla). During flight, the feather must withstand bending and torsion under cyclical aerodynamic loads in both the dorsal-ventral and lateral planes. It has been consistently shown that the cross-sectional geometry (diameter and second moment of area (I)) are primarily responsible for its flexibility[113,118,122,245,246].

Furthermore, it has been recently shown that there exists variations in rachis geometry within and between species due to adaptations to loading conditions of various flight requirements (i.e. flight styles) [247]. However, there lacks a rigorous investigation on the structural and mechanical properties of primary flight feathers across various flying styles.

The flying style of birds are typically distinguished into two general groups: (1) low wingbeat frequency which includes flapping and soaring, and flapping and gliding; and (2) high wingbeat frequency which includes continuous flapping, passerine-style flight, and hovering. This categorization was initially proposed by Pennycuick and has since been adapted. [248–251] With an increase in wingbeat frequency there is a penalty in energetic cost. Typically, larger species conserve energy with low-wingbeat frequency flying such as flapping-soaring flight (e.g. pelican, stork), where large wing-areas are used to soar in extended updrafts or thermals. Flapping and gliding is described as a long series of flapping followed by prolonged periods of gliding where the wings are fully extended (e.g. crow, owl). Continuous flapping is described by a sustained wing-beat frequency and is common for waterfowl with high wing-loading (e.g. mallard, geese). Additionally, there exists non-flying birds who are adapted for terrestrial modes of locomotion (e.g. emu). The categorization presented here will provide a framework for this study.

8.2 Structural Characterization of the Rachis

Figure 8.1 shows the cross section of the rachis at 50% of the total length of the feather shaft of birds with various sizes and flying styles. All flying birds exhibit a generalized sandwich structure with a compact cortex surrounding a foamy medullary center. The non-flying bird, the Emu, has a very limited foamy center and is almost entirely cortex and does not exhibit a sandwich structure as the thickness of the cortex is significantly larger than the foam. Despite the large size of the emu, its rachis cross-sectional area is significantly smaller than the flying birds even those who are much smaller in size such as the finches. This suggests the importance of a sandwich structure for flight which allows enhanced bending strength while maintaining lightweight.

Of the flying birds, there are distinct characteristics related to the cross-sectional area, geometry, and ratio of cortex to medulla. The cross-sectional area of the rachis scales with the size of the bird and therefore its relative flying style. Typically smaller birds (Finches, starling, and screech owl) have smaller cross-sectional areas that are more round and have a higher ratio of the cortex than the medulla. Meaning that the smaller birds have less relative amount of foam than the larger birds (Stork, mallard, flamingo, and pelican). This suggests that the density of the rachis is less than the density of smaller birds. The larger birds have a generally more square cross section where the dorsal surface is relatively flat. The larger birds also tend to localize more cortex material on the ventral corners. These trends in cross-sectional area, geometry, and relative distribution of the cortex and medulla can potentially influence the mechanical properties of the rachis.

In addition to the rachis scaling in cross-sectional area with the size of the bird, the cell size of the foam also scales with size. For a rachis with a larger cross-sectional area the length of the cellular foam increases which has an influence on the density and therefore modulus of the foam. The relative density of the foam can be calculated from the following:

$$\frac{\rho^*}{\rho_s} = \frac{2}{\sqrt{3}}\frac{t_f}{l}\left\{1 + \frac{\sqrt{3}}{2A_r}\right\} \tag{8.1}$$

Where the relative density(ρ^*/ρ_s) is the density of the foam (ρ^*) with respect to the density of the solid material (ρ_s), t_f is the thickness of the foam cell wall, l, is the length of the foam cell edge, and A_r is the aspect ratio of the foam cell (h/l). The relative density can be used to determine the modulus assuming that the foam is categorized as a closed-cell foam and the internal gas pressure is negligible as follows:

$$\frac{E^*}{E_s} \approx \phi^2 \left(\frac{\rho^*}{\rho_s}\right)^2 + (1-\phi)\,\frac{\rho^*}{\rho_s} \tag{8.2}$$

Where ϕ is the volume fraction of the cell located in the edges.

$$\phi = \frac{t_e^2}{t_e^2 + \frac{Z_f}{\bar{n}} t_f l} \tag{8.3}$$

Where t_e is the thickness of the foam cell edge at the corner and Z_f is the number of faces that meet at the edge on a single cell.

Not only do larger feathers have a higher ratio of foamy center, the foamy center is also less dense as the foam cell scales with the size of the feather. This additionally contributes to the lightweightness of larger feathers which helps to conserve energy with the demands of having a larger mass. Figure 8.2 shows the relative densities of the medulla with respect to wing loading. Wing loading is defined as the total mass of the bird divided by the wing area. Wing loading can describe the pressure the wing must overcome to maintain steady flight. Additionally, there is a relationship between wing loading and flying style. Typically larger wing loading is predictive of slower flying while high wing loading is predictive of faster flying.

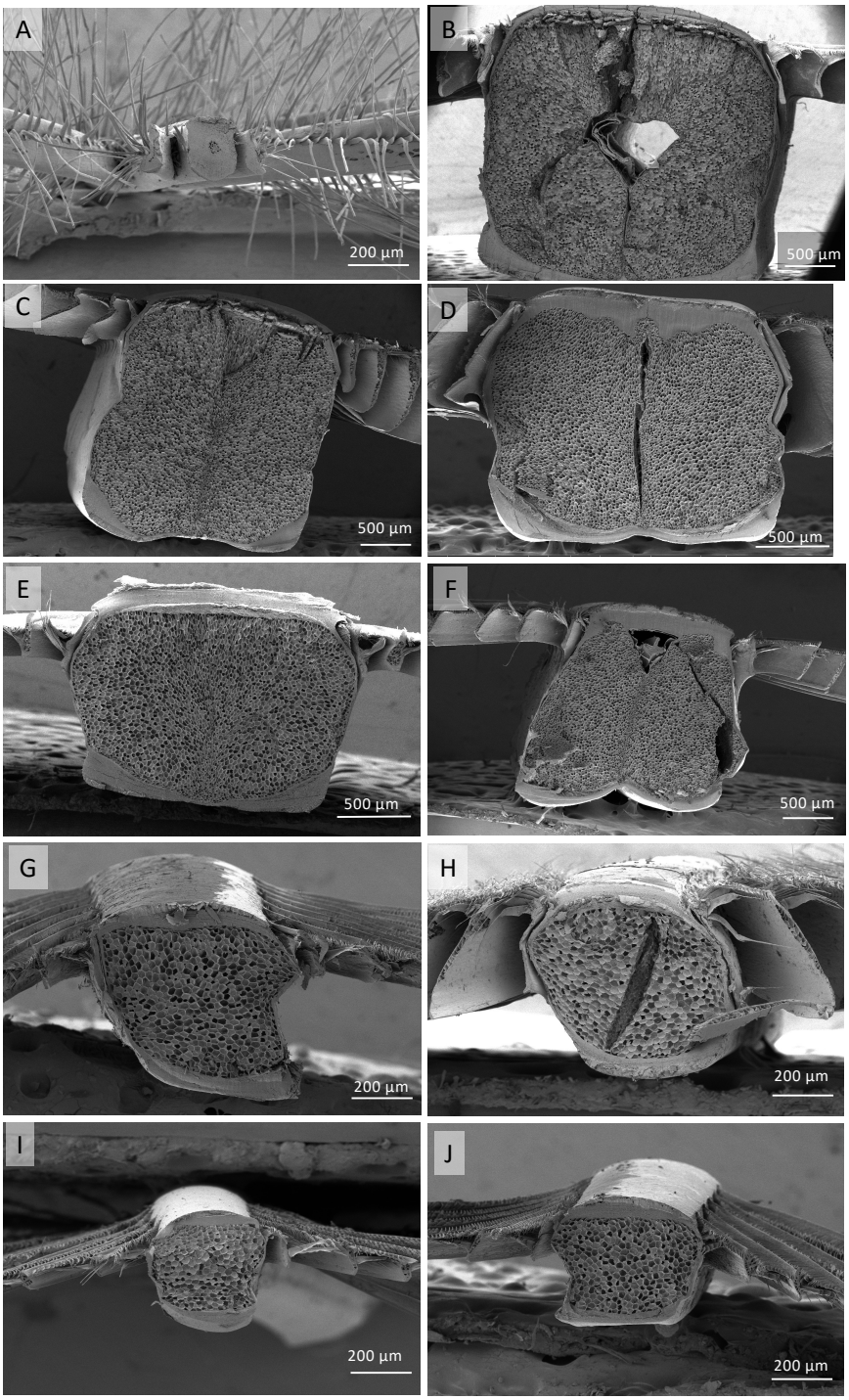

Figure 8.1 SEM images of the rachis cross section at 50% of the length of the total feather shaft. A) Emu. B) Stork. C) Pelican. D) Mallard. E) Flamingo. F) Crow. G) Starling. H) Screech Owl. I) Gouldian Finch. J) Double-barreled Finch.

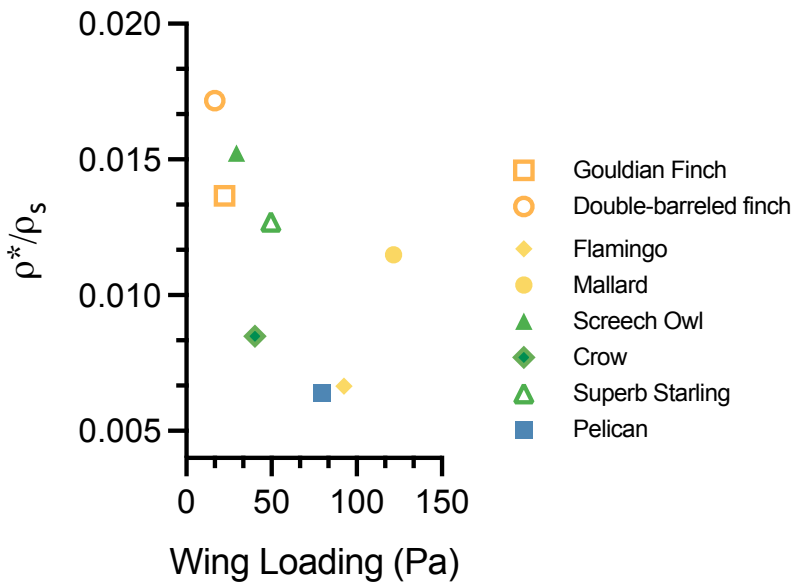

Figure 8.2 The relative density of the medulla with respect to wing loading.

8.3 Viscoelastic Properties of the Rachis

Figure 8.3 shows the storage moduli, loss moduli, and tangent delta (equivalent to the ratio of loss and storage moduli) of the rachis of various avian species. The tangent delta parameter represent the dampening coefficient of the beta-keratinous materials. The storage and loss moduli and tangent delta are not influenced by the frequency ranged explored here (0.1 to 20 Hz) which encapsulates the range of wingbeat frequency seen in nature. The Emu has both the highest storage and loss moduli at 3.4 GPa and 0.23 GPa respectively. This is primarily attributed to the dominating effects of the cortex with minimal foam present. The stork, which is the largest feather studied here, has the lowest storage and loss moduli at 0.19 GPa and 9.9 MPa respectively. The low storage and loss moduli of the stork are due to its low density as the foamy medullary center is the predominate constituent.

Despite differences in storage and loss moduli among birds with various sizes, tan(delta) remains relatively constant in the range of 0.04 to 0.08 (Figure 8.3C). Tan(delta) is defined as the

ratio between the loss moduli and the storage moduli and thus equivalent changes in both would lead to a constant value. This is further understood as all birds being composed of β-keratin have fundamentally similar material properties.

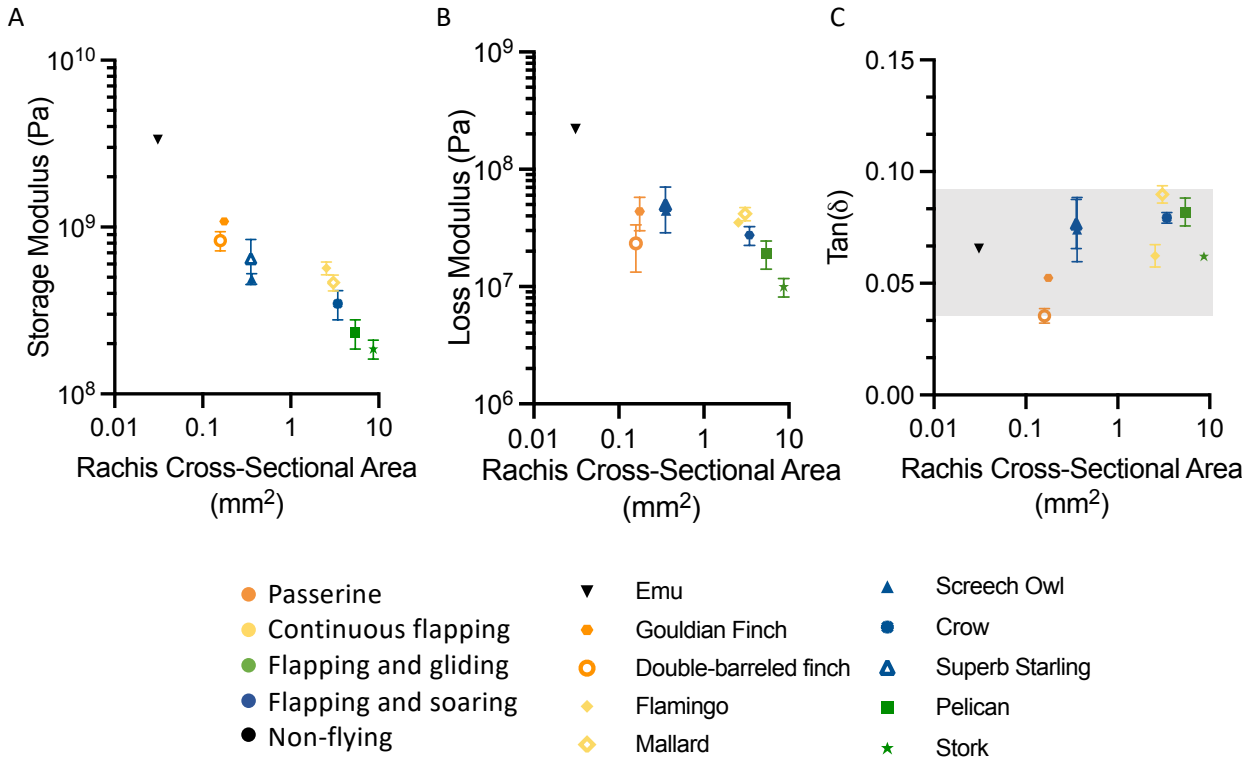

Figure 8.3 Viscoelastic properties of the rachis. A) Storage modulus. The storage modulus decreases as the feather increases in size. B) Loss modulus. The loss modulus similarly decreases as the feather increases in size. C) Tan(delta). The dampening factor is in a consistent range due to the fundamental properties of β-keratin.

8.4 Conclusions

In this present investigation, different structural and mechanical properties of the feather rachis of avian birds with various sizes and flying styles are explored. All avian feathers being composed of beta-keratin have similar fundamental structures (general sandwich structure) and

material properties (density), but slight differences in composition and geometry allow for variation in viscoelasticity (storage and loss modulus). The major findings are summarized below:

- The medullar foam density scales inversely with the size of the feather and thus the size of the bird. Larger birds have a less dense foamy center.
- The viscoelastic properties of the feather rachis are related to their densities. The more dense the higher the storage and loss moduli.
- Tan(delta) is conserved across feathers (~0.05-0.10) due to inherent properties of β-keratin.

8.5 Experimental Methods

Specimens

All feather samples used in experiments were primary flight feathers obtained postmortem and stored in ambient conditions. The San Diego Zoo provided all feathers. Sections of the rachis were sliced with a razor and measured using calipers to ensure similar dimensions between species. For DMA the feather samples were used as is. For the four-point bending tests the ends of each feather shaft section were fixed in the center of a 5 mm aluminum tube with epoxy. Each completed sample had 18 mm of exposed rachis between the blocks.

Scanning electron microscopy

For SEM imaging, samples were sputter coated with iridium at 85 μA for 8 seconds at a deposition pressure of 10^{-2} Pa of Ar gas to reduce charging using a sputter coater (Emitech K575X, Quorum Technologies Ltd, East Sussex, UK). Micrographs were collected using FEI Quanta 250 operating at 5 kV with a spot size of 3 in high vacuum mode.

Dynamic mechanical analysis (DMA)

The dynamic mechanical behavior of the feather rachis was analyzed using a DMA 800 Dynamic Mechanical Analyzer (Perkin Elmer). The specimens were clamped in the cantilever setting with the proximal end fixed and the distal end subjected to displacement which mimics the natural loading conditions of the feather shaft. The specimens underwent an oscillated test within the elastic region with a displacement of 0.05 mm with a linear increasing frequency of 0.1 to 20 Hz while at room temperature. This frequency range was chosen as it captures the range of wingbeat frequencies achieved in natural flying conditions. Regression data analysis from Graphpad prism was used to test the significance of the slopes of the storage modulus, loss modulus, and tan(delta) with respect to frequency. With a 95% confidence interval all birds where shown to have a not-significant deviation from a zero slope. This suggests that frequency does not influence the dynamic moduli at the range tested. This allows us to compare the averages across frequencies for various bird species.

Flexure tests on the feather rachis

Rachis samples taken at 50% of the length of the total feather shaft were tested in four-point bending to mitigate the effects of the naturally curved shaft and to prevent local stresses due to crushing that would be expected in a three-point bending setup. This method is adapted from Corning and Biewener[245] and Sullivan et al.[252] Feather samples were tested with their dorsal side facing upwards which mimics the main loading orientation of the feather shaft during flight. Steel rollers were placed on the top and bottom fixtures in conctact with the inner and outer most locations of the aluminum blocks. A rate of displacement of 0.01 mm/s was applied using an Instron Universal Testing Machine model 3347 (Instron Corporation, Norwood, MA, USA).

Mechanical testing of bioinspired prototypes

The bioinspired prototypes with differing interfaces (flat vs interdigitating) were designed in Autodesk Fusion 360 and printed using the Objet360 Connex3 (Stratasys, Poway, CA USA) with UV-cured material Veroclear (representing the enameloid) and Flex (representing the dentin). After printing, the support material was physically removed. The prototypes were designed as cubes with a side length of 20 mm. Both prototypes have equal masses as material composition was preserved.

Quasi-static compression tests were performed using a mechanical testing machine, Instron 3367 load frame (Instron, High Wycombe, United Kingdom). Three samples of each prototype were tested (flat interface vs triangular suture interface). A load was applied with a constant speed of 0.20 mm/s. The force-displacement curves and failure mechanisms were highly repeatable and consistent for all samples.

8.6 Acknowledgements

Chapter 8 is under preparation for submission authored by A. Velasco-Hogan, and M. A. Meyers. The dissertation author is the third author on this work.

The authors thank the generosity of Prof. Michael Tolley and Ben Shih for assistance and allowing us to use their 3D printer which made much of this work viable. The authors thank Isaac Cabrera for his insightful discussions on the feather rachis. We thank the San Diego Zoo (April Gorow, Research Coordinator) for providing feather samples to us. This work is supported by the AFOSR MURI (AFSOR-FA9550-15-1-0009). This work was performed in part at the San Diego Nanotechnology Infrastructure (SDNI) of UCSD, a member of the National Nanotechnology

Coordinated Infrastructure (NNCI), which is supported by the National Science Foundation (Grant ECCS-1542148).

Chapter 9: Summary and Conclusions

This project has been dedicated to unearthing the riches that nature has surreptitiously employed to not only better understand their success, but to also use these strategies to develop superior synthetic analogs. Our preliminary findings on the teeth of the dragonfish, piranha, and pacu; the tubule structure found in hooves and horns; and the rachis of primary flight feathers have demonstrated the success of applying a materials science and engineering approach to biological systems. These combined findings shed light on unexplored biological materials and their structure-property relationships with respect to their relative ecological functions and environment. This work analyzed both mineralized systems (teeth) and non-mineralized systems in the form of keratin (feather) to highlight how structural advantages can be found an applied to materials regardless of bulk material properties. This is predominant in the exploration of the transparent teeth of the deep-sea dragonfish and how their hierarchical structure imparts significant optical performance for camouflage. The comparative study of the piranha and the pacu elucidates how across several length scales micro, meso, and macro there exists significant structural designs tailored for bite performance (crushing vs slicing). Furthermore this work highlights how structure plays an important role in developing impact resistant, tough, stiff, and lightweight materials with the support of additively manufactured bioinspired designs.

9.1 Transparent teeth of the deep-sea dragonfish

The hierarchical structure, composition, and optical properties of the transparent teeth of the deep-sea dragonfish were characterized. We show that the teeth of dragonfish owe their transparency to a nanoscale structure of hydroxyapatite and collagen, which is devoid of

microscale features such as dentin tubules; they are also sufficiently thin (~60 μm) to reduce Rayleigh scattering.

To summarize the conclusions of this study:

- The teeth are hollow with the inner diameter decreasing towards to the tip.
- Longitudinal striations on the concave surface of the tooth are found and hypothesized to decrease frictional resistance upon puncturing soft materials.
- There is a gradient in mineralization which increases toward the tip as visualized by μ-CT.
- The enamel-like layer is highly mineralized, consisting of amorphous/nanocrystalline hydroxyapatite (~ 20 nm grain size)
- The dentin consists of an array of interpenetrating nanorods (~ 5 nm diameter) of hydroxyapatite embedded within a collagen matrix
- Transparency is an adaptation to thriving in the aphotic zone, where biological light (bioluminescence) drives the predator-prey interactions.
- The transmittance of the teeth in sea water ranges from ~38% to ~73% and depends on tooth location (tip, middle, base) and the wavelength of light.
- Transmittance is greatest at the tip due to it being thinner and solid (not hollow). There are less interfaces for light to scatter at.
- Transmittance is greatest with respect to red light and least with respect to blue light. This agrees with Rayleigh scattering which suggests scattering is inversely proportional to the fourth power of wavelength.
- The mechanical properties of the enamel-like layer are similar to those of the piranha and the great white shark, despite vast differences in size, morphology, and habitat.

- The dentin, comparatively, is much harder and stiffer with a higher degree of mineralization and a lack of tubules.
- The absence of tubules in the dentin layer of the deep-sea dragonfish promotes transparency at the cost of being more brittle.

9.2 Bite Force Mechanics and Allometry of Piranha (Serrasalmidae)

The impressive biting capabilities of the piranha have sparked considerable investigation into *in-vivo* and calculated anterior bite forces which have extensively shown a positive allometric relationship. Here, we contribute to the growing literature by providing a mechanics based understanding of this allometric relationship. We propose that $F_{output}\ \alpha\ l^2$ which is derived from a third-order lever approximation, This allometric scaling is in agreement with our *in-vivo* and calculated lever approach which includes data from Huby et al.[177] on *Pygocentrus nattereri.*

To summarize the conclusions of this study:

- A third-order lever approach is a good approximation for the mandibular system in piranhas
- Both calculated and *in-vivo* bite forces of the piranha show an allometric scaling of $F_{output}\ \alpha\ l^2$
- This allometric scaling is attributed to the dependence of the force on the area of mandibular muscle.
- Assuming the jaw length and muscles scale isometrically with the fish, and that the muscle stress is constant the bite force will scale with the length of the fish squared.
- Our findings agree with other *in-vivo* and calculated studies on the bite force of piranhas.

9.3 Relationship Between Tooth Structure and Feeding Mechanics of Piranha and Pacu (Serrasalmidae)

Dentition is a great indicator of diet and often only the macro-scale and general morphological features such as tooth shape and enamel thickness is studied. This leaves the meso and microstructural features typically unexplored. We expand our understanding of diet specialization in the Serrasalmidae family by investigating the influence of elemental composition and hierarchical structure on the local mechanical properties, stress distribution, and deformation mechanics of teeth from piranha (*Pygocentrus nattereri*) and pacu (*Colossoma macropomum*). Microscopic and spectroscopic analyses combined with nanoindentation and finite element simulations are used to probe the hierarchical features to uncover the structure-property relationships in piranha and pacu teeth. We show that the pacu teeth support a durophagous diet through its broad cusped-shaped teeth, thicker-irregular enameloid, interlocking interface of the dentin-enameloid junction, and increased hardness of the cuticle layer due to the larger concentrations of iron present. Comparatively, the piranha teeth are well suited for piercing due to its conical-shaped tooth

To summarize the conclusions of this study:

- The piranha is capable of expending greater bite forces than the pacu due to its larger mandibular muscles.
- However, the pacu tooth is more optimally structured to withstand compressive forces than the piranha.
- Both species show allometric scaling of theoretical bite force with respect to fish length.
- Both teeth have conserved meso- and microstructures which include enameloid and dentin.

- The enameloid layer in both teeth can be distinguished into two sublayers: (1) Outer enameloid (parallel organization of mineralized rods) and (2) Inner enameloid (woven structure of mineralized collagen fibers).
- The pacu has prominent cusps and thicker enameloid to more evenly distribute compressive loads.
- The pacu is embedded in the jaw on its lingual surface which provides more stability during compression.
- The cuticle of the pacu has a larger concentration of iron.
- Iron is found to occur in a gradient in both species which increases outwardly.
- The larger concentration of iron in the pacu leads to a high hardness (5.80 ± 0.23 in the pacu, 4.92 ± 0.57 in the piranha).
- The pacu cuticle also shows resistance to acid etching.
- The piranha has a larger modulus found in the cuticle (104.3 ± 10.8 in the piranha, 78.7 ± 2.35 in the pacu).
- The mechanical properties in both cuticle layers confer to their diets. High hardness is more suitable to wear-resistance and strength needed for a durophagous diet. High modulus is needed to ensure rigidity upon penetration into flesh for a carnivorous diet.
- The suturing of the dentin-enamel junction better distributes the compressive load and delocalizes the maximum stress at the triangular tips which terminate in the enameloid layer.

9.4 Reinforced Tubule Architecture

The tubule architecture is inherent to many impact resistant biological materials such as horns, hooves, exoskeletons, and teeth. However, little has been explored on the influence of porosity, tubule size, and degree of mineralized reinforcing layer on the mechanical properties of these architectures. With use of additive manufacturing, bioinspired prototypes were 3D printed and mechanically studied to parametrically explore the effects of porosity, tubule size, and degree of mineralized reinforcing layer

To summarize the conclusions of this study:

- As porosity (volume fraction of tubules) increases, the stiffness and ultimate compressive strength decrease.
- With respect to porosity, loading parallel to the main axis of the tubules is stronger and more rigid when compared to loading perpendicular.
- As porosity increases, fracture toughness (K_{IC}) decreases.
- As porosity increases, the material becomes more deformable as larger displacements and larger strains are achieved during bending.
- As porosity increases, the loss modulus and tan-delta increases. This suggests that greater porosity allows for an increase in dampening ability and energy absorption.
- When porosity is conserved and the radius of the tubules is adjusted, fracture toughness remains constant. This suggest that radius does not influence fracture toughness.

9.5 Exploration of the Foam Core in the Feather Rachis

The exquisite architecture of the rachis, consisting of a hollow cavity filled with foam, was simulated in a bioinspired design that demonstrates the synergy of the two components in

enhancing the flexural strength. These structures provide an enhanced understanding of the mechanisms operating in feathers and suggest highly efficient solutions which can contribute to creating innovative materials inspired by the feather. Two prototypes were 3D printed and mechanically tested and modeled computationally using finite element analysis: thin-walled-square-cross-section shells (1) without a foam-filled core and (2) with a foam-filled core.

To summarize the conclusions of this study:

- While the foam does not influence the stiffness, it does affect the maximum force and the maximum bending stress.
- The foam-filled core acts as an elastic foundation that resists the buckling of the shell.
- The maximum force and maximum bending stress are significantly greater for the foam-filled shell than the hollow shell.
- Even when normalized for the additional weight of the foam, the maximum bending stress for the foam-filled composite is far superior to the hollow.
- This demonstrates that the addition of a foam core increases both the force and the maximum bending stress while maintaining a lightweight structure.
- FEA was used to model the stress distribution of both cases under three-point bending which shows how the outer-cortex concentrates the maximum bending stresses and the foam core resists buckling.
- FEA results are comparable to experimental results.

9.6 Morphological Characterization and Mechanical Properties of Primary Flight Feathers from Various Flying Styles

In this present investigation, different structural and mechanical properties of the feather

rachis of avian birds with various sizes and flying styles are explored. All avian feathers being composed of beta-keratin have similar fundamental structures (general sandwich structure) and material properties (density), but slight differences in composition and geometry allow for variation in mechanical properties such as viscoelasticity (storage and loss modulus).

To summarize the conclusions of this study:

- The medullar foam density scales inversely with the size of the feather and thus the size of the bird. Larger birds have a less dense foamy center.
- The viscoelastic properties of the feather rachis are related to their densities. The more dense the higher the storage and loss moduli.
- Tan(delta) is conserved across feathers (~0.05-0.10) due to the inherent viscoelastic properties of β-keratin found in all feathers.

9.7 Future Outlook

In closing, this dissertation points to the possibility of framing the study of biological materials as a combined material and structural optimization problem subject to the constraints of the functional needs of the material which includes optical transparency, crushing, slicing, impact resistance, and lightweight yet resistant to bending and torsion under aerodynamic conditions.

References

[1] M.A. Meyers, P.-Y. Chen, A.Y.-M. Lin, Y. Seki, Biological materials: Structure and mechanical properties, Prog. Mater. Sci. 53 (2008) 1–206. doi:10.1016/j.pmatsci.2007.05.002.

[2] M.A.A. Meyers, J. McKittrick, P.-Y. Chen, Structural Biological Materials: Critical Mechanics-Materials Connections, Science (80-.). 339 (2013) 773–779. doi:10.1126/science.1220854.

[3] M.A. Meyers, P.-Y. Chen, M.I. Lopez, Y. Seki, A.Y.M. Lin, Biological materials: a materials science approach., J. Mech. Behav. Biomed. Mater. 4 (2011) 626–57. doi:10.1016/j.jmbbm.2010.08.005.

[4] R.O. Ritchie, In pursuit of damage tolerance in engineering and biological materials, MRS Bull. 39 (2014) 880–890. doi:10.1557/mrs.2014.197.

[5] U.G.K. Wegst, H. Bai, E. Saiz, A.P. Tomsia, R.O. Ritchie, C. Ortiz, M. Boyce, U.G.K. Wegst, H. Bai, E. Saiz, A.P. Tomsia, R.O. Ritchie, Bioinspired structural materials, Nat. Mater. 14 (2014) 23–36. doi:10.1038/nmat4089.

[6] A. Velasco-Hogan, J. Xu, M.A. Meyers, Additive Manufacturing as a Method to Design and Optimize Bioinspired Structures, Adv. Mater. (2018). doi:10.1002/adma.201800940.

[7] B.S. Lazarus, A. Velasco-Hogan, T. Gómez-del Río, M.A. Meyers, I. Jasiuk, A review of impact resistant biological and bioinspired materials and structures, J. Mater. Res. Technol. (2020). doi:10.1016/j.jmrt.2020.10.062.

[8] E. Arzt, Biological and artificial attachment devices: Lessons for materials scientists from flies and geckos, Mater. Sci. Eng. C. 26 (2006) 1245–1250. doi:10.1016/j.msec.2005.08.033.

[9] P.-Y. Chen, J. McKittrick, M.A.A. Meyers, Biological materials: Functional adaptations and bioinspired designs, Prog. Mater. Sci. 57 (2012) 1492–1704. doi:10.1016/j.pmatsci.2012.03.001.

[10] S. Zhang, Building from the bottom up, Mater. Today. 6 (2003) 20–27. doi:10.1016/S1369-7021(03)00530-3.

[11] V. Charpentier, P. Hannequart, S. Adriaenssens, O. Baverel, E. Viglino, S. Eisenman, Kinematic amplification strategies in plants and engineering, Smart Mater. Struct. (2017). doi:10.1088/1361-665X/aa640f.

[12] P.-Y. Chen, a Y.M. Lin, Y.-S. Lin, Y. Seki, a G. Stokes, J. Peyras, E. a Olevsky, M. a Meyers, J. McKittrick, Structure and mechanical properties of selected biological materials., J. Mech. Behav. Biomed. Mater. 1 (2008) 208–26. doi:10.1016/j.jmbbm.2008.02.003.

[13] S. Weiner, H.D. Wagner, The material bone: Structure mechanical function relations, Annu. Rev. Mater. Sci. 28 (1998) 271–298. doi:DOI 10.1146/annurev.matsci.28.1.271.

[14] J.Y. Rho, L. Kuhn-Spearing, P. Zioupos, Mechanical properties and the hierarchical structure of bone, Med. Eng. Phys. 20 (1998) 92–102. doi:10.1016/S1350-4533(98)00007-1.

[15] P. Fratzl, H.S. Gupta, E.P. Paschalis, P. Roschger, Structure and mechanical quality of the collagen–mineral nano-composite in bone, J. Mater. Chem. 14 (2004) 2115–2123. doi:10.1039/B402005G.

[16] M.F. Ashby, L.J. Gibson, U. Wegst, R. Olive, The Mechanical Properties of Natural Materials. I. Material Property Charts, Proc. R. Soc. A Math. Phys. Eng. Sci. 450 (1995) 123–140. doi:10.1098/rspa.1995.0075.

[17] H.D. Espinosa, J.E. Rim, F. Barthelat, M.J. Buehler, Merger of structure and material in nacre and bone - Perspectives on de novo biomimetic materials, Prog. Mater. Sci. 54 (2009) 1059–1100. doi:10.1016/j.pmatsci.2009.05.001.

[18] W. Gao, Y. Zhang, D. Ramanujan, K. Ramani, Y. Chen, C.B. Williams, C.C.L. Wang, Y.C. Shin, S. Zhang, P.D. Zavattieri, The status, challenges, and future of additive manufacturing in engineering, Comput. Des. 69 (2015) 65–89. doi:10.1016/j.cad.2015.04.001.

[19] S.E. Naleway, M.M. Porter, J. McKittrick, M.A. Meyers, Structural Design Elements in Biological Materials: Application to Bioinspiration, Adv. Mater. 27 (2015) 5455–5476. doi:10.1002/adma.201502403.

[20] M.W. Barclift, C.B. Williams, Examing Variability in the Mechanical Properties of Parts Manufactured via PolyJet Direct 3D Printing, in: Int. Solid Free. Fabr. Symp., 2012: pp. 876–890. doi:10.1017/CBO9781107415324.004.

[21] R.L. Truby, J.A. Lewis, Printing soft matter in three dimensions, Nature. 540 (2016) 371–378. doi:10.1038/nature21003.

[22] L.S. Dimas, G.H. Bratzel, I. Eylon, M.J. Buehler, Tough composites inspired by mineralized natural materials: Computation, 3D printing, and testing, Adv. Funct. Mater. 23 (2013) 4629–4638. doi:10.1002/adfm.201300215.

[23] M.A. Meyers, P.-Y. Chen, A.Y.-M. Lin, Y. Seki, Biological materials: Structure and mechanical properties, Prog. Mater. Sci. 53 (2008) 1–206. doi:10.1016/j.pmatsci.2007.05.002.

[24] W. Yang, S.E. Naleway, M.M. Porter, M.A. Meyers, J. McKittrick, The armored carapace of the boxfish, Acta Biomater. 23 (2015) 1–10. doi:10.1016/j.actbio.2015.05.024.

[25] Z. Sun, E. Lee, S.W. Herring, Cranial sutures and bones: Growth and fusion in relation to masticatory strain, Anat. Rec. 276A (2004) 150–161. doi:10.1002/ar.a.20002.

[26] I.H. Chen, W. Yang, M.A. Meyers, Leatherback sea turtle shell: A tough and flexible biological design, Acta Biomater. 28 (2015) 2–12. doi:10.1016/j.actbio.2015.09.023.

[27] B. Achrai, H. Daniel Wagner, The red-eared slider turtle carapace under fatigue loading: The effect of rib-suture arrangement, Mater. Sci. Eng. C. 53 (2015) 128–133. doi:10.1016/j.msec.2015.04.040.

[28] I.A.A. Malik, M. Mirkhalaf, F. Barthelat, Bio-inspired "jigsaw"-like interlocking sutures: Modeling, optimization, 3D printing and testing, J. Mech. Phys. Solids. 102 (2017) 224–238. doi:10.1016/j.jmps.2017.03.003.

[29] E. Lin, Y. Li, C. Ortiz, M.C. Boyce, 3D printed, bio-inspired prototypes and analytical models for structured suture interfaces with geometrically-tuned deformation and failure behavior, J. Mech. Phys. Solids. 73 (2014). doi:10.1016/j.jmps.2014.08.011.

[30] R.O. Ritchie, The conflicts between strength and toughness, Nat. Mater. 10 (2011) 817–822. doi:10.1038/nmat3115.

[31] V. Khare, S. Sonkaria, G.Y. Lee, S.H. Ahn, W.S. Chu, From 3D to 4D printing – design, material and fabrication for multi-functional multi-materials, Int. J. Precis. Eng. Manuf. - Green Technol. 4 (2017) 291–299. doi:10.1007/s40684-017-0035-9.

[32] L.L. Erskine, A. a Heikal, S.M. Kuebler, M. Rumi, X. Wu, S.R. Marder, J.W. Perry, Two-photon polymerization initiators for three- dimensional optical data storage and microfabrication, Solid State Phys. 398 (1999) 51–54. doi:10.1038/17989.

[33] J. Mueller, D. Courty, M. Spielhofer, R. Spolenak, K. Shea, Mechanical Properties of Interfaces in Inkjet 3D Printed Single- and Multi-Material Parts, 3D Print. Addit. Manuf. 4 (2017) 193–199. doi:10.1089/3dp.2017.0038.

[34] J. Straub, Initial Work on the Characterization of Additive Manufacturing (3D Printing) Using Software Image Analysis, Machines. 3 (2015) 55–71. doi:10.3390/machines3020055.

[35] E. MacDonald, R. Wicker, Multiprocess 3D printing for increasing component functionality, Science (80-.). 353 (2016). doi:10.1126/science.aaf2093.

[36] Z. Sun, T. Liao, W. Li, Y. Dou, K. Liu, L. Jiang, S.W. Kim, J.H. Kim, S. Xue Dou, Fish-scale bio-inspired multifunctional ZnO nanostructures, NPG Asia Mater. 7 (2015). doi:10.1038/am.2015.133.

[37] J. Ivancik, D.D. Arola, The importance of microstructural variations on the fracture toughness of human dentin, Biomaterials. (2013). doi:10.1016/j.biomaterials.2012.10.032.

[38] C.P. Lin, W.H. Douglas, S.L. Erlandsen, Scanning electron microscopy of type I collagen at the dentin-enamel junction of human teeth, J. Histochem. Cytochem. (1993). doi:10.1177/41.3.8429200.

[39] P. Magne, W.S. Oh, M.R. Pintado, R. DeLong, Wear of enamel and veneering ceramics after laboratory and chairside finishing procedures., J. Prosthet. Dent. (1999). doi:10.1016/S0022-3913(99)70008-9.

[40] M. Goldberg, A.B. Kulkarni, M. Young, A. Boskey, Dentin: Structure, composition and mineralization, Front. Biosci. - Elit. (2011). doi:10.2741/e281.

[41] J.J. Kruzic, R.K. Nalla, J.H. Kinney, R.O. Ritchie, Crack blunting, crack bridging and resistance-curve fracture mechanics in dentin: Effect of hydration, Biomaterials. (2003). doi:10.1016/S0142-9612(03)00458-7.

[42] S. Habelitz, S.J. Marshall, G.W. Marshall, M. Balooch, Mechanical properties of human dental enamel on the nanometre scale, Arch. Oral Biol. (2001). doi:10.1016/S0003-9969(00)00089-3.

[43] R.L. Bowen, M.S. Rodriguez, Tensile strength and modulus of elasticity of tooth structure and several restorative materials., J. Am. Dent. Assoc. (1962). doi:10.14219/jada.archive.1962.0090.

[44] S.T. Rasmussen, R.E. Patchin, D.B. Scott, A.H. Heuer, Fracture Properties of Human Enamel and Dentin, J. Dent. Res. (1976). doi:10.1177/00220345760550010901.

[45] S.T. Rasmussen, Fracture Properties of Human Teeth in Proximity to the Dentinoenamel Junction, J. Dent. Res. (1984). doi:10.1177/00220345840630110501.

[46] O.M. el Mowafy, D.C. Watts, Fracture Toughness of Human Dentin, J. Dent. Res. (1986). doi:10.1177/00220345860650050901.

[47] C.P. Lin, W.H. Douglas, Structure-Property Relations and Crack Resistance at the Bovine Dentin-Enamel Junction, J. Dent. Res. (1994). doi:10.1177/00220345940730050901.

[48] S. Lees, F.R. Rollins, Anisotropy in hard dental tissues, J. Biomech. (1972). doi:10.1016/0021-9290(72)90027-9.

[49] F.R. von der Fehr, A study of carious lesions produced in vivo in unabraded, abraded, exposed, and F-treated human enamel surfaces, with emphasis on the X-ray dense outer layer, Arch. Oral Biol. (1967). doi:10.1016/0003-9969(67)90103-3.

[50] C.L. Davidson, I.S. Hoekstra, J. Arends, Microhardness of sound, decalcified and etched tooth enamel related to the calcium content, Caries Res. (1974). doi:10.1159/000260101.

[51] H.H.K. Xu, D.T. Smith, S. Jahanmir, E. Romberg, J.R. Kelly, V.P. Thompson, E.D. Rekow, Indentation damage and mechanical properties of human enamel and dentin, J. Dent. Res. (1998). doi:10.1177/00220345980770030601.

[52] D.D. Arola, R.K. Reprogel, Tubule orientation and the fatigue strength of human dentin, Biomaterials. (2006). doi:10.1016/j.biomaterials.2005.10.005.

[53] L. Angker, M. V. Swain, N. Kilpatrick, Micro-mechanical characterisation of the properties of primary tooth dentine, J. Dent. (2003). doi:10.1016/S0300-5712(03)00045-9.

[54] M. Giannini, C.J. Soares, R.M. De Carvalho, Ultimate tensile strength of tooth structures, Dent. Mater. (2004). doi:10.1016/S0109-5641(03)00110-6.

[55] K.J. Koester, J.W. Ager, R.O. Ritchie, The effect of aging on crack-growth resistance and toughening mechanisms in human dentin, Biomaterials. (2008). doi:10.1016/j.biomaterials.2007.12.008.

[56] B. Wang, W. Yang, J. McKittrick, M.A. Meyers, Keratin: Structure, mechanical properties, occurrence in biological organisms, and efforts at bioinspiration, Prog. Mater. Sci. (2016). doi:10.1016/j.pmatsci.2015.06.001.

[57] R.D.B. Fraser, T.P. MacRae, G.E. Rogers, Keratins: Their Composition, Structure, and Biosynthesis, 52 (1972) 29–30.

[58] J. McKittrick, P.Y. Chen, S.G. Bodde, W. Yang, E.E. Novitskaya, M.A. Meyers, The structure, functions, and mechanical properties of keratin, JOM. (2012). doi:10.1007/s11837-012-0302-8.

[59] B. Wang, T.N. Sullivan, A review of terrestrial, aerial and aquatic keratins: the structure and mechanical properties of pangolin scales, feather shafts and baleen plates, J. Mech. Behav. Biomed. Mater. (2017). doi:10.1016/j.jmbbm.2017.05.015.

[60] J.G. Rouse, M.E. Van Dyke, A review of keratin-based biomaterials for biomedical applications, Materials (Basel). (2010). doi:10.3390/ma3020999.

[61] W. Huang, Impact resistant and energy absorbent natural keratin materials: horns and hooves, (2018) 1–213.

[62] D. Labonte, C.J. Clemente, A. Dittrich, C.-Y. Kuo, A.J. Crosby, D.J. Irschick, W. Federle, Extreme positive allometry of animal adhesive pads and the size limits of adhesion-based climbing, Proc. Natl. Acad. Sci. 113 (2016) 1297–1302. doi:10.1073/pnas.1519459113.

[63] B. Wang, W. Yang, V.R. Sherman, M.A. Meyers, Pangolin armor: Overlapping, structure, and mechanical properties of the keratinous scales, Acta Biomater. 41 (2016) 60–74. doi:10.1016/j.actbio.2016.05.028.

[64] R.D.B. Fraser, T.P. MacRae, E. Suzuki, Structure of the α-keratin microfibril, J. Mol. Biol. (1976). doi:10.1016/S0022-2836(76)80129-5.

[65] C.N. Pace, J.M. Scholtz, A helix propensity scale based on experimental studies of peptides and proteins, Biophys. J. (1998). doi:10.1016/s0006-3495(98)77529-0.

[66] F.H.C. Crick, Is α-keratin a coiled coil?, Nature. (1952). doi:10.1038/170882b0.

[67] D.J. Bray, T.R. Walsh, M.G. Noro, R. Notman, Complete structure of an epithelial keratin

dimer: Implications for intermediate filament assembly, PLoS One. (2015). doi:10.1371/journal.pone.0132706.

[68] M. Toni, L. Dalla Valle, L. Alibardi, Hard (beta-)keratins in the epidermis of reptiles: Composition, sequence, and molecular organization, J. Proteome Res. (2007). doi:10.1021/pr0702619.

[69] R.D.B. Fraser, D.A.D. Parry, The structural basis of the filament-matrix texture in the avian/reptilian group of hard β-keratins, J. Struct. Biol. (2011). doi:10.1016/j.jsb.2010.09.020.

[70] B. Wang, W. Yang, J. McKittrick, M.A. Meyers, Keratin: Structure, mechanical properties, occurrence in biological organisms, and efforts at bioinspiration, Prog. Mater. Sci. 76 (2016) 229–318.

[71] R.D.B. Fraser, D.A.D. Parry, Amino acid sequence homologies in the hard keratins of birds and reptiles, and their implications for molecular structure and physical properties, J. Struct. Biol. (2014). doi:10.1016/j.jsb.2014.10.012.

[72] D.A. Greenberg, D.S. Fudge, Regulation of hard α-keratin mechanics via control of intermediate filament hydration: Matrix squeeze revisited, Proc. R. Soc. B Biol. Sci. (2013). doi:10.1098/rspb.2012.2158.

[73] J.E. Bertram, J.M. Gosline, Functional design of horse hoof keratin: the modulation of mechanical properties through hydration effects., J. Exp. Biol. (1987).

[74] B.P. Korge, W.D. James, Keratin and keratinization, J. Am. Acad. Dermatol. (1994). doi:10.1016/S0190-9622(94)70012-5.

[75] C.C. Chou, M.J. Buehler, Structure and mechanical properties of human trichocyte keratin intermediate filament protein, Biomacromolecules. (2012). doi:10.1021/bm301254u.

[76] A.N. Parbhu, W.G. Bryson, R. Lal, Disulfide bonds in the outer layer of keratin fibers confer higher mechanical rigidity: Correlative nano-indentation and elasticity measurement with an AFM, Biochemistry. (1999). doi:10.1021/bi990746d.

[77] S.N. Collins, B.C. Cope, L. Hopegood, R.J. Latham, R.G. Linford, J.D. Reilly, Stiffness as a function of moisture content in natural materials: Characterisation of hoof horn samples, J. Mater. Sci. (1998). doi:10.1023/A:1004479803611.

[78] K.L. Johnson, M.W. Trim, D.K. Francis, W.R. Whittington, J.A. Miller, C.E. Bennett, M.F. Horstemeyer, Moisture, anisotropy, stress state, and strain rate effects on bighorn sheep horn keratin mechanical properties, Acta Biomater. (2017). doi:10.1016/j.actbio.2016.10.033.

[79] T.M. Winegard, D.S. Fudge, Deployment of hagfish slime thread skeins requires the transmission of mixing forces via mucin strands, J. Exp. Biol. (2010). doi:10.1242/jeb.038075.

[80] D.S. Fudge, K.H. Gardner, V.T. Forsyth, C. Riekel, J.M. Gosline, The mechanical properties of hydrated intermediate filaments: Insights from hagfish slime threads, Biophys. J. (2003). doi:10.1016/S0006-3495(03)74629-3.

[81] J. Cao, Is the α-β transition of keratin a transition of α-helices to β-pleated sheets. II. Synchrotron investigation for stretched single specimens, J. Mol. Struct. (2002). doi:10.1016/S0022-2860(01)00901-2.

[82] R. Paquin, P. Colomban, Nanomechanics of single keratin fibres: A Raman study of the α-helix → β-sheet transition and the effect of water, J. Raman Spectrosc. (2007). doi:10.1002/jrs.1672.

[83] L. Kreplak, J. Doucet, P. Dumas, F. Briki, New aspects of the α-helix to β-sheet transition in stretched hard α-keratin fibers, Biophys. J. (2004). doi:10.1529/biophysj.103.036749.

[84] Y. Yu, W. Yang, B. Wang, M.A. Meyers, Structure and mechanical behavior of human hair, Mater. Sci. Eng. C. (2017). doi:10.1016/j.msec.2016.12.008.

[85] Y. Yu, W. Yang, M. André Meyers, Viscoelastic properties of α-keratin fibers in hair, Acta Biomater. (2017). doi:10.1016/j.actbio.2017.09.012.

[86] B. Song, W.Y. Lu, C.J. Syn, W. Chen, The effects of strain rate, density, and temperature on the mechanical properties of polymethylene diisocyanate (PMDI)-based rigid polyurethane foams during compression, J. Mater. Sci. (2009). doi:10.1007/s10853-008-3105-0.

[87] M.A. Kasapi, J.M. Gosline, Strain-rate-dependent mechanical properties of the equine hoof wall, J. Exp. Biol. 199 (1996) 1133–1146.

[88] Y. Seki, M.S. Schneider, M.A. Meyers, Structure and mechanical behavior of a toucan beak, Acta Mater. (2005). doi:10.1016/j.actamat.2005.04.048.

[89] J.E. Bertram, J.M. Gosline, Fracture toughness design in horse hoof keratin., J. Exp. Biol. 125 (1986) 29–47.

[90] W. Huang, A. Zaheri, W. Yang, D. Kisailus, R.O. Ritchie, H. Espinosa, J. McKittrick, How Water Can Affect Keratin: Hydration-Driven Recovery of Bighorn Sheep (Ovis Canadensis) Horns, Adv. Funct. Mater. (2019). doi:10.1002/adfm.201901077.

[91] X. Xiao, J. Hu, Animal Hairs as Water-stimulated Shape Memory Materials: Mechanism and Structural Networks in Molecular Assemblies, Sci. Rep. (2016). doi:10.1038/srep26393.

[92] X. Xiao, H. Zhou, K. Qian, Mechanism study of biopolymer hair as a coupled thermo-water responsive smart material, Smart Mater. Struct. (2017). doi:10.1088/1361-665X/aa52da.

[93] Z.Q. Liu, D. Jiao, Z.F. Zhang, Remarkable shape memory effect of a natural biopolymer

in aqueous environment, Biomaterials. (2015). doi:10.1016/j.biomaterials.2015.06.032.

[94] T.N. Sullivan, Y. Zhang, P.D. Zavattieri, M.A. Meyers, Hydration-Induced Shape and Strength Recovery of the Feather, Adv. Funct. Mater. (2018). doi:10.1002/adfm.201801250.

[95] Z.Q. Liu, D. Jiao, Z.Y. Weng, Z.F. Zhang, Water-assisted self-healing and property recovery in a natural dermal armor of pangolin scales, J. Mech. Behav. Biomed. Mater. (2016). doi:10.1016/j.jmbbm.2015.10.031.

[96] J. McKittrick, P.Y. Chen, L. Tombolato, E.E. Novitskaya, M.W. Trim, G.A. Hirata, E.A. Olevsky, M.F. Horstemeyer, M.A. Meyers, Energy absorbent natural materials and bioinspired design strategies: A review, Mater. Sci. Eng. C. 30 (2010) 331–342. doi:10.1016/j.msec.2010.01.011.

[97] P.-Y. Chen, A.Y.M. Lin, J. McKittrick, M.A. Meyers, Structure and mechanical properties of crab exoskeletons, Acta Biomater. 4 (2008) 587–596. doi:10.1016/j.actbio.2007.12.010.

[98] D.A. Grosenbaugh, D.M. Hood, Keratin and associated proteins of the equine hoof wall., Am. J. Vet. Res. (1992).

[99] C.Y.J. Hémonnot, J. Reinhardt, O. Saldanha, J. Patommel, R. Graceffa, B. Weinhausen, M. Burghammer, C.G. Schroer, S. Köster, X-rays Reveal the Internal Structure of Keratin Bundles in Whole Cells, ACS Nano. (2016). doi:10.1021/acsnano.5b07871.

[100] M.A. Kasapi, J.M. Gosline, Exploring the possible functions of equine hoof wall tubules., Equine Vet. J. Suppl. (1998). doi:10.1111/j.2042-3306.1998.tb05116.x.

[101] M.A. Kasapi, J.M. Gosline, Micromechanics of the equine hoof wall: Optimizing crack control and material stiffness through modulation of the properties of keratin, J. Exp. Biol. (1999).

[102] W. Huang, N.A. Yaraghi, W. Yang, A. Velazquez-Olivera, Z. Li, R.O. Ritchie, D. Kisailus, S.M. Stover, J. McKittrick, A natural energy absorbent polymer composite: The equine hoof wall, Acta Biomater. (2019). doi:10.1016/j.actbio.2019.04.003.

[103] A. Kitchener, An analysis of the forces of fighting of the blackbuck (Antilope cervicapra) and the bighorn sheep (Ovis canadensis) and the mechanical design of the horn of bovids, J. Zool. (1988). doi:10.1111/j.1469-7998.1988.tb04983.x.

[104] M. Courtney, A. Courtney, Sheep Collisions: the Good, the Bad, and the TBI, (2007). http://arxiv.org/abs/0711.3804.

[105] R.C. Marshall, D.F.G. Orwin, J.M. Gillespie, Structure and biochemistry of mammalian hard keratin, Electron Microsc. Rev. (1991). doi:10.1016/0892-0354(91)90016-6.

[106] C.R. Jaslow, Mechanical properties of cranial sutures, J. Biomech. (1990). doi:10.1016/0021-9290(90)90059-C.

[107] N. Lee, M.F. Horstemeyer, H. Rhee, B. Nabors, J. Liao, L.N. Williams, Hierarchical multiscale structure–property relationships of the red-bellied woodpecker Beak, J. R. Soc. Interface. (2014).

[108] Z.Q. Zhang, J.L. Yang, Biomechanical dynamics of cranial sutures during simulated impulsive loading, Appl. Bionics Biomech. (2015). doi:10.1155/2015/596843.

[109] N. Lee, L.N. Williams, S. Mun, H. Rhee, R. Prabhu, K.R. Bhattarai, M.F. Horstemeyer, Stress wave mitigation at suture interfaces, Biomed. Phys. Eng. Express. (2017). doi:10.1088/2057-1976/aa777e.

[110] A. Maloul, J. Fialkov, D. Wagner, C.M. Whyne, Characterization of craniofacial sutures using the finite element method, J. Biomech. (2014). doi:10.1016/j.jbiomech.2013.09.009.

[111] J.E. McMurry, R.C. Fay, Chemistry 4th Edition, Pearson Educ. (2004). doi:10.1017/CBO9781107415324.004.

[112] T. Lingham-soliar, R.H.C. Bonser, J. Wesley-smith, Selective biodegradation of keratin matrix in feather rachis reveals classic bioengineering, Proc. R. Soc. B Biol. Sci. 277 (2010) 1161–1168.

[113] T.N. Sullivan, B. Wang, H.D. Espinosa, M.A. Meyers, Extreme lightweight structures: avian feathers and bones, Mater. Today. (2017). doi:10.1016/j.mattod.2017.02.004.

[114] L. Alibardi, Cell organization of barb ridges in regenerating feathers of the quail: Implications of the elongation of barb ridges for the evolution and diversification of feathers, Acta Zool. (2007). doi:10.1111/j.1463-6395.2007.00257.x.

[115] T.N. Sullivan, M. Chon, R. Ramachandramoorthy, M.R. Roenbeck, T.-T. Hung, H.D. Espinosa, M.A. Meyers, Reversible Attachment with Tailored Permeability: The Feather Vane and Bioinspired Designs, Adv. Funct. Mater. 27 (2017).

[116] Bonser, Purslow, The Young's modulus of feather keratin, J. Exp. Biol. (1995).

[117] I.M. Weiss, H.O.K. Kirchner, The peacock's train (Pavo cristatus and Pavo cristatus mut. alba) I. structure, mechanics, and chemistry of the tail feather coverts, J. Exp. Zool. Part A Ecol. Genet. Physiol. (2010). doi:10.1002/jez.641.

[118] T. Bachmann, J. Emmerlich, W. Baumgartner, J.M. Schneider, H. Wagner, Flexural stiffness of feather shafts: Geometry rules over material properties, J. Exp. Biol. (2012). doi:10.1242/jeb.059451.

[119] D.G. Crenshaw, Design and materials of feather shafts: very light, rigid structures., Symp. Soc. Exp. Biol. (1980). doi:10.1016/0021-9290(80)90226-2.

[120] R.H.C. Bonser, The mechanical properties of feather keratin, J. Zool. (1996). doi:10.1111/j.1469-7998.1996.tb05937.x.

[121] Mechanical Properties of Primary Feathers From the Pigeon, J. Exp. Biol. (1978).

[122] B. Wang, M.A. Meyers, Light Like a Feather: A Fibrous Natural Composite with a Shape Changing from Round to Square, Adv. Sci. 4 (2016).

[123] O. Lilienthal, Der Vogelflug als Grundlage der Fliegekunst, 2019. doi:10.1515/9783486775181.

[124] L.J. Gibson, M.F. Ashby, Cellular solids: Structure and properties, second edition, 2014. doi:10.1017/CBO9781139878326.

[125] B. Wang, M.A. Meyers, Seagull feather shaft: Correlation between structure and mechanical response, Acta Biomater. 48 (2016) 270–288.

[126] Q. Wu, C. Yang, A. Ohrndorf, H.J. Christ, J. Han, J. Xiong, Impact behaviors of human skull sandwich cellular bones: Theoretical models and simulation, J. Mech. Behav. Biomed. Mater. 104 (2020) 103669. doi:10.1016/j.jmbbm.2020.103669.

[127] R.M. Kulin, P.Y. Chen, F. Jiang, K.S. Vecchio, A study of the dynamic compressive behavior of Elk antler, Mater. Sci. Eng. C. 31 (2011) 1030–1041. doi:10.1016/j.msec.2011.03.002.

[128] Y. Seki, B. Kad, D. Benson, M.A. Meyers, The toucan beak: Structure and mechanical response, Mater. Sci. Eng. C. 26 (2006) 1412–1420. doi:https://doi.org/10.1016/j.msec.2005.08.025.

[129] H. Rhee, M.F. Horstemeyer, Y. Hwang, H. Lim, H. El Kadiri, W. Trim, A study on the structure and mechanical behavior of the Terrapene carolina carapace: A pathway to design bio-inspired synthetic composites, Mater. Sci. Eng. C. 29 (2009) 2333–2339. doi:10.1016/j.msec.2009.06.002.

[130] M. Thielen, T. Speck, R. Seidel, Viscoelasticity and compaction behaviour of the foam-like pomelo (Citrus maxima) peel, J. Mater. Sci. (2013). doi:10.1007/s10853-013-7137-8.

[131] G.B. Chai, S. Zhu, A review of low-velocity impact on sandwich structures, in: Proc. Inst. Mech. Eng. Part L J. Mater. Des. Appl., 2011. doi:10.1177/1464420711409985.

[132] S. Abrate, Localized impact on sandwich structures with laminated facings, Appl. Mech. Rev. (1997). doi:10.1115/1.3101689.

[133] J.P. Dear, H. Lee, S.A. Brown, Impact damage processes in composite sheet and sandwich honeycomb materials, Int. J. Impact Eng. (2005). doi:10.1016/j.ijimpeng.2005.02.005.

[134] P.M. Schubel, J.J. Luo, I.M. Daniel, Impact and post impact behavior of composite sandwich panels, Compos. Part A Appl. Sci. Manuf. (2007). doi:10.1016/j.compositesa.2006.06.022.

[135] K.S. Raju, B.L. Smith, J.S. Tomblin, K.H. Liew, J.C. Guarddon, Impact damage

resistance and tolerance of honeycomb core sandwich panels, J. Compos. Mater. (2008). doi:10.1177/0021998307088596.

[136] J.R.A. Taylor, Aquatic versus terrestrial crab skeletal support: Morphology, mechanics, molting and scaling, J. Exp. Biol. (2018). doi:10.1242/jeb.185421.

[137] E.E. de Obaldia, C. Jeong, L.K. Grunenfelder, D. Kisailus, P. Zavattieri, Analysis of the mechanical response of biomimetic materials with highly oriented microstructures through 3D printing, mechanical testing and modeling, J. Mech. Behav. Biomed. Mater. 48 (2015) 70–85. doi:10.1016/j.jmbbm.2015.03.026.

[138] L.K. Grunenfelder, E.E. De Obaldia, Q. Wang, D. Li, B. Weden, C. Salinas, R. Wuhrer, P. Zavattieri, D. Kisailus, Stress and damage mitigation from oriented nanostructures within the radular teeth of cryptochiton stelleri, Adv. Funct. Mater. (2014). doi:10.1002/adfm.201401091.

[139] S.E. Naleway, J.R.A. Taylor, M.M. Porter, M.A. Meyers, J. McKittrick, Structure and mechanical properties of selected protective systems in marine organisms., Mater. Sci. Eng. C. Mater. Biol. Appl. 59 (2016) 1143–67. doi:10.1016/j.msec.2015.10.033.

[140] S.H.D. Haddock, M.A. Moline, J.F. Case, Bioluminescence in the Sea, Ann. Rev. Mar. Sci. 2 (2010) 443–493. doi:10.1146/annurev-marine-120308-081028.

[141] M.J. Bakes, N.G. Elliott, G.J. Green, P.D. Nichols, Variation in lipid composition of some deep-sea fish (Teleostei: Oreosomatidae and Trachichthyidae), Comp. Biochem. Physiol. -- Part B Biochem. 111 (1995) 633–642. doi:10.1016/0305-0491(95)00024-3.

[142] M.A. Neighbors, B.G. Nafpaktitis, Lipid compositions, water contents, swimbladder morphologies and buoyancies of nineteen species of midwater fishes (18 myctophids and 1 neoscopelid), Mar. Biol. 66 (1982) 207–215. doi:10.1007/BF00397024.

[143] T. a Clarke, Feeding Habits of Stomiatoid Fishes From Hawaiian Waters, Fish. Bull. 80 (1982) 287–304.

[144] T.L. Hopkins, Trophic ecology of the stomiid (Pisces: Stomiidae) fish assemblage of the eastern Gulf of Mexico: strategies, selectivity and impact of a top mesopelagic predator group, Mar. Biol. 127 (1996) 179–192. doi:10.1007/BF00942102.

[145] C.P. Kenaley, Exploring feeding behaviour in deep-sea dragonfishes (Teleostei: Stomiidae): Jaw biomechanics and functional significance of a loosejaw, Biol. J. Linn. Soc. 106 (2012) 224–240. doi:10.1111/j.1095-8312.2012.01854.x.

[146] L. Li, C. Ortiz, Biological design for simultaneous optical transparency and mechanical robustness in the shell of placuna placenta, Adv. Mater. (2013). doi:10.1002/adma.201204589.

[147] J.G. Carter, J.A. Schneider, Condensing lenses and shell microstructure in Corculum (Mollusca: Bivalvia), J. Paleontol. (1997). doi:10.1017/S0022336000038956.

[148] S. Johnsen, E.A. Widder, Transparency and visibility of gelatinous zooplankton from the Northwestern Atlantic and Gulf of Mexico, Biol. Bull. (1998). doi:10.2307/1543145.

[149] A.F. Mensinger, J.F. Case, Luminescent properties of deep sea fish, J. Exp. Mar. Bio. Ecol. 144 (1990) 1–15. doi:10.1016/0022-0981(90)90015-5.

[150] R.H. Douglas, J.C. Partridge, K.S. Dulai, D.M. Hunt, C.W. Mullineaux, P.H. Hynninen, Enhanced retinal longwave sensitivity using a chlorophyll-derived photosensitiser in Malacosteus niger, a deep-sea dragon fish with far red bioluminescence, Vision Res. 39 (1999) 2817–2832. doi:10.1016/S0042-6989(98)00332-0.

[151] D.M. Hunt, K.S. Dulai, J.C. Partridge, P. Cottrill, J.K. Bowmaker, The molecular basis for spectral tuning of rod visual pigments in deep-sea fish., J. Exp. Biol. 204 (2001) 3333–3344.

[152] W.K. Gregory, Fish Skulls: A study of the Evolution of Natural Mechanisms, 1933.

[153] R.P. Shellis, B.K.B. Berkovitz, Observations on the dental anatomy of piranhas (Characidae) with special reference to tooth structure, J. Zool. 180 (1976) 69–84. doi:10.1111/j.1469-7998.1976.tb04664.x.

[154] S. V. Hainsworth, R.J. Delaney, G.N. Rutty, How sharp is sharp? Towards quantification of the sharpness and penetration ability of kitchen knives used in stabbings, Int. J. Legal Med. 122 (2008) 281–291. doi:10.1007/s00414-007-0202-6.

[155] J. Mahamid, A. Sharir, L. Addadi, S. Weiner, Amorphous calcium phosphate is a major component of the forming fin bones of zebrafish: Indications for an amorphous precursor phase, Proc. Nat. Acad. Sci. USA. 105 (2008) 12748–12753. doi:10.1073/pnas.0803354105.

[156] P.M. de Wolff, A simplified criterion for the reliability of a powder pattern indexing, J. Appl. Crystallogr. 1 (1968) 108–113. doi:10.1107/S002188986800508X.

[157] H.C. Benedict, A Note on the Fluorescence of Teeth in Ultra-Violet Rays, Science (80-.). 67 (1928) 442–442. doi:10.1126/science.67.1739.442.

[158] H.J. Horsley, Isolation of Fluorescent Material Present in Calcified Tissues, J. Dent. Res. 46 (1967) 106.

[159] C.A. McDevitt, W.G. Armstrong, Investigation into the nature of the fluorescent material in calcified tissues, J. Dent. Res. 48 (1969) 1108. doi:10.1177/00220345720510050901.

[160] R. Winter, Visualizing the Natural Dentition, J. Esthet. Restor. Dent. 5 (1993) 103–118. doi:10.1111/j.1708-8240.1993.tb00761.x.

[161] H. Matsumoto, S. Kitamura, T. Araki, Applications of fluorescence microscopy to studies of dental hard tissue., Front. Med. Biol. Eng. 10 (2001) 269–84. doi:10.1163/156855700750265459.

[162] Y.-K. Lee, Fluorescence properties of human teeth and dental calculus for clinical applications, J. Biomed. Opt. 20 (2015) 040901. doi:10.1117/1.JBO.20.4.040901.

[163] C. de C.A. Lopes, P.H.J.O. Limirio, V.R. Novais, P. Dechichi, Fourier transform infrared spectroscopy (FTIR) application chemical characterization of enamel, dentin and bone, Appl. Spectrosc. Rev. 53 (2018) 747–769. doi:10.1080/05704928.2018.1431923.

[164] M.M. Figueiredo, J.A.F. Gamelas, A.G. Martins, Characterization of Bone and Bone-Based Graft Materials Using FTIR Spectroscopy, in: Infrared Spectrosc. - Life Biomed. Sci., 2012. doi:10.5772/36379.

[165] L. Bachmann, R. Diebolder, R. Hibst, D.M. Zezell, Infrared absorption bands of enamel and dentin tissues from human and bovine teeth, Appl. Spectrosc. Rev. 38 (2003) 1–14. doi:10.1081/ASR-120017479.

[166] P.J. Wyatt, Measurement of special nanoparticle structures by light scattering, Anal. Chem. (2014). doi:10.1021/ac500185w.

[167] K.A. Shapovalov, Light scattering of cylindrical particles in Rayleigh- Gans-Debye approximation. 2. Randomly oriented particles, Atmos. Ocean Opt. 17 (2004) 627–629.

[168] P.-Y. Chen, J. Schirer, A. Simpson, R. Nay, Y.-S. Lin, W. Yang, M.I. Lopez, J. Li, E.A. Olevsky, M.A. Meyers, Predation versus protection: Fish teeth and scales evaluated by nanoindentation, J. Mater. Res. 27 (2012) 100–112. doi:10.1557/jmr.2011.332.

[169] N. Vargas-Becerril, R. García-García, J. Reyes-Gasga, Structural Changes in Human Teeth after Heating up to 1200°C in Argon Atmosphere, Mater. Sci. Appl. (2018). doi:10.4236/msa.2018.97046.

[170] G.W. Marshall, M. Balooch, R.R. Gallagher, S.A. Gansky, S.J. Marshall, Mechanical properties of the dentinoenamel junction: AFM studies of nanohardness, elastic modulus, and fracture, J. Biomed. Mater. Res. (2001). doi:10.1002/1097-4636(200101)54:1<87::AID-JBM10>3.0.CO;2-Z.

[171] J.R. Zijp, J.J. ten Bosch, Theoretical model for the scattering of light by dentin and comparison with measurements, Appl. Opt. (2009). doi:10.1364/ao.32.000411.

[172] L.E. Bagge, K.J. Osborn, S. Johnsen, Nanostructures and Monolayers of Spheres Reduce Surface Reflections in Hyperiid Amphipods, Curr. Biol. 26 (2016) 3071–3076. doi:10.1016/j.cub.2016.09.033.

[173] G. Ortí, A. Sivasundar, K. Dietz, M. Jégu, Phylogeny of the Serrasalmidae (Characiformes) based on mitochondrial DNA sequences, Genet. Mol. Biol. 31 (2008) 343–351. doi:10.1590/s1415-47572008000200030.

[174] G.T. Prance, M. Goulding, The Fishes and the Forest: Explorations in Amazonian Natural History., Brittonia. 33 (1981) 257. doi:10.2307/2806336.

[175] M.A. Kolmann, K.E. Cohen, K.E. Bemis, A.P. Summers, F.J. Irish, L.P. Hernandez, Tooth and consequences: Heterodonty and dental replacement in piranhas and pacus (Serrasalmidae), Evol. Dev. 21 (2019) 278–293. doi:10.1111/ede.12306.

[176] J.R. Grubich, S. Huskey, S. Crofts, G. Orti, J. Porto, Mega-Bites: Extreme jaw forces of living and extinct piranhas (Serrasalmidae), Sci. Rep. 2 (2012). doi:10.1038/srep01009.

[177] A. Huby, A. Lowie, A. Herrel, R. Vigouroux, F. Bruno, X. Raick, G. Kurchevski, A.L. Godinho, E. Parmentier, Functional diversity in biters: The evolutionary morphology of the oral jaw system in pacus, piranhas and relatives (Teleostei: Serrasalmidae), Biol. J. Linn. Soc. 127 (2019) 722–741. doi:10.1093/biolinnean/blz048/5486927.

[178] J.S. Huxley, G. Tesissier, Terminology of Relative Growth, Nature. 137 (1936) 780–781. doi:10.1038/148225a0.

[179] C.R. White, R.S. Seymour, Allometric scaling of mammalian metabolism, J. Exp. Biol. (2005). doi:10.1242/jeb.01501.

[180] J.C.J. Wei, G.A. Edwards, D.J. Martin, H. Huang, M.L. Crichton, M.A.F. Kendall, Allometric scaling of skin thickness, elasticity, viscoelasticity to mass for micro-medical device translation: From mice, rats, rabbits, pigs to humans, Sci. Rep. (2017). doi:10.1038/s41598-017-15830-7.

[181] M.W. Westneat, A biomechanical model for analysis of muscle force, power output and lower jaw motion in fishes, J. Theor. Biol. 223 (2003) 269–281. doi:10.1016/S0022-5193(03)00058-4.

[182] M.A. Meyers, Y.S. Lin, E.A. Olevsky, P.Y. Chen, Battle in the Amazon: Arapaima versus piranha, Adv. Eng. Mater. 14 (2012) B279–B288. doi:10.1002/adem.201180027.

[183] L.C. Rome, A. Sosnicki, I.H. Choi, The influence of temperature on muscle function in the fast swimming scup. II. The mechanics of red muscle., J. Exp. Biol. (1992).

[184] R.S. James, N.J. Cole, M.L.F. Davies, I.A. Johnston, Scaling of intrinsic contractile properties and myofibrillar protein composition of fast muscle in the fish Myoxocephalus scorpius L., J. Exp. Biol. (1998).

[185] B.A. Richard, P.C. Wainwright, Scaling the feeding mechanism of largemouth bass (Micropterus salmoides): Kinematics of prey capture, J. Exp. Biol. (1995).

[186] P.S. Ungar, Mammal teeth: Origin, evolution, and diversity, 2010. doi:10.5860/choice.48-3875.

[187] L.P. Bergqvist, The role of teeth in mammal history, Brazilian J. Oral Sci. (2003).

[188] P. Lucas, P. Constantino, B. Wood, B. Lawn, Dental enamel as a dietary indicator in mammals, BioEssays. (2008). doi:10.1002/bies.20729.

[189] P.S. Ungar, Mammalian dental function and wear: A review, Biosurface and Biotribology. (2015). doi:10.1016/j.bsbt.2014.12.001.

[190] A.H. Jheon, K. Seidel, B. Biehs, O.D. Klein, From molecules to mastication: The development and evolution of teeth, Wiley Interdiscip. Rev. Dev. Biol. (2013). doi:10.1002/wdev.63.

[191] W. Maier, Tooth Morphology and Dietary Specialization, in: Food Acquis. Process. Primates, 1984. doi:10.1007/978-1-4757-5244-1_13.

[192] D.S. Koussoulakou, L.H. Margaritis, S.L. Koussoulakos, A curriculum vitae of teeth: Evolution, generation, regeneration, Int. J. Biol. Sci. (2009). doi:10.7150/ijbs.5.226.

[193] P.W. Lucas, Dental Functional Morphology, 2004. doi:10.1017/cbo9780511735011.

[194] P.C.J. Donoghue, M. Rücklin, The ins and outs of the evolutionary origin of teeth, Evol. Dev. (2016). doi:10.1111/ede.12099.

[195] B. Berkovitz, P. Shellis, The Teeth of Non-Mammalian Vertebrates, 2016. doi:10.1016/c2014-0-02210-1.

[196] B. Berkovitz, P. Shellis, Tooth Formation, in: Teeth Non-Mammalian Vertebr., 2017. doi:10.1016/b978-0-12-802850-6.00009-6.

[197] B. Berkovitz, P. Shellis, Enameloid and Enamel, in: Teeth Non-Mammalian Vertebr., 2017. doi:10.1016/b978-0-12-802850-6.00012-6.

[198] N. Assaraf-Weill, B. Gasse, J. Silvent, C. Bardet, J.Y. Sire, T. Davit-Béal, Ameloblasts express type I collagen during amelogenesis, J. Dent. Res. (2014). doi:10.1177/0022034514526236.

[199] I. Sasagawa, Fine structural and cytochemical observations of dental epithelial cells during the enameloid formation stages in red stingrays Dasyatis akajei, J. Morphol. (2002). doi:10.1002/jmor.1097.

[200] I. Sasagawa, Mineralization patterns in elasmobranch fish, Microsc. Res. Tech. (2002). doi:10.1002/jemt.10219.

[201] I. Sasagawa, M. Ishiyama, H. Yokosuka, M. Mikami, T. Uchida, Tooth enamel and enameloid in actinopterygian fish, in: Front. Mater. Sci. China, 2009. doi:10.1007/s11706-009-0030-3.

[202] B. Berkovitz, P. Shellis, Dentine and Dental Pulp, in: Teeth Non-Mammalian Vertebr., 2017. doi:10.1016/b978-0-12-802850-6.00011-4.

[203] P.C. Wainwright, D.R. Bellwood, Ecomorphology of Feeding in Coral Reef Fishes, in: Coral Reef Fishes, 2002. doi:10.1016/b978-012615185-5/50004-9.

[204] K.F. Liem, Acquisition of Energy by Teleosts: Adaptive Mechanisms and Evolutionary Patterns, in: Environ. Physiol. Fishes, 1980. doi:10.1007/978-1-4899-3659-2_10.

[205] P.C. Wainwright, S.H. Huskey, R.G. Turingan, A.M. Carroll, Ontogeny of suction feeding capacity in snook, Centropomus undecimalis, J. Exp. Zool. Part A Comp. Exp. Biol. (2006). doi:10.1002/jez.a.255.

[206] P. Wainwright, A.M. Carroll, D.C. Collar, S.W. Day, T.E. Higham, R.A. Holzman, Suction feeding mechanics, performance, and diversity in fishes, Integr. Comp. Biol. (2007). doi:10.1093/icb/icm032.

[207] P.C. Wainwright, B.A. Richard, Predicting patterns of prey use from morphology of fishes, Environ. Biol. Fishes. (1995). doi:10.1007/BF00005909.

[208] M.J. Sonnefeld, R.G. Turingan, T.J. Sloan, Functional Morphological Drivers of Feeding Mode in Marine Teleost Fishes, Adv. Zool. Bot. (2014).

[209] A.W. Thompson, R. Betancur-R., H. López-Fernández, G. Ortí, A time-calibrated, multi-locus phylogeny of piranhas and pacus (Characiformes: Serrasalmidae) and a comparison of species tree methods, Mol. Phylogenet. Evol. (2014). doi:10.1016/j.ympev.2014.06.018.

[210] T.G. Northcote, R.G. Northcote, M.S. Arcifa, Differential cropping of the caudal fin lobes of prey fishes by the piranha, Serrasalmus spilopleura Kner, Hydrobiologia. (1986). doi:10.1007/BF00014215.

[211] A.T. da Silva, J. Zina, F.C. Ferreira, L.M. Gomiero, R. Goitein, Caudal fin-nipping by serrasalmus maculatus (Characiformes: Serrasalmidae) in a small water reservoir: Seasonal variation and prey selection, Zoologia. (2015). doi:10.1590/S1984-46702015000600004.

[212] R.P. Shellis, B.K.B. Berkovitz, Observations on the dental anatomy of piranhas (Characidae) with special reference to tooth structure, J. Zool. (1976). doi:10.1111/j.1469-7998.1976.tb04664.x.

[213] W.E. Burgess, Check List of the Freshwater Fishes of South and Central America, Copeia. (2004). doi:10.1643/ot-04-142.

[214] M.C. Andrade, T. Giarrizzo, M. Jégu, Tometes camunani (Characiformes: Serrasalmidae), a new species of phytophagous fish from the Guiana Shield, rio Trombetas basin, Brazil, Neotrop. Ichthyol. (2013). doi:10.1590/S1679-62252013000200008.

[215] S.B. Correa, K.O. Winemiller, H. LóPez-Fernández, M. Galetti, Evolutionary Perspectives on Seed Consumption and Dispersal by Fishes, Bioscience. (2007). doi:10.1641/b570907.

[216] M. Goulding, M.L. Carvalho, Life history and management of the tambaqui (Colossoma macropomum, Characidae): an important Amazonian food fish, Rev. Bras. Zool. (1982). doi:10.1590/s0101-81751982000200001.

[217] M.A. Kolmann, R. Dean Grubbs, D.R. Huber, R. Fisher, N.R. Lovejoy, G.M. Erickson, Intraspecific variation in feeding mechanics and bite force in durophagous stingrays, J. Zool. (2018). doi:10.1111/jzo.12530.

[218] D.R. Huber, T.G. Eason, R.E. Hueter, P.J. Motta, Analysis of the bite force and mechanical design of the feeding mechanism of the durophagous horn shark Heterodontus francisci, J. Exp. Biol. (2005). doi:10.1242/jeb.01816.

[219] R.S. Mehta, Ecomorphology of the moray bite: Relationship between dietary extremes and morphological diversity, in: Physiol. Biochem. Zool., 2009. doi:10.1086/594381.

[220] A. Herrel, S. Petrochic, M. Draud, Sexual dimorphism, bite force and diet in the diamondback terrapin, J. Zool. (2018). doi:10.1111/jzo.12520.

[221] A. Herrel, V. Holanova, Cranial morphology and bite force in Chamaeleolis lizards - Adaptations to molluscivory?, Zoology. (2008). doi:10.1016/j.zool.2008.01.002.

[222] A. Herrel, J.C. O'Reilly, A.M. Richmond, Evolution of bite performance in turtles, J. Evol. Biol. (2002). doi:10.1046/j.1420-9101.2002.00459.x.

[223] K.R. Mara, P.J. Motta, D.R. Huber, Bite force and performance in the durophagous bonnethead shark, Sphyrna tiburo, J. Exp. Zool. Part A Ecol. Genet. Physiol. (2010). doi:10.1002/jez.576.

[224] Y. Delaunois, A. Huby, C. Malherbe, G. Eppe, É. Parmentier, P. Compère, Microstructural and compositional variation in pacu and piranha teeth related to diet specialization (Teleostei: Serrasalmidae), J. Struct. Biol. (2020). doi:10.1016/j.jsb.2020.107509.

[225] L.M. Gordon, M.J. Cohen, K.W. MacRenaris, J.D. Pasteris, T. Seda, D. Joester, Amorphous intergranular phases control the properties of rodent tooth enamel, Science (80-.). 347 (2015) 746–750. doi:10.1126/science.1258950.

[226] Y.F. Jia, F.Z. Xuan, Anisotropic fatigue behavior of human enamel characterized by multi-cycling nanoindentation, J. Mech. Behav. Biomed. Mater. (2012). doi:10.1016/j.jmbbm.2012.10.008.

[227] Y.R. Jeng, T.T. Lin, H.M. Hsu, H.J. Chang, D. Bin Shieh, Human enamel rod presents anisotropic nanotribological properties, J. Mech. Behav. Biomed. Mater. (2011). doi:10.1016/j.jmbbm.2010.12.002.

[228] M. Yahyazadehfar, D. Bajaj, D.D. Arola, Hidden contributions of the enamel rods on the fracture resistance of human teeth, Acta Biomater. (2013). doi:10.1016/j.actbio.2012.09.020.

[229] J.E. Lambert, C.A. Chapman, R.W. Wrangham, N. Lou Conklin-Brittain, Hardness of cercopithecine foods: Implications for the critical function of enamel thickness in exploiting fallback foods, Am. J. Phys. Anthropol. (2004). doi:10.1002/ajpa.10403.

[230] M. Yahyazadehfar, D. Arola, The role of organic proteins on the crack growth resistance of human enamel, Acta Biomater. 19 (2015). doi:10.1016/j.actbio.2015.03.011.

[231] S. Krauss, E. Monsonego-Ornan, E. Zelzer, P. Fratzl, R. Shahar, Mechanical function of a complex three-dimensional suture joining the bony elements in the shell of the red-eared slider turtle, Adv. Mater. (2009). doi:10.1002/adma.200801256.

[232] I.C. Gebeshuber, J.H. Kindt, J.B. Thompson, Y. Del Amo, H. Stachelberger, M.A. Brzezinski, G.D. Stucky, D.E. Morse, P.K. Hansma, Atomic force microscopy study of living diatoms in ambient conditions, J. Microsc. 212 (2003) 292–299. doi:10.1111/j.1365-2818.2003.01275.x.

[233] A. Nanci, Ten Cate's Oral Histology, in: Elsevier, 2013.

[234] S.J. Marshall, M. Balooch, S. Habelitz, G. Balooch, R. Gallagher, G.W. Marshall, The dentin - enamel junction - a natural, multilevel interface, J. Eur. Ceram. Soc. (2003). doi:10.1016/S0955-2219(03)00301-7.

[235] M.P. Walker, B. Fricke, Dentin-Enamel Junction of Human Teeth, in: Wiley Encycl. Biomed. Eng., 2006. doi:10.1002/9780471740360.ebs1431.

[236] D. Shimizu, G.A. Macho, Functional significance of the microstructural detail of the primate dentino-enamel junction: A possible example of exaptation, J. Hum. Evol. (2007). doi:10.1016/j.jhevol.2006.08.004.

[237] D.S. Brauer, G.W. Marshall, S.J. Marshall, Variations in human DEJ scallop size with tooth type, J. Dent. (2010). doi:10.1016/j.jdent.2010.03.010.

[238] Y. Li, C. Ortiz, M.C. Boyce, Stiffness and strength of suture joints in nature, Phys. Rev. E - Stat. Nonlinear, Soft Matter Phys. (2011). doi:10.1103/PhysRevE.84.062904.

[239] R.W. Thresher, G.E. Saito, The stress analysis of human teeth, J. Biomech. (1973). doi:10.1016/0021-9290(73)90003-1.

[240] L. Tombolato, E.E. Novitskaya, P. Chen, F.A. Sheppard, J. Mckittrick, Microstructure , elastic properties and deformation mechanisms of horn keratin, Acta Biomater. 6 (2010) 319–330. doi:10.1016/j.actbio.2009.06.033.

[241] M.A. Kasapi, J.M. Gosline, Design complexity and fracture control in the equine hoof wall, J. Exp. Biol. (1997).

[242] W. Huang, A. Zaheri, J. Jung, H.D. Espinosa, J. Mckittrick, Hierarchical structure and compressive deformation mechanisms of bighorn sheep (Ovis canadensis) horn, Acta Biomater. 64 (2017) 1–14. doi:10.1016/j.actbio.2017.09.043.

[243] L. Tombolato, E.E. Novitskaya, P.Y. Chen, F.A. Sheppard, J. McKittrick, Microstructure, elastic properties and deformation mechanisms of horn keratin, Acta Biomater. (2010). doi:10.1016/j.actbio.2009.06.033.

[244] M.W. Trim, M.F. Horstemeyer, H. Rhee, H. El, L.N. Williams, J. Liao, K.B. Walters, J. Mckittrick, S. Park, The effects of water and microstructure on the mechanical properties of bighorn sheep (Ovis canadensis) horn keratin, Acta Biomater. 7 (2011) 1228–1240. doi:10.1016/j.actbio.2010.11.024.

[245] W.R. Corning, A.A. Biewener, In vivo strains in pigeon flight feather shafts: Implications for structural design, J. Exp. Biol. (1998).

[246] P.L. Tubaro, A comparative study of aerodynamic function and flexural stiffness of outer tail feathers in birds, J. Avian Biol. (2003). doi:10.1034/j.1600-048X.2003.03084.x.

[247] G. Osváth, O. Vincze, D.-C. David, L.J. Nagy, Á.Z. Lendvai, R.L. Nudds, P.L. Pap, Morphological characterization of flight feather shafts in four bird species with different flight styles, Biol. J. Linn. Soc. (2020). doi:10.1093/biolinnean/blaa108.

[248] C.J. Pennycuick, Modelling the Flying Bird, 1st ed., Elsevier, Burlington, USA, 2008.

[249] P.L. Pap, G. Osváth, K. Sándor, O. Vincze, L. Bărbos, A. Marton, R.L. Nudds, C.I. Vágási, Interspecific variation in the structural properties of flight feathers in birds indicates adaptation to flight requirements and habitat, Funct. Ecol. (2015). doi:10.1111/1365-2435.12419.

[250] B. Bruderer, D. Peter, A. Boldt, F. Liechti, Wing-beat characteristics of birds recorded with tracking radar and cine camera, Ibis (Lond. 1859). (2010). doi:10.1111/j.1474-919X.2010.01014.x.

[251] B. Baliga, I. Szabo, D.L. Altshuler, Range of motion in the avian wing is strongly associated with flight behavior and body mass, Sci. Adv. (2019). doi:10.1126/sciadv.aaw6670.

[252] T.N. Sullivan, Y. Zhang, P. Zavattieri, M.A. Meyers, Hydration-induced shape and strength recovery of the feather, Submitted. (2018).